

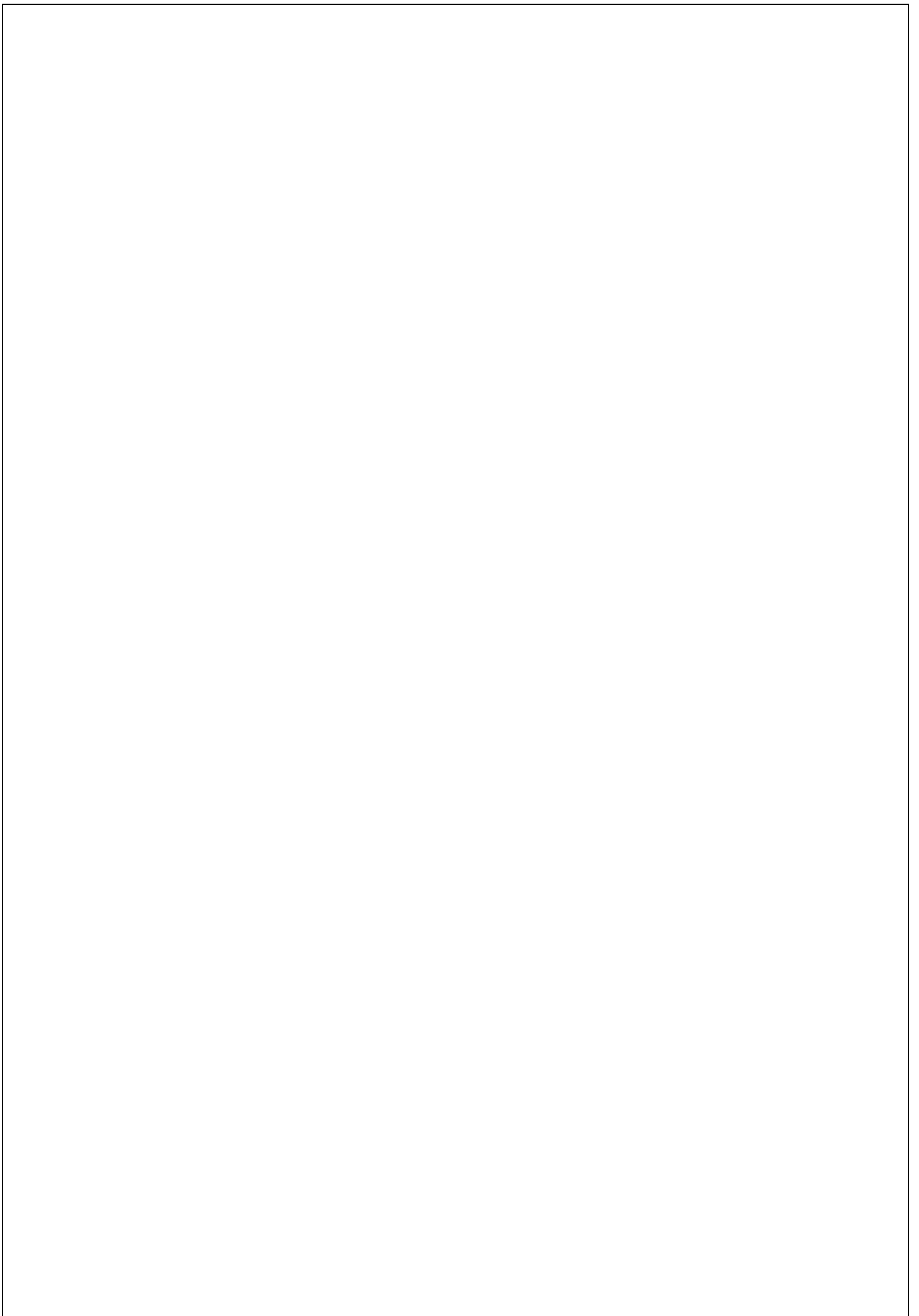


NATIONAL TECHNICAL UNIVERSITY OF ATHENS
SCHOOL OF ELECTRICAL AND COMPUTER ENGINEERING
DIVISION OF INFORMATION TRANSMISSION AND MATERIAL
TECHNOLOGY

Optical Beamforming Networks for Next Generation Mobile Communication Systems

by
Christos V. Tsokos

Αθήνα, Οκτώβριος 2022





NATIONAL TECHNICAL UNIVERSITY OF ATHENS
SCHOOL OF ELECTRICAL AND COMPUTER ENGINEERING
DIVISION OF INFORMATION TRANSMISSION AND MATERIAL
TECHNOLOGY

Optical Beamforming Networks for Next Generation Mobile Communication Systems

Doctoral dissertation

by
Christos V. Tsokos

Συμβουλευτική Επιτροπή : Ηρακλής Αβραμόπουλος
Νικόλαος Ουζούνογλου
Νικόλαος Πλέρος

Εγκρίθηκε από την επταμελή εξεταστική επιτροπή την 11^η Οκτωβρίου 2022.

.....
Ηρακλής Αβραμόπουλος
Καθηγητής Ε.Μ.Π.

.....
Νικόλαος Πλέρος
Αναπληρωτής Καθηγητής Α.Π.Θ.

.....
Νικόλαος Ουζούνογλου
Ομότιμος Καθηγητής Ε.Μ.Π.

.....
Νεκτάριος Κοζύρης
Καθηγητής Ε.Μ.Π.

.....
Αθανάσιος Παναγόπουλος
Καθηγητής Ε.Μ.Π.

.....
Δημήτριος Σούντιρας
Καθηγητής Ε.Μ.Π.

.....
Εμμανουήλ Βαρβαρίγος
Καθηγητής Ε.Μ.Π.

Αθήνα, Οκτώβριος 2022

.....
Χρήστος Β. Τσώκος

Διδάκτωρ Ηλεκτρολόγος Μηχανικός και Μηχανικός Υπολογιστών Ε.Μ.Π.

Copyright © Χρήστος Β. Τσώκος, 2022.
Με επιφύλαξη παντός δικαιώματος. All rights reserved.

Απαγορεύεται η αντιγραφή, αποθήκευση και διανομή της παρούσας εργασίας, εξ ολοκλήρου ή τμήματος αυτής, για εμπορικό σκοπό. Επιτρέπεται η ανατύπωση, αποθήκευση και διανομή για σκοπό μη κερδοσκοπικό, εκπαιδευτικής ή ερευνητικής φύσης, υπό την προϋπόθεση να αναφέρεται η πηγή προέλευσης και να διατηρείται το παρόν μήνυμα. Ερωτήματα που αφορούν τη χρήση της εργασίας για κερδοσκοπικό σκοπό πρέπει να απευθύνονται προς τον συγγραφέα.

Οι απόψεις και τα συμπεράσματα που περιέχονται σε αυτό το έγγραφο εκφράζουν τον συγγραφέα και δεν πρέπει να ερμηνευθεί ότι αντιπροσωπεύουν τις επίσημες θέσεις του Εθνικού Μετσόβιου Πολυτεχνείου.

Abstract

The 5G vision for a fully mobile and connected society defines a set of performance requirements for next-generation wireless networks, which is very broad and demanding and is still unfulfilled. Compared to the current generation, different system performance indicators are required for the 5G communication systems, including peak data rates on the gigabit per second level, end-to-end latencies in the order of a few milliseconds, very high traffic volume density, and improved spectral, energy, and cost efficiencies. With these requirements on the table and in particular, because of the huge growth of mobile data demand, it has become apparent to the research community that the very limited spectrum resources available in the sub 6-GHz band can no longer meet the system needs. Therefore, high-speed mobile communication systems at frequencies above 6 GHz became a promising path. However, as the operating frequency shifts deeper into the millimetre band, the system performance starts to deteriorate due to the severe free-space loss and blockage effects experienced by the electromagnetic signals at these bands. To overcome this hurdle, high-gain antenna arrays with hundreds or even thousands of antenna elements can be deployed, forming very directional beams which greatly enhance the signal-to-noise ratio. However, these beams provide only limited spatial coverage, which is not compliant with a dynamic environment with multiple users. Within this context, beamforming, a well-known functionality in modern wireless networks thanks to its ability to steer a single or multiple wireless beams to a user or group of users that should be served at each point of time, is expected to become even more important.

Both in the case of single- and the case of multi-beam operation, beamforming networks apply proper excitation signals to each antenna element with time delays that correspond to the intended beam directions. In current beamforming networks operating in the sub 6-GHz band, adjustment of these delays is realized in the electronic domain using digital electronic platforms, analog microwave components, or hybrid implementations. However, at higher operating frequencies these electronic solutions start having significant limitations. In order to overcome this problem, solutions based on microwave photonics (MWP) technology have been proposed as a powerful alternative for the processing of microwave or mm-wave signals and the implementation of high-performance beamforming networks in the optical domain.

Within this framework, the present dissertation deals with the design, implementation, system integration, and performance evaluation of optical beamforming networks (OBFNs) for multi-element array antennas. Following a holistic and systematic approach, we start by analysing the theory that dictates the operation of such complex systems and we continue with the design, implementation, system integration as well as performance evaluation of four different OBFNs.

In particular, the theoretical analysis starts from the fundamental theory of a single antenna element and continues with the theory that dictates the operation of multi-element antenna arrays. Before introducing the concept of the OBFNs, a thorough analysis of the principle operation of the MWP systems is provided.

Having a solid theoretical background, the design, implementation, system integration, and performance evaluation of a 2×4 OBFN based on bulk micro-optics elements are reported. More specifically, the 2×4 TTD-OBFN is developed using commercial off-the-shelf optical modulators, optical delay lines (ODLs), optical attenuators, optical couplers, and photodiodes. It can support single-beam, multi-beam, and multicast beamforming with continuous tuning of the beam angles and feed an array antenna with four elements. The operation of the proposed OBFN is based on a number of ODLs for introducing time delays to the copies of the signals that correspond to different wireless beams and different antenna

elements. As a first step, through extensive simulation studies, its principle of operation is validated and then, by using signals with high-order quadrature amplitude modulation formats at 15 GHz, the OBFN is evaluated for all three modes of operation (single-beam, multi-beam, and multicast).

Leveraging the advancements in photonic integration technology, a 1×4 OBFN photonic integrated circuit (PIC) based on the hybrid integration of InP components in a Si₃N₄ platform is presented. Apart from measuring its key figure of merits, the prototype is extensively tested using modulated signals at 5 GHz and 10 GHz and evaluated in terms of bit-error ratios, exhibiting error-free operation for all the experimental scenarios. This is the very first time that a fully functional and self-contained OBFN is evaluated within system experiments in lab settings.

For the first time, a solid background for the design and operation of a multi-beam optical beamforming network based on Blass matrix is provided via a mathematical analysis and extensive simulation studies. The analysis starts from the processing steps that are required for the microwave photonics signals at the input and output of the Blass matrix and a simple design and an algorithm for the configuration of the matrix, taking into account the properties of the Mach-Zehnder Interferometers (MZIs) as tunable optical couplers is proposed. The multi-beam capability of the beamforming network is validated and the impact of the beam squinting effect which is inherent to this design is evaluated as a function of the symbol rate, modulation format and pulse shaping of the signals. Furthermore, assuming operation with quadrature amplitude modulation (QAM) signals at 28.5 GHz, it is proven through error-vector magnitude (EVM) calculations that the beam squinting effect is not critical in typical cases, where the symbol rate remains below 3 Gbaud. Moreover, the additional frequency dependence of the proposed beamforming network due to inevitable asymmetries of the MZIs and length variations of the waveguides inside the Blass matrix, and the additional impact of imperfections is investigated with respect to the couplers inside the MZIs and the phase shifters inside the Blass matrix. In all cases, the impact of the asymmetries and the imperfections remain negligible for realistic fabrication and operation conditions. Within the framework of the European-funded project, ICT-HAMLET, the first-ever fully integrated optical beamforming networks based on the Blass-matrix architecture were designed, fabricated, and evaluated. A 2×2 and an 8×8 optical beamforming networks have been fabricated based on the hybrid integration of the InP, PolyBoard and TriPleX photonic platforms. The optical beam forming networks are based on PZT-based phase actuators for fast and low-power configuration. Both prototypes are extensively characterized in lab settings and the main individual building blocks are evaluated. As demonstrated in this dissertation, thanks to the advancements in photonic integrated circuit technology, MWP enables the realization of key functionalities in microwave systems that either are complex or even not directly possible in the RF domain. Among the several systems that MWP can radically transform, mobile wireless communication systems stand on top of this list, and it is expected that MWP will enable the commercial deployment of the 5G mobile communication networks as well as the next generations in beyond 5G era.

Keywords: 5G networks, millimeter wave communication systems, multi-element array antennas, optical beamforming networks, single-beam beamforming, multi-beam beamforming, multicast, microwave photonics, photonic integration circuit technology, Blass matrix architecture, optical true-time delay lines, optical phase shifters.

Περίληψη

Τα ασύρματα δίκτυα πέμπτης Γενεάς (5G) βρίσκονται ήδη σε προχωρημένο στάδιο ανάπτυξης, ανοίγοντας νέους ορίζοντες όχι μόνο για το κόσμο των τηλεπικοινωνιών αλλά και για τις ανθρώπινες κοινωνίες. Για να εκπληρωθούν όμως αυτές οι φιλόδοξες απαιτήσεις των 5G δικτύων, έχει γίνει φανερό ότι οι περιορισμένοι φασματικοί πόροι που είναι διαθέσιμοι κάτω από τα 6 GHz δεν επαρκούν. Ως εκ τούτου, τα συστήματα κινητών επικοινωνιών υψηλής χωρητικότητας σε συχνότητες άνω των 6 GHz, θεωρούνται το μέσο όχι μόνο για την πλήρη αξιοποίηση των δυνατοτήτων των δικτύων 5G αλλά και για την ανάπτυξη των επόμενων Γενεών. Ωστόσο, όσο η συχνότητα λειτουργίας μετατοπίζεται σε υψηλότερες φασματικές ζώνες, η απόδοση του συστήματος αρχίζει να επιδεινώνεται λόγω των σοβαρών απωλειών διάδοσης. Για να ξεπεραστεί αυτό το εμπόδιο, στοιχειοκεραίες αποτελούμενες από εκατοντάδες ή ακόμα και χιλιάδες στοιχεία πρέπει να χρησιμοποιηθούν ώστε να δημιουργήσουν κατευθυντικές δέσμες έτσι ώστε να αυξήσουν το κέρδος της ασύρματης ζεύξης και να βελτιώσουν το σηματοθορυβικό λόγο του συστήματος. Ωστόσο, αυτές οι δέσμες παρέχουν μόνο περιορισμένη χωρική κάλυψη, η οποία δεν ενδείκνυται για χρήση σε ένα γρήγορα μεταβαλλόμενο περιβάλλον με πολλούς χρήστες. Σε αυτό το πλαίσιο, ο ρόλος της λειτουργίας της σχηματοποίησης δεσμών, χάρη στην ικανότητά της να κατευθύνει μία ή περισσότερες ασύρματες δέσμες προς τις επιθυμητές κατευθύνσεις, αναμένεται να γίνει ακόμη σπουδαιότερος.

Τόσο στην περίπτωση λειτουργίας μιας δέσμης όσο και στην περίπτωση λειτουργίας πολλαπλών δεσμών, τα δίκτυα σχηματοποίησης δεσμών εφαρμόζουν κατάλληλα σήματα διέγερσης σε κάθε ξεχωριστό στοιχείο μιας στοιχειοκεραίας με σχετικές χρονικές καθυστερήσεις ή σχετικές φάσεις που αντιστοιχούν στις επιθυμητές γωνίες στόχευσής των μικροκυματικών δεσμών. Στα τρέχοντα δίκτυα σχηματοποίησης δεσμών που λειτουργούν στη φασματική περιοχή κάτω των 6 GHz, η προσαρμογή αυτών των καθυστερήσεων πραγματοποιείται είτε ψηφιακά, είτε αναλογικά είτε με υβριδικές υλοποιήσεις. Ωστόσο, στις υψηλότερες συχνότητες, το εύρος ζώνης των σημάτων σε σχέση με την φέρουσα συχνότητα αυξάνεται όπως και ο αριθμός των κεραιών, με αποτέλεσμα αυτές οι ηλεκτρονικές λύσεις να αρχίζουν να έχουν σημαντικούς περιορισμούς. Για να ξεπεραστεί αυτό το εμπόδιο, έχουν προταθεί λύσεις που βασίζονται στην τεχνολογία μικροκυματικής φωτονικής ως μια ισχυρή εναλλακτική τεχνολογία για την επεξεργασία σημάτων μικροκυμάτων και την υλοποίηση δικτύων σχηματοποίησης δεσμών υψηλής απόδοσης, αμιγώς στο οπτικό πεδίο.

Στο πλαίσιο αυτό, η παρούσα διατριβή πραγματεύεται το σχεδιασμό, την υλοποίηση, την ολοκλήρωση συστημάτων και την πειραματική αξιολόγηση της απόδοσης των οπτικών δικτύων σχηματοποίησης δεσμών για στοιχειοκεραίες πολλαπλών στοιχείων. Ακολουθώντας μια ολιστική και συστηματική προσέγγιση, η ανάλυση ξεκινάει από τη θεωρία που υπαγορεύει τη λειτουργία τέτοιων πολύπλοκων συστημάτων και συνεχίζει με το σχεδιασμό, την υλοποίηση, καθώς και την πειραματική αξιολόγηση τεσσάρων διαφορετικών οπτικών δικτύων σχηματοποίησης δεσμών.

Συγκεκριμένα, προτάθηκε και αναλύθηκε μια αρχιτεκτονική ενός $M \times N$ οπτικού δικτύου σχηματοποίησης δεσμών, η οποία υποθέτοντας λειτουργία στη καθοδική ζεύξη ενός τηλεπικοινωνιακού καναλιού μπορεί να οδηγήσει μια στοιχειοκεραία με N στοιχεία και να συνθέσει M ανεξάρτητες μικροκυματικές δέσμες, ενώ υποθέτοντας λειτουργία στην ανοδική ζεύξη, μπορεί να υποστηρίξει την λήψη M ανεξάρτητων δεσμών. Για την πειραματική επαλήθευση της αρχής λειτουργίας της παραπάνω αρχιτεκτονικής, αναπτύχθηκε ένα πλήρως λειτουργικό σύστημα το οποίο μοντελοποιεί ένα 2×4 οπτικό δίκτυο σχηματοποίησης δεσμών. Η ανάπτυξη του συστήματος ακολούθησε τις βασικές αρχές της προτεινόμενης αρχιτεκτονικής και η υλοποίηση της βασίστηκε σε εμπορικά διαθέσιμα

οπτικά και οπτό-ηλεκτρονικά στοιχεία. Χρησιμοποιώντας διαμορφωμένα QAM σήματα με φέρουσες συχνότητες στα 15 GHz, το οπτικό δίκτυο αξιολογήθηκε, υπολογίζοντας τον αριθμό των εσφαλμένων ψηφίων και για τις τρεις διαφορετικές λειτουργίες (σηματοποίηση μονής δέσμης, σηματοποίηση πολλαπλών δεσμών και πολυεκπομπή).

Στη συνέχεια, παρουσιάζεται και αξιολογείται πειραματικά ένα πλήρως ολοκληρωμένο 1×4 οπτικό δίκτυο σηματοποίησης δέσμης χάρη στις InP και Si₃N₄ φωτονικές πλατφόρμες ολοκλήρωσης. Το ολοκληρωμένο δίκτυο υποστηρίζει τη δημιουργία και σηματοποίηση μιας μικροκυματικής δέσμης με κεντρικές συχνότητες έως και 40 GHz και μπορεί να επιλέγει γωνίες στόχευσης με συνεχές βήμα. Η πειραματική αξιολόγηση του συστήματος πραγματοποιήθηκε σε δυο στάδια. Στο πρώτο στάδιο, μετρήθηκε το κέρδος ζεύξης μέχρι τα 40 GHz, η εικόνα θορύβου καθώς και το SFDR_{2,3} στις συχνότητες 5 GHz και 10 GHz. Στο δεύτερο στάδιο, θεωρώντας το οπτικό δίκτυο είναι μέρος μιας καθοδικής ζεύξης ενός ασύρματου τηλεπικοινωνιακού συστήματος και χρησιμοποιώντας σήματα QAM με ρυθμό συμβόλων ίσο με 500 Mbaud στα 5 και 10 GHz ως σήματα εισόδου, αξιολογήσαμε την απόδοση του ως προς το ρυθμό εσφαλμένων ψηφίων και το διανυσματικό μέγεθος σφάλματος για γωνίες στόχευσης από 45° έως 135°.

Έπειτα, για πρώτη φορά, παρέχεται ένα στέρεο υπόβαθρο για το σχεδιασμό και τη λειτουργία ενός δικτύου οπτικής διαμόρφωσης δέσμης πολλαπλών δεσμών με βάση τη μήτρα Blass μέσω μαθηματικής ανάλυσης και εκτεταμένων μελετών προσομοίωσης. Αρχικά, επιβεβαιώνεται η αρχή λειτουργίας της αρχιτεκτονικής και συγκεκριμένα, αναλύεται πως η στροφή της οπτικής φάσης των διαμορφωμένων οπτικών σημάτων, η οποία επιτυγχάνεται χάρη στην οπτική μήτρα, μεταφράζεται σε ισοδύναμη στροφή φάσης στα μικροκυματικά σήματα στην έξοδο του δικτύου. Στη συνέχεια, παρουσιάζεται η ανάπτυξη ενός αλγορίθμου ο οποίος καθορίζει την λειτουργία τόσο οπτικών ολισθητών φάσεων αλλά και των συμβολόμετρων MZIs της μήτρας, έτσι ώστε να επιτευχθεί η σηματοποίηση πολλαπλών και ανεξάρτητων δεσμών.

Στα πλαίσια του Ευρωπαϊκού έργου, ICT-HAMLET, αναπτύχθηκε μια καινοτόμα υβριδική οπτική πλατφόρμα ολοκλήρωσης, συνδυάζοντας δυο παθητικές πλατφόρμες, την πολυμερική (PolyBoard) και την TriPleX, με την ενεργή InP πλατφόρμα. Συγκεκριμένα, αναπτύχθηκαν και χαρακτηρίστηκαν δυο πρωτότυπα. Το πρώτο πρωτότυπο (Precursor-1), φιλοξενεί ένα 2×2 οπτικό δίκτυο σηματοποίησης μικροκυματικών δεσμών βασισμένο στην αρχιτεκτονική Blass-matrix. Λαμβάνοντας υπόψιν όλες τις πληροφορίες και ευρήματα από τον χαρακτηρισμό του Precursor-1 πρωτότυπου, η κοινοπραξία προχώρησε στον σχεδιασμό και κατασκευή ενός 8×8 οπτικού δικτύου σηματοποίησης μικροκυματικών δεσμών (Module-1). Εκτός από το μεγαλύτερο Blass-matrix δίκτυο, το οποίο βασίζονταν αμιγώς σε οπτικούς πιεζό-ηλεκτρικούς (PZT) ολισθητές φάσης, το πρωτότυπο Module-1 σε σχέση με το Precursor-1, φιλοξενούσε μια οπτική πηγή άμεσης διαμόρφωσης για την επικοινωνία με τον οπτικό δίκτυο fronthaul, 8 InP διαμορφωτές πλάτους, 8 οπτικά φίλτρα και 16 φωτοδιόδους.

Στο τελευταίο κεφάλαιο αυτής της διατριβής, συγκεντρώνονται και παρουσιάζονται τα συμπεράσματα καθώς και προτάσεις για μελλοντική μελέτη.

Λέξεις κλειδιά: Δίκτυα 5ης Γενεάς, μικροκυματικά ασύρματα δίκτυα, μικροκυματική φωτονική, στοιχειοκεραίες, οπτικά δίκτυα σηματοποίησης μικροκυματικών δεσμών, σηματοποίηση μονής δέσμης, σηματοποίηση πολλαπλών δεσμών, πολυεκπομπή, φωτονική ολοκλήρωση, αρχιτεκτονική Blass-matrix, οπτικά στοιχεία πραγματικής καθυστέρησης, οπτικοί ολισθητές φάσης.

Εκτεταμένη Περίληψη

Από τις αρχές της δεκαετίας του 1980, παρατηρούμε την ταχεία εξέλιξη των ασύρματων συστημάτων επικοινωνιών, τα οποία από απλά συστήματα μετάδοσης φωνής, έχουν εξελιχθεί σε προηγμένα ευρυζωνικά συστήματα, ικανά να μεταδίδουν σε εικόνες και βίντεο υψηλής ευκρίνειας. Η εμφάνιση μιας νέας γενιάς ασύρματων συστημάτων, σχεδόν κάθε δεκαετία, έχει επιφέρει θεμελιώδεις και βαθιές επιπτώσεις στην καθημερινή ζωή και στις κοινωνικές δραστηριότητες των ανθρώπων, με αποτέλεσμα τη συνεχιζόμενη αύξηση του όγκου των δεδομένων που μεταδίδονται καθώς και των τερματικών συσκευών που χρησιμοποιούνται.

Πολύ σύντομα μετά την επιτυχημένη ανάπτυξη και εξάπλωση των ασυρμάτων δικτύων τέταρτης Γενεάς (4G), τα μεγάλα ερευνητικά ιδρύματα και οι πάροχοι ασύρματων δικτύων έστρεψαν το βλέμμα τους στην επόμενη Γενεά, γνωστή και έως, πέμπτη Γενεά (5G). Σύμφωνα με τις προβλέψεις, ο αριθμός των συνδρομητών κινητής τηλεφωνίας των δικτύων 5G θα φτάσει τον αντίστοιχο αριθμό των συνδρομητών των 4G δικτύων έως το τέλος του 2026 και θα τον ξεπεράσει ένα χρόνο αργότερα, φτάνοντας τις 4.4 δισεκατομμύρια συνδρομές.

Σε σύγκριση με τα 4G δίκτυα, τα 5G δίκτυα υπόσχονται 10 με 100 φορές πιο γρήγορες συνδέσεις στο διαδίκτυο με εξαιρετικά χαμηλή καθυστέρηση και θα είναι σε θέση να εξυπηρετούν ταυτόχρονα περισσότερους χρήστες ή συσκευές. Για να υλοποιηθούν όμως όλες αυτές οι προδιαγραφές, οι φέρουσες συχνότητες των 5G δικτύων θα πρέπει να μεταπηδήσουν σε νέες υψηλότερες φασματικές περιοχές στις οποίες υπάρχουν διαθέσιμοι φασματικοί πόροι που μπορούν να μεταφέρουν μεγαλύτερο ποσό πληροφορίας με μεγαλύτερους ρυθμούς μετάδοσης. Συγκεκριμένα, η μικροκυματική φασματική περιοχή γύρω από τα 28 GHz, με διαθέσιμο εύρος ζώνης 5.25 GHz (24.25-29.5 GHz) έγινε ευρέως αποδεκτή από τους μεγάλους παρόχους ως η ζώνη συχνοτήτων των δικτύων 5G.

Όμως, είναι γνωστό ότι σε αυτές τις υψηλές συχνότητες, το ηλεκτρομαγνητικό κύμα υποφέρει από τις σημαντικές απώλειες ελεύθερου χώρου γεγονός που υποβαθμίζει σημαντικά τον σηματοθορυβικό λόγο. Για να αντιμετωπιστεί αυτό το φαινόμενο και να αυξηθεί η εκπεμπόμενη ή λαμβανόμενη ισχύς του σήματος, στοιχειοκεραίες με πολύ υψηλό κέρδος μπορούν να χρησιμοποιηθούν έτσι ώστε να δημιουργήσουν πολύ κατευθυντικές δέσμες. Ωστόσο, η στενή δέσμη παρέχει περιορισμένη χωρική κάλυψη, καθιστώντας την ακατάλληλη για την εξυπηρέτηση πολλαπλών χρηστών, οι οποίοι θα απέχουν χωρικά. Μέσα σε αυτό το πλαίσιο, ο ρόλος της τεχνικής της σχηματοποίησης δεσμών (beamforming), μιας τεχνικής πολύ γνωστής στα σύγχρονα ασύρματα δίκτυα, χάρη στην ικανότητά της να κατευθύνει μία ή περισσότερες ασύρματες δέσμες σε έναν χρήστη ή ομάδα χρηστών που θα πρέπει να εξυπηρετούνται σε κάθε χρονική στιγμή, αναμένεται να γίνει ακόμη σπουδαιότερος.

Τόσο στην περίπτωση λειτουργίας μιας δέσμης όσο και στην περίπτωση λειτουργίας πολλαπλών δεσμών, τα δίκτυα σχηματοποίησης δεσμών εφαρμόζουν κατάλληλα σήματα διέγερσης σε κάθε ξεχωριστό στοιχείο μιας στοιχειοκεραίας με σχετικές χρονικές καθυστερήσεις ή σχετικές φάσεις που αντιστοιχούν στις επιθυμητές γωνίες στόχευσής των μικροκυματικών δεσμών. Στα τρέχοντα beamforming δίκτυα που λειτουργούν στη φασματική περιοχή κάτω των 6 GHz, η προσαρμογή αυτών των καθυστερήσεων πραγματοποιείται είτε ψηφιακά, είτε αναλογικά με τη χρήση αναλογικών μικροκυμάτων στοιχείων είτε με υβριδικές υλοποιήσεις. Ωστόσο, στις υψηλότερες συχνότητες, το εύρος ζώνης των σημάτων σε σχέση με την φέρουσα συχνότητα αυξάνεται όπως και ο αριθμός των κεραιών, με αποτέλεσμα αυτές οι ηλεκτρονικές λύσεις να αρχίζουν να έχουν σημαντικούς περιορισμούς όσον αφορά την ακρίβεια χρονικής καθυστέρησης, τις απώλειες, το μέγεθος, το βάρος, τις ηλεκτρομαγνητικές παρεμβολές, τη κατανάλωση ισχύος (ειδικά

στην περίπτωση ψηφιακών λύσεων) αλλά και το κόστος. Για να ξεπεραστεί αυτό το εμπόδιο, έχουν προταθεί λύσεις που βασίζονται στην τεχνολογία μικροκυματικής φωτονικής (Microwave Photonics – MWP) ως μια ισχυρή εναλλακτική τεχνολογία για την επεξεργασία μικροκυμάτων σημάτων και την υλοποίηση δικτύων σχηματοποίησης δεσμών υψηλής απόδοσης, αμιγώς στο οπτικό πεδίο.

Στο πλαίσιο αυτό, η παρούσα διατριβή πραγματεύεται το σχεδιασμό, την υλοποίηση, την ολοκλήρωση συστημάτων και την πειραματική αξιολόγηση οπτικών δικτύων σχηματοποίησης δεσμών (Optical Beamforming Networks) για στοιχειοκεραίες πολλαπλών στοιχείων. Πιο συγκεκριμένα, οι στόχοι αλλά και τα κύρια αποτελέσματα της διατριβής συνοψίζονται ως εξής:

Στόχος 1: Ανάπτυξη πλατφόρμας προσομοίωσης MWP συστημάτων και μικροκυματικών στοιχειοκεραίων, καθώς και μιας εργαλειοθήκης ψηφιακής επεξεργασίας σήματος για την αποδιαμόρφωση σημάτων με σχήματα διαμόρφωσης φάσης και πλάτους.

Κύρια αποτελέσματα: Για την ανάπτυξη της πλατφόρμας προσομοίωσης μικροκυματικών φωτονικών συστημάτων και συγκεκριμένα τη προσομοίωση οπτικών δικτύων σχηματοποίησης δεσμών, ήταν αναγκαίο να μελετηθούν και να αναλυθούν τόσο οι αρχές λειτουργίας μιας στοιχειοκεραίας αλλά όσο και ενός μικροκυματικού φωτονικού συστήματος. Για το λόγο αυτό, στο **Κεφάλαιο 2** γίνεται εκτενής αναφορά στις βασικές αρχές και κύρια χαρακτηριστικά των κεραίων ενώ στο **Κεφάλαιο 3** αναλύονται τα βασικά στοιχεία ενός μικροκυματικού φωτονικού συστήματος.

Συγκεκριμένα, στο **Κεφάλαιο 2**, η θεωρητική ανάλυση ξεκινάει με τον βασικό ορισμό μιας απλής κεραίας. Στη συνέχεια, γίνεται αναφορά στις τρεις περιοχές ακτινοβολίας μιας κεραίας οι οποίες είναι η κοντινή περιοχή, η περιοχή Fresnel και η μακρινή περιοχή. Δεδομένης της εφαρμογής που διαπραγματεύεται η παρούσα διατριβή και ότι σε κλασσικά συστήματα τηλεπικοινωνιών η απόσταση μεταξύ του πομπού και του δέκτη είναι της τάξεως τουλάχιστον κάποιων δεκάδων μέτρων, στην ανάλυση αυτού του κεφαλαίου θεωρούμε λειτουργία μόνο στη μακρινή περιοχή. Έπειτα, εισάγεται ο ορισμός του διανύσματος Poynting, το οποίο εκφράζει τη στιγμιαία ροή ηλεκτρομαγνητικής ισχύος ανά μονάδα επιφάνειας και της έντασης ακτινοβολίας που χαρακτηρίζει τη μακρινή περιοχή μιας κεραίας και εκφράζει την ισχύ που ακτινοβολείται ανά μονάδα στερεάς γωνίας. Επίσης, εισάγονται οι έννοιες του διαγράμματος ακτινοβολίας, που αποτελεί τη γραφική παράσταση του τρόπου ακτινοβολίας μιας κεραίας καθώς μεταβάλλεται το σημείο παρατήρησης του ηλεκτρομαγνητικού πεδίου και της κατευθυντικότητας η οποία ορίζεται ως ο λόγος της έντασης ακτινοβολίας μιας κεραίας προς την ένταση ακτινοβολίας ενός ισοτροπικού ακτινοβολητή που εκπέμπει την ίδια ισχύ ακτινοβολίας. Έπειτα, η προσοχή μας εστιάζεται στην λειτουργία των στοιχειοκεραίων που αποτελούν και σημαντικό σύστημα της παρούσας διατριβής. Συγκεκριμένα, οι στοιχειοκεραίες είναι διατάξεις που αποτελούνται από πολλούς όμοιους ακτινοβολητές του ίδιου προσανατολισμού και ακτινοβολούν ή λαμβάνουν ταυτοχρόνως. Το συνολικό μακρινό πεδίο προκύπτει πολλαπλασιάζοντας το μακρινό πεδίο ενός από τα όμοια στοιχεία ακτινοβολίας που αποτελούν τη στοιχειοκεραία με τον παράγοντα διάταξης που προσδιορίζεται συναρτήσει των συντεταγμένων θέσης και των ρευματικών διεγέρσεων των ακτινοβολίας. Συνεπώς, μπορούμε να σχηματοποιήσουμε την δέσμη ακτινοβολίας μιας γραμμικής στοιχειοκεραίας είτε αλλάζοντας την χωρική απόσταση των στοιχείων που την αποτελούν είτε αλλάζοντας την σχετική διαφορά φάσης και πλάτους των ρευμάτων διέγερσης. Δεδομένης λοιπόν μιας στοιχειοκεραίας, το δίκτυο σχηματοποίησης δέσμης, που τροφοδοτεί τους ακτινοβολητές της κεραίας, είναι εκείνο που καθορίζει τόσο την γωνία στόχευσης όσο και το πλάτος των πλευρικών λοβών ακτινοβολίας. Εν συνεχεία, ορίζονται οι έννοιες των λειτουργιών σχηματοποίησης μονής δέσμης (single-beam beamforming), σχηματοποίησης πολλαπλών δεσμών (multi-beam beamforming) και την πολλαπλής εκπομπής (multicast). Με βάση τον

μηχανισμό εισαγωγής της καθυστέρησης, υπάρχουν δυο κατηγορίες συστημάτων σχηματοποίησης δεσμών. Στη πρώτη κατηγορία, τα δίκτυα εισάγουν πραγματική καθυστέρηση στα ρεύματα διέγερσης ενώ στη δεύτερη κατηγορία χρησιμοποιούνται ολισθητές φάσης, οι οποίοι καθορίζουν τις σχετικές φάσεις των ρευμάτων. Στην περίπτωση επεξεργασίας σημάτων με μεγάλο φασματικό περιεχόμενο, τα δίκτυα που εμπίπτουν στην δεύτερη κατηγορία είναι επιρρεπή στο φαινόμενο αλληθωρίσματος (beam squint). Το φαινόμενο αυτό έχει ως αποτέλεσμα οι διάφορες φασματικές συχνότητες που αποτελούν το σήμα να κατευθύνονται σε διαφορετικές γωνίες στόχευσης. Συνεπώς, όπως θα δειχθεί στο Κεφάλαιο 6, τα δίκτυα σχηματοποίησης δέσμης βασισμένα σε ολισθητές φάσης πρέπει να σχεδιάζονται προσεκτικά ώστε να μην αλλοιώνουν την ποιότητα των ασύρματων δικτύων. Τέλος, στο Κεφάλαιο 2, γίνεται αναφορά στις τεχνικές που καθορίζουν τα σχετικά πλάτη των ρευμάτων διέγερσης με στόχο την μείωση της ισχύος των πλευρικών λοβών με τίμημα όμως την αύξηση του εύρους του κύριου λοβού.

Στο **Κεφάλαιο 3**, ορίζεται η μικροκυματική φωτονική τεχνολογία ως το πεδίο το οποίο συνδυάζει τις αρχές της μικροκυματικής τεχνολογίας με εκείνες της φωτονικής, με σκοπό να υλοποιήσει λειτουργίες οι οποίες είτε είναι πολύπλοκες ή ακόμα και αδύνατες να υλοποιηθούν με κλασσικά μικροκυματικά στοιχεία. Τρία θεωρούνται τα δομικά στοιχεία κάθε μικροκυματικού φωτονικού δικτύου, η οπτική πηγή, ο ηλεκτρο-οπτικός διαμορφωτής και η φωτοδιόδος. Για κάθε ένα από αυτά τα στοιχεία αναλύεται με τη βοήθεια μαθητικών σχέσεων η βασική αρχή λειτουργίας τους. Στη συνέχεια, εισάγονται τρεις βασικοί δείκτες απόδοσης ενός μικροκυματικού φωτονικού δικτύου. Ο πρώτος έχει να κάνει με το κέρδος της ζεύξης και ορίζεται ως ο λόγος της ισχύος του σήματος στην έξοδο ενός μικροκυματικού φωτονικού συστήματος ως προς την ισχύ του σήματος στην είσοδο. Ο δεύτερος αναφέρεται στην εικόνα θορύβου, που όπως και στα κλασσικά μικροκυματικά δίκτυα, καθορίζει πόσο θόρυβο προσθέτει το δίκτυο. Τέλος, ο τρίτος ονομάζεται spurious free dynamic range (SFDR₃) και αναφέρεται στην επίδραση των μη-γραμμικοτήτων. Συγκεκριμένα, το SFDR₃, υποδεικνύει το εύρος των ισχύων του σήματος εισόδου κατά το οποίο το αντίστοιχο σήμα στην έξοδο έχει ισχύ μεγαλύτερη από το επίπεδο θορύβου ενώ παράλληλα οι μη γραμμικοί τόνοι τρίτης τάξης έχουν ισχύ χαμηλότερη από το επίπεδο θορύβου και συνεπώς δεν μπορούν να ανιχνευθούν.

Παράλληλα, με την ανάλυση των θεωριών που διέπουν τη λειτουργία των στοιχειοκεραιών και κατά συνέπεια των συστημάτων σχηματοποίησης δεσμών αλλά και της μικροκυματικής φωτονικής τεχνολογίας, αναπτύχθηκε μια ολοκληρωμένη εργαλειοθήκη ψηφιακής επεξεργασίας σημάτων (Digital Signal Processing – DSP) για την ορθή αποδιαμόρφωση των ληφθέντων σημάτων. Η εργαλειοθήκη παρουσιάζεται στο **Παράρτημα I**. Συγκεκριμένα, ο πρώτος αλγόριθμος αντισταθμίζει τα σφάλματα δειγματοληψίας δεδομένου ότι το ρολόι του πομπού δεν είναι συγχρονισμένο με το αντίστοιχο στον δέκτη. Στη συνέχεια, ο δεύτερος αλγόριθμος αντισταθμίζει τυχόν διαφορές πλατών των αποδιαμορφωμένων σημάτων σε σύγκριση με τα αρχικά. Ο τρίτος αλγόριθμος αντισταθμίζει διαφορές πλάτους και φάσης μεταξύ των In-phase και Quadrature συνιστωσών ενός Quadrature Amplitude Modulation (QAM) σήματος. Έπειτα, ο τέταρτος αλγόριθμος πρόκειται για μια οικογένεια προσαρμοστικών ισοσταθμιστών αλγορίθμων. Τέλος, ο πέμπτος αλγόριθμος είναι υπεύθυνος για την διόρθωση τόσο της φάσης όσο και της συχνότητας του αποδιαμορφωμένου σήματος. Χάρη στην πλατφόρμα, η κάθε μικροκυματική δέσμη μπορεί να μεταφέρει είτε απλά ημιτονοειδή σήματα είτε QAM σήματα κωδικοποιώντας έως και 8 ψηφία ανά σύμβολο (256-QAM). Επίσης, η πλατφόρμα περιλαμβάνει ένα μοντέλο μετάδοσης σημάτων μέσα από ένα additive white Gaussian noise (AWGN) κανάλι και υπολογίζει το ηλεκτρομαγνητικό πεδίο των σημάτων σε διάφορα σημεία παρατήρησης σε σχέση με τη θέση του πομπού. Με βάση αυτό το πεδίο και χρησιμοποιώντας την εργαλειοθήκη ψηφιακής επεξεργασίας σημάτων, η πλατφόρμα

αξιολογεί την απόδοση του τηλεπικοινωνιακού συστήματος απεικονίζοντας τα διαγράμματα αστερισμού και υπολογίζοντας τον ρυθμό εσφαλμένων ψηφίων καθώς και το διανυσματικό μέγεθος σφάλματος (error vector magnitude).

Συνοψίζοντας, το αποτέλεσμα της παραπάνω ερευνητικής δραστηριότητας ήταν η ανάπτυξη μιας πλατφόρμας προσομοίωσης στο προγραμματιστικό περιβάλλον MATLAB, η οποία μοντελοποιεί οπτικά συστήματα σχηματοποίησης δεσμών και προσομοιώνει την λειτουργία τους θεωρώντας ότι τροφοδοτούν γραμμικές στοιχειοκεραίες με N στοιχεία, δημιουργώντας M διαφορετικές δέσμες.

Στόχος 2: Σχεδιασμός και υλοποίηση ενός οπτικού δικτύου σχηματοποίησης δεσμών με τη χρήση εμπορικά διαθέσιμων μικροοπτικών διατάξεων.

Κύρια αποτελέσματα: Έχοντας αναλύσει την αρχή λειτουργίας των οπτικών συστημάτων σχηματοποίησης δεσμών, το επόμενο βήμα ήταν ο σχεδιασμός μιας καινοτόμου αρχιτεκτονικής. Συγκεκριμένα, στο **Κεφάλαιο 4**, προτάθηκε και αναλύθηκε μια αρχιτεκτονική ενός $M \times N$ οπτικού δικτύου σχηματοποίησης δεσμών, η οποία υποθέτοντας λειτουργία στην καθοδική ζεύξη (downlink) ενός τηλεπικοινωνιακού καναλιού μπορεί να οδηγήσει μια στοιχειοκεραία με N στοιχεία και να συνθέσει M ανεξάρτητες μικροκυματικές δέσμες, ενώ υποθέτοντας λειτουργία στην ανοδική ζεύξη, μπορεί να υποστηρίξει την λήψη M ανεξάρτητων δεσμών. Η λειτουργία του δικτύου βασίζεται στη χρήση μιας συστοιχίας ρυθμιζόμενων οπτικών γραμμών καθυστέρησης καθώς και στη χρήση μιας συστοιχίας ρυθμιζόμενων οπτικών εξασθενητών.

Χρησιμοποιώντας την πλατφόρμα προσομοίωσης, η οποία αναπτύχθηκε και περιεγράφηκε στον Στόχο 1, η αρχή λειτουργίας της παραπάνω αρχιτεκτονικής και της ικανότητας της να υποστηρίξει την σχηματοποίηση είτε μονής δέσμης είτε πολλαπλών δεσμών αλλά και πολλαπλή εκπομπή, επαληθεύτηκε. Συγκεκριμένα, στο πλαίσιο αυτών των μελετών, το μέγεθος του οπτικού δικτύου σχηματοποίησης δεσμών επιλέχθηκε να είναι είτε 2×4 είτε 2×8 και να λειτουργεί και στις δυο περιπτώσεις στην καθοδική ζεύξη ενός τηλεπικοινωνιακού συστήματος. Με αυτό τον τρόπο, το δίκτυο μπορούσε να τροφοδοτεί στοιχειοκεραίες με τέσσερα και οχτώ στοιχεία, αντίστοιχα. Για την υποδοχή των εκπεμπόμενων σημάτων, θεωρήθηκε ότι στην πλευρά του δέκτη, δηλαδή στο σημείο παρατήρησης, υπάρχει μια μονή κεραία η οποία λαμβάνει το πεδίο προς αυτή την κατεύθυνση. Τόσο για την στοιχειοκεραία στον πομπό αλλά όσο και για την κεραία στον δέκτη, θεωρήθηκε η χρήση ισοτροπικών κεραίων.

Στην περίπτωση σχηματοποίησης μονής δέσμης, το πλάτος του οπτικού φέροντος διαμορφώθηκε από ένα μικροκυματικό σήμα με συχνότητα 15 GHz, το οποίο έφερε είτε QPSK, 16-QAM ή 64-QAM σχήμα διαμόρφωσης με ρυθμό συμβόλων 1 Gbaud. Το διαμορφωμένο οπτικό σήμα συζεύχθηκε με την πρώτη σειρά του του 2×4 οπτικού δικτύου ενώ η είσοδος της δεύτερης σειράς θεωρήθηκε τερματισμένη σε φορτίο. Οι σχετικές σχέσεις καθυστέρησης και πλάτους των οπτικών σημάτων πριν από το στάδιο φωτοανίχνευσης ρυθμίστηκαν σύμφωνα με τη επιθυμητή γωνία στόχευσης και την αντίστοιχη επιθυμητή κατανομή των πλατών. Στις θύρες εξόδου του οπτικού δικτύου και μετά το στάδιο φωτοανίχνευσης, τα μικροκυματικά σήματα εκπεμπόντουσαν από την στοιχειοκεραία και μεταδίδονταν μέσω ενός AWGN καναλιού. Για όλες τις περιπτώσεις που μελετήθηκαν, το σύστημα λειτουργούσε χωρίς την ανίχνευση λαθών.

Για την περίπτωση σχηματοποίησης πολλαπλών δεσμών, θεωρήθηκε το ίδιο 2×4 οπτικό δίκτυο με μοναδική διαφορά ότι ένα δεύτερο ανεξάρτητο μικροκυματικό σήμα διαμορφώνεται από μια δεύτερη οπτική πηγή και τροφοδοτείται στην δεύτερη είσοδο του δικτύου. Φέροντας διαφορετικά σχήματα διαμόρφωσης και στοχεύοντας δυο διαφορετικές γωνίες, τα σήματα ανιχνεύτηκαν χωρίς λάθη και για τις δυο ζεύξεις.

Στη περίπτωση πολλαπλής εκπομπής, θεωρήσαμε τη χρήση του ίδιου 2×4 οπτικού δικτύου σχηματοποίησης δεσμών, έχοντας ενεργή μόνο τη μια είσοδο. Διαμορφώνοντας

κατάλληλα τόσο τις χρονικές καθυστερήσεις και θεωρώντας ομοιόμορφη κατανομή των πλατών, δημιουργήθηκαν δυο μικροκυματικές δέσμες φέροντας την ίδια πληροφορία αλλά στοχεύοντας διαφορετικές γωνίες. Σε αυτή την περίπτωση, παρατηρώντας τα διαγράμματα αστερισμού παρατηρήθηκε μια στροφή φάσης. Ο λόγος ήταν η παρεμβολή των πλευρικών λοβών της μιας δέσμης στην γωνία στόχευσης της δεύτερης δέσμης. Όπως αναλύθηκε στο Κεφάλαιο 2, τροποποιώντας κατάλληλα τη σχέση πλατών των σημάτων διέγερσης, μειώσαμε την ισχύ των πλευρικών λοβών, βελτιώνοντας την απόδοση του συστήματος. Επίσης, χρησιμοποιώντας ένα 2×8 οπτικό δίκτυο, δημιουργήθηκαν επιτυχώς, χωρίς την ανίχνευση λαθών, τρεις δέσμες σε τρεις διαφορετικές γωνίες στόχευσης, φέροντας ξανά την ίδια πληροφορία. Συνεπώς, με τις παραπάνω μελέτες, επαληθεύτηκε σε θεωρητικό επίπεδο η ικανότητα της προτεινόμενης αρχιτεκτονικής να υποστηρίξει επιτυχώς τη σχηματοποίηση είτε μονής δέσμης είτε πολλαπλών δεσμών αλλά και τη λειτουργία πολυεκπομπής.

Για την πειραματική επαλήθευση της αρχής λειτουργίας της παραπάνω αρχιτεκτονικής, αναπτύχθηκε ένα πλήρως λειτουργικό σύστημα το οποίο μοντελοποιεί ένα 2×4 οπτικό δίκτυο σχηματοποίησης δεσμών, για λειτουργία στη καθοδική ζεύξη ενός τηλεπικοινωνιακού συστήματος. Η ανάπτυξη του συστήματος βασίστηκε σε εμπορικά διαθέσιμα οπτικά και οπτό-ηλεκτρονικά στοιχεία. Συγκεκριμένα, η πειραματική διάταξη περιελάμβανε δυο οπτικές πηγές οι οποίες λειτουργούσαν σε ξεχωριστές συχνότητες, δυο ελεγκτές πόλωσης, έναν ηλεκτρο-απορροφητικό και έναν Mach-Zehnder διαμορφωτή, δυο πολυπλέκτες οπτικών σημάτων, έναν οπτικό ενισχυτή, δέκα οπτικούς συζεύκτες, οκτώ ρυθμιζόμενους οπτικούς εξασθενητές, οκτώ ρυθμιζόμενες οπτικές γραμμές καθυστέρησης και τέσσερις φωτοδιόδους. Η επέκταση της αρχιτεκτονικής από 2×4 σε μεγαλύτερες διαστάσεις, θα μπορούσε να υλοποιηθεί με την βασική προϋπόθεση ότι περισσότερα οπτικά στοιχεία είναι διαθέσιμα.

Λόγω των πολλών στοιχείων, η πειραματική διάταξη κάλυπτε μια επιφάνεια 4 m² και αυτό δυσκόλευε τη δυναμική ρύθμιση και παραμετροποίηση του δικτύου. Για τον λόγο αυτόν, η πειραματική διάταξη τροποποιήθηκε έτσι ώστε να μειωθεί δραστικά η πολυπλοκότητα και ο απαιτούμενος χρόνος για τη παραμετροποίηση του συστήματος. Συγκεκριμένα, οι κεφαλές έξι οπτικών γραμμών καθυστέρησης, οι οποίες ελέγχουν την εισαγόμενη χρονική καθυστέρηση στα μεταδιδόμενα οπτικά σήματα, αντικαταστάθηκαν από ισάριθμους προγραμματιζόμενους σερβοκινητήρες. Εν συνεχεία, οι σερβοκινητήρες προγραμματίστηκαν με τη βοήθεια ενός μικροελεγκτή Raspberry Pi 3 Model B+ και μεταφράστηκε με μεγάλη ακρίβεια η γωνιακή θέση του εμβόλου του κινητήρα σε οπτική καθυστέρηση. Έχοντας πλέον αυτή την ένα-προς-ένα σχέση, το επόμενο βήμα ήταν η ανάπτυξη ενός εύχρηστου γραφικού περιβάλλοντος χρήστη. Χάρη σε αυτό, ο χρήστης μπορεί να εισάγει τις επιθυμητές γωνίες στόχευσης των δυο δεσμών και μέσα σε ένα χρονικό διάστημα λίγων δευτερολέπτων, το δίκτυο επαναρυθμίζεται κατάλληλα. Παράλληλα, για την μείωση της απαιτούμενης επιφάνειας, σχεδιάστηκαν τρία ράφια Rack, μέσα στα οποία τοποθετήθηκε όλη η πειραματική διάταξη.

Στόχος 3: Πειραματική επαλήθευση της ικανότητας των οπτικών δικτύων σχηματοποίησης δεσμών να υποστηρίζουν τη σχηματοποίηση μιας μονής δέσμης (single-beam beamforming), τη σχηματοποίηση πολλαπλών δεσμών (multi-beam beamforming), αλλά και να υποστηρίζουν λειτουργία πολλαπλής εκπομπής (multicast).

Κύρια αποτελέσματα: Στην μέχρι τώρα ανάλυση, η ικανότητα των οπτικών δικτύων για τη σχηματοποίηση δεσμών περιορίστηκε σε εκτενείς προσομοιώσεις. Για την πειραματική επαλήθευση, χρησιμοποιήθηκε η πειραματική διάταξη που αναπτύχθηκε και αναλύθηκε στο Στόχο 2. Η πειραματική αξιολόγηση του 2×4 οπτικού δικτύου αναλύεται στο **Κεφάλαιο 4**. Για την αξιολόγηση του οπτικού δικτύου για σχηματοποίηση μονής δέσμης, χρησιμοποιήθηκε η μια από τις δυο μικροκυματικές είσοδους του δικτύου και συγκεκριμένα, εκείνη που αντιστοιχούσε στον MZM διαμορφωτή. Τα μικροκυματικά σήματα που

χρησιμοποιήθηκαν έφεραν QPSK και 16-QAM σχήματα διαμόρφωσης με ρυθμό συμβόλων 1 Gbaud, ενώ η φέρουσα μικροκυματική συχνότητα ήταν 15 GHz. Οι γωνίες στοχεύσεις της δέσμης ήταν 40°, 60°, 75°, 90°, 105°, 120° και 140°, ενώ τα πλάτη των σημάτων διέγερσης ακολουθούσαν ομοιόμορφη κατανομή. Η αξιολόγηση του συστήματος πραγματοποιήθηκε υπολογίζοντας τον ρυθμό εσφαλμένων ψηφίων ως προς την ισχύ των οπτικών σημάτων πριν το στάδιο της φωτοανίχνευσης από 0 dBm μέχρι -14 dBm. Στην περίπτωση QPSK σημάτων, για όλες τις περιπτώσεις δεν ανιχνεύτηκαν λάθη ενώ για τη περίπτωση 16-QAM σημάτων, το σύστημα εμφάνισε λάθη για οπτικές ισχύς μικρότερες των -10 dBm.

Για την περίπτωση σχηματοποίησης πολλαπλών δεσμών, χρησιμοποιήθηκαν ταυτόχρονα και οι δυο είσοδοι του δικτύου. Το ένα μικροκυματικό σήμα έφερε QPSK διαμόρφωση ενώ το δεύτερο 16-QAM. Ο ρυθμός συμβόλων των σημάτων ήταν είτε 0.5 Gbaud είτε 1 Gbaud. Η φέρουσες συχνότητες και των δυο σημάτων ήταν 15 GHz. Τα ζεύγη των γωνιών στόχευσης ήταν (135°, 60°), (120°, 45°), (75°, 150°) και (60°, 105°) ενώ τα πλάτη των σημάτων ακολουθούσαν είτε ομοιόμορφη είτε Γκαουσιανή κατανομή. Όπως και στην προηγούμενη πειραματική αξιολόγηση έτσι και σε αυτή την περίπτωση, η απόδοση του συστήματος κρίθηκε με βάση των ρυθμών εσφαλμένων ψηφίων στις γωνίες παρατήρησης για οπτικές ισχύς από 1 dBm μέχρι -10 dBm. Για όλες τις περιπτώσεις το σύστημα εμφάνισε ρυθμό εσφαλμένων ψηφίων χαμηλότερο από 10^{-3} για οπτικές ισχύς υψηλότερες από -5 dBm, επαληθεύοντας έτσι την ικανότητα του να σχηματοποιήσει πολλαπλές δέσμες.

Τέλος, το οπτικό δίκτυο αξιολογήθηκε ως προς την ικανότητα του να υποστηρίζει λειτουργία πολυεκπομπής. Για τη μελέτη αυτή, χρησιμοποιήθηκε μόνο μια είσοδος, στην οποία οδηγήθηκαν εναλλάξ μικροκυματικά σήματα με QPSK και 16-QAM σχήματα διαμόρφωσης. Στην πρώτη περίπτωση, οι γωνίες στόχευσης ήταν (75° και 140°) ενώ στη δεύτερη περίπτωση (40°, 90° και 140°). Όσον αφορά τα πλάτη των σημάτων, στη πρώτη περίπτωση ακολουθούσαν Γκαουσιανή κατανομή ενώ στη δεύτερη περίπτωση τα σήματα διέγερσης που αντιστοιχούσαν στις γωνίες στοχεύσεις 40° και 140° ακολουθούσαν Γκαουσιανή κατανομή ενώ αντίθετα τα σήματα για την γωνία 90° ακολουθούσαν ομοιόμορφη κατανομή. Για όλες τις περιπτώσεις το σύστημα εμφάνισε ρυθμό εσφαλμένων ψηφίων χαμηλότερο από 10^{-3} για οπτικές ισχύς υψηλότερες από -4 dBm, επαληθεύοντας έτσι την ικανότητα του για λειτουργία πολυεκπομπής.

Στόχος 4: Πειραματικός χαρακτηρισμός ενός αμιγώς ολοκληρωμένου οπτικού κυκλώματος σχηματοποίησης δέσμης.

Κύρια αποτελέσματα: Στο **Κεφάλαιο 5**, παρουσιάζεται και αξιολογείται πειραματικά ένα πλήρως φωτονικά ολοκληρωμένο 1×4 οπτικό δίκτυο σχηματοποίησης δέσμης χρησιμοποιώντας τις InP και Si_3N_4 (TriPleX) φωτονικές πλατφόρμες ολοκλήρωσης. Το ολοκληρωμένο δίκτυο μπορεί να υποστηρίξει τη δημιουργία και σχηματοποίηση μιας μικροκυματικής δέσμης με κεντρικές συχνότητες έως και 40 GHz και να επιλέξει γωνίες στόχευσης με συνεχές βήμα. Στην InP πλατφόρμα έχουν ολοκληρωθεί ένα ζεύγος 40 GHz οπτικών διαμορφωτών φάσης και μια τετραπλή συστοιχία 40 GHz φωτοδιόδων, ενώ η TriPleX πλατφόρμα φιλοξενεί ένα οπτικό φίλτρο και τέσσερις παράλληλες ρυθμιζόμενες οπτικές γραμμές πραγματικής καθυστέρησης χρόνου. Συγκεκριμένα, οι οπτικές γραμμές καθυστέρησης χρόνου βασίζονται στη χρήση πολλαπλών οπτικών συντονιστών μικρό-δακτυλίου, οι οποίοι μπορούν να εισάγουν πραγματική καθυστέρηση στα διερχόμενα οπτικά σήματα. Συνολικά, η κάθε παράλληλη γραμμή φιλοξενεί 8 οπτικούς συντονιστές μικρό-δακτυλίου. Επίσης, το ολοκληρωμένο δίκτυο περιλαμβάνει μια οπτική πηγή εξωτερικής κοιλότητας, της οποίας το ενεργό στοιχείο έχει ολοκληρωθεί στην InP πλατφόρμα ενώ η κοιλότητα στην Si_3N_4 πλατφόρμα. Το δίκτυο είναι διαστάσεων $16 \text{ mm} \times 19 \text{ mm}$ και περιλαμβάνει έξι μικροκυματικές θύρες, δυο για τους διαμορφωτές και τέσσερις για τις φωτοδιόδους και κατάλληλες ηλεκτρικές διεπαφές για την οδήγηση των 79 θερμό-οπτικών στοιχείων.

Χάρη στην ολοκληρωμένη οπτική πηγή και στους οπτικούς διαμορφωτές, η φάση ενός οπτικού φέροντος μπορούσε να διαμορφωθεί σύμφωνα με το μικροκυματικό σήμα που οδηγούσε τον εκάστοτε διαμορφωτή. Αξίζει να σημειωθεί ότι παρόλο που υπήρχαν δυο διαμορφωτές, μόνο ο ένας ήταν ενεργός κατά τη διάρκεια των πειραμάτων ενώ ο δεύτερος είχε τον ρόλο του εφεδρικού. Το οπτικό σήμα στην έξοδο του διαμορφωτή αποτελούταν από δυο πλευρικά σήματα (sideband) εκατέρωθεν του οπτικού φέροντος με σχετική κεντρική συχνότητα ως προς το φέρον \pm την συχνότητα του μικροκυματικού σήματος. Για την αποδιαμόρφωση ενός σήματος διαμορφωμένου κατά φάση είναι αναγκαία η απόρριψη του ενός από τα δυο πλευρικά σήματα. Για τον λόγο αυτό, μετά το στάδιο της διαμόρφωσης ένα οπτικό φίλτρο καταπίεζε την ισχύ του ενός πλευρικού σήματος. Έπειτα, το σήμα χωρίζονταν σε τέσσερα παράλληλα οπτικά μονοπάτια, όπου το καθένα από αυτά είχε οκτώ οπτικούς συντονιστές μικρό-δακτυλίου, οι οποίοι καθυστερούσαν τον οπτικό σήμα έτσι ώστε να επιτευχθεί η επιθυμητή γωνία στόχευσης. Τέλος, τα τέσσερα οπτικά σήματα ανιχνεύονταν από τις φωτοδιόδους και χάρη στη χρήση ενός παλμογράφου δειγματοληπτούνταν και έπειτα επεξεργάζονταν από την DSP εργαλειοθήκη.

Η πειραματική αξιολόγηση του συστήματος πραγματοποιήθηκε σε δυο στάδια. Στο πρώτο στάδιο, μετρήθηκε το κέρδος ζεύξης μέχρι τα 40 GHz, η εικόνα θορύβου καθώς και το SFDR_{2,3} στις συχνότητες 5 GHz και 10 GHz. Συγκεκριμένα, η μέγιστη τιμή του κέρδους ζεύξης ήταν -36.98 dB στα 2.6 GHz, η εικόνα θορύβου ήταν ίση με 38.28 dB και 41.95 dB στα 5 GHz και 10 GHz, αντίστοιχα, το SFDR₂ και SFDR₃ στα 5 GHz ήταν 70.5 dB·Hz^{1/2} και 89.9 dB·Hz^{2/3} ενώ στα 10 GHz ήταν 67.7 dB·Hz^{1/2} και 88.8 dB·Hz^{2/3}. Στο δεύτερο στάδιο, θεωρώντας το οπτικό δίκτυο μέρος μιας καθοδικής ζεύξης ενός ασύρματου τηλεπικοινωνιακού συστήματος και χρησιμοποιώντας σήματα QAM με ρυθμό συμβόλων ίσο με 500 Mbaud στα 5 και 10 GHz ως σήματα εισόδου, αξιολογήσαμε την απόδοση του ως προς το ρυθμό εσφαλμένων ψηφίων και το διανυσματικό μέγεθος σφάλματος για γωνίες στόχευσης από 45° έως 135°. Σε όλες τις περιπτώσεις, δεν ανιχνεύτηκαν λάθη στα ληφθέντα σήματα.

Στόχος 5: Θεωρητική ανάλυση της αρχής λειτουργίας ενός οπτικού δικτύου σχηματοποίησης δέσμης βασισμένο στην αρχιτεκτονική Blass matrix και ανάπτυξη καινοτόμου αλγορίθμου ελέγχου των οπτικών στοιχείων για την επίτευξη της επιθυμητής γωνίας στόχευσης.

Κύρια αποτελέσματα: Στο **Κεφάλαιο 6**, παρουσιάζεται μια εκτενής ανάλυση για τον σχεδιασμό και τη λειτουργία ενός οπτικού δικτύου σχηματοποίησης μικροκυματικών δεσμών βασισμένο στην αρχιτεκτονική Blass-matrix. Η σχεδιάσή του βασίζεται στην χρήση μιας οπτικής μήτρας (Blass-matrix), η οποία αποτελείται από οπτικούς ολισθητές φάσης και οπτικά συμβολόμετρα τύπου Mach-Zehnder (MZIs) και επιτρέπει την παραγωγή Μ-μικροκυματικών δεσμών από Ν στοιχεία μιας στοιχειοκεραίας. Αρχικά, επιβεβαιώνεται η αρχή λειτουργίας της αρχιτεκτονικής και συγκεκριμένα, αναλύεται πως η στροφή της οπτικής φάσης των διαμορφωμένων οπτικών σημάτων, η οποία επιτυγχάνεται χάρη στην οπτική μήτρα, μεταφράζεται σε ισοδύναμη στροφή φάσης στα μικροκυματικά σήματα στην έξοδο του δικτύου. Στη συνέχεια, παρουσιάζεται η ανάπτυξη ενός αλγορίθμου ο οποίος καθορίζει την λειτουργία τόσο οπτικών ολισθητών φάσεων αλλά και των συμβολόμετρων MZIs της μήτρας, έτσι ώστε να επιτευχθεί η σχηματοποίηση πολλαπλών και ανεξάρτητων δεσμών. Μέσω εκτενών προσομοιώσεων, επιβεβαιώνεται η ορθότητα του αλγορίθμου και αξιολογείται η επίδραση του φαινομένου beam-squint στην απόδοση του συστήματος συναρτήσει του ρυθμού συμβόλων και του σχήματος διαμόρφωσης των μικροκυματικών σημάτων, θεωρώντας διαφορετικά pulse shaping σχήματα. Υποθέτοντας λειτουργία με QAM μικροκυματικά σήματα με φέρουσες συχνότητας γύρω από τα 28.5 GHz, αποδεικνύεται μέσω υπολογισμών του EVM ότι το beam-squinting φαινόμενο δεν επηρεάζει την απόδοση του συστήματος σε τυπικές περιπτώσεις, όπου ο ρυθμός συμβόλων

παραμένει κάτω από 3 Gbaud. Επιπλέον, διερευνάται η επιπρόσθετη φασματική εξάρτησή του δικτύου λόγω αναπόφευκτών ασυμμετριών των MZIs, διακυμάνσεων των φυσικών διαστάσεων των κυματοδηγών εντός της μήτρας καθώς και η πρόσθετη επίδραση των κατασκευαστικών ατελειών των MZIs αλλά και των ολισθητών φάσεων. Σε όλες τις περιπτώσεις, η επίδραση των ασυμμετριών και των ατελειών παραμένει αμελητέα για ρεαλιστικές συνθήκες κατασκευής και λειτουργίας.

Στόχος 6: Πειραματικός χαρακτηρισμός ολοκληρωμένων οπτικών κυκλωμάτων για τη σχηματοποίηση πολλαπλών δεσμών βασισμένα στην αρχιτεκτονική Blass-matrix.

Κύρια αποτελέσματα: Στα πλαίσια του Ευρωπαϊκού έργου, ICT-HAMLET, αναπτύχθηκε μια καινοτόμα υβριδική οπτική πλατφόρμα ολοκλήρωσης, συνδυάζοντας δυο παθητικές πλατφόρμες, την πολυμερική (PolyBoard) και την TriPleX, με την ενεργή InP πλατφόρμα, με στόχο την ανάπτυξη οπτικών πομποδεκτών οι οποίοι θα λειτουργούν στη διεπαφή μεταξύ του fronthaul δικτύου και του δικτύου ασύρματης πρόσβασης των 5G συστημάτων. Στο **Κεφάλαιο 6**, παρουσιάζεται η σχεδίαση, ανάπτυξη και ο χαρακτηρισμός ενός ολοκληρωμένου πρωτότυπου (Precursor-1), το οποίο υλοποιεί ένα 2×2 οπτικό δίκτυο σχηματοποίησης μικροκυματικών δεσμών βασισμένο στην αρχιτεκτονική Blass-matrix και ενός δεύτερου ολοκληρωμένου πρωτότυπου (Module-1), το οποίο υλοποιεί ένα 8×8 οπτικό δίκτυο σχηματοποίησης μικροκυματικών δεσμών βασισμένο και αυτό στην αρχιτεκτονική Blass-matrix. Αντικειμενικός στόχος του πρώτου πρωτότυπου ήταν η επιτυχημένη οπτική ολοκλήρωση των τριών πλατφορμών και η πειραματική επιβεβαίωση της αρχής λειτουργίας του οπτικού δικτύου σχηματοποίησης δεσμών. Κατά την πειραματική αξιολόγηση του, μετρήθηκαν υψηλές απώλειες διάδοσης και ζεύξεις μεταξύ των διαφορετικών πλατφορμών, οι οποίες δεν κατέστησαν δυνατό τον πλήρη χαρακτηρισμό του. Παρόλα αυτά, αναπτύχθηκαν τρεις διαφορετικές πειραματικές διατάξεις, χρησιμοποιώντας εξωτερικά οπτο-ηλεκτρονικά στοιχεία για την πειραματική αξιολόγηση του ολοκληρωμένου φίλτρου και του οπτικού δικτύου σχηματοποίησης δεσμών. Στην πρώτη πειραματική διάταξη, χρησιμοποιήθηκε μια οπτική πηγή με ευρύ φασματικό περιεχόμενο ως είσοδο του οπτικού φίλτρου με στόχο τον προσδιορισμό της συνάρτησης μεταφοράς του. Σε συμφωνία με τις αρχικές απαιτήσεις του δικτύου, το οπτικό φίλτρο επέδειξε εύρος ζώνης διέλευσης ίσο με 22 GHz με εξασθένιση στη ζώνη αποκοπής ίση με 14 dB. Με τη δεύτερη πειραματική διάταξη μελετήθηκε η ικανότητα του οπτικού φίλτρου να μετατρέπει σήματα διπλής πλευρικής ζώνης (double-sideband) σε σήματα μονής πλευρικής ζώνης (single-sideband). Σαν είσοδο στον οπτικό φίλτρο χρησιμοποιήθηκε ένα διαμορφωμένο οπτικό σήμα διπλής πλευρικής ζώνης το οποίο δημιουργήθηκε με εξωτερικά στοιχεία. Ρυθμίζοντας κατάλληλα το οπτικό φίλτρο, έτσι ώστε μόνο ο οπτικός φορέας και μια πλευρική ζώνη να βρίσκονται εντός της ζώνης διέλευσης, το σήμα επιτυχώς μετατράπηκε από double-sideband σε single-sideband. Όπως αναλύεται επίσης στο Κεφάλαιο 6, για την ορθή λειτουργία των οπτικών δικτύων σχηματοποίησης μικροκυματικών δεσμών Blass-matrix, τα οπτικά σήματα προς επεξεργασία πρέπει να είναι single-sideband, έτσι ώστε να μεταφραστεί επιτυχώς η στροφή φάσης που υπεισέρχεται στο οπτικό πεδίο, στο μικροκυματικό μετά τη φωτοανίχνευση. Για τον χαρακτηρισμό του ολοκληρωμένου 2×2 οπτικού δικτύου σχηματοποίησης δεσμών, αναπτύχθηκε μια τρίτη πειραματική διάταξη, η οποία περιελάμβανε όλα τα αναγκαία οπτο-ηλεκτρονικά στοιχεία για τη δημιουργία ενός single-sideband σήματος. Το σήμα αυτό μαζί με ένα οπτικό φέρων χρησιμοποιήθηκαν σαν είσοδοι στο οπτικό δίκτυο, το οποίο ρυθμίστηκε έτσι ώστε να εισάγει μια σχετική οπτική φάση μεταξύ των σημάτων. Η χρήση όμως των εξωτερικών οπτικών δικτύων δεν επέτρεψε την σωστή λειτουργία του οπτικού δικτύου σχηματοποίησης δεσμών καθώς δεν ήταν δυνατόν να επιτευχθεί μια σταθερή σχετική φάση, αφού τα δυο σήματα ήταν μεταξύ τους ασυσχέτιστα.

Λαμβάνοντας υπόψιν όλες τις πληροφορίες και ευρήματα από τον χαρακτηρισμό του Precursor-1 πρωτότυπου, η κοινοπραξία προχώρησε στον σχεδιασμό και κατασκευή ενός

8×8 οπτικού δικτύου σχηματοποίησης μικροκυματικών δεσμών (Module-1). Εκτός από το μεγαλύτερο Blass-matrix δίκτυο, το οποίο βασίζονταν αμιγώς σε οπτικούς πιεζο-ηλεκτρικούς (PZT) ολισθητές φάσης, το πρωτότυπο Module-1 σε σχέση με το Precursor-1, φιλοξενούσε μια οπτική πηγή άμεσης διαμόρφωσης για την επικοινωνία με τον οπτικό δίκτυο fronthaul, 8 InP διαμορφωτές πλάτους, 8 οπτικά φίλτρα και 16 φωτοδιόδους. Ο χαρακτηρισμός του Module-1 ξεκίνησε από την οπτική πηγή άμεσης διαμόρφωσης. Αρχικά, μετρήθηκε η εκπεμπόμενη οπτική ισχύ σε σχέση με τον ρεύμα άντλησης. Η μέγιστη οπτική ισχύ ήταν -1 dBm για ρεύματα άντλησης ίσα με 90 mA. Στη συνέχεια, αναπτύχθηκε μια πειραματική διάταξη, ώστε να μελετηθεί η ικανότητα της πηγής να διαμορφώσει το πλάτος του οπτικού φέροντος. Για τον λόγο αυτό, ηλεκτρικά σήματα διαμορφωμένα με On-Off keying διαμόρφωση και ρυθμούς συμβόλων μέχρι 4 Gbaud χρησιμοποιήθηκαν για να διαμορφώσουν το ρεύμα άντλησης, το οποίο εν συνεχεία διαμόρφωνε ανάλογα το πλάτος του οπτικού φέροντος. Τα διαμορφωμένα οπτικά σήματα ανιχνεύθηκαν με τη βοήθεια μιας εξωτερικής φωτοδιόδου και ενός παλμογράφου. Έπειτα από επεξεργασία από την εργαλειοθήκη ψηφιακής επεξεργασίας σήματος, τα διαγράμματα οφθαλμού υπολογίστηκαν και υπέδειξαν ότι η μετάδοση σημάτων με ρυθμούς μετάδοσης έως 4 Gbaud ήταν εφικτή. Εν συνεχεία, αναπτύχθηκε η μεθοδολογία για τον χαρακτηρισμό του 8×8 οπτικού δικτύου σχηματοποίησης μικροκυματικών δεσμών. Στόχος ήταν ο χαρακτηρισμός όλων των συμβολόμετρων της μήτρας ως προς τον λόγο σβέσης. Τα αποτελέσματα υπέδειξαν ότι μόνο το 36 % από τα συνολικά 64 MZIs λειτουργούσαν ικανοποιητικά επιδεικνύοντας λόγους σβέσης από 1.75 dB μέχρι 23.3 dB. Το γεγονός αυτό κατέστησε αδύνατον τον περαιτέρω χαρακτηρισμό του οπτικού δικτύου καθώς ο μικρός αριθμός λειτουργικών συμβολόμετρων δεν επέτρεπε την δρομολόγηση των σημάτων εισόδων στους αντίστοιχους κυματοδηγούς στην έξοδο.

Παρά το γεγονός ότι και τα δυο πρωτότυπα δεν ήταν πλήρως λειτουργικά, τα πειραματικά ευρήματα συνέβαλαν καθοριστικά στην απόκτηση της απαιτούμενης τεχνογνωσίας για την ανάπτυξη τέτοιων περίπλοκων κυκλωμάτων καθώς βελτίωσαν σημαντικά τις τεχνικές ολοκλήρωσης μεταξύ των τριών οπτικών πλατφορμών. Το Ευρωπαϊκό έργο HAMLET καθώς και οι παραπάνω πειραματικές μελέτες αποτέλεσαν το εφαλτήριο για το Ευρωπαϊκό έργο TERAWAY, το οποίο στοχεύει στην ανάπτυξη πομποδεκτών για τα ασύρματα δίκτυα επικοινωνιών των επόμενων Γενεών, με ικανότητα λειτουργίας στις φασματικές περιοχές W (92-114.5 GHz), D (130-174.8 GHz) και THz (252-322). Τα πρωτότυπα βασίζονται στην υβριδική ολοκλήρωση των τριών φωτονικών πλατφορμών και στον πυρήνα τους βρίσκονται οπτικά δίκτυα σχηματοποίησης δεσμών ακολουθώντας την αρχιτεκτονική Blass-matrix.

*To my family
for their endless love, support, and encouragement*

Contents

Chapter 1 - Introduction	21
1.1 The short history of the mobile technology evolution.....	21
1.2 5G requirements and high-level use case categories	23
1.3 5G architecture and the importance for beamforming.....	24
1.4 The role of microwave photonics for wideband beamforming.....	31
1.5 Research objectives.....	33
1.6 Organization of this dissertation	34
References of Chapter 1	36
Chapter 2 - Antenna and beamforming theory	41
2.1 Antenna characteristics	41
2.2 Antenna array.....	44
2.3 Single-beam beamforming.....	47
2.4 Multi-beam beamforming	48
2.5 Multicast beamforming.....	49
2.6 Beamforming networks based on phase shifters and true time delay elements....	51
2.7 Amplitude tapering	54
References of Chapter 2	55
Chapter 3 - Fundamentals of Microwave Photonics	57
3.1 Light generation.....	58
3.2 Optical modulation	59
3.3 Photodetection	63
3.4 Key performance metrics of MWP links	64
References of Chapter 3	68
Chapter 4 - System design, development, and experimental performance evaluation of a 2×4 true time delay optical beamforming network.....	71
4.1 OBFN system architecture.....	71
4.2 Theoretical validation of single-beam, multi-beam, and multicast beamforming	75
4.3 System design and development of experimental testbed	83
4.4 Automation of the reconfiguration process	86
4.5 Experimental performance evaluation for single-beam beamforming	88
4.6 Experimental performance evaluation for multi-beam beamforming	90
4.7 Experimental performance evaluation for multicast beamforming	92
Conclusions of Chapter 4	93
References of Chapter 4	93
Chapter 5 - A 1×4 fully integrated true time delay optical beamforming network based on tunable micro-ring resonators	95
5.1 Photonic integration platforms and key optical components.....	95
5.1.1 TriPleX platform	96
5.1.2 InP platform.....	105
5.1.3 InP-TriPleX integration.....	107
5.2 Experimental performance evaluation of the OBFN-PIC.....	108
5.2.1 Link gain.....	109
5.2.2 Noise figure and spurious free dynamic range	110
5.2.3 System evaluation.....	111
Conclusions of Chapter 5	120

References of Chapter 5	121
Chapter 6 - System design, development, and baseline characterization of integrated optical beamforming network based on Blass matrix architecture.....	123
6.1 Operating principle and design of optical Blass matrix beamforming network .	123
6.2 Configuration of optical Blass matrix.....	127
6.3 Validation of configuration algorithm and simulation studies	133
6.4 The HAMLET project: Development of the first generation of fully integrated Blass-matrix optical beamformers.....	144
6.5 Baseline characterization of a 2×2 Blass matrix optical beamformer	146
6.6 Baseline characterization of an 8×8 Blass matrix optical beamformer	151
Conclusions of Chapter 6	156
References of Chapter 6	158
Chapter 7 – Conclusions and future work	159
7.1 Conclusions.....	159
7.2 Future work.....	162
References of Chapter 7	166
Appendix I: Digital signal processing toolbox.....	167
Timing recovery algorithm.....	167
Amplitude level control.....	169
IQ imbalance compensation	169
Adaptive equalization.....	171
Carrier recovery.....	172
References of Appendix I.....	174
List of figures	175
List of tables	182
Abbreviations	183
List of own publications	187
Acknowledgements	191

Chapter 1 - Introduction

1.1 The short history of the mobile technology evolution

In 1979, the first generation of a wireless communication technology (1G) was introduced when the Japanese telecommunication provider Nippon Telephone and Telegraph Company (NTT) launched the very first commercial cellular network in Tokyo [1], [2]. Two years later, 1G networks reached Europe and more specifically, the Nordic countries of Norway and Sweden which built their first 1G mobile network based on the Nordic Mobile Telephone (NMT) standard [3]. With another two years of extra delay, on 13 October 1983, the USA eventually had its first commercial cellular network launched by Ameritech in Chicago, based on the Advanced Mobile Phone Systems (AMPS) standards [1], [2]. As the NMT specifications were free and open, many new companies like Nokia, Ericsson, and Motorola, came to the fore and set the pace in manufacturing communication equipment. The outcome of this informal technological race was the first hand-held mobile phone which was invented by Martin Cooper and manufactured by Motorola [4]. Despite its truly groundbreaking capability to support wireless and mobile communications, 1G networks had very poor performance which was translated to bad voice quality mainly due to the use of pure analog signals.

The second generation (2G) was launched in Finland in 1991 and it was complied with the Global System for Mobile Communications (GSM) standard which was developed by the European Telecommunications Standards Institute (ETSI) [1], [2]. 2G brought digital voice instead of analog and began to introduce data services with short message service (SMS) text messages and multi-media messages (MMS).

The truly revolution of the wireless communication networks came with the advent of the third generation (3G) which was introduced by NTT DoCoMo in mid-2001 [1], [2], [5]. 3G technology was the result of research and development work carried out by the International Telecommunication Union (ITU) in the early 1980s. The technical specifications were made available to the public under the name IMT-2000 [6]. The first commercial network in Europe was opened for business by Telenor in December 2001 and in USA was launched by Verizon. The 3G systems could support unprecedented, until then, data rates up to 385 kb/s in wide coverage areas and 2 Mb/s in local coverage areas, offering among other data services, video calling, Web browsing, TV streaming and access to navigational maps.

With the widespread adoption of smartphones, it was evident that a new generation of wireless communication technology was needed to meet the ever-increasing needs of the consumers. This technological leap was made with the advent of the fourth generation (4G) which was first deployed in Stockholm, Sweden and Oslo, Norway in 2009 as the Long Term Evolution (LTE) 4G standard [7], [8]. It was subsequently introduced throughout the world and made high-quality video streaming a reality for millions of consumers. 4G offers fast mobile web access, up to 1 Gb/s for stationary users which facilitates gaming services, HD videos and HQ video conferencing. 4G itself continues to evolve and eventually, 4G LTE-Advanced (LTE-A) and 4G LTE-A Pro were introduced as improved versions.

Very short after the first deployments of 4G wireless networks, the fifth generation (5G) of wireless communication technology was emerged in the spotlight of the research community. However, this was not a just a mere intellectual exercise. Cisco had already predicted the global mobile data explosion from 2015, mentioning that the overall mobile data traffic is expected to grow to 24.3 exabytes per month by 2019, nearly a tenfold increase over 2014 [13]. From that point, this daunting forecast was validated every year and the efforts for deploying the next generation were ramped up. Eventually, the 5G networks began deploying worldwide in 2018 [9]-[12].

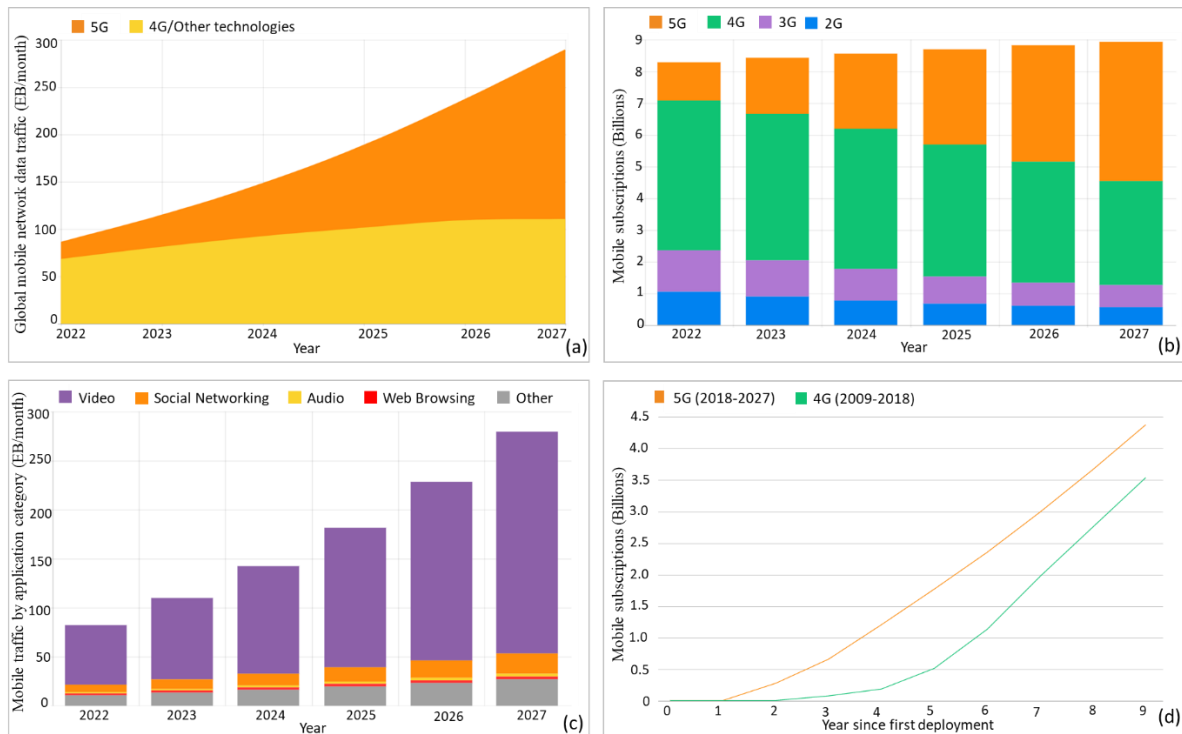


Figure 1.1: (a) Global mobile network data traffic forecast for 5G and 4G networks. (b) Total number of mobile subscriptions forecast for four generations of wireless communications technologies. (c) Mobile traffic by application category forecast. (d) Graphical comparison between the total number of mobile subscriptions of 5G and 4G networks during the first nine years since their first deployment. (Source: Ericsson [14])

5G is designed to build upon the existing 4G technology, using the radio frequency spectrum differently and more efficiently; for this reason, 5G is often referred to as 5G New Radio (NR). Still today, the first roll out of 5G NR require existing 4G LTE infrastructure and are referred to as 5G NR Non-Standalone (NSA). The standards on which 5G is being built, define 5G NR NSA as an interim step, but one that may be around for quite a while. Deployments of 5G NR Standalone (SA), which do not require legacy 4G LTE infrastructure, are just beginning in select areas globally.

Despite the hype around the emerging 5G networks, the telecom industry has been impacted by the COVID-19 pandemic, but to a lesser extent than other industries. The 5G era is here now and continues to unfold globally. While the pandemic has caused significant delays in its roll out in some areas, these delays will be overcome. As shown in Figure 1.1 (a), Ericsson estimates that the total global mobile data traffic will reach 288 EB per month by 2027 utilizing both legacy and 5G wireless communications networks [14]. Figure 1.1 (c) presents that the reason of this traffic explosion will be mainly the use of video related services [14]. At the same time, the number of mobile subscriptions of 5G networks will increase exponentially and will reach the number of subscriptions of 4G networks by the end of 2026 and will exceed it a year later, reaching 4.4 B subscriptions (see Figure 1.1 (b)) [14]. Consequently, despite what many people believe, the growth and uptake of 5G is happening faster than expected. As shown in Figure 1.1 (d), this would make 5G the fastest deployed mobile network ever, quicker than both 3G and 4G/LTE [14].

1.2 5G requirements and high-level use case categories

Summary of 5G Use Cases

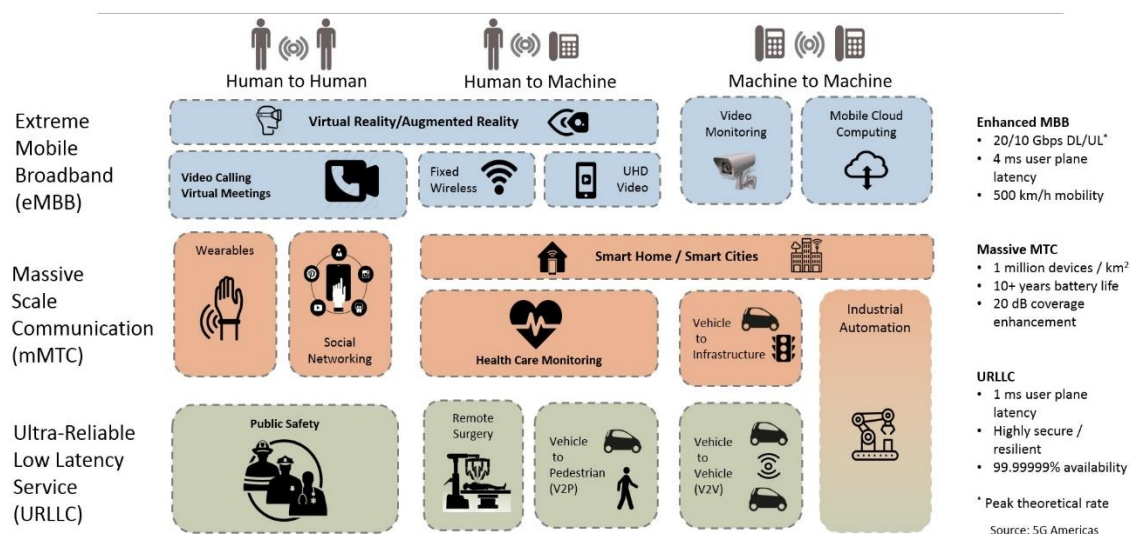


Figure 1.2: The 5G use cases are categorized into three families; the extreme Mobile Broadband (blue color), the Massive Scale Communication (orange color), and the Ultra-Reliable Low Latency Service (green color). Each of these families poses a different set of requirements in the 5G networks. In some use cases, these sets may overlap, such as in the industrial automation sector (source: [15]).

5G requirements: The vision of the 5G for “desktop-like experience on the go”, “lifelike media everywhere”, “an intelligent web of connected things”, and “real-time remote control of machines” [14] is setting a new set of requirements for the wireless network, which is very broad and demanding. The main technical objectives of 5G that should achieve are:

- Extremely high data rates per device (multiple tens of Gb/s).
- High data rates per area and massive deployment of connected devices with minimum interference.
- Ultra-low latency links with less than a microsecond round trip time.
- Ultra-reliable links, reaching at least 99.999 % availability for critical services.
- Reduction in energy usage by almost 90%. Development and use of green technology.
- High battery life. Reduction in power consumption by devices is crucial.
- Perception of 100% coverage

With this set of requirements, 5G will heavily assist the development not only of the communication industry but also other industry sectors, such as medical science, transportation, and education. In the near future, broadband connectivity will acquire the same level of importance as access to electricity and users will generate more content and share this content without being limited by time and location. At the same time, 5G networks will reform the societies and facilitates the fast formation and sharing of public opinions for political or social issues through social networks.

High-level 5G use case categories: Of course, not all of the 5G use cases will require such a high data rate or such a low latency. Each specific 5G use case will require a different set of requirements which will be a subset of these seven main technical objectives. In industry literature, it is common to see discussions around 3 high-level categories of use cases, proposed by the ITU. As shown in Figure 1.2, these categories are:

- Enhanced Mobile Broadband (eMBB)
- Ultra-Reliable and Low-Latency Communications (URLLC)

- Massive Machine Type Communications (mMTC)

For most 5G customers, the extremely fast mobile broadband speeds are what we all naturally require. Thus, this is an obvious case of use that we can easily relate to today. eMBB use cases are data-intensive use cases which require high bandwidth, high connection density, large deployment and coverage, and high user mobility. Such cases include cloud and UHD, 8K video streaming, immersive gaming (including AR and VR) gaming, video analytics, and immersive event experience.

For the URLLC use case family the high data rates are not required but instead, the prime focus is on the latency, reliability, and availability. As defined by the ETSI, end-to-end (E2E) latency is “the time it takes to transfer a given piece of information from a source to a destination, measured at the application level, from the moment it is transmitted by the source to the moment it is received at the destination.” [18]. The effect of latency can be seen during gaming or simply web browsing. High latency will result in a slower response time, whereas lower latency will result in a faster, more instantaneous response. Applications such as AR and VR must respect the human vestibular reflex (a movement that stabilizes vision) to prevent motion sickness and therefore require very low latency. Reliability is measured as a percentage and is defined as “the amount of sent network layer packets successfully delivered to a given node within the time constraint required by the targeted service, divided by the total number of sent network layer packets.” [18] Availability is measured as a percentage of the uptime of whatever service is being measured. Five nines availability (99.999%) means the service can only be down for approximately 5 minutes per year, whereas six nines availability (99.9999%) reduces downtime to approximately 30 seconds per year. Critical use cases identified for 5G URLLC are the autonomous driving, intelligent transport, remote guided vehicles for factories, drones control, remote surgeries, financial services, and smart grid [19].

The definition of mMTC use case family is somewhat elusive, as it has to include a large variety of emerging concepts, such as the Internet of Things (IoT), Internet of Everything (IoE), Industry 4.0, Smart X, etc. Regardless the application, mMTC deals with communication of low-cost and energy efficient devices that may have limited embedded intelligence, typically transmitting a relatively low volume of non-delay sensitive data. These devices can be fitness bands, smartwatches, connected home appliances, and so on.

1.3 5G architecture and the importance for beamforming

Basic concepts and network architectures: In order to meet this set of requirements and enable the commercial uptake of the use cases and applications that have been emerged, radical but cost-efficient technology changes are needed. As it is discussed in the previous paragraph, at the top of the list of requirements is the need of high system capacity and uniform user experience regardless of the user location. As far as the former is concerned, high available bandwidth, areal reuse and spectral efficiency are the parameters that define it. The need for high bandwidth dictates the migration of operation to high frequencies. As shown in Figure 1.3, beyond 6 GHz, there are available frequency slots (i.e., contiguous spectrum of more than 500 MHz) that remain available and can constitute a frequency band for the operation of 5G systems. Among the possible options, which included bands around 18.5 GHz, 28 GHz, 39 GHz or even 60 GHz [22], [23], the 28 GHz band with 5.25 GHz available bandwidth (24.25-29.5 GHz) was widely accepted by large industrial players as the frequency band of the 5G networks above the sub-6 GHz frequency band [20], [24]. As presented in Figure 1.4 (a), the 28 GHz has been already deployed in USA and already licenced or even tested in most of the European countries, including Greece [25]. Additionally, more than the 33% of the new user devices can now support operation in the mmWave, as shown in Figure 1.4 (b).

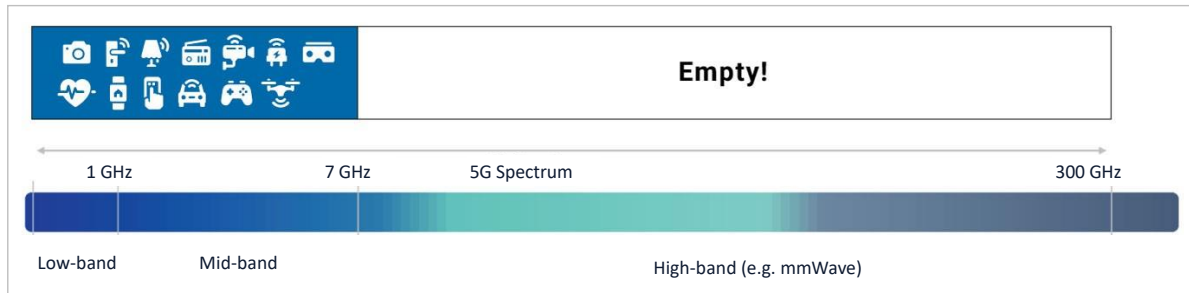


Figure 1.3: Frequency spectrum bands and bandwidth availability (source: [21]).

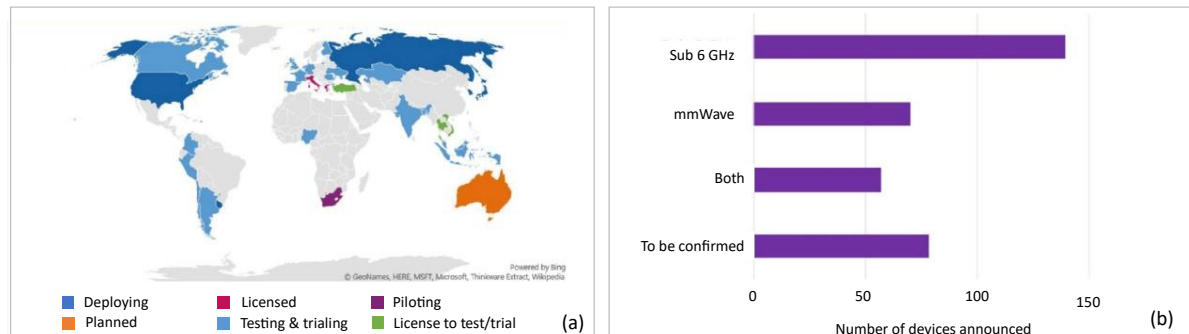


Figure 1.4: (a) Use of 5G spectrum between 24.5 GHz and 29.5 GHz, countries plotted by status of most advanced operator activities and (b) announced devices by the Global Mobile Suppliers Association with known spectrum support (source: Hellenic Telecommunications and Post Commission [20]).

The use of a high frequency band, the need for high levels of areal reuse, and the need for uniform user experience, make the use of small cells necessary, which requires in turn a very dense network of antennas. Figure 1.5 (a) shows an artistic representation of an urban environment with indicative allocation of 5G cells and antennas, which is by comparison at least 3-4 times denser than the current allocation of 4G cells and antennas in similar environments. As an example, the Federal Communications Commission (FCC) of the USA estimated that the US needs 800,000 small cells to make 5G a reality, 4 times more than the deployed 4G towers [29]. This densification of 5G network infrastructure is both costly and time-consuming, which is why 5G small cell technology, for the time being, will be the prerogative of dense urban environments as well as buildings in busy places, such as sports stadiums.

The large number of cells and the emergence of novel system concepts, like the coordinated multi-point transmission (CoMP) [30], the cloud-radio access network (cloud-RAN) concept and the relevant RAN virtualization [31], make also necessary the decoupling between the baseband processing unit (BBU) and the antenna unit of each base-station (BS), and the centralization of the BBUs in large pools, as shown on the right side of Figure 1.5. Each pool will control a large number (40 or even 100) of remote antenna units (RAUs), allowing for better coordination between the RAUs, and higher system capacity. The connectivity between the RAUs and the BBU pool will rely on an optical fronthaul network based on a simple star topology or on a more efficient – in terms of cell number scaling, installation costs and resilience – ring topology with WDM [32].

The analog radio-over-fiber (ARoF) and digital radio-over-fiber (DRoF) scenarios: The two basic scenarios for the optical interconnect between the BBU pool and the RAU over the optical fronthaul include the analog radio-over-fiber (ARoF) scenario and the digital radio-over-fiber scenario (DRoF), as shown in Figure 1.6 [32]. In the first one, the total of the baseband processing takes place at the BBU pool. The digital-to-analog converter

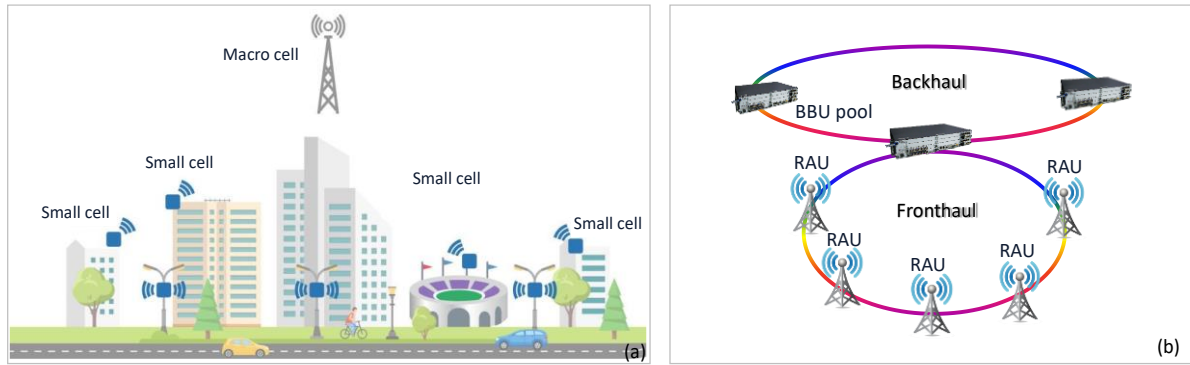


Figure 1.5: (a) Artistic representation of an urban environment with indicative definition of 5G cells and allocation of RAUs (from [26]). (b) Reference architecture of 5G networks with centralization of base-band processing units (BBUs) in large pools and connection of each BBU pool to a large number of remote antenna units (RAU) via a ring-based optical fronthaul [27].

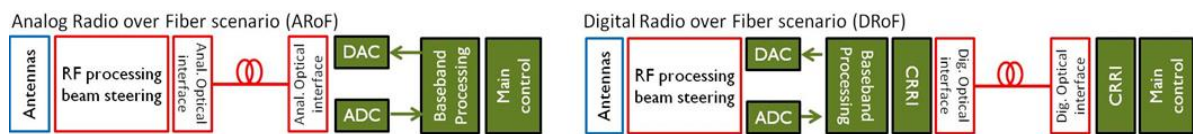


Figure 1.6: (Left) Analog radio over fiber (ARoF) scenario for the interconnection of each BBU with the corresponding RAU, based on the execution of all digital processing (including the DAC/ADC functions for the wireless transmission) taking place at the BBU site. (Right) Digital radio over fiber (DRoF) scenario for the same interconnection, based on digital optical transmission over the fronthaul link and execution of a large part of the digital processing at the site of the RAU [28].

(DAC) is also placed at the BBU and takes care of creating the analog signal that can be up converted to the final RF frequency and modulate an optical carrier at the analog optical interface of the pool. The optical signal in this case carries the data in the form of an RF signal that is ready for wireless transmission by the antenna system after optical detection and analog processing in the electrical domain. Despite its attractiveness due to the stripped-down design of the RAUs, the ARoF scenario is not the preferred choice today for next generation systems due to the very low tolerance to nonlinear effects during the optical transmission, and thus the severe limitations in the performance of the system. In the DRoF scenario on the other hand, the data are transmitted to the RAU using the CPRI standard over a digital optical link [32]. After optical detection, the baseband processing associated with the wireless transmission (i.e. framing, encoding and FEC) takes place at the RAU, and subsequently the data are digital-to-analog converted, up-converted to the RF carrier frequency, processed in the analog domain, and transmitted by the antenna. Despite the complexity at the RAU due to the need for both digital and analog processing utilizing a high number of DACs and analog-to-digital converters (ADCs), the DRoF scenario is considered by the industrial players as the most reliable and efficient one, as it has much higher tolerance to nonlinear effects, and potential for band-pass sampling and higher dynamic range, which are directly related to increased bandwidth of operation and longer wireless propagation distance [32].

The need for beamforming networks in 5G systems: The use of multi-element antenna arrays at the antenna system of each RAU will be a key technology for the realization of the truly 5G vision, due to the significant improvement in the throughput of a wireless link that antenna arrays can offer [33]-[35]. Depending on the channel and system characteristics, the multi-element antenna arrays can have two modes of operation described under the general terms spatial diversity and beamforming. The former refers to a set of transmission and reception schemes that are used to improve the quality and reliability of a wireless link. At the transmitter, spatial diversity is actually the transmission of the same information by multiple sources using the same coordinates in the space, frequency, time and code domain,

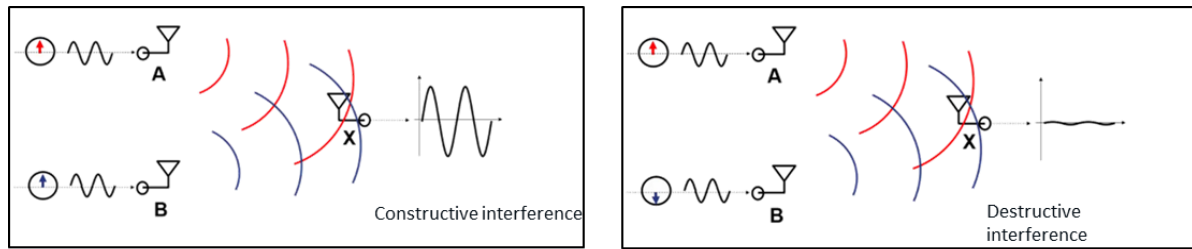


Figure 1.7: A beamforming network process the signals transmitted or received by a multi-element antenna in such a way that wireless signals at particular angles experience constructive interference (right) while others experience destructive interference (left).

while at the receiver, it is the selection or combination of the arriving signals in a way that improves the signal-to-noise ratio (SNR). In the simplest form, the received signal from the antenna element with the highest signal strength is selected. In more sophisticated forms, the signals from all antenna elements are combined, appropriately weighted in order to maximize the SNR using data-aided multiple-input-multiple-output (MIMO) channel estimation algorithms and added in-phase after compensation of the phase-shifts [37]. Beamforming on the other hand represents the next step, being practically a precoding scheme, where the transmitter uses properly selected weights on the data in order to form the beam and focus the radiated energy towards the mobile user. In order to do that, as shown in Figure 1.7, a beamforming network process the signals that will be transmitted by a multi-element antenna array in such a way that at the angle of the users, the signals will be combined constructively and destructively in all others [38]. At the receiver, the same principle is applied in order to generate the same beam pattern, maximize the received energy from the users, minimize interference from other sources. System flexibility and possibility to fully exploit the beam forming concept at the system level are only possible when a large number of antenna elements (at least 16) are available in a 2D array, and when the possibility to have dynamic beam pattern adjustment with very fine resolution in both space and time over the total bandwidth of the signal is present. Beamforming can be extended to multiple beams from a single antenna [39], [40]. In this way, parallel links to multiple groups of users inside the same communication cell can be accommodated with low crosstalk, and substantial increase in the total system capacity can be achieved [40]. In the current systems, three beamforming architectures are used (i) analog beamforming, (ii) digital beamforming, and (iii) hybrid beamforming.

Analog beamforming: Figure 1.8 (a) depicts the reference architecture of an analog beamforming network (BFN) that feeds a multi-element antenna array, operating at the receiver side of communication link. The RF signals received by the antenna array are fed to the amplitude control stage which amplifies them and defines their relative amplitude relationship. This technique is known as tapering and in most cases assigns highest gains at the central elements in order to reduce the power of the sidelobes [40]. Then, the signals are fed to the second stage where the signals are either delayed or phase shifted according to the incident angle of the received signal. At the output of this stage, the signals are in phase and so, they can be coherently combined by a power combiner. The output port of the combiner is coupled to an external mixer which is responsible for the frequency down-conversion of the signal from the RF domain to the baseband or to an intermediate frequency (IF). Finally, an analog-to-digital converted is used to sample the signal and feed a digital signal processing (DSP) unit. The best-known analog BFNs is the Butler matrix [41], [42], the Nolen matrix [43], [44], and the Blass matrix [45], [46].

Introduced in the early 1960's, the Blass matrix was the first described method to provide multiple beams for antenna systems. The functional layout of a Blass matrix is presented in

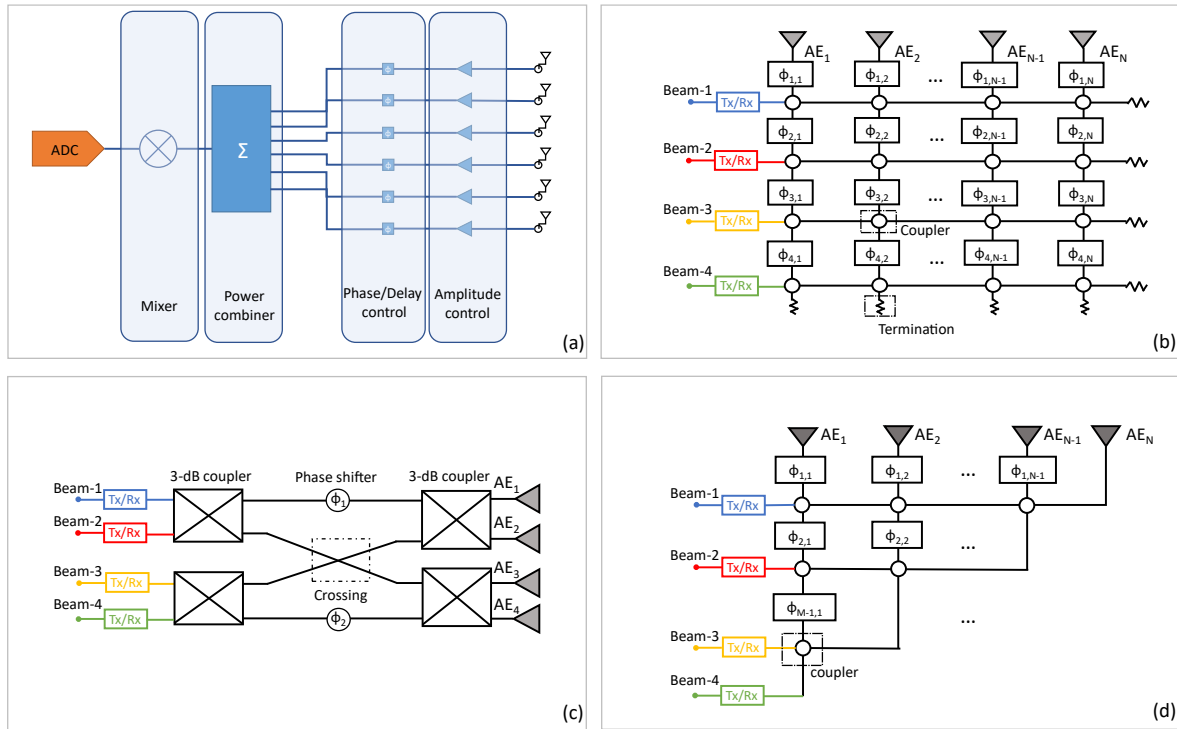


Figure 1.8: (a) Reference architecture of a receive analog beamforming network (BFN). (b) Schematic representation of an $M \times N$ BFN based on Blass matrix architecture capable of forming M beams and feeding N AEs. (c) Schematic representation of a 4×4 BFN based on Butler architecture for forming up to 4 orthogonal beams and feeding a 4-element antenna array and (d) schematic representation of an $M \times N$ BFN based on Nolen architecture capable of forming M orthogonal beams, feeding an antenna array with N AEs.

Figure 1.8 (b). It consists of an array of N radiating elements excited in series by M feeder lines. The lines are interconnected by directional couplers and they are terminated with matched loads at each line end. The great advantage of the Blass matrix is that it can be scaled to any number of antenna elements (AEs) and feeder lines, which makes it the prominent candidate for large MIMO systems.

Shortly after the introduction of the Blass matrix, a new architecture was introduced called Butler matrix. As it can be seen from its functional layout which is presented in Figure 1.8 (c), the main difference compared to a Blass matrix is that Butler matrix forms a parallel-fed BFNs while Blass matrix is considered to be a series-fed BFN, as it was explained. In its most common form, the number of inputs, M , is equal to the number of outputs, N , and it must be an integer power of 2 ($M = N = 2^n$, where n is an integer). Therefore, for each input port, signals with identical power and progressive phase shifts are generated in the output ports. The elementary component of this architecture is a 4-port coupler. Consequently, even though in general Butler matrices requires less components than the equivalent Blass matrices for a same antenna array, they do not scale efficiently for large arrays. This is why the most typical size of the commercial Butler matrices is either 4×4 or 8×8 . Moreover, the implementation as an integrated circuit requires large number of waveguide crossings, which are always problematic and can substantially deteriorate the circuit performance.

The Nolen matrix is a general form of orthogonal BFN, based on a series-fed topology similar to that of the Blass matrix. As it can be seen in Figure 1.8 (d), it can be considered as a lossless variant of the Blass matrix in which all the directional couplers below the diagonal have been removed and those on the diagonal are replaced by simple bends. Nolen matrices create orthogonal beams as the Butler matrices and as a result they are not fully flexible in

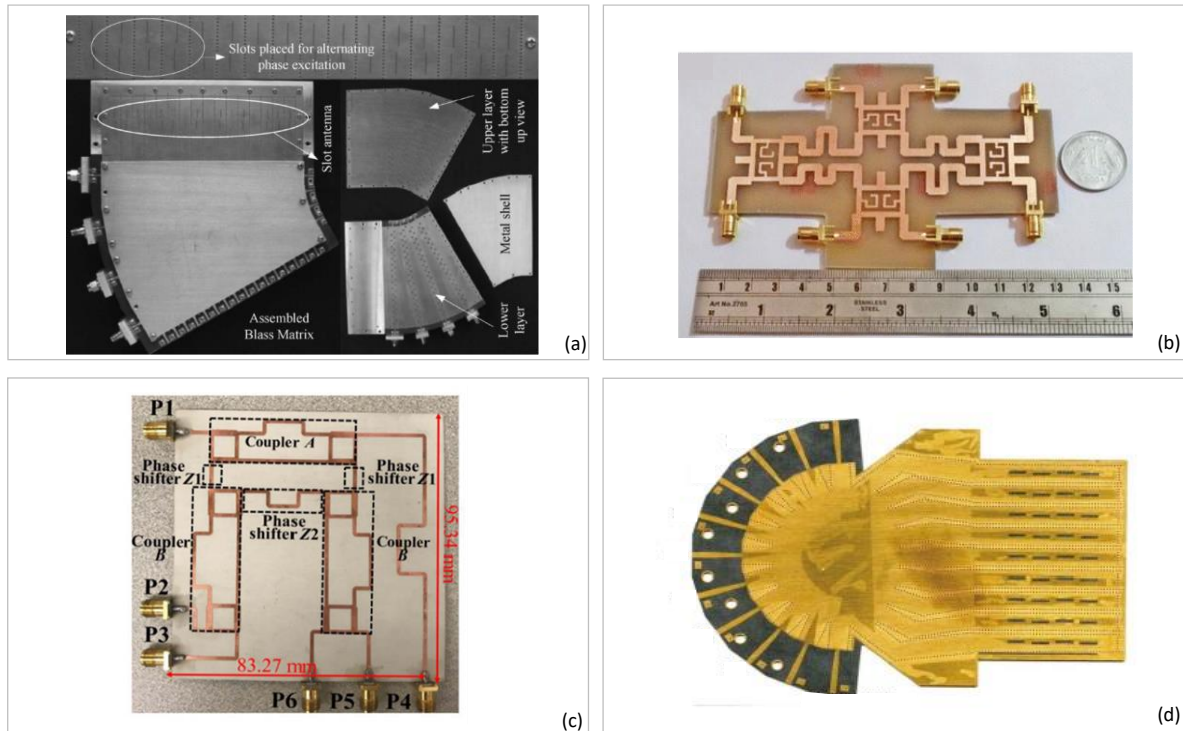


Figure 1.9: Pictures of assembled analog BFNs. (a) A 4×16 Blass matrix for operation in Ku-band (12-18 GHz) [48], (b) a 4×4 Butler matrix [49] (c) a 3×3 symmetrical Nolen matrix [50], and (d) 7×9 Rotman lens for operation in Ka-band (27-40 GHz) [51].

the selection of the steering angle of each beam independently from the other ones.

Another attractive BFN architecture, due to its low cost, reliability, design simplicity, and wide-angle scanning capabilities is the Rotman lens [52]. It is a passive structure that uses the free-space wavelength of a signal coupled into a geometrically configured waveguide to shift the phase of inputs into a linear antenna array in order to scan a beam in any desired signal pattern. Figure 1.9 shows four indicative assembled analog BFNs based on Blass, Butler, and Nolen matrices as well as a Rotman lens.

As however the frequency bands of modern wireless systems are shifted closer or deeper in the millimeter wave (mm-wave) regime, the fractional bandwidth of the signals gets higher, and the number of the AEs larger, these analog, dynamic BFNs solutions (Blass, Butler, and Nolen matrices) start having significant limitations in terms of time delay and phase shifting accuracy across the signal bandwidth, insertion loss across the same bandwidth, and physical size. On top of that, the Butler and Nolen matrices are not fully flexible in the selection of the steering angle of each beam independently from the other ones. Moreover, in the case of the Butler matrix, the implementation as an integrated circuit requires large number of waveguide crossings, which are always problematic and can substantially deteriorate the circuit performance. The Rotman lens despite its robustness, it is a passive device which limits its potential of using it in cellular communications systems. On the other hand, the Blass matrix is by default lossy due to the fact that a small part of the power is always directed to output ports other than the ones that feed the AEs. However, it does not require waveguide crossings, it is fully flexible in the selection of the steering angles for each beam and in the case, of large antenna arrays (i.e., many columns), the losses are negligible.

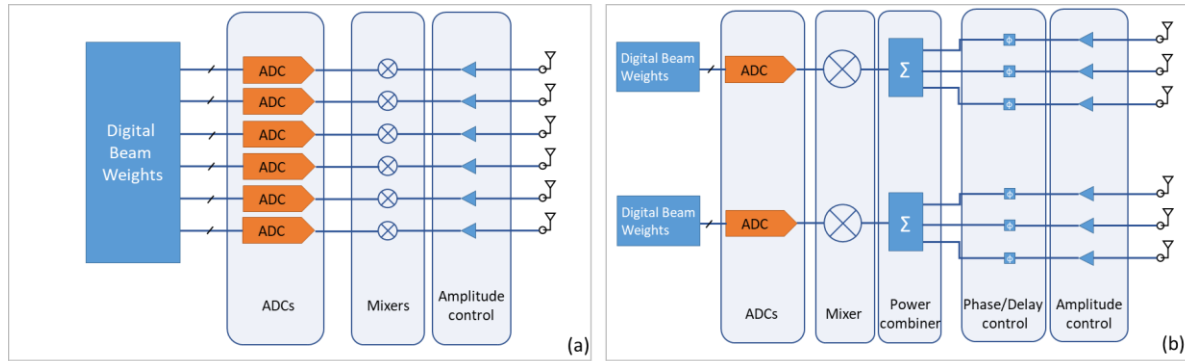


Figure 1.10: Reference architecture of a fully digital (a) and hybrid (b) BFNs, both operating at the receiver side of a communication system.

Digital beamforming: Unlike in analog beamforming, in digital beamforming, the RF beams are formed in the digital domain, using digital weights. Figure 1.10 (a) depicts the reference architecture of such an BFN, operating at the receiver side of a communication system. The detected RF signals are fed to an array of amplifiers to boost their power and then, they are frequency down converted to an IF or directly to the baseband by an array of mixers. Subsequently, the signals are sampled by an array of ADCs and the produced samples are processed by a DSP engine which applies the correct weights. So, it is evident that for each AE a unique RF chain is required. Therefore, despite its advantages over the analog approaches, especially, in terms of flexibility since every beam can be processed dynamically and independently of the other beams, this architecture can not support the operation of massive antenna arrays with thousands of elements mainly due to the cost and power consumption. Other significant challenges include the signal routing complexity, where multiple bits of I and Q lines should be routed to the DSP engine while at the same time a local oscillator should be distributed to the mixers.

Hybrid beamforming: Hybrid architectures have been emerged in the spotlights thanks to their ability to efficiently combined the best of analog and digital beamforming. As shown in Figure 1.10 (b), a hybrid BFN consists of an analog and a digital part. The analog part is responsible for the amplitude tapering, combining and frequency down conversion of signals while the digital part samples the resulting signals and applies the correct weights. Even though that only two beams are shown for simplicity, in fact, many beams can be formed following this approach alleviating the main disadvantages of the analog and digital beamforming related to flexibility and power consumption, respectively. This approach is widely accepted as the most prominent candidate architecture for the BFNs in the 5G networks. However, this approach is limited due to the disadvantages of the analog part and more specifically, the inherent narrowband nature of the analog components which allows processing of signals with bandwidths up to 500 MHz which makes the beamforming option practically unavailable. Additionally, especially within the context of the 5G networks, where mobility is one the main prerequisite, the ability of the analog BFNs to dynamically reconfigure their components and the steering angle of the beams is limited in the millisecond regime which is not acceptable for a plethora of applications.

1.4 The role of microwave photonics for wideband beamforming

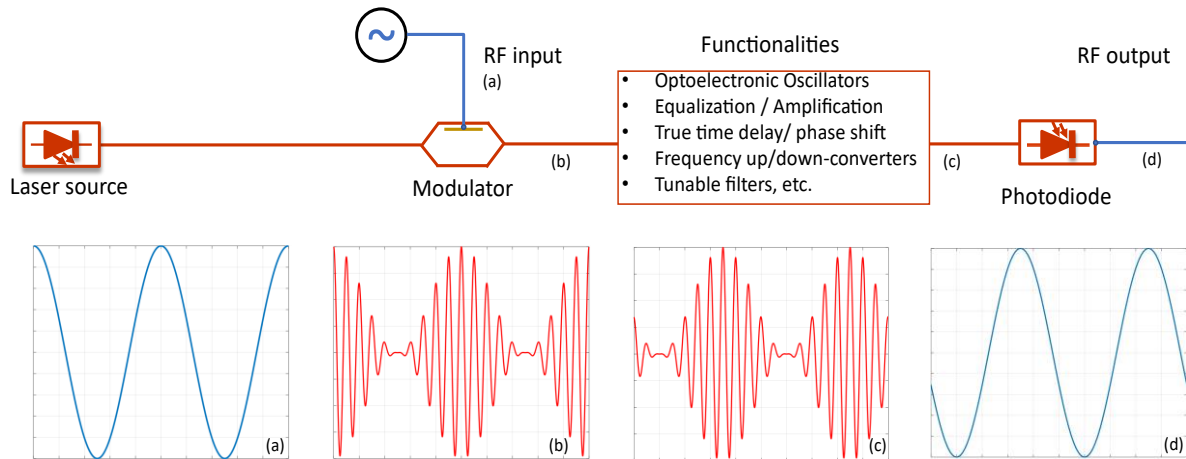


Figure 1.11: Artistic layout of an indicative microwave photonics system. A representative functionality of such a system is the true-time delay of RF signals. As an example of such a system, the inset graphs show how a time delay is introduced to an RF signal. More specifically, insets (a)-(d) depict the time-domain representation of the input (a) and output (d) microwave signal as well as the modulated signal optical signal before (b) and (c) the insertion of the time delay.

Microwave photonics (MWP) is defined as the interdisciplinary field that studies the interaction between microwave and optical signals and it has been always acknowledged over the last 30 years as a research discipline with bright future [53]-[55]. Being able to bring together the worlds of microwave engineering and photonics and enable processing functionalities in microwave systems that are either complex or even not possible at all in the microwave domain, MWP have created expectations for true commercial uptake.

As depicted in Figure 1.11, a simple MWP link consists of light source, an optical modulation for the electrical-to-optical conversion and a photodiode for the optical-to-electrical conversion. Apart from the capability of such systems to generate and distribute, microwave signals, they can introduce true time delays and phase shifts to broadband microwave signals at very high reconfiguration speeds, implement frequency tunable and high selectivity microwave filters and also support frequency up or down conversions. The reason for implementing all of these functionalities in the optical domain rather than in the microwave domain is that the MWP systems can offer broadband operation, constant attenuation over the entire microwave frequency range, small footprint, lightweight, immunity to electromagnetic interference and the potential of large tunability and low power consumption.

Despite the fact that MWP has not yet reached its fully potential, the discipline remains very active and continues to expand in terms of interest from the research and industrial community and in terms of productivity in new ideas, concepts and techniques [53]-[55]. What is more, a second wave of expectations for commercial uptake of MWP technology has been created over the last 10 years in view of the development of a new generation of broadband microwave systems in the fields of wireless communications, satellite communications, sensing, and medical imaging with very high requirements in terms of carrier frequency, bandwidth, dynamic range, size, power consumption, tunability, and immunity to electromagnetic interference. Systems for emerging 5G wireless technology stand out on the top of the relevant list.

Optical beamforming networks: Initial efforts involve mainly implementations of true time delay (TTD) optical beamforming networks (OBFNs) based on fiber segments of various length [56], [57], multi-core [58], [59] and highly dispersive fibers [60], [61], fiber Bragg gratings [62], [63], spatial light modulators [64], [65], micro-optics [66], and

semiconductor optical amplifiers [67], [68]. In addition, implementations that approximate the TTD operation using optical phase shifters has also been proposed [69].

The efforts cited above have been limited to the single-beam beamforming case, aiming to confirm the fundamental operating principles and the high bandwidth potential of the optical beamforming solutions. Other efforts have aimed to make the next step exploring the extension of the optical solutions to the case of multi-beam operation. These include the early works describing the use of an optical setup for multi-beam operation of phased array antennas in radar and communication applications [70]-[72], as well as follow-on works based on fiber-based TTDs [73]-[76], Bragg-gratings [77]-[78], Fourier transform lenses [79], acousto-optic tunable filters [80], and spatial light modulators [81]-[83]. On the same path, OBFNs implemented with the help of TTDs or optical phase shifters inside a Butler [84]-[86], Nolen [87] or Blass matrix architecture [89], [90] have also been studied and reported.

Although important for validating the potential of optical beamformers for multi-beam operation, these works have been based on bulk implementations suffering from fundamental limitations in their scaling to large numbers of wireless beams and AEs. Photonic integration on the other hand can facilitate this type of scaling through the fabrication of large-scale photonic integrated circuits (PICs), where the optical beamforming network is implemented with the help of TTDs.

The integrated TTD-OBFNs (iOBFNs) process the signals using optical true time delay lines (OTTDLs). Representative works include OTTDLs based on highly dispersive photonic structures such as photonic crystal waveguides and subwavelength grating waveguides [90]-[92]. In these approaches, the group index and the dispersion coefficient of the waveguides are controlled by the design characteristics of these structures, which, however, impose strict requirements on the lithography process. Alternative approaches are based on switchable waveguide delay lines (SWDLs), which control the introduced time delay in each optical path by switching between waveguides with various lengths [93]-[97]. Despite their simplicity in terms of configuration, these schemes feature by default limitations in their scaling, when a large set of steering angles is required. Within the context of satellite communication networks, a modular photonic-aided payload receiver based on four Mach-Zehnder delay interferometers has also been reported [98]. However, for its system demonstration, a high number of optical amplifiers and fiber-optic components were required, thus increasing the system complexity. Finally, OTTDLs utilizing optical all-pass filters in the form of micro ring-resonators (MRRs) have been extensively investigated and reported, thanks to their small footprint and ability to select in a continuous way the intended beam angle [99]-[102]. Due the constant delay-bandwidth product of the MRR, multiple cascaded MRRs are required to achieve broadband operation.

In most of the aforementioned works, the PICs comprise only the OTTDL network, and in only two demonstrations, they also comprise optical modulators and photodetectors but not the laser sources [94], [98].

The technological leap that enabled the demonstration for the first time of a fully functional OBFN in integrated form was the combination of two photonic integration platforms, i.e., the ultra-low loss (0.1 dB/cm) proprietary Si₃N₄ platform of LioniX Int., known as TriPleX, and the InP platform of Fraunhofer Heinrich Hertz Institute [103]. Their hybrid combination brings the best-of-breed of both platforms and leads to fully functional PIC without need of utilizing external optical components (neither active nor passive ones). Two types of such fully integrated OBFNs have been reported so far [104], [105]. The first one involves an SWDL-based OBFN with 3-bit resolution [104], while the second one a 1×4 OBFN based on four parallel OTTDLs with 8 cascaded MRRs each [105].

Therefore, provided that a suitable MWP technology is available for this kind and scale of broadband processing, the potential of beamforming concept can be fully deployed, contributing in a very decisive way to the 5G vision in terms of capacity, flexibility, connectivity, and security.

1.5 Research objectives

The aim of the research presented in this dissertation is to showcase the use of integrated photonics as an enabling technology to provide unprecedented performance within the context of the 5G networks, focusing on the analog BFNs. Apart from being ambitious and beyond the state-of-the-art, which is the essence of every Ph.D. work, this research target is quite challenging itself since iOBFNs should directly compete with the mature technology and industry of the microwave world while at the same time MWP is still in its infancy. The stepwise approach to conduct this development plan is presented below through the following 6 objectives:

Objective 1: Develop a simulation platform for emulating the performance of MWP systems and multi-element antenna arrays as well as a digital signal processing toolkit for demodulating signals with high-order modulation formats

Within this objective, a powerful simulation engine will be developed to unify and co-simulate MWP systems, and in particular OBFNs, and linear antenna arrays. More specifically, the engine will include the modelling of laser sources, optical modulators, photodiodes and of course, the under-test OBFNs. Assuming that the OBFNs are part of wireless system operating either in the downlink or uplink direction utilizing a linear antenna array, it will generate the expected radiation patterns. Additionally, the engine will include a DSP toolbox to generate and process signals with high-order modulation formats.

Objective 2: Design and implement an OBFN based on bulk micro-optics components

In order to gain insight into the design process of an OBFN, a 2×4 OBFN based on micro-optics elements will be designed and subsequently, implemented. The OBFN will be able to generate up to two independent beams and feed up an antenna array with up to four antenna elements. For ease of use, the configuration of the OBFN will be automatized to reduce its reconfiguration time from several minutes in case of manually tuning all the optical elements down to a few seconds using a microprocessor and an array of servo motors. The OBFN will be used for validating the simulation engine, described into the Objective 1.

Objective 3: Experimentally validate the ability of the OBFNs to support single-beam, multi-beam and multicast operation

The 2×4 OBFN will be used as a testing vehicle to demonstrate the ability of OBFNs to support single-beam, multi-beam, and multicast operation. Its performance will be assessed under various experimental cases that will include among others the processing of microwave signals with frequencies up to 15 GHz with modulation formats up to 16-QAM.

Objective 4: Characterize a fully integrated TTD-OBFNs

A fully functional MWP system including a continuous tuning TTD-OBFN will be tested. The experimental evaluation of the OBFN-PIC will be performed in two stages. In the first one, the link gain, the noise figure (NF), and the spurious-free dynamic range (SFDR) of the microwave photonics link will be derived. In the second stage, its beamforming performance will be assessed using modulated microwave signals with 5 and 10 GHz carrier frequencies and considering that the OBFN-PIC is part of a wireless system operating in the downlink direction and feeds a multi-element antenna array.

Objective 5: Analyse the operating principle of OBFNs based on Blass-matrix architecture and develop a novel configuration algorithm for controlling the optical components

As mentioned earlier in the introduction, the most promising OBFN architecture that can scale up gracefully in terms of the number of beams but also in terms of AEs is the Blass matrix. Even though that an integrated implementation of this type of optical Blass matrix network has been briefly discussed in the literature [89], no details were given in this specific work to explain in depth the optical Blass matrix concept, describe the methods for its design, its configuration and give an insight into its expected beamforming performance. To fill this gap a mathematical analysis will be conducted including extensive simulation studies for the design and operation of a multi-beam optical beamforming network based on Blass matrix.

Objective 6: Characterize the performance of integrated OBFNs based on Blass-matrix architecture

Following the methodology, developed under Objective 5, the system performance of an 2×2 and an 8×8 OBFN based on Blass-matrix architectures will be evaluated. The prototypes will bring together two different photonic integration platforms, the silicon-nitride platform, and the polymer platform, which are both passive, flexible and feature very low loss. In order to enhance the PICs with active components, the polymer platform will host arrays of InP intensity modulators and InP photodiodes.

1.6 Organization of this dissertation

The technical work that has been carried out to address these objectives is reported in the following 7 Chapters.

In **Chapter 2**, the fundamental characteristics that define the operation of an antenna are presented. Starting from the inherent characteristics such as the power density, radiation intensity and directivity of a single antenna element, the concept of an antenna array is introduced. Focusing on the operation of linear antenna arrays, which will be extensively utilized across this dissertation, the equation of the array factor and its relationship with the antenna feeding network is derived as well as the conditions for achieving single-beam, multi-beam, and multicast beamforming. Special emphasis is placed on the two types of beamforming networks which are based on the use of either TTD elements or phase shifters and their impact on the resulting radiation pattern. Finally, the amplitude tapering technique is discussed as an efficient tool to reduce the unwanted power of the grating lobes.

In **Chapter 3**, the fundamentals of the microwave photonics technology are introduced. The key building blocks of the MWP links and systems used during the course of this dissertation are extensively analyzed and modelled. Additionally, the key figure of merits of a MWP link are discussed.

In **Chapter 4**, the system design, development, and experimental performance evaluation of a 2×4 true time delay optical beamforming network that supports the generation and steering of up to two independent beams over a continuous set of angles is demonstrated. The OBFN is based on a matrix of optical delay lines and a matrix of variable optical attenuators (VOAs) that control the relative time delays and relative amplitudes of the signals that excite the antenna elements in accordance with the intended beam directions and shapes. The performance evaluation of the OBFN is performed under single-beam, multi-beam and multicast operation. An aspect of the experimental setup is shown in Figure 1.12 (a).

In **Chapter 5**, a fully integrated 1×4 TTD-OBFN based on the InP and TriPleX platforms is presented and experimentally evaluated. The OBFN consists of four parallel optical paths each of one having 8 micro-ring resonators and was designed for operation up to 40 GHz.

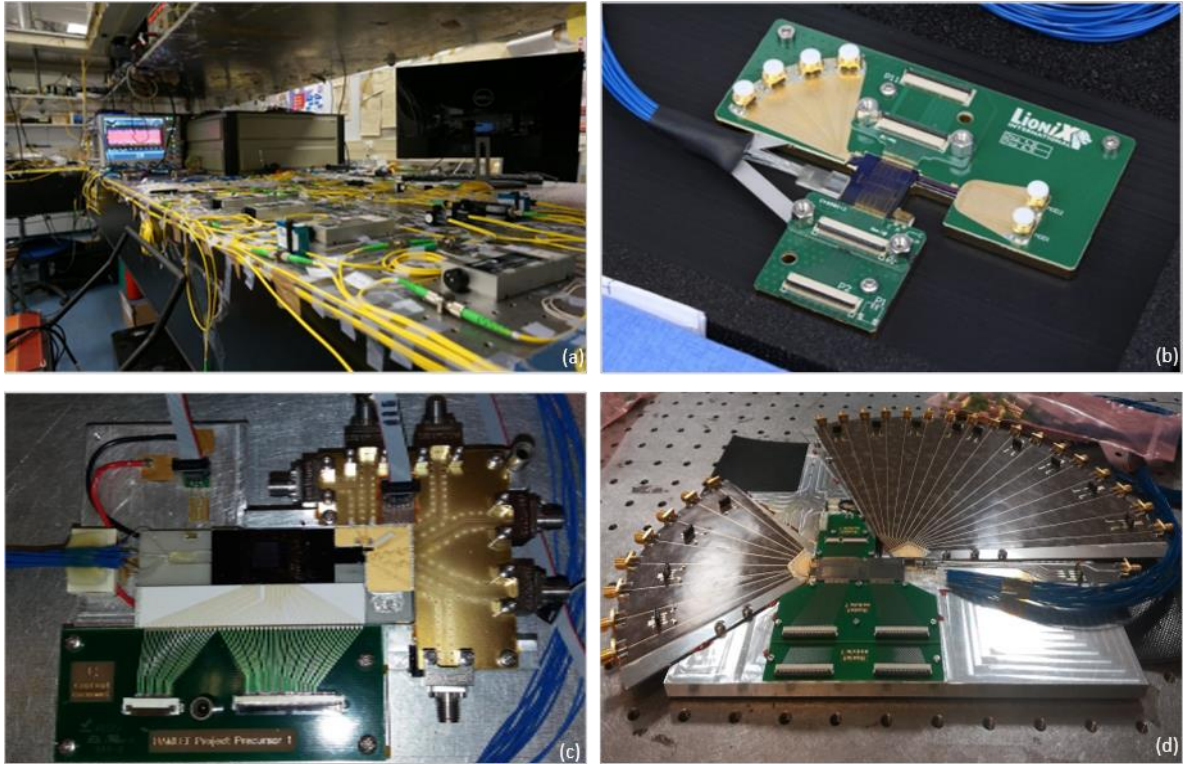


Figure 1.12: Pictures of optical beamforming networks reported in this dissertation. (a) 2×4 OBFN based on bulk optical delay lines and optical attenuators, serving as a testing vehicle for validating the principle of operation of single-beam, multi-beam, and multicast operations (see Chapter 4). (b) The first-ever 1×4 fully integrated Si₃N₄-InP OBFN based on a binary architecture with tunable optical true time delay elements, tested with high-order modulated RF signals (see Chapter 5). (c) 2×2 OBFN based on Blass matrix architecture (see Chapter 6), and (d) 8×8 OBFN based on Blass matrix architecture (see Chapter 6).

The prototype was extensively characterized, and the results are presented. A picture of the OBFN is shown in Figure 1.12 (b).

In **Chapter 6**, the principle of operation of an $M \times N$ OBFN based on Blass matrix is described. More specifically, we start with an analysis of the processing steps that are necessary for the microwave photonics signals at the input and output of the Blass matrix and propose a simple design and an algorithm for the configuration of the matrix, taking into account the properties of the Mach-Zehnder Interferometers (MZIs) as tunable optical couplers. The performance of the OBFN is assessed through extensive simulation studies. In addition, the characterization results of a 2×2 and an 8×8 OBFN based on Blass matrices are provided. The prototypes are depicted in Figure 1.12 (c) and (d), respectively.

In **Chapter 7**, the achievements of this work are summarized and a short outlook on the future development of the MWP technology and especially, of the OBFNs is provided.

References of Chapter 1

- [1] M. A. M. Albreem, "5G wireless communication systems: Vision and challenges," 2015 International Conference on Computer, Communications, and Control Technology (I4CT), 2015, pp. 493-497, doi: 10.1109/I4CT.2015.7219627.
- [2] Seymour, T., & Shaheen, A. (2011). History of wireless communication. Review of Business Information Systems (RBIS), 15(2), 37-42.
- [3] Lehenkari, J., & Miettinen, R. (2002). Standardisation in the construction of a large technological system—the case of the Nordic mobile telephone system. Telecommunications policy, 26(3-4), 109-127.
- [4] Escher JS (1997) Wireless portable communications trends and challenges. In: 1997 IEEE radio frequency integrated circuits (RFIC) symposium. Digest of Technical Papers, Denver, CO, USA, pp 1–3.
- [5] Smith, C., & Collins, D. (2002). 3G wireless networks. McGraw-Hill Education.
- [6] Chaudhury, Propid, Werner Mohr, and Seizo Onoe. "The 3GPP proposal for IMT-2000." IEEE Communications magazine 37.12 (1999): 72-81.
- [7] Varshney, U. (2012). 4G wireless networks. IT Professional, 14(5), 34-39.
- [8] Glisic, S., & Makela, J. P. (2006, August). Advanced wireless networks: 4G technologies. In 2006 IEEE Ninth International Symposium on Spread Spectrum Techniques and Applications (pp. 442-446). IEEE.
- [9] Akpakwu, G. A., Silva, B. J., Hancke, G. P., & Abu-Mahfouz, A. M. (2017). A survey on 5G networks for the Internet of Things: Communication technologies and challenges. IEEE access, 6, 3619-3647.
- [10] M. Agiwal, A. Roy and N. Saxena, "Next Generation 5G Wireless Networks: A Comprehensive Survey," in IEEE Communications Surveys & Tutorials, vol. 18, no. 3, pp. 1617-1655, thirdquarter 2016, doi: 10.1109/COMST.2016.2532458.
- [11] Karjalainen, J., Nekovee, M., Benn, H., Kim, W., Park, J., & Sungsoo, H. (2014, June). Challenges and opportunities of mm-wave communication in 5G networks. In 2014 9th international conference on cognitive radio oriented wireless networks and communications (CROWNCOM) (pp. 372-376). IEEE.
- [12] J. G. Andrews et al., "What Will 5G Be?," in IEEE Journal on Selected Areas in Communications, vol. 32, no. 6, pp. 1065-1082, June 2014, doi: 10.1109/JSAC.2014.2328098.
- [13] Cisco, Visual Networking Index, Feb. 2014, white paper at Cisco.com.
- [14] <https://www.ericsson.com/en/reports-and-papers/mobility-report/mobility-visualizer?f=8&ft=2&r=1&t=1.20&s=4&u=3&y=2021.2027&c=3>
- [15] <https://blog.3g4g.co.uk/>
- [16] W. Roh, "5G Mobile Communications for 2020 and Beyond," in Proc. IEEE WCNC 2014, Istanbul, April 2014
- [17] https://www.itu.int/dms_pubrec/itu-r/rec/m/R-REC-M.2083-0-201509-1!PDF-E.pdf
- [18] https://www.etsi.org/deliver/etsi_ts/122100_122199/122186/15.03.00_60/ts_122186v150300p.pdf
- [19] Li, Z., Usitalo, M. A., Shariatmadari, H., & Singh, B. (2018, August). 5G URLLC: Design challenges and system concepts. In 2018 15th international symposium on wireless communication systems (ISWCS) (pp. 1-6). IEEE.
- [20] Hellenic Telecommunications & Post Commission "Public Consultation on Granting of Radiofrequency Usage Rights in the 700 MHz, 2 GHz, 3400 – 3800 MHz and 26 GHz bands.
- [21] <https://www.exfo.com/es/recursos/blog/rf-5g-new-radio-top-5-questions/>
- [22] Al-Falahy, Naser, and Omar Y. Alani. "Technologies for 5G networks: Challenges and opportunities." It Professional 19.1 (2017): 12-20.
- [23] https://www.nttdocomo.co.jp/english/info/media_center/pr/2014/0508_00.html
- [24] <https://www.cambiumnetworks.com/blog/cambium-networks-announces-28-ghz-cnwave-multi-gigabit-5g-fixed-wireless-solution/>
- [25] https://www.eett.gr/opencms/export/sites/default/EETT/library_videos/Proceedings/PDFs/2020.pdf
- [26] <https://iotindustriel.com/glossaire-iiot/5g-small-cell/>
- [27] Cheng Liu et al., "Key Microwave-Photonics Technologies for Next-Generation Cloud-Based Radio Access Networks," Lightwave Technology, Journal of, vol.32, no.20, pp.3452,3460, Oct.15, 15 2014
- [28] J. E. Mitchell, "Integrated Wireless Backhaul Over Optical Access Networks," J Light Tech, vol. 32, no. 20, 2014
- [29] <https://gsma.force.com/mwcoem/servlet/servlet.FileDownload?file=00P1r000025E2yhEAC>
- [30] Bassoy, S., Farooq, H., Imran, M. A., & Imran, A. (2017). Coordinated multi-point clustering schemes: A survey. IEEE Communications Surveys & Tutorials, 19(2), 743-764.
- [31] Jun Wu et al., "Cloud radio access network (C-RAN): a primer," Network, IEEE, vol.29, no.1, pp.35,41, 2015
- [32] Cheng Liu et al., "Key Microwave-Photonics Technologies for Next-Generation Cloud-Based Radio Access Networks," Lightwave Technology, Journal of, vol.32, no.20, pp.3452,3460, Oct.15, 15 2014
- [33] J.G. Andrews et al., "What Will 5G Be?," Selected Areas in Communications, IEEE Journal on, vol.32, no.6, pp.1065,1082, June 2014
- [34] Ali, E., Ismail, M., Nordin, R., & Abdulah, N. F. (2017). Beamforming techniques for massive MIMO systems in 5G: overview, classification, and trends for future research. Frontiers of Information Technology & Electronic Engineering, 18(6), 753-772.
- [35] Shevada, L., Raut, H. D., Malekar, R., & Kumar, S. (2021). Comparative Study of different beamforming techniques for 5G: A Review. Inventive Communication and Computational Technologies, 589-595.
- [36] <https://www.cellnex.com/>
- [37] Cheng-Xiang Wang et al., "Cellular Architecture and Key Technologies for 5G Wireless Communication Networks", IEEE Communication Magazine, pp 122-130, February 2014
- [38] T. Kim et al., "Tens of Gbps Support with mmWave Beamforming Systems for Next Generation Communications", IEEE GLOBECOM '13, pp. 3790–95, Dec. 2013

- [39] Y. Lo, S. Lee, and Q. Lee, "Optimization of directivity and signal-to-noise 1114 ratio of an arbitrary antenna array," *Proc. IEEE*, vol. 54, no. 8, pp. 1033–1115 1045, Aug. 1966.
- [40] R. Mailloux, *Phased Array Antenna Handbook*. Norwood, MA, USA:1121 Artech House, 2005.
- [41] J. Butler and R. Lowe, "Beam-forming matrix simplifies design of electronically scanned antenna," *Electron. Des.*, vol. 9, pp. 170–173, 1961.
- [42] H. Moody, "The systematic design of the Butler matrix," *IEEE Trans. Antennas Propag.*, vol. 12, no. 6, pp. 786–788, 1964.
- [43] J. Nolen, "Synthesis of multiple beam networks for arbitrary illuminations," Ph.D. dissertation, Radio Div., Bendix Corp., Baltimore, MD, USA, 1965.
- [44] N. J. G. Fonseca, "Printed S-band 4x4 Nolen matrix for multiple beam antenna applications," *IEEE Trans. Antennas Propag.*, vol. 57, no. 6, pp. 1673–1678, Jun. 2009.
- [45] J. Blass, "Multidirectional antenna - A new approach to stacked beams," *Proc. IRE*, vol. 48, no. 3, pp. 402–402, 1960.
- [46] S. Mosca, F. Bilotti, A. Toscano, and L. Vegni, "A novel design method for Blass matrix beam-forming networks," *IEEE Trans. Antennas Propag.*, vol. 50, no. 2, pp. 225–232, Feb. 2002.
- [47] W. Hong et al., "Multibeam Antenna Technologies for 5G Wireless Communications", in *IEEE Transactions on Antennas and Propagation*, vol. 65, no. 12, pp. 6231-6249, Dec. 2017.
- [48] P. Chen, W. Hong, Z. Kuai and J. Xu, "A Double Layer Substrate Integrated Waveguide Blass Matrix for Beamforming Applications," in *IEEE Microwave and Wireless Components Letters*, vol. 19, no. 6, pp. 374-376, June 2009, doi: 10.1109/LMWC.2009.2020020.
- [49] Bhowmik, P., Moyra, T. Modelling and Validation of a Compact Planar Butler Matrix by Removing Crossover. *Wireless Pers Commun* 95, 5121–5132 (2017). <https://doi.org/10.1007/s11277-017-4158-7>
- [50] P. Li, H. Ren, and B. Arigong, "A symmetric beam-phased array fed by a Nolen matrix using 180° couplers," *IEEE Microw. Wireless Compon. Lett.*, vol. 30, no. 4, pp. 387–390, Apr. 2020.
- [51] Y. J. Cheng, W. Hong, K. Wu, Z. Q. Kuai, C. Yu, J. X. Chen, J. Y. Zhou, and H. J. Tang, "Substrate integrated waveguide (SIW) Rotman lens and its Ka-band multibeam array antenna applications," *IEEE Trans. Antennas Propag.*, vol. 56, no. 8, pp. 2504–2513, Aug. 2008.
- [52] Vashist, S., Soni, M. K., & Singhal, P. K. (2014). A review on the development of Rotman lens antenna. *Chinese Journal of Engineering*, 2014(11), 1-9.
- [53] Seeds, "Microwave photonics," *IEEE Trans. Microw. Theory Tech.* 50(3), 877–887 (2002).
- [54] J. Capmany and D. Novak, "Microwave photonics combines two worlds," *Nat. Photonics* 1(6), 319–330 (2007).
- [55] J. Yao, "Microwave Photonics," *J. Lightwave Technol.* 27(3), 314–335 (2009).
- [56] B. Jung, D. Kim, I. Jeon, S. Shin and H. Kim, "Optical true time-delay beamformer based on microwave photonics for phased array radar," 2011 3rd International Asia-Pacific Conference on Synthetic Aperture Radar (APSAR), Seoul, Korea (South), 2011, pp. 1-4.
- [57] B. Jung, J. Shin and B. Kim, "Optical True Time-Delay for Two-Dimensional X-Band Phased Array Antennas," in *IEEE Photonics Technology Letters*, vol. 19, no. 12, pp. 877-879, June 15, 2007, doi: 10.1109/LPT.2007.897530.
- [58] S. Garcia and I. Gasulla, "Design of heterogeneous multicore fibers as sampled true-time delay lines," *Opt. Lett.* 40, 621-624 (2015)
- [59] S. García, M. Ureña and I. Gasulla, "Heterogeneous multicore fiber for optical beamforming," 2019 International Topical Meeting on Microwave Photonics (MWP), Ottawa, ON, Canada, 2019, pp. 1-4, doi: 10.1109/MWP.2019.8892123.
- [60] L. Zhang, M. Li, N. Shi, X. Zhu, S. Sun, J. Tang, W. Li, and N. Zhu, "Photonic true time delay beamforming technique with ultra-fast beam scanning," *Opt. Express* 25, 14524-14532 (2017).
- [61] P. Wu, S. Tang, and D. E. Raible, "A prototype high-speed optically-steered X-band phased array antenna," *Opt. Express* 21, 32599-32604 (2013).
- [62] H. Zmuda, R. A. Soref, P. Payson, S. Johns, and E. N. Toughlian, "Photonic beamformer for phased array antennas using a fiber grating prism," in *IEEE Photonics Technology Letters*, vol. 9, no. 2, pp. 241-243, Feb. 1997, doi: 10.1109/68.553105.
- [63] J. Zhang and J. Yao, "Photonic True-Time Delay Beamforming Using a Switch-Controlled Wavelength-Dependent Recirculating Loop," in *Journal of Lightwave Technology*, vol. 34, no. 16, pp. 3923-3929, 15 Aug. 15, 2016, doi: 10.1109/JLT.2016.2583918.
- [64] R. Bonjour, S. Welschen, J. F. Johansson and J. Leuthold, "Steering and Shaping of Multiple Beams with a Spatial Light Modulator based Beamformer," 2018 International Topical Meeting on Microwave Photonics (MWP), Toulouse, France, 2018, pp. 1-4, doi: 10.1109/MWP.2018.8552916.
- [65] B. Vidal, T. Mengual, C. Ibanez-Lopez and J. Marti, "Optical Beamforming Network Based on Fiber-Optical Delay Lines and Spatial Light Modulators for Large Antenna Arrays," in *IEEE Photonics Technology Letters*, vol. 18, no. 24, pp. 2590-2592, Dec. 15, 2006, doi: 10.1109/LPT.2006.887347.
- [66] J. Wang, P. Hou, H. Cai, J. Sun, S. Wang, L. Wang, and F. Yang, "Continuous angle steering of an optically-controlled phased array antenna based on differential true time delay constituted by micro-optical components," *Opt. Express* 23, 9432-9439 (2015).
- [67] N. Hamdash, A. Shariha, T. Rampone, C. Quando, N. Martin and D. Le Berre, "Optically Controlled RF Phase Shifts in SOAs by Adding the XGM Response of an Optical Signal," in *IEEE Photonics Technology Letters*, vol. 31, no. 13, pp. 1060-1063, 1 July 1, 2019, doi: 10.1109/LPT.2019.2918074.
- [68] P. Berger, J. Bourderionnet, F. Bretenaker, D. Dolfi, and M. Alouini, "Time delay generation at high frequency using SOA based slow and fast light," *Opt. Express* 19, 21180-21188 (2011).

- [69] R. Bonjour, S. A. Gebrewold, D. Hillerkuss, C. Hafner and J. Leuthold, "Ultra-fast tunable true-time delay using complementary phase-shifted spectra (CPSS)," 2015 Optical Fiber Communications Conference and Exhibition (OFC), Los Angeles, CA, USA, 2015, pp. 1-3, doi: 10.1364/OFC.2015.W2A.67.
- [70] N. A. Riza, "Novel acousto-optic systems for spectrum analysis and phased array radar signal processing," Ph.D. dissertation (California Institute of Technology, Pasadena, Calif., 1989), Chap. 6.
- [71] N. Riza, "An acoustooptic-phased-array antenna beamformer for multiple simultaneous beam generation", IEEE Photonics Technology Letters, vol. 4, no. 7, pp. 807-809, 1992.
- [72] N. Riza, "Optical multiple beam-forming systems for wireless communication antennas", Proceedings of SPIE, 1995.
- [73] M. Frankel and R. Esman, "True time-delay fiber-optic control of an ultrawideband array transmitter/receiver with multibeam capability", IEEE Transactions on Microwave Theory and Techniques, vol. 43, no. 9, pp. 2387-2394, 1995.
- [74] P. Matthews, M. Frankel and R. Esman, "A wide-band fiber-optic true-time-steered array receiver capable of multiple independent simultaneous beams", IEEE Photonics Technology Letters, vol. 10, no. 5, pp. 722-724, 1998.
- [75] H. Subbaraman, M. Chen and R. Chen, "Photonic Crystal Fiber-Based True-Time-Delay Beamformer for Multiple RF Beam Transmission and Reception of an X-Band Phased-Array Antenna", Journal of Lightwave Technology, vol. 26, no. 15, pp. 2803-2809, 2008.
- [76] L. Yaron, R. Rotman, S. Zach and M. Tur, "Photonic Beamformer Receiver With Multiple Beam Capabilities", IEEE Photonics Technology Letters, vol. 22, no. 23, pp. 1723-1725, 2010.
- [77] S. Granieri, M. Jaeger and A. Siahmakoun, "Multiple-beam fiber-optic beamformer with binary array of delay lines", Journal of Lightwave Technology, vol. 21, no. 12, pp. 3262-3272, 2003.
- [78] Yanyan Liu, G. Burnham, Guanghai Jin and Jing Zhao, "Wideband multi-beam photonics-based RF beamformer", 2010 IEEE International Symposium on Phased Array Systems and Technology, 2010
- [79] Y. Ji, K. Inagaki, R. Miura and Y. Karasawa, "Optical processor for multibeam microwave array antennas", Electronics Letters, vol. 32, no. 9, p. 822, 1996.
- [80] N. Riza, "High speed multi-beamforming for wideband phased arrays", MWP 2003 Proceedings. International Topical Meeting on Microwave Photonics, 2003.
- [81] O. Shibata, K. Inagaki, Y. Karasawa and Y. Mizuguchi, "Spatial optical beam-forming network for receiving-mode multibeam array antenna - proposal and experiment", IEEE Transactions on Microwave Theory and Techniques, vol. 50, no. 5, pp. 1425-1430, 2002.
- [82] T. Akiyama et al., "Spatial light modulator based optically controlled beamformer for variable multiple-spot beam antenna," 2011 International Topical Meeting on Microwave Photonics jointly held with the 2011 Asia-Pacific Microwave Photonics Conference, 2011.
- [83] T. Mengual et al., "Optical Beamforming Network with Multibeam Capability based on a Spatial Light Modulator", OFC/NFOEC 2008 - 2008 Conference on Optical Fiber Communication/National Fiber Optic Engineers Conference, 2008.
- [84] W. Charczenko, M. Surette, P. Matthews, H. Klotz and A. Mickelson, "Integrated optical Butler matrix for beam forming in phased-array antennas", Optoelectronic Signal Processing for Phased-Array Antennas II, 1990.
- [85] J. Gallo and R. DeSalvo, "Experimental demonstration of optical guided-wave Butler matrices", IEEE Transactions on Microwave Theory and Techniques, vol. 45, no. 8, pp. 1501-1507, 1997.
- [86] D. Madrid et al., "A novel 2N beams heterodyne optical beamforming architecture based on N×N optical Butler matrices", 2002 IEEE MTT-S International Microwave Symposium Digest.
- [87] C. Roeloffzen, et al., "Integrated Optical Beamformers", *Optical Fiber Communication Conference*, 2015.
- [88] B. Li, Y. Chen, N. Jiang, Z. Fu, S. Tang and R. Chen, "Photonic phased-array antenna system based on detector-switched optical Blass matrix true-time-delay steering and heterodyne rf generation", Applications of Photonic Technology 4, 2000.
- [89] J. Anzalchi, et al., "Optical beamforming based on microwave photonic signal processing", International Conference on Space Optics — ICSO 2016, 2017.
- [90] C. J. Chung, X. Xu, G. Wang, Z. Pan, and R. T. Chen, "On-chip optical true time delay lines featuring one-dimensional fishbone photonic crystal waveguide." Applied Physics Letters 112.7 (2018): 071104.
- [91] J. Sancho, J. Bourderionnet, J. Lloret, S. Combrie, I. Gasulla, S. Xavier, S. Sales, P. Colman, G. Lehoucq, D. Dolfi, J. Capmany, and A. D. Rossi, "Integrable microwave filter based on a photonic crystal delay line." Nat Commun 3, 1075 (2012). <https://doi.org/10.1038/ncomms2092>.
- [92] J. Wang, R. Ashrafi, R. Adams, I. Glesk, I. Gasulla, J. Capmany, and L. R. Chen, "Subwavelength grating enabled on-chip ultra-compact optical true time delay line." Sci Rep 6, 30235 (2016). <https://doi.org/10.1038/srep30235>.
- [93] J. Xie, L. Zhou, Z. Li, J. Wang, and J. Chen, "Seven-bit reconfigurable optical true time delay line based on silicon integration," Opt. Express 22, 22707-22715 (2014).
- [94] C. Zhu, L. Lu, W. Shan, W. Xu, G. Zhou, L. Zhou, and J. Chen, "Silicon integrated microwave photonic beamformer," Optica 7, 1162-1170 (2020)
- [95] P. Zheng, X. Xu, D. Lin, P. Liu, G. Hu, B. Yun, Y. Cui, "A wideband 1×4 optical beam-forming chip based on switchable optical delay lines for Ka-band phased array, " Optics Communications, Vol 488, (2021).
- [96] R. L. Moreira, J. Garcia, W. Li, J. Bauters, J. S. Barton, M. J. R. Heck, J. E. Bowers, and D. J. Blumenthal, "Integrated Ultra-Low-Loss 4-Bit Tunable Delay for Broadband Phased Array Antenna Applications," in IEEE Photonics Technology Letters, vol. 25, no. 12, pp. 1165-1168, June15, 2013, doi: 10.1109/LPT.2013.2261807.
- [97] Q. Cheng, S. Zheng, Q. Zhang, J. Ji, H. Yu, and X. Zhang, "An integrated optical beamforming network for two-dimensional phased array radar." Optics Communications (2021): 126809.
- [98] V. Duarte, J. G. Prata, C. F. Ribeiro, R. N. Nogueira, G. Winzer, L. Zimmermann, R. Walker, S. Clements, M. Filipowicz, M. Napierala, T. Nasilowski, J. Crabb, M. Kechagias, L. Stampoulidis, J. Anzalchi, and M. V.

- Drummond, "Modular coherent photonic-aided payload receiver for communications satellites." *Nature communications* 10.1 (2019): 1-9.
- [99] L. Zhuang, C. G. H. Roeloffzen, R. G. Heideman, A. Borreman, A. Meijerink and W. van Etten, "Single-Chip Ring Resonator-Based 1x8 Optical Beam Forming Network in CMOS-Compatible Waveguide Technology," in *IEEE Photonics Technology Letters*, vol. 19, no. 15, pp. 1130-1132, Aug.1, 2007, doi: 10.1109/LPT.2007.900313.
- [100] Y. Liu, A. R. Wichman, B. Isaac, J. Kalkavage, E. J. Adles, T. R. Clark, and Jonathan Klamkin, "Ultra-Low-Loss Silicon Nitride Optical Beamforming Network for Wideband Wireless Applications," in *IEEE Journal of Selected Topics in Quantum Electronics*, vol. 24, no. 4, pp. 1-10, July-Aug. 2018, Art no. 8300410, doi: 10.1109/JSTQE.2018.2827786.
- [101] M. Burla, David A. I. Marpaung, L. Zhuang, M. R. Khan, A. Leinse, W. Beeker, M. Hoekman, R. G. Heideman, and C. G. H. Roeloffzen, "Multiwavelength-Integrated Optical Beamformer Based on Wavelength Division Multiplexing for 2-D Phased Array Antennas," in *Journal of Lightwave Technology*, vol. 32, no. 20, pp. 3509-3520, 15 Oct.15, 2014, doi: 10.1109/JLT.2014.2332426.
- [102] N. M. Tessema Z. Cao, J. H. C. Van Zantvoort, K. A. Mekonnen, A. Dubok, E. Tangdionga, A. B. Smolders, and A. M. J. Koonen, "A Tunable Si₃N₄ Integrated True Time Delay Circuit for Optically-Controlled K-Band Radio Beamformer in Satellite Communication," in *Journal of Lightwave Technology*, vol. 34, no. 20, pp. 4736-4743, 15 Oct.15, 2016, doi: 10.1109/JLT.2016.2585299.
- [103] A. Leinse, K. Wörhoff, I. Visscher, A. Alippi, C. Taddei, R. Dekker, D. Geskus, R. Oldenbeuving, D. H. Geuzebroek, and C. G. H. Roeloffzen, "Hybrid interconnection of InP and TriPleX photonic integrated circuits for new module functionality." *Optical Interconnects XIX*. Vol. 10924. International Society for Optics and Photonics, 2019.
- [104] I. Visscher, C. Roeloffzen, C. Taddei, M. Hoekman, L. Wevers, R. Grootjans, P. Kapteijn, D. Geskus, A. Alippi, R. Decker, R. Oldenbeuving, J. Epping, R. B. Timens, E. Klein, A. Leinse, P. V. Dijk, and R. Heideman, "Broadband True Time Delay Microwave Photonic Beamformer for Phased Array Antennas," 2019 13th European Conference on Antennas and Propagation (EuCAP), Krakow, Poland, 2019, pp. 1-5.
- [105] R. Grootjans, C. Roeloffzen, C. Taddei, M. Hoekman, L. Wevers, I. Visscher, R. Kapteijn, D. Geskus, A. Alippi, R. Dekker, R. Oldenbeuving, J. Epping, R. B. Timens, R. Heuvink, E. Klein, A. Leinse, P.V. Dijk, and R. Heideman, "Broadband Continuously Tuneable Delay Microwave Photonic Beamformer for Phased Array Antennas," 2019 14th European Microwave Integrated Circuits Conference (EuMIC), Paris, France, 2019, pp. 258-261, doi: 10.23919/EuMIC.2019.8909572.

Chapter 2 - Antenna and beamforming theory

2.1 Antenna characteristics

An antenna is defined as a metallic device (as a rod or wire) for radiating or receiving radio waves [1]. In other words, an antenna can be seen as the impedance transformer between the characteristic impedance of a transmission line and the intrinsic impedance of the free space. Based on the application, antennas can be found in all shapes and sizes; from little ones integrated into smartphones and tablets [2] to big ones that captures signals from satellites millions of kilometers away [3]. Therefore, in order to describe the performance of an antenna, the definitions of various parameters are necessary. Throughout this dissertation, a Cartesian coordinate system with axis labels x , y , and z will be used along with spherical coordinates θ (polar angle ranging from 0 to π , measured off the z -axis) and ϕ (azimuth angle ranging from 0 to 2π , measured off the x -axis).

Field regions: In principle, the radiation pattern of an antenna varies with respect to the direction and the operating frequency [1]. Thanks to the inherent reciprocity, the radiation pattern is the same regardless of whether the antenna is used to transmit or receive an electro-magnetic signal [1]. The radiation pattern has different shape depending on its distance from the antenna and this is why it is widely acceptable to divide the space surrounding an antenna into three regions: the near-field, the Fresnel region, and the far-field (Fraunhofer) region.

Table 1 Boundaries for near field, Fresnel region, and far-field [1]

Region	IEEE distance
Near field	$r < 0.62 \sqrt{D_A^3/\lambda}$
Fresnel	$0.62 \sqrt{D_A^3/\lambda} < r < 2D_A^2/\lambda$
Far-field	$r > 2D_A^2/\lambda$

r : distance from the antenna, D_A : the size of the antenna, and λ : operating wavelength

In the near field region, the radiated fields are reactive since the electrical and magnetic fields are out of phase by 90° to each other. In the Fresnel region, the radiative fields are already dominated, but the field patterns still depend on the distance from the antenna. On the contrary, in the far-field region, the radiation pattern does not change shape as the distance increases. While there is some interest in the near field region within the context of the near-field communications in practice, antennas communicate in the far-field region, and this is assumed throughout.

Radiation power density (Poynting vector) and radiation intensity: An important parameter for characterizing electromagnetic waves is the measure of power flowing through a surface, called the Poynting vector, defined as:

$$\vec{S} = \vec{E} \times \vec{H} \quad (2.1)$$

, where E the electric field (in V/m) and H the magnetic field (in A/m) of the wave. In other words, the Poynting vector represents the instantaneous power per unit area of the wave while its direction is the direction of the wave. In the far-field of the antenna, the electromagnetic field generated by the antenna can be locally approximated as a plane wave. Assuming propagation in an isotropic lossless medium, the magnitude of the magnetic field is given by the magnitude of the electric field vector divided by, η , the intrinsic impedance of the transmission medium:

$$|\vec{H}| = \frac{|\vec{E}|}{\eta} \quad (2.2)$$

, where $|\cdot|$ represents the vector norm. Substituting equation 2.2 into 2.3, the Poynting vector can be now expressed as:

$$\vec{S} = \frac{|\vec{E}|^2}{\eta} \quad (2.3)$$

Taking into account that in most of cases, both fields are oscillating around a certain frequency, it is of practical interest to calculate the time-average value of the Poynting vector. In the important case that the electric field is sinusoidally varying at some frequency with peak amplitude E_{peak} and rms voltage $E_{\text{peak}}/2$, the Poynting vector is given by:

$$\langle \vec{S} \rangle = \frac{E_{\text{peak}}^2}{2\eta} \text{ [W/m}^2\text{]} \quad (2.4)$$

Since the Poynting vector is a power density, the total power crossing a closed surface can be obtained by integrating the Poynting vector over the entire surface:

$$P_{\text{rad}} = \oint \vec{S} \cdot \vec{ds} = \oint \vec{S} \cdot \hat{n} da \quad \text{[W]} \quad (2.5)$$

, where P the instantaneous power, \vec{ds} the vector of the closed surface, \hat{n} unit vector normal to the surface, and da infinitesimal area of the closed surface. For an isotropic antenna, the power is radiated equally to all directions. However, such antennas are only hypothetical because in practice no real antenna can produce a truly isotropic radiation. Nevertheless, isotropic antennas remain a useful mathematical model that is commonly used as the base of comparison to calculate the directionality or gain of real antennas. For a such ideal antenna, the power density (Poynting vector) can be expressed as:

$$S_{\text{iso}} = \frac{P_{\text{rad}}}{4\pi r^2} \quad (2.6)$$

From Eq. (2.6) can be easily derived that for an isotropic source the power density decay corresponds to the increasing area of a sphere, located at the position of the source with a radius r . A graphical representation of the inverse square law is shown in Figure 2.1. The radiation intensity, U , in a given direction is defined as the power radiated from an antenna per unit solid angle. The radiation intensity is a far-field parameter, and it can be obtained by multiplying the radiation power density, S by the square of the distance. In mathematical form, the radiation intensity can be expressed as:

$$U = r^2 \cdot S \quad (2.7)$$

For an isotropic source, the radiation intensity can be expressed as follows:

$$U_{\text{iso}} = r^2 \cdot S_{\text{iso}} = \frac{P_{\text{rad}}}{4\pi} \quad (2.8)$$

Radiation pattern and directivity: The radiation pattern of an antenna describes how the radiation intensity is distributed in the space as a function of the direction away from the antenna. In other words, the radiation pattern is the two- or three-dimensional spatial

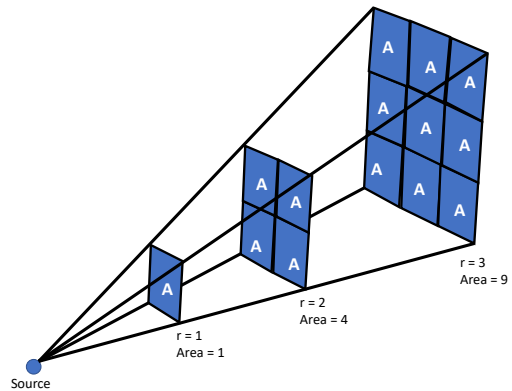


Figure 2.1: Inverse square law of the power decay.

distribution of the power transmitted or received by an antenna as a function of the observer's position. For an ideal isotropic antenna, the radiation pattern is identical in all directions. The antenna structure that approaches this ideal response is the omnidirectional. Unlike the isotropic, the omnidirectional antennas radiate equal power in the azimuth plane but in the elevation plane the radiated power varies with the respect the elevation angle, θ , and is decreased to zero along the antenna's vertical axis.

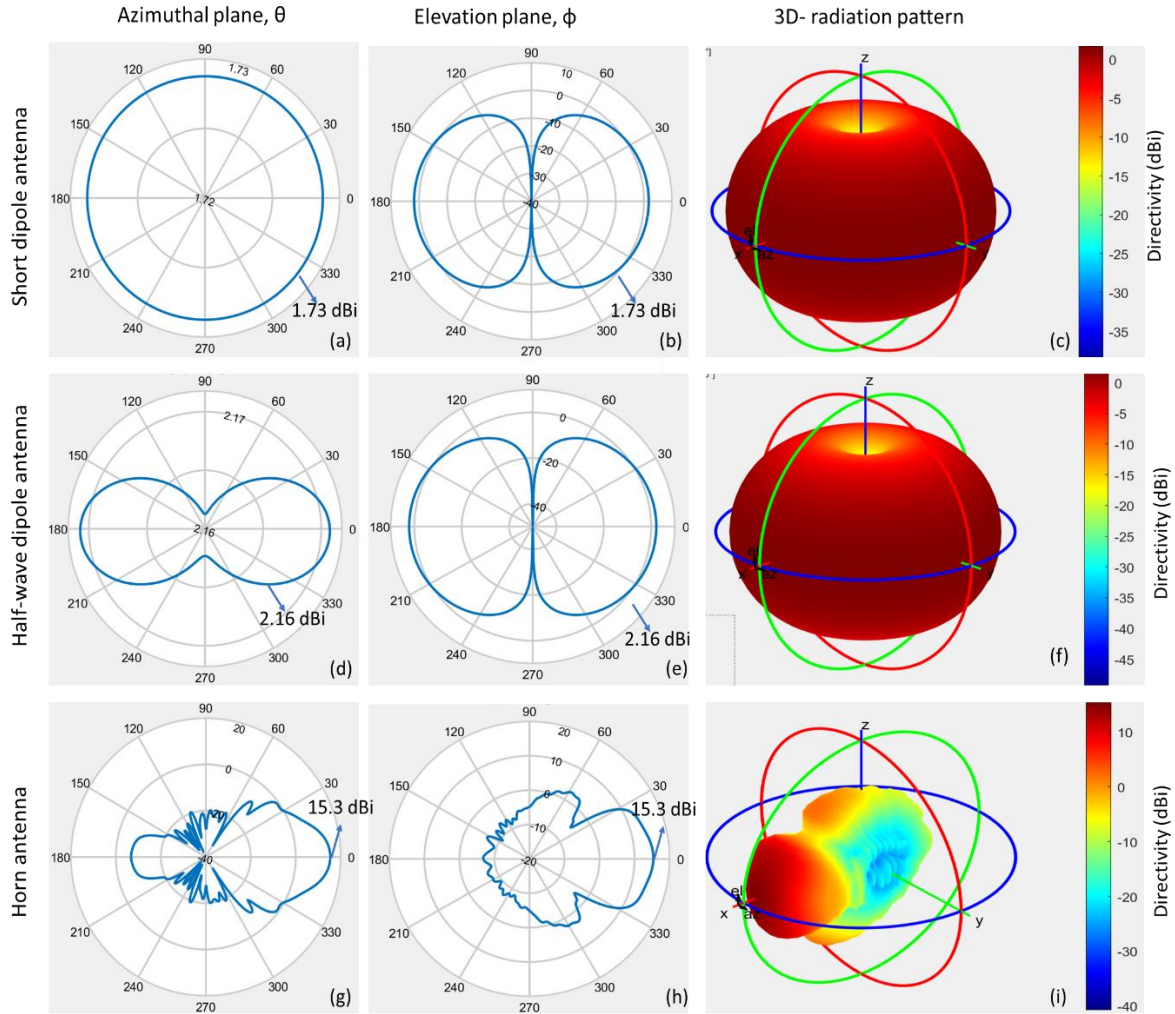


Figure 2.2: Typical 2D radiation patterns at the azimuthal plane and elevation plane as well as 3D radiation patterns of a short dipole antenna (a-c), half-wave dipole antenna (d-f), and a horn antenna (g-i).

Directivity is a measure of how 'directional' an antenna's radiation pattern is. An isotropic antenna has effectively zero directionality, and the directivity of this type of antenna would be 1 (or 0 dB). Mathematically, the directivity is the radiation intensity of an antenna at a specific direction, usually expressed in the polar coordinates, (θ, ϕ) , divided by the radiation intensity of an isotropic antenna, radiating the same amount of total power into space [1]:

$$D(\theta, \phi) = \frac{U(\theta, \phi)}{U_{\text{iso}}} = \frac{U(\theta, \phi)}{P_{\text{rad}}/4\pi} \quad (2.9)$$

Directivity is rarely expressed as the unitless number, D , but rather it is expressed in its logarithmic scale:

$$D_{\text{dBi}} = 10\log_{10}\left(\frac{U(\theta, \phi)}{P_{\text{rad}}/4\pi}\right) \quad (2.10)$$

, where dBi stands for decibel relative to an isotropic antenna. Figure 2.2 shows typical 2D and 3D radiation patterns of a short dipole, half-wave dipole, and horn antennas. The short dipole antenna having the length of its waveguide shorter than the wavelength of the radiated wave exhibits a directivity approximately equal to 1.73 dBi. The half-wave dipole antenna as implies its name has half the length of the wavelength of the radiated wave and exhibits a directivity approximately equal to 2.16 dBi. As can be easily observed, especially, from the 3D radiation patterns both antennas are not highly directional. On the other hand, the horn antennas are highly directional antennas with typical directivity between 10-20 dBi. It is evident that having large directivity in a one direction implies having lower directivity in other directions. The selection of the antenna type is highly dependent on the system requirements and hence the application scenario.

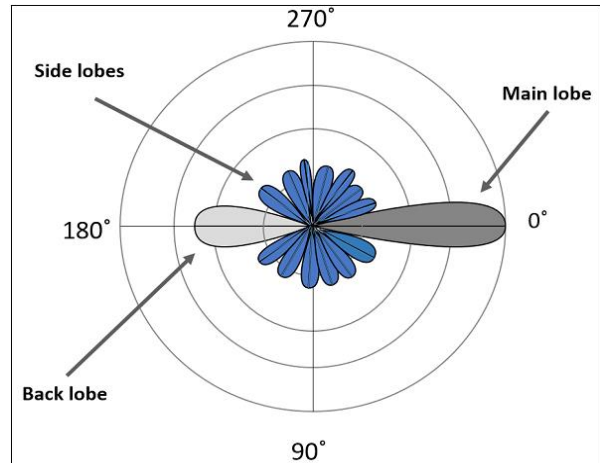


Figure 2.3: Indicative radiation pattern in polar coordinates presenting the three types of lobes, the main, side, and back lobes [4].

As shown in Figure 2.3 the lobes are categorized into three types, the main lobe, side lobe, and back lobe. The main lobe is defined as the portion of the radiation pattern that encloses the maximum radiation. In some cases, such as in multi-beam or multi-cast operations, there may exist more than one major lobes in different directions. A side lobe is defined as the lobes in any other direction other than the direction of the main lobe. Therefore, side lobes indicate the amount of power radiated in undesired directions. Within the context of wireless communication systems, side lobes are of great importance since they dictate the signal-to interference plus noise ratio (SNIR) of the systems. The back lobe represents the portion of radiated pattern whose axis forms an angle of 180° with the axis of the main lobe.

2.2 Antenna array

In many applications, such as the cellular communication networks, it is highly desirable to employ highly directional antennas to meet the demands of long-distance communication and at the same time to minimize the radiation at directions other than the desired. By using a single antenna the radiation pattern is relatively wide and provides low directivity. One way to overcome this limitation is to increase the dimensions of the antenna. However, this approach leads to cumbersome antennas which eventually limits their use in many applications. A more elegant approach, retaining the physical dimensions of the antennas, is to form an assembly of antennas in an electrical and geometrical configuration. This antenna structure that is formed by multi-elements is known as an array [5]-[7]. The total radiation pattern of the array is determined by following parameters:

1. the radiation pattern of the individual AE
2. the geometrical configuration of the array
3. the relative displacement between the AEs
4. the excitation amplitude of each AE
5. the excitation phase of each AE

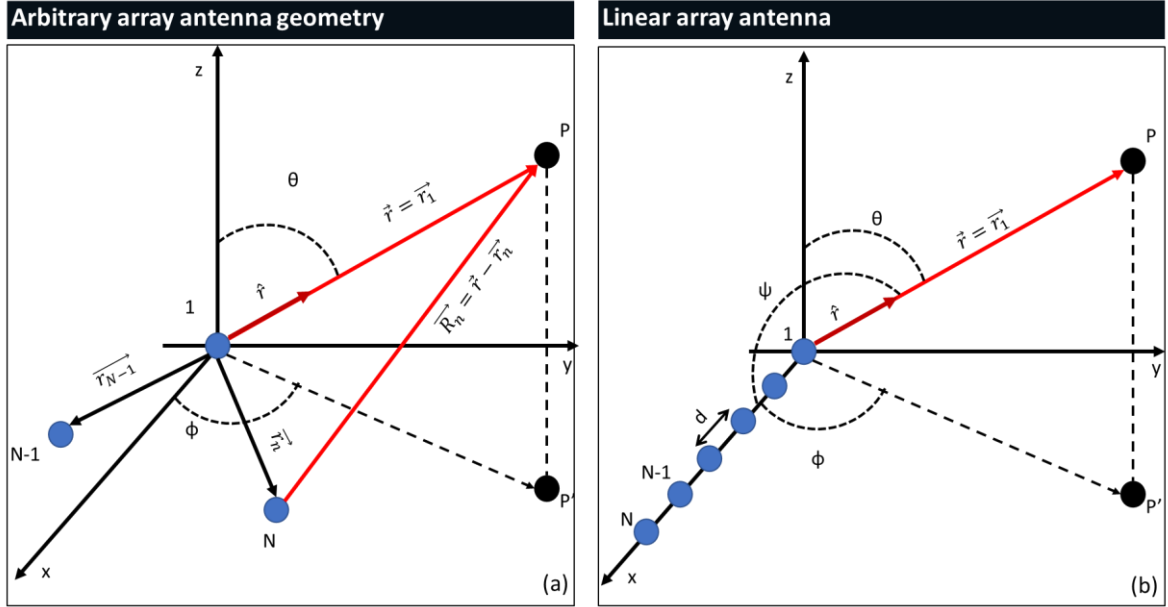


Figure 2.4: Schematic representation of (a) an arbitrary array antenna geometry and (b) a linear array antenna with antenna elements placed along the x-axis.

While the first parameter is provided by the manufacturer of the AEs and cannot be modified once it has been fabricated, the other parameters can be modified according to the desired radiation pattern. It is evident that once the spatial arrangement and orientation of the array antenna is fixed, the remaining degrees of freedom are the amplitude, $|C_i|$, and phase, a_i , of the excitation signals that are fed to the individual AEs. The network that is responsible for providing the excitation signal with the desired amplitude and phase is called beamformer. Therefore, the excitation signals determine the radiation characteristics of the array antenna according to well-defined mathematical relation that it will be analysed in the following paragraphs.

The array antennas can be found in various spatial arrangements such as linear, rectangular, and circular. For deriving the antenna characteristics of a such antenna structure, let us consider an arbitrary array antenna as the one shown in Figure 2.4 (a). The N-th antenna is excited by a complex signal $C_i = |C_i|e^{ia_i}$ and its location is described by the vector \vec{r}_n , expressed in polar coordinates with respect to the origin of coordinate system as follows:

$$\vec{r}_n = (r_n, \theta_n, \varphi_n), \quad (2.11)$$

The radiation field at the observation point, P, assuming that only the antenna placed at the origin of the coordinate system radiates, can be expressed as follows:

$$E_1 = |c_1| \cdot e^{ia_1} \cdot f(\theta, \varphi) \cdot \frac{e^{-ik_0 \vec{r}_1}}{r_1} \quad (2.12)$$

, where $f(\theta, \varphi)$ the electric field radiated by the antenna element and k_0 the angular wavenumber expressed as $k_0 = 2\pi/\lambda_0$, λ_0 the emitted wavelength. Thanks to the superposition principle [5]-[7], when all the antenna elements radiate, the received radiation at the observation point can be calculated by adding the radiations coming from of all the antenna elements of the array and can be expressed as follows:

$$E_P = \sum_{n=1}^N |c_n| \cdot e^{ia_n} \cdot f(\theta, \varphi) \cdot \frac{e^{-ik_0 \vec{R}_n}}{R_n} \quad (2.13)$$

, where $\overline{R}_n = |\vec{r} - \vec{r}_n|$. Assuming that the observation point is located at the far-field region, by using a first order Taylor approximation, the norm can be simplified as follows:

$$\overline{R}_n = |\vec{r} - \vec{r}_n| = |\vec{r}| - \hat{r} \cdot \vec{r}_n \quad (2.14)$$

, with \hat{r} the unit vector of \vec{r} . This allows two useful approximations in the Eq. 2.13 Without the loss of generality, the term $1/|\vec{r} - \vec{r}_n|$ in the denominator can be replaced by the term $1/r$ (amplitude approximation) while the same term in the phase argument of the nominator by the term $|\vec{r}| - \hat{r} \cdot \vec{r}_n$. Consequently, the total radiation pattern of the antenna array is now expressed as:

$$\begin{aligned} E_p &= \sum_{n=1}^N |c_n| \cdot e^{ia_n} \cdot f(\theta, \varphi) \cdot \frac{e^{-ik_0(r - \hat{r} \cdot \vec{r}_n)}}{r} \\ &= f(\theta, \varphi) \cdot \frac{e^{-ik_0 r}}{r} \sum_{n=1}^N |c_n| \cdot e^{ia_n} \cdot e^{ik_0 \hat{r} \cdot \vec{r}_n} \end{aligned} \quad (2.15)$$

From the above equation, it can be derived that the total radiation field at the point P depends on the electrical field radiated by a single antenna and a second term, called array factor (AF) which is given by the following equation:

$$AF = \sum_{n=1}^N |c_n| \cdot e^{ia_n} \cdot e^{ik_0 \hat{r} \cdot \vec{r}_n} \quad (2.16)$$

The radiation field received at the observation point can be now expressed as follows:

$$E_p = \frac{e^{-ik_0 r}}{r} \cdot f(\theta, \varphi) \cdot AF \quad (2.17)$$

In other words, the radiated field at the far-field region of any antenna array is equal to the product of the field of a single element, at a selected reference point and the AF.

$$E_p = [E(\text{single element at reference point})] \times [AF] \quad (2.18)$$

Additionally, by combining the Eq. 2.4 and 2.7 with the above equations, we can calculate the radiation intensity as well:

$$U_p = U(\theta, \varphi)_1 \cdot AF^2 \quad (2.19)$$

, where $U(\theta, \varphi)_1$ the radiation intensity of a single antenna element of the array antenna. The inherent characteristic of the radiated field at the far-field region is called pattern multiplication for arrays of identical antenna elements and is valid for arrays with any number of identical elements which do not necessarily have identical excitation magnitudes, phases and spacings. This is of utmost importance because it dictates that the radiation characteristics of an antenna array can be modified without modifying their individual radiation characteristics but simply by adjusting the antenna geometry ($\hat{r} \cdot \vec{r}_n$), the operating frequency and thus the wavenumber (k_0), and the amplitude and phase of the excitation signals ($|C_i|e^{ia_i}$). While the antenna geometry and the operating frequency are fixed during the operation of an antenna array, the reconfigurability of the array factor is achieved through the use of a so-called beamforming network, or beamformer which is a feed network that generates the desired amplitude and phase excitations at each specific antenna element of the array [5]-[7].

To our specific interest, in the next paragraphs, we will focus on the linear array antennas geometry, deriving their AFs, and subsequently, we will present the principles of operation of the beamformers and their relationship with the AF.

Linear antenna array: The linear array antennas are a class of antennas with a particular practical interest since they are the simplest geometry for phased array antennas. As an example, let us consider the linear array antenna of Figure 2.4 (b). The antenna comprises of N identical antenna elements, placed on along the x -axis and separated by a distance of d . Thus, the distance of each antennas element from the origin of the coordinate system is:

$$\vec{r}_n = (n - 1) \cdot d, n=1,\dots,N \quad (2.20)$$

Consequently, the scalar product in the phase argument of Eq.2.16 is:

$$\hat{r} \cdot \vec{r}_n = (n - 1) \cdot d \cdot \cos(\psi) = (n - 1) \cdot d \cdot \sin(\theta) \cdot \cos(\varphi) \quad (2.21)$$

, where ψ is the angle expressed in polar coordinates between the origin of the coordinate system in use and the observation point, P, at the far-field region of the antenna. The AF of a linear array can be calculated by combining the Eq. 2.21 with Eq. 2.16.

$$\begin{aligned} AF(\psi) = AF(\theta, \varphi) &= \sum_{n=1}^N |c_n| \cdot e^{ia_n} \cdot e^{ik_0(n-1) \cdot d \cdot \cos(\psi)} \\ &= \sum_{n=1}^N |c_n| \cdot e^{i(a_n + k_0(n-1) \cdot d \cdot \sin(\theta) \cdot \cos(\varphi))} \end{aligned} \quad (2.22)$$

As observed, for a specific operating wavelength and spacing, the AF depends only on the angle ψ . The angle ψ is known as scanning angle and it can take any value from 0 to π rad.

2.3 Single-beam beamforming

As discussed in the previous paragraph, the AF of a linear antenna array can be modified in such a way to control the shape and direction of the radiation intensity and in particular to select the angular position at which the maximum radiation occurs. In order to do that, we have just to modify accordingly the phase and amplitude of the excitation signals that feed the antenna. More specifically, the phase relationship of the excitation signals defines the direction of the maximum radiation point while the amplitude relationship the shape of the radiation pattern. To better explain these relationships, let us firstly assume that all the antenna elements are fed with equal amplitude $|c_n| = C, \forall n$. Now, let's further assume that the desired maximum radiation occurs at a specific point at the far-field region that corresponds to a specific angular angle ψ_{\max} and thus, a specific set of coordinates $(\theta_{\max}, \varphi_{\max})$. Under this condition, using Eq. 2.21 we can calculate the phase of excitation signals that maximize the AF.

$$a_n = -k_0(n - 1) \cdot d \cdot \cos(\psi_{\max}) = -k_0(n - 1) \cdot d \cdot \sin(\theta_{\max}) \cdot \cos(\varphi_{\max}) \quad (2.23)$$

By substituting Eq. 2.23 to Eq.2.22, the AF can be now expressed as follows:

$$\begin{aligned} AF(\psi) &= \sum_{n=1}^N C \cdot e^{-ik_0(n-1) \cdot d \cdot \cos(\psi_{\max})} \cdot e^{ik_0(n-1) \cdot d \cdot \cos(\psi)} \\ &= \sum_{n=1}^N C \cdot e^{ik_0(n-1) \cdot d \cdot (\cos(\psi) - \cos(\psi_{\max}))} \end{aligned} \quad (2.24)$$

Let's take as an example a 4-element linear array antenna with $\lambda/2$ spacing. Figure 2.5 presents the normalized AFs of this antenna in the case of steering the main lobe at 60° and 130° , by controlling the amplitude and phase of the excitation signals. Table 2 presents the values of the amplitude and phase of each excitation signal for both cases. In this scenario,

the underlying beamformer receive one information signal and configure the excitation signals in such a way that the array antenna radiates the information signal at one direction. For the rest of this dissertation, this scenario is called single-beam beamforming.

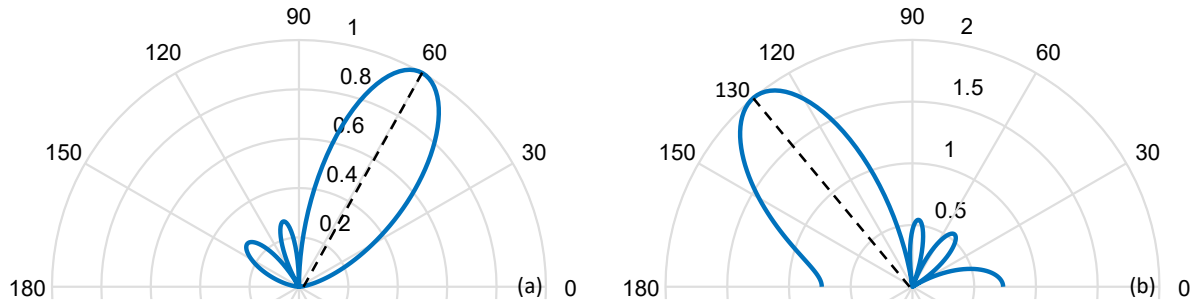


Figure 2.5: Normalized AFs of a 4-element linear array antenna with $d=\lambda/2$ spacing configured for single-beam operation and maximum radiation at (a) 60° and (b) 130° .

Table 2 Amplitude and phase coefficients of the excitation signals that correspond to the AFs of Figure 2.5

Exc. signal	Beam angle (ψ_{\max}) = 60°		Beam angle (ψ_{\max}) = 130°	
	Norm. amplitude	Phase (rad)	Norm. amplitude	Phase (rad)
1	0.5	0	0.5	0
2	0.5	-1.57	0.5	2.02
3	0.5	-3.14	0.5	4.04
4	0.5	-4.71	0.5	6.06

2.4 Multi-beam beamforming

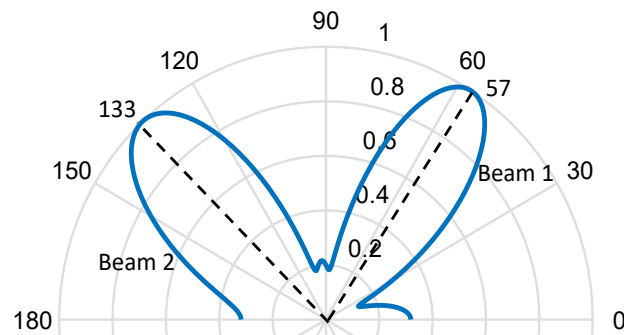


Figure 2.6: Normalized AFs of a 4-element linear array antenna with $d=\lambda/2$ spacing configured for multi-beam operation and maximum radiation at (a) 60° and (b) 130° .

Table 3: Amplitude and phase coefficients of the excitation signals that correspond to the AF of Figure 2.6.

Exc. signal	Beam angle 1(ψ_{\max}) = 60° & Beam angle 2(ψ_{\max}) = 130°	
	Norm. amplitude	Phase (rad)
1	1	0
2	0.22	-2.92
3	0.9	-2.69
4	0.62	0.67

The single-beam beamforming concept can be extended to multi-beam beamforming where the antenna systems transmit simultaneously multiple beams having different pointing directions. In this case, the total AF can be calculated by summing the AFs that corresponds to the different beams and can be expressed as follows:

$$AF(\psi) = \sum_{m=1}^M AF_m = \sum_{n=1}^N \sum_{m=1}^M C \cdot e^{ik_0(n-1) \cdot d \cdot (\cos(\psi) - \cos(\psi_{\max,m}))} \quad (2.25)$$

, where m is the number of the independent beams. In order to visualize the total AF in such a scenario, let's assume that in the array antenna of the previous example, we configure the beamforming network to receive two independent information signals and generates four excitation signals that feed the antenna which transmits the first beam to 60° and the second to 130° . As observed in Figure 2.6, the AF comprises of two main lobes as expected. However, the peak of both lobes deviates from the targeted directions. This is a direct result of the spatial interference of the two beams. More specifically, since the total AF is given by the sum of the individual AFs, if close to a main lobe there is a strong interference of a sidelobe of a different beam, this will diverge the main will cause the main lobe to deviate from the targeted direction.

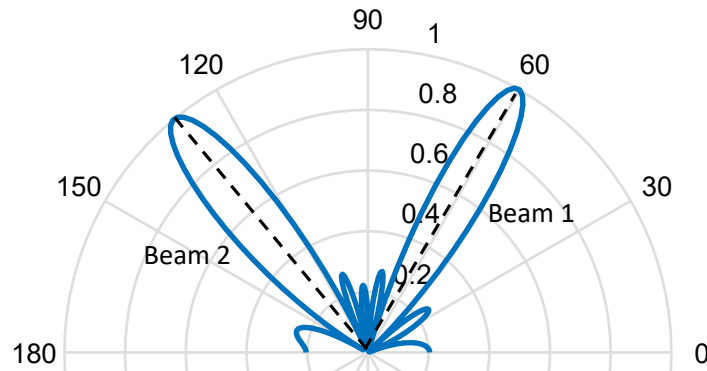


Figure 2.7: Normalized AFs of an 8-element linear array antenna with $d=\lambda/2$ spacing configured for multi-beam operation and maximum radiation at (a) 60° and (b) 130° .

Table 4: Amplitude and phase coefficient of the excitation signals that correspond to the AF of Figure 2.7

Exc. signal	Beam angle 1(ψ_{\max}) = 60° & Beam angle 2 (ψ_{\max}) = 130°	
	Norm. amplitude	Phase (rad)
1	0.7	0
2	0.16	-2.92
3	0.64	-2.69
4	0.44	0.67
5	0.44	0.9
6	0.64	-2.02
7	0.16	-1.8
8	0.7	1.57

A workaround is to increase the number of the antenna elements in order to narrow the width of each beam and minimize in this way the interference. As shown in Figure 5.2, by increasing the number of the antenna elements of the array antenna of the previous example from 4 to 8, both beams become pencil and are centred at the targeted directions. An alternative solution would be to apply an amplitude tapering in order to suppress the sidelobes. This technique will be analyzed in the paragraph 2.7.

2.5 Multicast beamforming

Addition to the single-beam and multi-beam beamforming operation, an array antenna can be configured to radiates the same information signal at different steering angles.

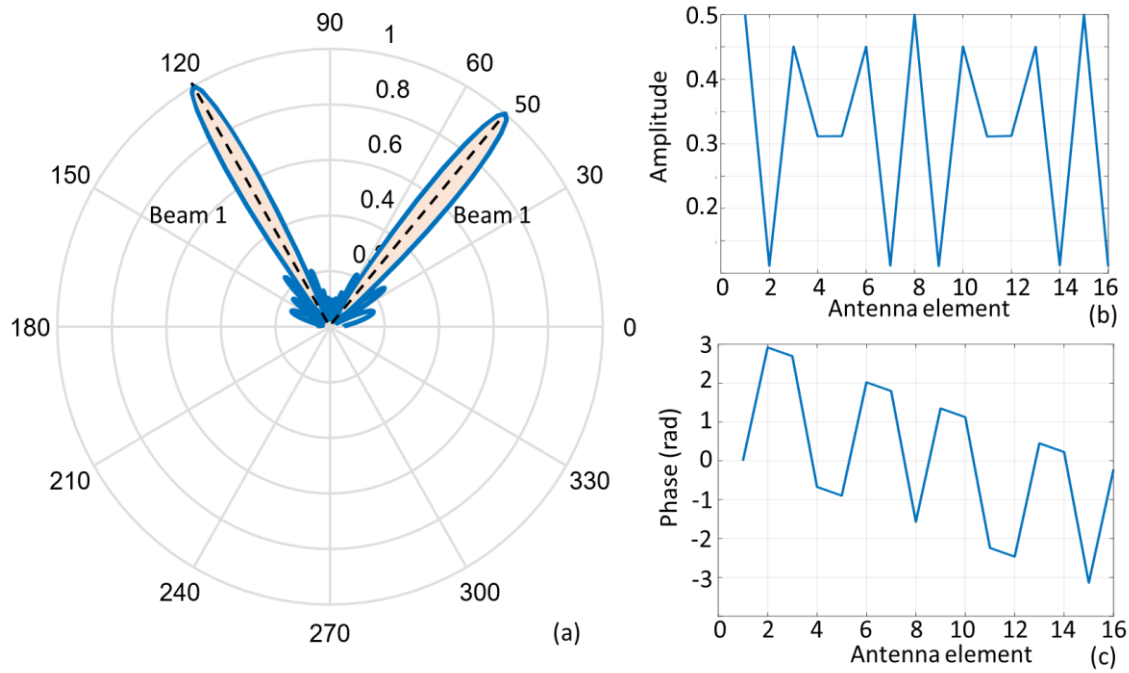


Figure 2.8: (a) Normalized Afs of a 16-element linear array antenna with $d=\lambda/2$ spacing configured for multi-cast operation with a single information signal and maximum radiations at 50° and 120° . The amplitude and phase of the excitation signals are plotted in (b) and (c), respectively.

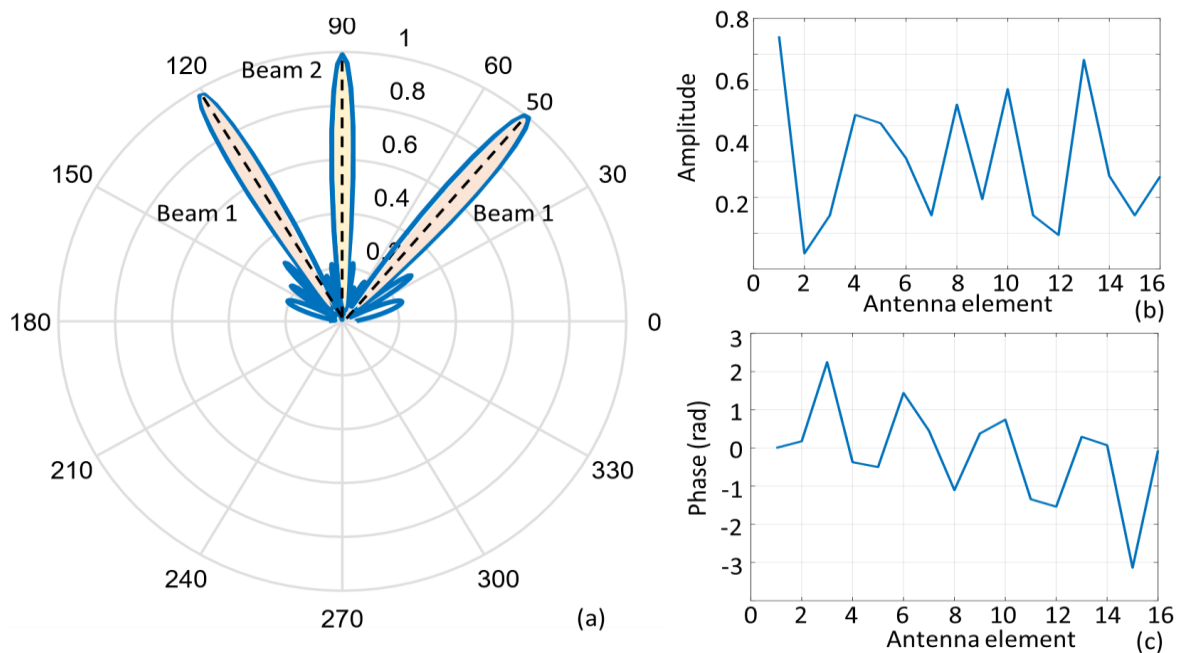


Figure 2.9: (a) Normalized Afs of a 16-element linear array antenna with $d=\lambda/2$ spacing configured for multi-cast operation with a two information signals. The first beam is steered to 50° and 120° while the second to 90° . The amplitude and phase of the excitation signals are plotted in (b) and (c), respectively.

In this case, the total AF is configured as in the multi-beam beamforming operation but only one information signal is fed as an input. As a result, the excitation signals are configured with respect to the desired steering angles but all of them carry the same information signal. As an example, in Figure 2.8, we consider a 16-element antenna array with $\lambda/2$ spacing. Following the same methodology as in the case of multi-beam beamforming, we calculate the total AF and thus, the amplitude and phase of the excitation signals for generating and steering two main lobes to 50° and 120° . However, in this case both beams carry the same

information signals. This mode of operation is called multicast with a single information signal. Of course, the concept of multicast can be extended to support the radiation of different information signals at different but also multiple steering angles. This mode of operation is called multicast with multiple information signals. Using the same antenna structure as in the previous example, we further assume that now the beamforming network is fed by two independent information signals targeting different users. Let's assume that the first signal will be steered to 50° and 120° while the second to 90° . Based on this, the beamforming network will carefully configure the excitation signals and it is shown in Figure 2.9 (a), the total normalized AF consists of three main lobes at the targeted steering angles, radiating correctly the first information signal (Beam 1) to 50° and 120° and the second (Beam 2) to 90° . Figure 2.9 (b) and (c) depict the amplitudes and phases of the excitation signals, respectively.

2.6 Beamforming networks based on phase shifters and true time delay elements

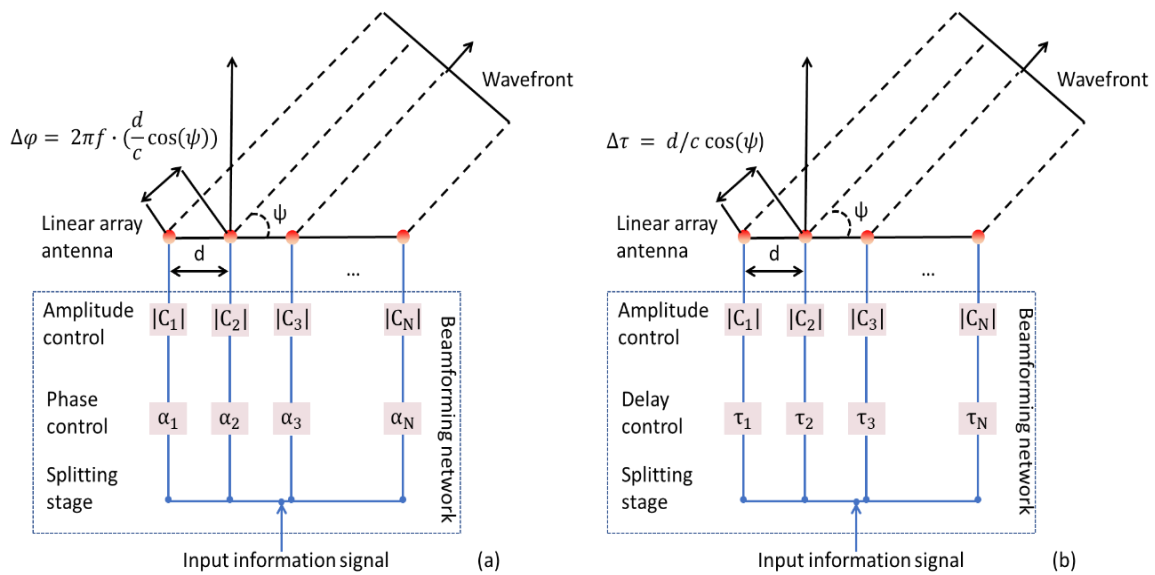


Figure 2.10: Schematic representation of beamforming networks based on (a) phase shifters and (b) true time delay elements.

In the analysis that has followed up to this point, it has been shown that the beamforming networks regardless of the mode of operation (single-beam, multi-beam, and multicast), are responsible for tuning the relative amplitudes and phases of the excitation signals. Within this context, the beamformer networks can be seen as three stage networks, as it is presented in Figure 2.10. The first stage consists of the splitting network that splits equally the input information signal(s) into N paths. The second stage refers to the stage that is responsible for tuning the relative phase of the signals and finally, the third stage refers to amplitude control stage. Regardless of the underlying technology used in the first and third stage, the beamforming networks are categorized based on the technology that deploy for tuning the relative phases of the excitation signals. More specifically, there are two categories depending on the tuning mechanism used in the second stage:

1. **Constant-time delay elements** (true time delay elements). With this technology, the beamforming networks introduce relative time delays in the processed excitation signals equivalent to the desired phase shifts.

2. **Constant-phase shifter:** With this technology, the beamforming networks introduce phase shifts in the processed excitation signals which are constant with respect to central operating frequency.

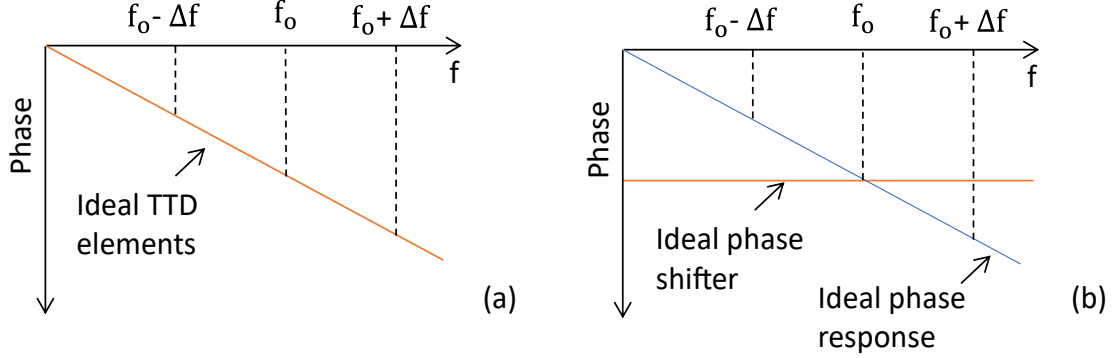


Figure 2.11: Ideal phase response of (a) TTD element and (b) a phase shifter.

TTD elements: In most practical cases, true-time delay elements are implemented as delay lines, which increase the physical length of the propagation path in order for the propagated signal to acquire the required phase shift at a given frequency, f_0 . Assuming a delay line with length equal to L , the time delay is:

$$\tau_n = \frac{L}{v_p} \quad (2.26)$$

, where v_p the phase velocity of the propagating signal which is equal to the speed at which a point of fixed phase propagates, and it is not always the speed that signal travels. The phase velocity of a delay line can be expressed as follows:

$$v_p = \frac{c}{\sqrt{\epsilon_r \cdot \mu_r}} = \frac{1}{\sqrt{\epsilon_r \cdot \epsilon_0 \cdot \mu_r \cdot \mu_0}} \quad (2.27)$$

, where the pair of ϵ_r, μ_r and ϵ_0, μ_0 the permittivity and permeability of the medium, and of the free space, respectively. To our specific interest, optical fibers have a permeability equal to 1 and thus the phase velocity can be rewritten as:

$$v_p = \frac{1}{\sqrt{\epsilon_r \cdot \epsilon_0 \cdot \mu_0}} \quad (2.28)$$

Given a desired scanning angle and reusing Eq. 2.23, the introduced time delay should be equivalent to the desired phase shift.

$$\begin{aligned} -2\pi f \cdot \tau_n &= a_n \\ -2\pi \cdot f \cdot L \cdot \sqrt{\epsilon_r(f_0) \cdot \epsilon_0 \cdot \mu_0} &= -k_0(n-1) \cdot d \cdot \cos(\psi_{\max}) \end{aligned} \quad (2.29)$$

where f_0 the central frequency of the propagating signal. Consequently, by substituting the wavenumber $k_0 = 2\pi \cdot f \cdot \sqrt{\epsilon_0 \cdot \mu_0}$ in Eq. 2.29, the length of a delay line can be expressed as:

$$\begin{aligned} -2\pi \cdot f \cdot L \cdot \sqrt{\epsilon_r(f_0) \cdot \epsilon_0 \cdot \mu_0} &= -2\pi \cdot f \cdot \sqrt{\epsilon_0 \cdot \mu_0} (n-1) \cdot d \cdot \cos(\psi_{\max}) \\ L &= \frac{(n-1) \cdot d \cdot \cos(\psi_{\max})}{\sqrt{\epsilon_r(f_0)}} \end{aligned} \quad (2.30)$$

For a non-dispersive transmission line, ϵ_r is constant with frequency. This means that v_p is also constant with frequency, and thus all the frequency components of a signal propagate at the same phase velocity. Therefore, we can now calculate the induced phase shift.

$$\begin{aligned} a_n &= -2\pi \cdot f \cdot \frac{L}{v_p} = -2\pi \cdot f \cdot \frac{(n-1) \cdot d \cdot \cos(\psi_{\max})}{\sqrt{\epsilon_r(f_0)}} \sqrt{\epsilon_r \cdot \epsilon_0 \cdot \mu_0} \\ &= -2\pi \cdot f \cdot \frac{(n-1) \cdot d \cdot \cos(\psi_{\max})}{c_0} \end{aligned} \quad (2.31)$$

Consequently, the introduced phase shift by a TTD element exhibits a linear relationship with a constant slope with respect to the operating frequency range and thus, the resulted AF does not depend on the operating frequency.

Phase shifters: TTD elements have traditionally been impractical to implement and phase shifter designs are prevalent. In this case, the introduced phase shift is constant with frequency, f_0 .

$$a_n = -k_0(n-1) \cdot d \cdot \cos(\psi_{\max}) = -\frac{2\pi f_0}{c_0}(n-1) \cdot d \cdot \cos(\psi_{\max}) \quad (2.32)$$

By substituting Eq. 2.33 in Eq.2.24

$$\begin{aligned} \text{AF}(\psi) &= \sum_{n=1}^N |c_n| \cdot e^{-i\frac{2\pi f_0}{c_0}(n-1) \cdot d \cdot \cos(\psi_{\max})} \cdot e^{i\frac{2\pi f}{c_0}(n-1) \cdot d \cdot \cos(\psi)} \\ &= \sum_{n=1}^N |c_n| \cdot e^{i\frac{2\pi f}{c_0}(n-1) \cdot d \cdot [\cos(\psi) - \frac{f_0}{f} \cos(\psi_{\max})]} \end{aligned} \quad (2.33)$$

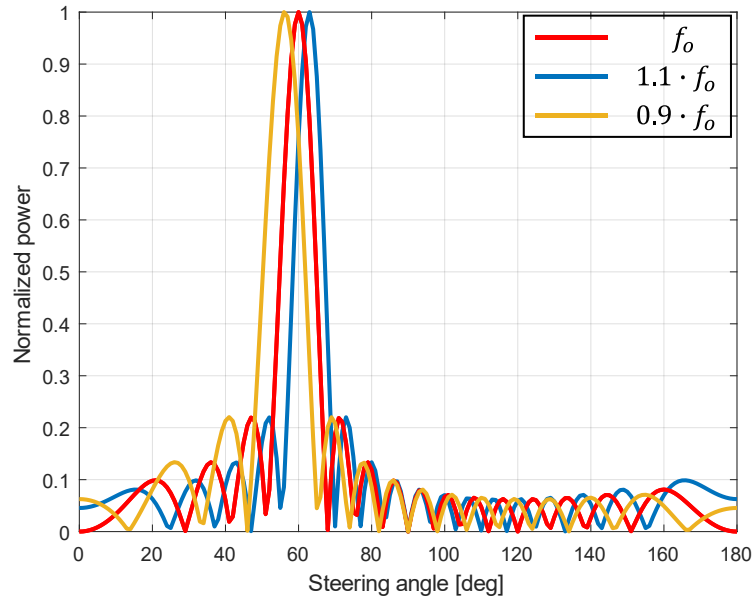


Figure 2.12: Frequency squint effect in a 16-elements linear array. The nominal pointing direction is $\psi = 60^\circ$. A percentage variation of $\pm 0.1\%$ creates already visible change in the pointing direction

From Eq. 2.33, it is evident that the formed beam is steered to a desired direction ψ_{\max} , but unlike in the case of TTD elements steering angle depends also on the frequency. In particular, as the frequency, f , deviates from the central operating frequency, f_0 , the beam will be steered at adjacent angles. This effect is known as beam squint and is present in beamforming networks based on phase shifters. As an example, Figure 2.12 presents the impact of beam squint in the AF of 16-element linear array antenna which is configured to

steer the center frequency f_0 at 60° . As observed, the steering angle deviates subsequently even for $\pm 0.1 \cdot f_0$ frequencies. More details about this effect will be presented in Chapter 6.

2.7 Amplitude tapering

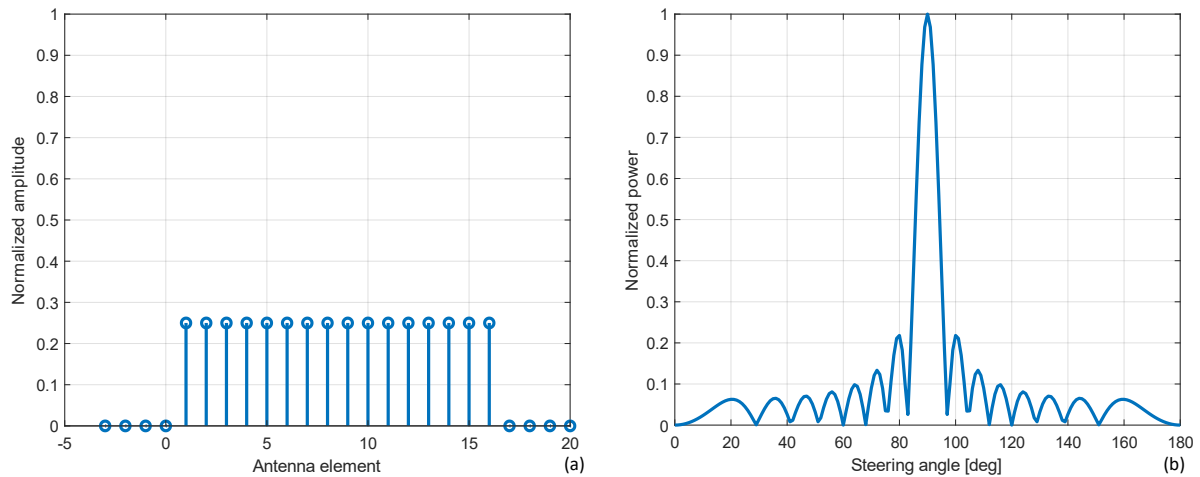


Figure 2.13: (a) The normalized amplitudes of the excitation signals of a 16-element linear array antenna with $d=\lambda/2$ spacing in case of uniform distribution and (b) the resulted normalized AF.

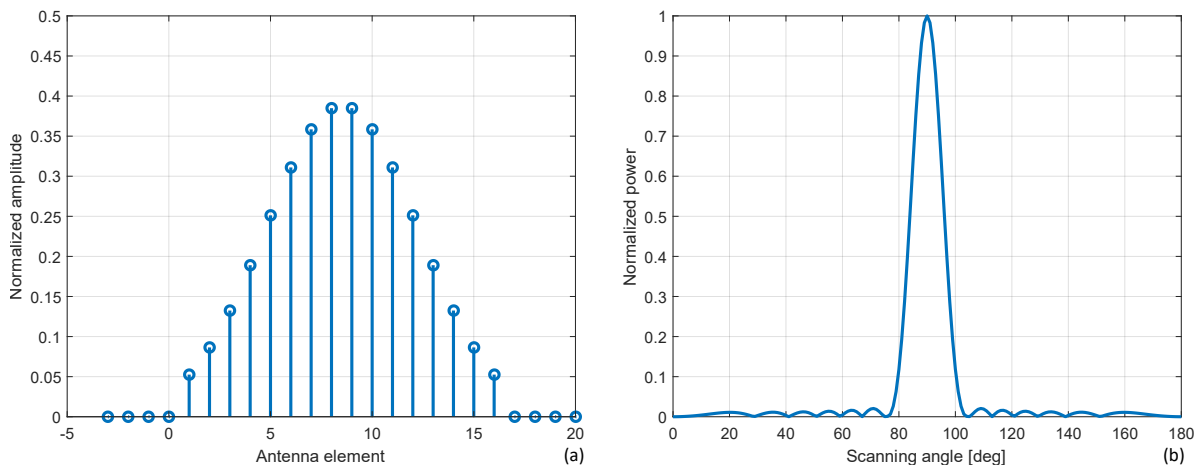


Figure 2.14: The normalized amplitudes of the excitation signals of a 16-element linear array antenna with $d=\lambda/2$ spacing in case of Gaussian distribution with $\gamma=2$ and (b) the resulted normalized AF.

Amplitude tapering, known also as amplitude weighting refers to the manipulation of the amplitude contribution of each excitation signals to the overall antenna response. Thanks to this method, the power of the sidelobes can be suppressed however, at expense of broadening the beamwidth of the main lobe. Intuitively, the amplitude tapering method can be considered and analyzed with the help of the discrete Fourier transformation (DFT) [8]. To do so, we can replace the time domain signals used as an input in a DFT with the amplitude of the excitation signals and the resulted power spectral density with the radiation pattern. More specifically, this technique is better explained with the help of Figure 2.13 and Figure 2.14 in which we evaluate the impact of an uniform and a Gaussian distribution on the AF of a linear array antenna of 16 antenna elements. On the left of these graphs, the amplitude level of the excitation signals is presented while on the right, resulted AF assuming that the phases of the excitation signals are identical (no beam-steering). In case of a uniform distribution, all the excitation signals have equal amplitude which results in a flat amplitude response over the 16 antenna elements or in a rectangular response if we considered more non-radiated elements. The resulted AF is a sinc function and as expected

it is directly analogous of the DFT of a rectangular signal. In Figure 2.14, instead of a uniform distribution, a Gaussian distribution is considered. The amplitude is distributed over the antenna elements following the equation below:

$$c_n = \exp\left[-\frac{1}{2}\left(\gamma \cdot \frac{n}{N/2}\right)^2\right], \quad 0 \leq |n| \leq \frac{N}{2} \quad (2.34)$$

, where $N/2\gamma$ the standard deviation of the Gaussian function. As observed, the sidelobes are suppressed significantly in comparison to the uniform distribution but the beamwidth of the main lobe is now wider. Different amplitude tapering function can be applied to the array antennas depending on the desired radiation pattern. In particular, within the context of the present dissertation, the uniform and Gaussian distribution will be experimentally evaluated.

References of Chapter 2

- [1] Balanis, C. A. (2015). Antenna theory: analysis and design. John Wiley & sons.
- [2] Li, M. Y., Ban, Y. L., Xu, Z. Q., Wu, G., Kang, K., & Yu, Z. F. (2016). Eight-port orthogonally dual-polarized antenna array for 5G smartphone applications. *IEEE Transactions on Antennas and Propagation*, 64(9), 3820-3830.
- [3] Kolawole, M. O. (2017). Satellite communication engineering. CRC Press.
- [4] https://www.tutorialspoint.com/antenna_theory/antenna_theory_radiation_pattern.htm
- [5] Mailloux, R. J. (2017). Phased array antenna handbook. Artech house.
- [6] Hansen, R. C. (2009). Phased array antennas (Vol. 213). John Wiley & Sons.
- [7] Καψάλης, X., & Κωττής, Π. (2008). Κεραίες Ασύρματες Ζεύξεις. Εκδόσεις Τζιόλα.
- [8] Bracewell, R. N., & Bracewell, R. N. (1986). The Fourier transform and its applications (Vol. 31999, pp. 267-272). New York: McGraw-hill.

Chapter 3 - Fundamentals of Microwave Photonics

In its simplest form, as shown in Figure 3.1, a MWP link consists of a laser source, a modulator, and a photodetector, interconnected by an optical fiber. The input microwave signal is transferred from the electrical to the optical domain by modulating the characteristics of an optical carrier and subsequently is transmitted via the optical fiber to the receiver where it is transferred back to the electrical domain.

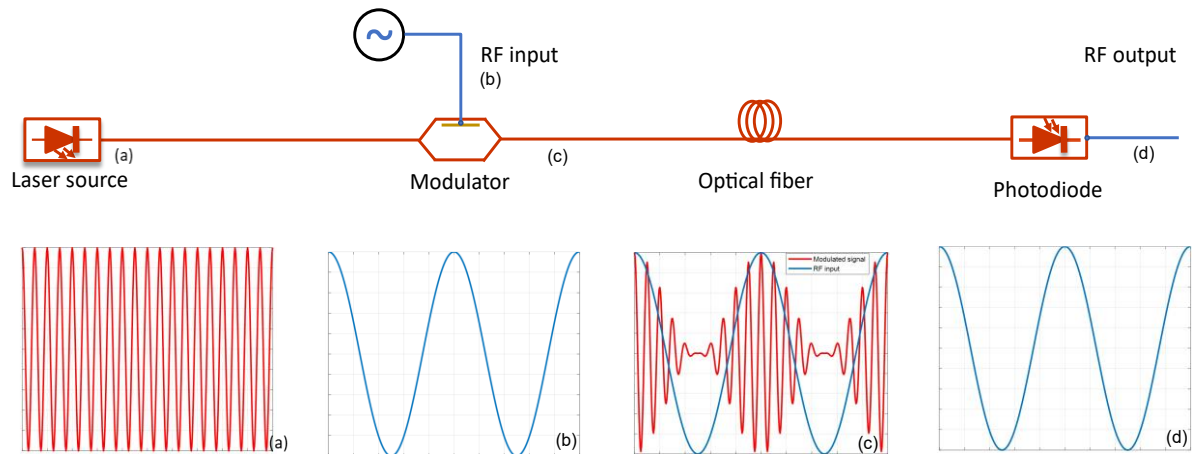


Figure 3.1: Artistic layout of a microwave photonics system for transmitting microwave signals over an optical fiber. The time-domain representation of the optical (a and c) and microwave signals (b and d) are presented as insets.

Therefore, as shown in Figure 3.2, a MWP system can be considered as a black box with input and output ports operating in the microwave domain while all the supported functionalities, such as complex tunable filters [[4]-[6], multi-tap equalizers [7]-[8], true time delay [9]-[11], and phase shifting [12] are implemented in the optical domain.

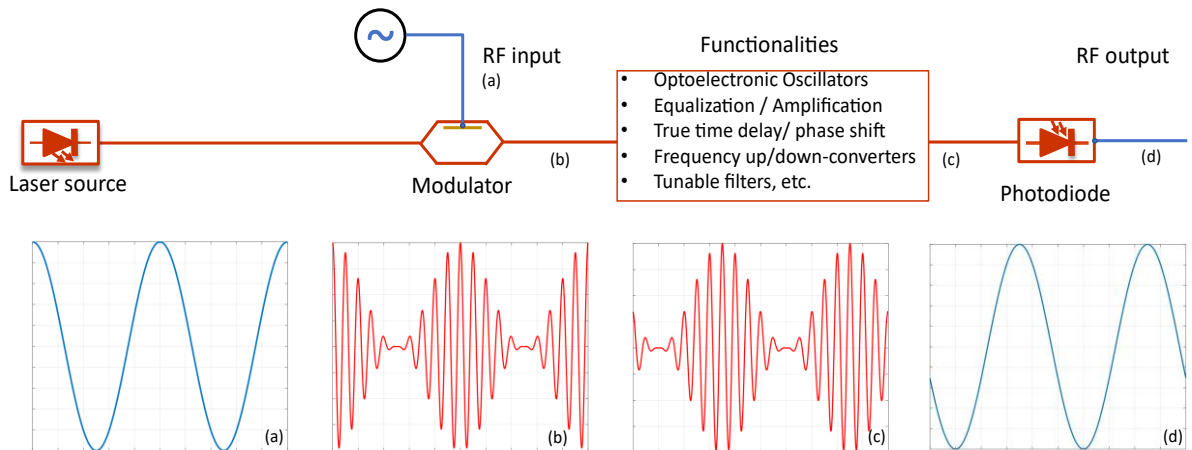


Figure 3.2: Artistic layout of an indicative microwave photonics system for delaying a microwave signal by 0.3 of its period. Insets (a)-(d) depict the time-domain representation of the input (a) and output (d) microwave signal as well as the modulated signal optical signal before (b) and (c) the insertion of the time delay.

A thorough understanding of MWP links and systems cannot be obtained without first understanding the characteristics and performance of the underlying technology. Consequently, the following paragraphs focus on the key optical components and techniques that dictate the performance of the MWP links and systems.

3.1 Light generation

The light generation in the optical communication networks is feasible thanks to the lasers. According to the scientific terminology, laser is the abbreviation of the “*Light Amplification by Stimulated Emission of Radiation*”. A laser is a unique light source. It is quite different from a light bulb or a flashlight as it produces highly directional light. It emits light through a process called stimulated emission of radiation which increases the intensity of light. Even though that light sources with such unique characteristics are not encountered in nature, we have figured ways to artificially create. Lasers produce a narrow beam of light in which all of the light waves have very similar wavelengths or in other words similar frequency. This is the reason why the emitted beams are very narrow, very bright, and can be focused into a very tiny spot.

Triggered by these features, lasers have been in the research spotlight for decades and as a result, today, there are a plethora of different lasers which can be classified into four types based on the type of the laser medium. These are the solid-state [13], [14], gas [15], [16], liquid [17], [18], and semiconductor lasers [19]-[26]. Among these types, semiconductor lasers play an important role in our everyday life but also in the optical communication networks. These lasers are very cheap, have compact size and consume low power. Most semiconductor lasers are pumped with an electrical current in a region where an n-doped and a p-doped semiconductor material meet. Common materials for semiconductor lasers all having a direct band gap, are Gallium Arsenide (GaAs), Indium Phosphide (InP), InGaAs (Indium Gallium Arsenide). As the photon energy of a laser diode is close to the bandgap energy compositions with different bandgap energies allow for different emission wavelengths across the O-band (1260 nm - 1360 nm), E-band (1360 nm - 1460 nm), S-band (1460 nm - 1530 nm), C-band (1530 nm - 1565 nm) and the L-band (1565 nm - 1625 nm). However, even though that semiconductor lasers are widely used, there are several types such as distributed-feedback (DFBs) lasers [19], [20], distributed Bragg reflector (DBR) lasers [21], [22], vertical-cavity surface-emitting lasers (VCSELs) [23], [24], and external cavity lasers (ECLs) [25], [26]. ECLs can exhibit narrow linewidth due to their long cavity length [25] are suitable for higher order modulation in coherent optical systems. Due to the complexity and footprint of the ECL's, DFB and DFB and DBR laser arrays are today widely used and are the preferred tunable laser options for commercial coherent transceivers and MWP systems. However, the linewidth of these devices is typically several hundred kHz [27] which limits their use with higher order modulation formats. A new structure of micro ring resonator external cavity laser (MRR-ECL) has recently been developed based on the silicon nitride waveguide platform and will be presented in Chapter 5 [28], [29].

Regardless the type and the material of the active region which are employed in a MWP link/system, the optical carrier should have high power, low intensity noise, and low linewidth. All of these parameters play an important role in the design and the performance of a MWP link/system as they can strongly influence the overall RF performance of the entire link/system.

In this thesis, the optical carrier field is considered to be a continuous wave (CW) and is written as the time-varying complex valued quantity given by the following equation:

$$E_o(t) = \sqrt{2P_o} \cdot e^{-j(\omega_o t + \varphi_o)} \quad (3.1)$$

, where ω_o and φ_o are the angular frequency and phase of the optical carrier, respectively, while P_o is the average optical power expressed as follows:

$$P_o = (E_o(t) \cdot E_o^*(t))/2 \quad (3.2)$$

In practice, laser phase ($\varphi_n(t)$) and intensity noise ($P_n(t)$) due to the spontaneous emission photons have to be taken also into account. More specifically, the phase noise is caused by generated photons that are not in phase with the stimulated emission photons but instead, they exhibit a random phase. In the time domain, the evolution of the phase noise can be understood as a random walk with variance given by the following equation:

$$\langle \Delta\varphi_n^2(\tau) \rangle = 2\pi\Delta\nu \tau \quad (3.3)$$

, where $\langle \cdot \rangle$ the time averaging function, $\Delta\nu$ the laser linewidth and τ the observed time interval. From equation (3.3), it can be easily understood the impact of the laser linewidth on the system performance, especially when the information signal is encoded into the phase of the optical carrier [30]. Intensity noise can also deteriorate the system performance and should be taken into account in the designing phase of a MWP link [30]. Intensity noise is also known as relative intensity noise (RIN), and it is a key figure of merit of every laser source because it quantifies how stable the laser output is as a function of time. RIN can be expressed as follows:

$$\text{RIN} = \frac{\langle \delta P_o^2(t) \rangle}{\langle P_o(t) \rangle^2} \quad (3.4)$$

, where $\langle \delta P_o^2(t) \rangle$ the optical intensity fluctuation and $\langle P_o(t) \rangle^2$ the average optical power. As it can be observed, RIN can be reduced as the average optical power is increased that is the reason why the laser sources should be configured for high output optical power.

3.2 Optical modulation

In order to exploit the advantages of the optoelectronic technology, the microwave signal should be frequency up-converted from the lower portion of the microwave frequency band (300 MHz – 300 GHz) [31] to the “optical” domain which most commonly correspond to frequencies of the O- and C-bands. This enormous frequency up-conversion is enabled by the proper modulation of a light beam by a microwave signal which carries the useful information. There are different modulation techniques based on how this information signal is encoded into the optical carrier. For example, using Eq. 3.1, it can be easily seen that the information signal can be encoded in the amplitude, frequency, or phase of the optical carrier. To do that, one can use only a single laser source (direct modulation) or combine a laser source with an external optical modulator (external modulation). In direct modulation, the information signal is applied as the injection current of the laser source and thus, the intensity of the output optical carrier is dictated by the information signal, as it is illustrated in Figure 3.1 (a) [32]. Direct modulation is an attractive approach thanks to its low complexity and low cost, but there is a major disadvantage. MWP links and systems employing a direct modulation scheme, suffer from a strong frequency chirp, meaning that the instantaneous frequency is time-dependent. Having a chirped-carrier is undesired as it would have a spectral broadening with respect to a chirp-free optical carrier, which may negatively influence the RF performances of the MWP system, especially when optical filters are used.

Instead of modulating lasers by changing the injection current, in external modulation scheme, the laser source emits a CW optical signal which has constant power, frequency and phase. As shown in Figure 3.3 (b), the CW signal is modulated by an external to the laser source, optical modulator. There are two main techniques of modulating the CW output of a laser: the electro-optic modulation (EOM) and the electro-absorption modulation (EAM) [33], [34]. The EO-based modulators utilize the Pockels Effect, which is the change in refractive index of a material due to the application of an electric field [33], [34]. When a voltage is applied across an EO material, the generated electric field changes the refractive

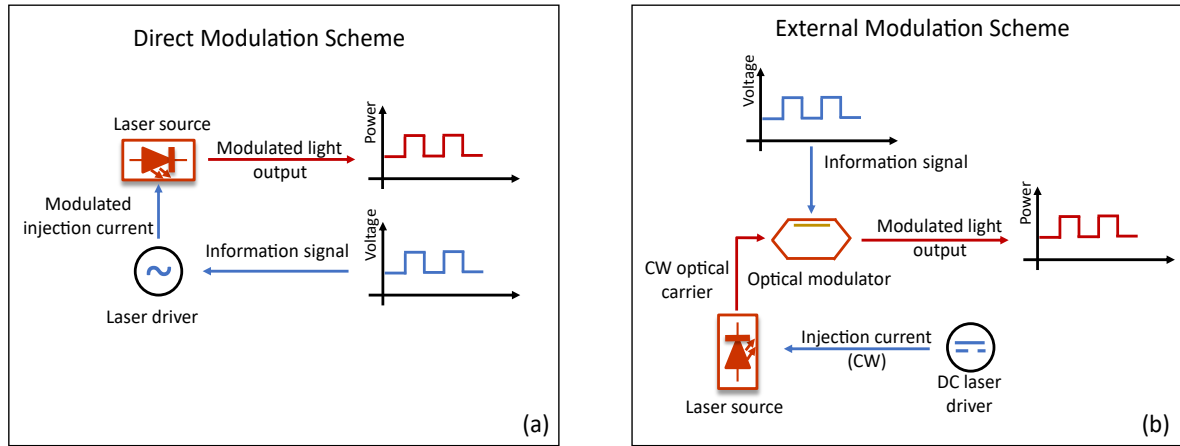


Figure 3.3: High-level representation of (a) direct and (b) external modulation schemes.

index of the material. Therefore, as light passes through this material, the phase of the light will be modified with respect to the voltage applied to the modulator. When such a phase modulator is combined with a Mach-Zehnder interferometer or modulator, the intensity or amplitude of the laser output can be modulated. When the beam is split in the interferometer, a Pockels Cell (in one arm) changes the phase of that specific arm and portion of light. When the two arms combine outputs, they will either constructively or destructively interfere, changing the final intensity of the light.

The EA-based modulators are based on the Franz-Keldysh, and quantum confined Stark effect (QCSE), which is the change in light absorption of a waveguide due to the application of an electric field [33], [34]. In this type of modulators, the semiconductor is transparent to light without the electric field present but in the presence of an electric field the bandgap energy decreases. The material will absorb the light once the photon energy exceeds the bandgap energy, attenuating the light transmission. When the voltage is modulated, the absorption of the material and the output light intensity can be modulated. Apart from intensity modulators, phase modulators can be implemented based on QCSE since as it is explained by the Kramer-Kronig relations [35], QCSE leads to a change of the refractive index at a given wavelengths. In the next sections, we will focus on intensity EO- and EA-based modulators as well as on EA-QCSE-based phase modulators since those are the three types of modulators used in Chapter 4 and Chapter 5, respectively.

Phase modulation: Figure 3.4 (a) presents the layout of an optical phase modulator. It consists of a single optical waveguide and a pair of electrodes. When the information signal is applied across these electrodes, the phase of the propagating optical signal is modified accordingly. The mathematical equations that dictate the operation of a phase modulators can be simplified in the case of assuming operation with a single tone. In this case, the information signal is monochromatic and can be expressed as follows:

$$V_m(t) = \hat{V}_m \cdot \sin(\omega_{RF}t) \quad (3.5)$$

, where \hat{V}_m the peak amplitude of the signal and ω_{RF} its angular frequency. Therefore, the modulated phase can be expressed as:

$$\phi_m(t) = \frac{\pi V_m(t)}{V_\pi} = \frac{\pi \hat{V}_m}{V_\pi} \cdot \sin(\omega_{RF}t) \quad (3.6)$$

, where V_π the frequency dependent voltage required to produce a π phase shift, known as halfwave voltage.

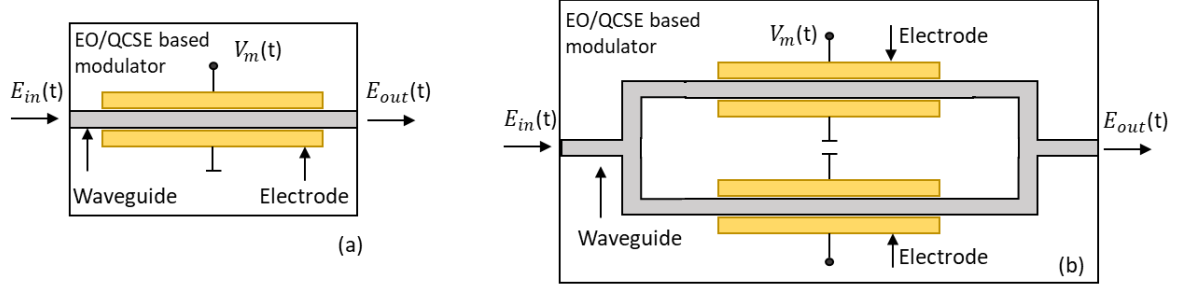


Figure 3.4: Schematic representation of a (a) optical phase modulator and (b) Mach-Zehnder modulator (MZM).

Assuming that the input optical field is given by the equation (3.1), the optical field at the output of the phase modulator is then obtained as:

$$E_{out}(t) = \frac{\sqrt{2P_o}}{\sqrt{I_{PM}}} \cdot e^{-j(\omega_o t + \frac{\pi \hat{V}_m}{V_\pi} \sin(\omega_{RF} t) + \phi_o)} \quad (3.7)$$

, where I_{PM} the power insertion loss of the phase modulator. As we will discuss in the next paragraphs, both I_{PM} and V_π are very important parameters which influence the overall RF performance of the MWP links. Eq. 3.7 can be further analysed by using the Jacobi-Anger expansion [36] and expressed as follows:

$$E_{out,PM}(t) = \frac{\sqrt{2P_o}}{\sqrt{I_{PM}}} \cdot \sum_{n=-\infty}^{\infty} J_n\left(\frac{\pi \hat{V}_m}{V_\pi}\right) e^{-j(\omega_o t + n\omega_{RF} t + \phi_o)} \quad (3.8)$$

, where J_n denotes the n -th Bessel function of the first kind. From Eq. 3.8, is derived that the output field of a phase modulation has infinite number of side-frequencies whose amplitudes are dictated by the Bessel functions.

Intensity modulation based on EO-MZM: By utilizing the principle of interference, phase modulation can also be used to cause an intensity modulation when an interferometric structure is employed, as it is shown in Figure 3.4 (b). When only one of its arms hosts a phase modulator, the MZM is denoted as single-drive and while both arms host two independent phase modulators, the MZM is denoted as dual-drive. In the case of dual-drive MZMs, the input optical signal is split into two paths, both equipped with phase modulators. After acquiring some phase differences relative to each other, the two optical fields are recombined. The interference varies from constructive to destructive, depending on the relative phase shift. Unlike phase modulators, the signals applied to both arms should also have a DC component. that, the two applied signals can be expressed as:

$$v_1(t) = \hat{v}_{dc,1} + \hat{v}_{m,1} \cdot \sin(\omega_{RF} t) \quad (3.9)$$

and

$$v_2(t) = \hat{v}_{dc,2} + \hat{v}_{m,2} \cdot \sin(\omega_{RF} t) \quad (3.10)$$

For push-pull operation, the information signal $v_m(t)$, is split equally into the two electrodes while of the two electrodes also alters its phase by π .

$$v_{dc}(t) = \hat{v}_{dc,1}/2 + \hat{v}_{dc,2}/2 \quad (3.11)$$

$$\hat{v}_m(t) = \hat{v}_{m,1}/2 + \hat{v}_{m,2}/2 \quad (3.12)$$

$$v_1(t) = \frac{\hat{v}_{dc}}{2} + \hat{v}_m \cdot \frac{\sin(\omega_{RF} t)}{2} = -v_2(t) \quad (3.13)$$

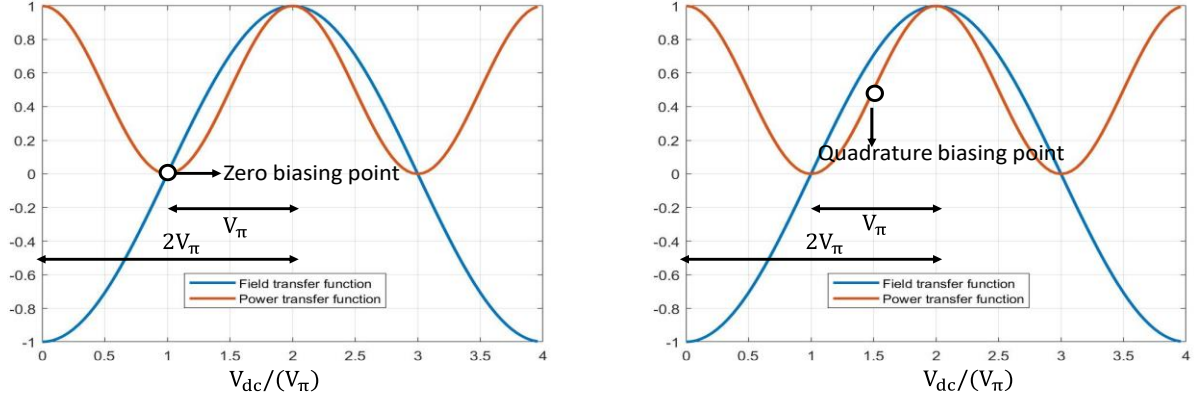


Figure 3.5: Operating the MZM at the (a) zero-transmission point and (b) quadrature point.

Assuming again that the input optical signal is given by equation (3.1), the optical field at the output of dual-drive MZM is :

$$\begin{aligned}
 E_{\text{out,MZM}}(t) &= \frac{\sqrt{2P_o}}{\sqrt{I_{\text{MZM}}}} \cdot (e^{-j\varphi_1(t)} + e^{-j\varphi_2(t)}) \cdot e^{-j(\omega_o t + \varphi_o)} \\
 &= \frac{\sqrt{2P_o}}{\sqrt{I_{\text{MZM}}}} \left(e^{-j\left(\frac{\hat{V}_{dc}\pi}{2V_{\pi,dc}} + \frac{\hat{V}_m\pi}{2V_{\pi,rf}} \sin(\omega_{RF}t)\right)} + e^{j\left(\frac{\hat{V}_{dc}\pi}{2V_{\pi,dc}} + \frac{\hat{V}_m\pi}{2V_{\pi,rf}} \sin(\omega_{RF}t)\right)} \right) \cdot e^{-j(\omega_o t + \varphi_o)}
 \end{aligned} \tag{3.14}$$

, where I_{MZM} the insertion loss and $\varphi_1(t)$ and $\varphi_2(t)$ the induced phase shift at the two arms. In MWP systems, the MZM is biased either at the quadrature operating (QP) point, i.e., $\hat{v}_{dc} = V_{\pi,dc}/2$, or at the zero-transmission point (ZP), i.e., $\hat{v}_{dc} = V_{\pi,dc}$. The output field at these two biasing points are given by the following equations:

$$\text{(QP)} \quad E_{\text{out,MZM}}(t) = \frac{\sqrt{2P_o}}{\sqrt{I_{\text{MZM}}}} \left(e^{-j\left(\frac{\pi}{4} + \frac{\hat{V}_m\pi}{2V_{\pi,rf}} \sin(\omega_{RF}t)\right)} + e^{j\left(\frac{\pi}{4} + \frac{\hat{V}_m\pi}{2V_{\pi,rf}} \sin(\omega_{RF}t)\right)} \right) \cdot e^{-j(\omega_o t + \varphi_o)} \tag{3.15}$$

$$\text{(ZP)} \quad E_{\text{out,MZM}}(t) = \frac{\sqrt{2P_o}}{\sqrt{I_{\text{MZM}}}} \left(e^{-j\left(\frac{\pi}{2} + \frac{\hat{V}_m\pi}{2V_{\pi,rf}} \sin(\omega_{RF}t)\right)} + e^{j\left(\frac{\pi}{2} + \frac{\hat{V}_m\pi}{2V_{\pi,rf}} \sin(\omega_{RF}t)\right)} \right) \cdot e^{-j(\omega_o t + \varphi_o)} \tag{3.16}$$

Figure 3.5 (a) and (b) present the field and power transfer function for operation in the zero and quadrature transmission points, respectively. For zero-biasing, the power transfer is minimized while for quadrature-biasing it is reduced to half of its maximum value. For example, let's assume that the MZM is driven by a sine wave with frequency f_{rf} and amplitude $\hat{v}_m \ll v_{\pi, \text{MZM}}$. For zero-biasing, at the output of the MZM, the power of the

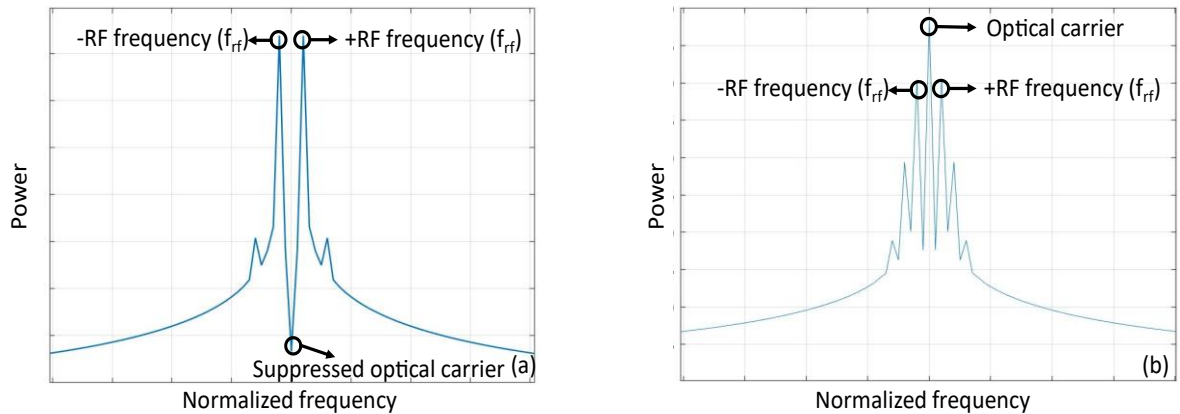


Figure 3.6: Optical spectra of an MZM operating in the (a) zero and (b) quadrature transmission point.

optical carrier is minimized and there are only two sidebands with frequencies ($f_0 \pm f_{rf}$) (see Figure 3.5 (a)), while for quadrature biasing, the optical carrier is reduced to half of its maximum value (see Figure 3.5 (b)). Finally, we should mention that for both biasing points, the amplitude of the information signal should be always smaller compared to $V_{\pi,MZM}$ ($\hat{v}_m \ll V_{\pi,MZM}$), to ensure that the modulating electric field and the optical output intensity are approximately linearly related to each other.

Intensity modulation based on EA-modulator: Unlike EO-MZM, the transfer function of an EA-based modulator cannot be described by a generic equation since the inherent characteristics of the modulator depend strongly on the type of the active material and its structure. Moreover, since the electro-absorption effect correlates the frequency of the photons with bandgap of the material, the transfer function (T) of the EAMs is wavelength dependent. Figure 3.7 presents the normalized power transfer function of a commercially available EAM (CIP-40G-PS-EAM-1550) [37]. As it can be observed, the EAM is always reverse biased and its transfer function is shifted to left as the operating wavelength is increased. For the purposes of comparison with MZMs, an equivalent voltage $V_{\pi,EAM} = \frac{\pi}{2} \left[\frac{(\partial T)}{(\partial V_m)} \right]^{-1}$, can be defined to express the slope efficiency of the EAMs [37].

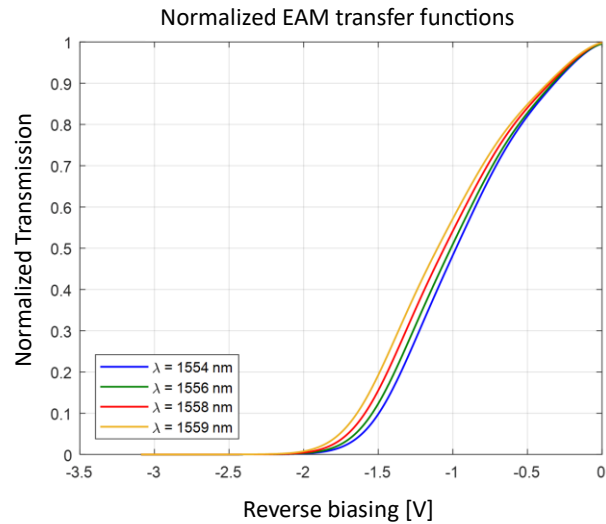


Figure 3.7: Normalized transfer curves for a commercial EAM for different operating wavelengths.

3.3 Photodetection

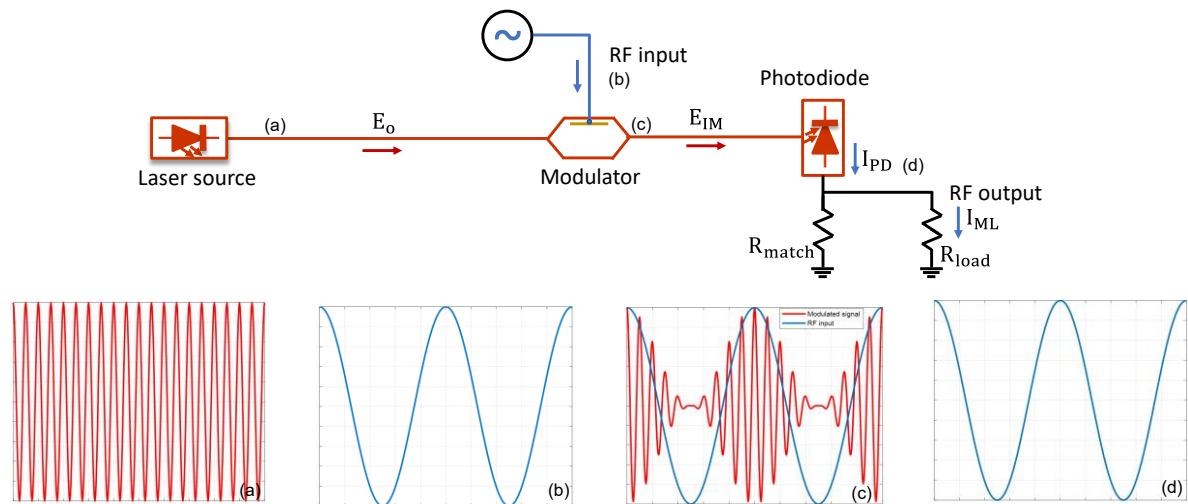


Figure 3.8: Schematic for intensity modulated optical carrier and direct detection (IM-DD), consisting of a lasers source, a modulator driven by cosine wave, and a photodiode. At each stage, the spectrum of the signal is presented.

Photodetection can be seen as the opposite process of the modulation as it frequency down-converts a signal from the optical to the microwave frequencies [30]. The photodiodes (PDs) are square-law detectors that respond to the power, rather than the field amplitude, of an optical signal. The electrical signal generated by an optical signal is a photocurrent that is proportional to the power of the optical signal. The most important parameters which

describe the quality of a photodiode is the responsivity, \mathfrak{R}_{PD} [A/W], the linearity, and the 3-dB electrical bandwidth. We can describe the operation of a photodiode taking as an example the MWP link presented at Figure 3.8: Schematic for intensity modulated optical carrier and direct detection (IM-DD), consisting of a lasers source, a modulator driven by cosine wave, and a photodiode. At each stage, the spectrum of the signal is presented.. More specifically, a laser diode emits a CW optical carrier ($E_o(t)$) whose amplitude is modulated by an intensity modulator, driven by single-tone cosine wave. The output optical field $E_{IM}(t)$ illuminates the photodiode for direct detection. The generated photocurrent can be expressed as follows:

$$I_{PD}(t) = \mathfrak{R} \cdot \{E_{IM}(t) \cdot E_{IM}^*(t)\} = \mathfrak{R} \cdot P_o \quad (3.17)$$

At the photodetector an impedance matching circuitry is used to maximize the power transfer from the photodiode to the load. If the two resistances, R_{match} and R_{load} , are equal, the photocurrent is equally split in the two branches and the current on the load is half of the total photocurrent, which means that such matching circuitry is lossy since half of the current is drawn by the matched resistor.

$$I_{ML}(t) = \frac{I_{PD}(t)}{2} = \frac{\mathfrak{R} \cdot P_o}{2} \quad (3.18)$$

From the equation above, it can be derived that a DD scheme is sensitive only to the power fluctuations and a results any information that can be encoded in the phase of the optical carrier is loss. Therefore, MWP links and systems which carry information in the phase domain should employ additional methods to enable the translation of the optical phase back to the microwave. These methods will be described in Chapter 6.

3.4 Key performance metrics of MWP links

As in any analog system, MWP systems are relatively susceptible to various signal impairments, such as signal loss, noise, and nonlinearities. These impairments characterize not only the performance of a MWP system but of any two-port radio-frequency (RF) component such as a RF amplifier, since a MWP system can be considered as a black box with RF inputs and RF outputs. The following paragraphs describe the link gain, noise figure and spurious-free dynamic range of MWP systems.

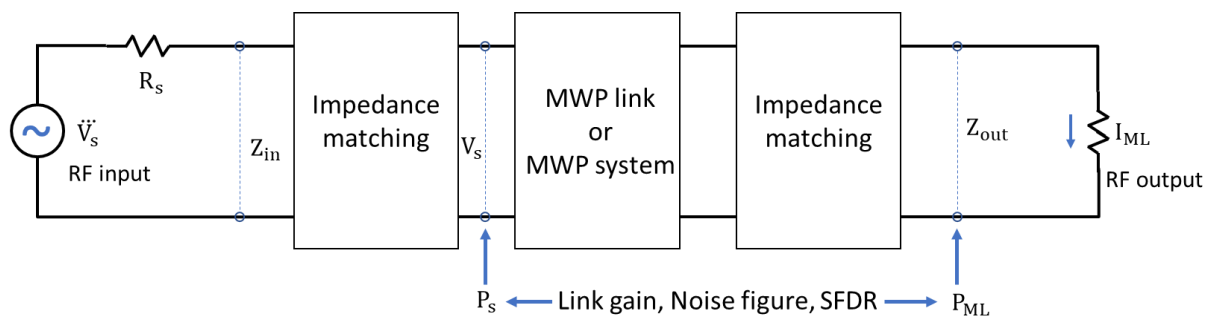


Figure 3.9: MWP link modelled as a 2-port microwave system, connected to source and a load.

Link gain: A fundamental figure of metric that describes how the power of RF signal is handled by a MWP link or MWP system is the link gain. More specifically, the link gain is defined as the ratio between the RF power delivered to the matched load, P_{ML} , and the available power at the source. Taking as a reference the schematic presented in Figure 3.9 and assuming that our MWP link/system input and output impedances are matched to the resistances of the source and load, respectively, and also that the signal source is calibrated

to deliver a nominal power at a matched load, the link gain, g , is given by the following equation:

$$g = \frac{P_{ML}}{P_s} \quad (3.19)$$

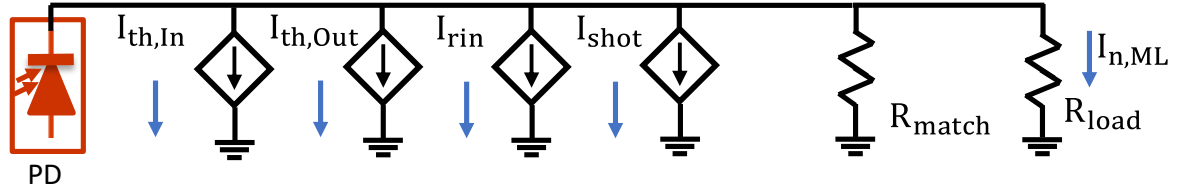


Figure 3.10: Circuit representation of noise source as current sources.

Noise sources and noise figure: In a MWP link, there are three main types of noise sources, that define the SNR. The input and output thermal noise [39], the RIN [39], and the shot noise [39]. When the MWP link includes an optical amplifier, we should also consider the noise contribution due to the amplitude spontaneous emission. A circuit representation of noise sources as current sources is shown in Figure 3.10. The noise currents are assumed to be wide-sense stationary, ergodic and statistically independent of each other and as a result, the total noise power can be calculated as the sum of noise powers generated by the individual sources. Moreover, due to the stationarity and ergodicity, the statistical properties can be calculated from the temporal average. Considering the lossy impedance matching condition ($R_{match} = R_{load}$), the total noise current through the load can be written as:

$$I_{n,ML}(t) = \frac{1}{2} [I_{th,In}(t) + I_{th,Out}(t) + I_{rin}(t) + I_{shot}(t)] \quad (3.20)$$

, where $I_{th,In}$ represents the thermal noise generated at the resistance of the optical modulator, $I_{th,Out}$ represents the thermal noise generated at the resistance of the photodiode, I_{rin} represents the noise due to RIN of the laser source, and I_{shot} represents the shot noise generated at the photodiode. For the calculation of the noise power, which is delivered at the matched load, we need to further define the time variance of each noise contributor as follows:

$$\langle I_{th}^2 \rangle = \frac{4k_B T B_n}{R} \quad (3.21)$$

$$\langle I_{rin}^2 \rangle = RIN \cdot I_{av}^2 B_n \quad (3.22)$$

$$\langle I_{shot}^2 \rangle = 2qI_{av} B_n \quad (3.23)$$

, where k_B is the Boltzmann constant and is equal to $1.38 \cdot 10^{-23} \text{J/K}$, T is the absolute temperature, B_n is the baseband bandwidth of the noise, q is the electron charge and is equal to $1.6 \cdot 10^{-19} \text{C}$, and I_{av} the average photocurrent. Note that the variance of the thermal noise generated at the modulator and the one generated at the photodetector have the same expression, where we assumed that the internal resistance of the modulator and the photodetector are both equal to R . The difference is that the current at the modulator is generated at the input of the link, thus experiences the MWP link gain, g , before being evaluated at the link output, while the noise current at the detector is generated directly at the link output. Since the link gain is generally negative (in dB scale), the thermal noise at the PD generally gives a much higher contribution to the total noise.

$$N_{PD} = (1 + g) \cdot N_{th} + N_{rin} + N_{shot} \quad (3.24)$$

, where P_{th} , P_{rin} , and P_{shot} the power of the noises generated at the photodiode. Taking into account that the current delivered to the load is half of the current generated by the photocurrent, the noise power at the output of a MWP link can be expressed as:

$$N_{ML} = (1 + g) \cdot k_B T B_n + \frac{1}{4} RIN \cdot I_{av}^2 B_n + \frac{1}{2} q I_{av} B_n \quad (3.25)$$

The impact of the noise in the system performance is usually expressed by the noise factor (F) or equivalently by its logarithm, the NF. Noise factor describes the reduction of the output SNR when compared to the input SNR and is expressed as follows:

$$F = \frac{SNR_{in}}{SNR_{out}} = \frac{(P_s) / (N_{in} B_n)}{(P_{ML}) / (N_{ML} B_n)} \quad (3.26)$$

, where $N_{in} = N_{th}$ the input thermal noise. By inserting equations (3.19) and (3.25) into (3.26), the noise factor can be calculated as:

$$F = \frac{(P_s) / (k_B T B_n)}{(g P_s) / (N_{ML} B_n)} = \frac{N_{ML}}{g k_B T} \quad (3.27)$$

From equation (3.27), the NF can be expressed as:

$$NF = N_{ML} \left[\frac{dBm}{Hz} \right] - G [dB] + 174 \left[\frac{dBm}{Hz} \right] \quad (3.28)$$

Non-linearities: Up to this point in our analysis, we have considered that both the modulator and the photodetector are working in the linear region of their transfer functions and therefore a small-signal analysis can be carried out. Nevertheless, both these optoelectronics elements are inherent non-linear [39]. Therefore, it is utmost important to investigate the impact of the non-linearities in MWP system. There are two main methods for evaluating the performance of a MWP system with respect to its non-linear behavior. The first method refers to the single-tone test with which we can calculate the harmonic distortion (HD) and the gain compression of the system [39]. The presence of the harmonic tones can deteriorate the system performance since firstly, it can lead to significant interference, both in the optical domain, especially in WDM systems, but also, in the RF domain after the photodetection, and secondly, the input RF power is divided over multiple frequency tones, apart from the fundamental. Nevertheless, HD can be neglected in narrow-band systems with sub-octave bandwidth (where the highest frequency is less than twice the lowest frequency [39]) since in this case, the harmonics fall relatively far from the fundamental frequency, and thus often out of the operational bandwidth. Within the framework of this thesis, narrow-band systems had been considered and as a result, the HD was neglected.

In the small-signal regime, the gain is independent of the input signal power; i.e. by increasing the power of the input signal we are obtaining the same gain. However, as we continue to increase the modulation power, we eventually notice that the gain begins to decrease. This reduction in gain from the small-signal value is called gain compression. Under large-signal operation, apart from the undesired non-linear behavior of the MWP systems, we should ensure that the power of the input RF signal would not damage the optical modulator. For these reasons, similarly, to the HD, the gain suppression was

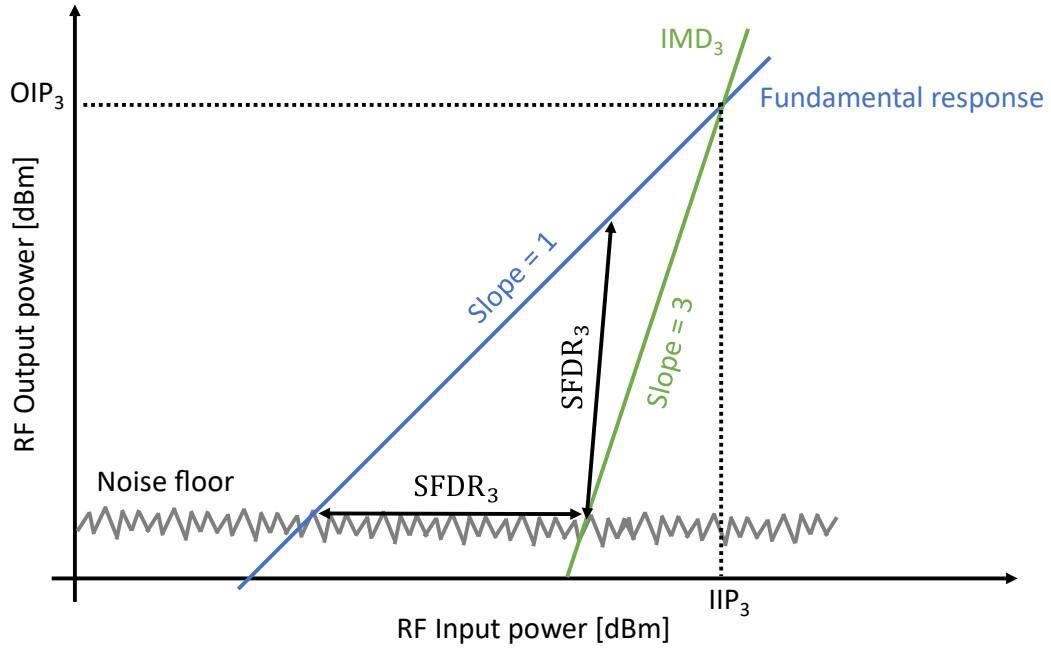


Figure 3.11: Representation of the third-order spurious-free dynamic range in a log-log scale.

neglected during the work of this thesis since in all the experiments, the MPW systems were operated in the small-signal regime. The second method refers to the two-tone test with which we can calculate the intermodulation distortion (IMD) and the SFDR. In this method, a signal composed of two pure sine waves with equal amplitudes and frequencies falling within the bandwidth of interest (f_1 and f_2) is coupled to the optical modulators. Due to the non-linear transfer function of the MWP link, at the output of the photodiode is not just the harmonics of each sine wave, but also frequency components at the sums and differences of the harmonics and the fundamental frequencies. Two of the most important products are the third-order distortion components that occurs at $2 \cdot f_1 - f_2$ and $2 \cdot f_2 - f_1$ frequencies. These distortion products are usually so close to the carrier that it is almost impossible to filter out and can cause interference in multichannel communications equipment. In most of the cases the linearity of a MWP link is expressed by the spurious-free dynamic range, $SFDR_n$, which is defined as the range of input powers over which the output signal is above the output noise floor and all the spurious signals are less than the output noise floor. As explained above, in most of the cases, we focus on the third-order distortion and so usually the linearity of the MWP links is expressed by the third-order SFDR ($SFDR_3$). A graphical representation is given in Figure 3.11 where the response of the fundamental response of the MWP link is plotted with slope of 1 (blue line) and the power of the third-order IMD (IMD_3) with slope of 3 (green line). This graph is of great importance since it indicates which is the RF input (IIP_3) and output (OIP_3) power for which the fundamental response and IMD_3 are equal in power. Usually, the $SFDR_3$ is defined in terms of OIP_3 or IIP_3 as follows:

$$SFDR_3[\text{dB} \cdot \text{Hz}^{2/3}] = 2/3 \cdot [OIP_3 [\text{dBm}] - N_{ML} [\text{dBm}/\text{Hz}] - 10\log_{10}(B_n)] G [\text{dB}] + 174 [\text{dBm}/\text{Hz}] \quad (3.29)$$

$$SFDR_3[\text{dB} \cdot \text{Hz}^{2/3}] = 2/3 \cdot [IIP_3 [\text{dBm}] + G [\text{dB}] - N_{ML} [\text{dBm}/\text{Hz}] - 10\log_{10}(B_n)] \quad (3.30)$$

References of Chapter 3

- [1] Seeds, "Microwave photonics," *IEEE Trans. Microw. Theory Tech.* 50(3), 877–887 (2002).
- [2] J. Capmany and D. Novak, "Microwave photonics combines two worlds," *Nat. Photonics* 1(6), 319–330 (2007).
- [3] J. Yao, "Microwave Photonics," *J. Lightwave Technol.* 27(3), 314–335 (2009).
- [4] Kumar, R. R., Wu, X., & Tsang, H. K. (2020). Compact high-extinction tunable CROW filters for integrated quantum photonic circuits. *Optics Letters*, 45(6), 1289-1292.
- [5] Brunetti, G., Sasanelli, N., Armenise, M. N., & Ciminelli, C. (2021). High performance and tunable optical pump-rejection filter for quantum photonic systems. *Optics & Laser Technology*, 139, 106978.
- [6] Marpaung, D., Morrison, B., Pant, R., Roeloffzen, C., Leinse, A., Hoekman, M., and Eggleton, B. J. (2013). Si₃N₄ ring resonator-based microwave photonic notch filter with an ultrahigh peak rejection. *Optics express*, 21(20), 23286-23294.
- [7] Sidhique, A., Chugh, S., Singh, A., & Gupta, S. (2021, July). Demonstration of an Integrated Optical Equalizer for Direct Detection Links. In *Signal Processing in Photonic Communications* (pp. SpTu4D-4). Optical Society of America.
- [8] Kouloumentas, C., Tsokos, C., Groumas, P., Gounaridis, L., Raptakis, A., Mylonas, E., & Avramopoulos, H. (2020). Multi-rate and multi-channel optical equalizer based on photonic integration. *IEEE Photonics Technology Letters*, 32(23), 1465-1468.
- [9] Chin, S., Thévenaz, L., Sancho, J., Sales, S., Capmany, J., Berger, P., ... & Dolfi, D. (2010). Broadband true time delay for microwave signal processing, using slow light based on stimulated Brillouin scattering in optical fibers. *Optics express*, 18(21), 22599-22613.
- [10] X. Wang, L. Zhou, R. Li, J. Xie, L. Lu, K. Wu, and J. Chen, "Continuously tunable ultra-thin silicon waveguide optical delay line," *Optica* 4(5), 507–515 (2017).
- [11] C.-J. Chung, X. Xu, G. Wang, Z. Pan, and R. T. Chen, "On-chip optical true time delay lines featuring one-dimensional fishbone photonic crystal waveguide," *Appl. Phys. Lett.* 112(7), 071104 (2018).
- [12] Everhardt, A. S., Tran, T. L. A., Mitsolidou, C., Horner, T. R., Grootjans, R., Oldenbeuving, R., & Heideman, R. G. (2022, March). Ultra-low power stress-based phase actuation in TriPleX photonic circuits. In *Integrated Optics: Devices, Materials, and Technologies XXVI* (Vol. 12004, pp. 15-21). SPIE.
- [13] Byer, R. L. (1988). Diode laser—pumped solid-state lasers. *Science*, 239(4841), 742-747.
- [14] Garrec, B. L. (2010, April). Laser-diode and Flash Lamp Pumped Solid-State Lasers. In *AIP Conference Proceedings* (Vol. 1228, No. 1, pp. 111-116). American Institute of Physics.
- [15] Aghbolagh, F. B. A., Nampootheri, V., Debord, B., G r me, F., Vincetti, L., Benabid, F., & Rudolph, W. (2019). Mid IR hollow core fiber gas laser emitting at 4.6 μm . *Optics Letters*, 44(2), 383-386.
- [16] Z. Zhou, N. Tang, Z. Li, W. Huang, Y. Cui and Z. Wang, "CW Tunable 3 μm Fiber Gas Laser Source," 2018 Conference on Lasers and Electro-Optics Pacific Rim (CLEO-PR), 2018, pp. 1-2.
- [17] Duarte, F. J., & Hillman, L. W. (1990). Dye laser principles, with applications.
- [18] Samelson, H., Lempicki, A., Brecher, C., & Brophy, V. (1964). ROOM-TEMPERATURE OPERATION OF A EUROPIUM CHELATE LIQUID LASER. *Applied Physics Letters*, 5(9), 173-174.
- [19] Zeller, W., Naehle, L., Fuchs, P., Gerschuetz, F., Hildebrandt, L., & Koeth, J. (2010). DFB Lasers Between 760 nm and 16 μm for Sensing Applications. *Sensors*, 10(4), 2492-2510.
- [20] Yelen, K., Hickey, L. M., & Zervas, M. N. (2004). A new design approach for fiber DFB lasers with improved efficiency. *IEEE Journal of Quantum Electronics*, 40(6), 711-720.
- [21] Happach, M., de Felipe, D., Friedhoff, V. N., Kleinert, M., Zawadzki, C., Rehbein, W., & Schell, M. (2017). Temperature-tolerant wavelength-setting and-stabilization in a polymer-based tunable DBR laser. *Journal of Lightwave Technology*, 35(10), 1797-1802.
- [22] Ward, A. J., Robbins, D. J., Busico, G., Barton, E., Ponnampalam, L., Duck, J. P., & Wale, M. J. (2005). Widely tunable DS-DBR laser with monolithically integrated SOA: Design and performance. *IEEE Journal of selected topics in quantum electronics*, 11(1), 149-156.

- [23] Simpanen, E., Gustavsson, J. S., Haglund, E., Haglund, E. P., Larsson, A., Sorin, W. V., ... & Tan, M. R. (2017). 1060 nm single-mode vertical-cavity surface-emitting laser operating at 50 Gbit/s data rate. *Electronics Letters*, 53(13), 869-871.
- [24] Liu, A., Wolf, P., Lott, J. A., & Bimberg, D. (2019). Vertical-cavity surface-emitting lasers for data communication and sensing. *Photonics Research*, 7(2), 121-136.
- [25] Y. Fan et al., "290 Hz intrinsic linewidth from an integrated optical chip-based widely tunable InP-Si₃N₄ hybrid laser," in Proc. Conf. Lasers Electro-Opt., San Jose, CA, USA, 2017, PaperJTh5C.9.
- [26] Komljenovic, T., Srinivasan, S., Norberg, E., Davenport, M., Fish, G., & Bowers, J. E. (2015). Widely tunable narrow-linewidth monolithically integrated external-cavity semiconductor lasers. *IEEE Journal of Selected Topics in Quantum Electronics*, 21(6), 214-222.
- [27] M. Larson et al., "Narrow linewidth high power thermally tuned sampled-grating distributed Bragg reflector laser," in Proc. Opt. Fiber Commun. Conf./Nat. Fiber Optic Eng. Conf., Paper OTh3I.4, 2013.
- [28] Y. Fan et al., "Optically integrated InP-Si₃N₄ hybrid laser," *IEEE Photon. J.*, vol. 8, no. 6, Dec. 2016, Art. no. 1505111.
- [29] J. L. Zhao et al., "Narrow-linewidth widely tunable hybrid external cavity laser using Si₃N₄/SiO₂ microring resonators," in Proc. IEEE 13th Int. Conf. Group IV Photon., Shanghai, China, 2016, pp. 24–25.
- [30] Seimetz, M. (2009). High-order modulation for optical fiber transmission (Vol. 143). Springer.
- [31] Hitchcock, R. Timothy (2004). Radio-frequency and Microwave Radiation. American Industrial Hygiene Assn. p. 1. ISBN 978-1931504553.
- [32] Hunsperger, R. G. (2002). Direct modulation of semiconductor lasers. In *Integrated Optics* (pp. 281-297). Springer, Berlin, Heidelberg.
- [33] G.L. Li, P.K.L. Yu, Optical intensity modulators for digital and analog applications. *J. Lightw. Technol.* 21(9), 2010–2030 (2003)
- [34] S.O. Kasap, *Optoelectronics and Photonics* (Prentice Hall, Englewood Cliffs, 2001).
- [35] Mansoor Sheik-Bahae (2005). "Nonlinear Optics Basics. Kramers–Kronig Relations in Nonlinear Optics". In Robert D. Guenther (ed.). *Encyclopedia of Modern Optics*. Amsterdam: Academic Press. ISBN 0-12-227600-0.
- [36] Abramowitz, M.; Stegun, I. A., eds. (1983). "Chapter 9". *Handbook of Mathematical Functions with Formulas, Graphs, and Mathematical Tables*. Applied Mathematics Series. Vol. 55. Washington D.C.; New York: United States Department of Commerce, National Bureau of Standards; Dover Publications. p. 355. ISBN 978-0-486-61272-0.
- [37] [http://www.amstechnologies.com/fileadmin/amsmmedia/downloads/3720_40G-PS-EAM-1550_\(J\).pdf](http://www.amstechnologies.com/fileadmin/amsmmedia/downloads/3720_40G-PS-EAM-1550_(J).pdf)
- [38] Liu, B., Shim, J., Chiu, Y. J., Keating, A., Piprek, J., & Bowers, J. E. (2003). Analog characterization of low-voltage MQW traveling-wave electroabsorption modulators. *Journal of Lightwave Technology*, 21(12), 3011.
- [39] Urick, V. J., Williams, K. J., & McKinney, J. D. (2015). *Fundamentals of microwave photonics*. John Wiley & Sons.

Chapter 4 - System design, development, and experimental performance evaluation of a 2×4 true-time delay optical beamforming network

In this chapter, a TTD M×N OBFN architecture that supports the generation and steering of a single or multiple independent beams over a continuous set of angles is demonstrated. The OBFN is based on a matrix of optical true-time delay lines (OTTDLs) and a matrix of variable optical attenuators (VOAs) that control the relative time delays and relative amplitudes of the signals that excite the antenna elements in accordance with the intended beam directions and shapes. The experimental evaluation of the OBFN architecture is realized using a 2×4 OBFN setup that can generate up to two beams and feed four antenna elements. The evaluation is based on the bit-error-rate (BER) measurements of the signals generated after the photodiodes of the setup, and correspond to the 15 GHz signals of the two wireless beams with quadrature phase shift keying (QPSK) and quadrature amplitude modulation (QAM) formats. Firstly, the single-beam operation is validated for different targeted steering angles and subsequently, both multi-beam and multicast operation are also validated, indicating the feasibility of the proposed OBFN architecture to support all these three modes of operation without deteriorating the system performance. Although this demonstration is related only to the transmission mode of the wireless antenna (downlink direction), the same architecture can be properly modified to serve the reception mode (uplink direction), too.

4.1 OBFN system architecture

Figure 4.1 and Figure 4.2 present the proposed OBFN architecture when the corresponding microwave links operate in the downlink and uplink direction, respectively. In the first case, the OBFN feeds an N-element antenna array, forming M independent wireless beams. The architecture consists of three sections that accommodate the functionalities of optical modulation, optical beamforming and photodetection. Within the first section, M optical carriers are generated at wavelengths on the C-band grid and enter an amplitude modulator array. The modulation components can be either MZMs or EAMs and are driven by the microwave signals that correspond to the wireless beams. Each modulated optical signal serves in turn as input to the second stage, where it is split by an array of N-1 optical couplers into N copies $E_{in,m,n}$ of equal power. Subsequently, the N copies of each optical signal are forwarded to the corresponding array of OTTDLs and VOAs in order to obtain the proper time delay differences and relative amplitudes. In order to steer the m-th beam to an intended angle φ_m , the optical delays $\tau_{m,n}$ should be set as it is described in Eq.2.31.

It is noted that the OTTDLs are not cascaded, but rather placed in parallel within the OTTDL matrix, allowing from the point of the optical power budget for efficient scaling of the OBFN. In a similar way, the VOAs can be properly configured in order to control the shape of the beams and their side-lobe suppression through proper apodization schemes in the excitation of the AEs.

Finally, within the third section of the OBFN architecture, the copies of the optical signals $E_{out,m,n}$ that are directed to the same AE are wavelength multiplexed using an M×1 arrayed waveguide grating (AWG) and detected by the corresponding PD as a single entity. However, summing multiple optical signals onto a single PD may lead the photodiodes to operate at the non-linear region of their transfer functions, deteriorating the system performance. This inherent issue, which is present to all multi-beam OBFNs, could be mitigated by ensuring that the photodiodes are operating in their linear region, minimizing

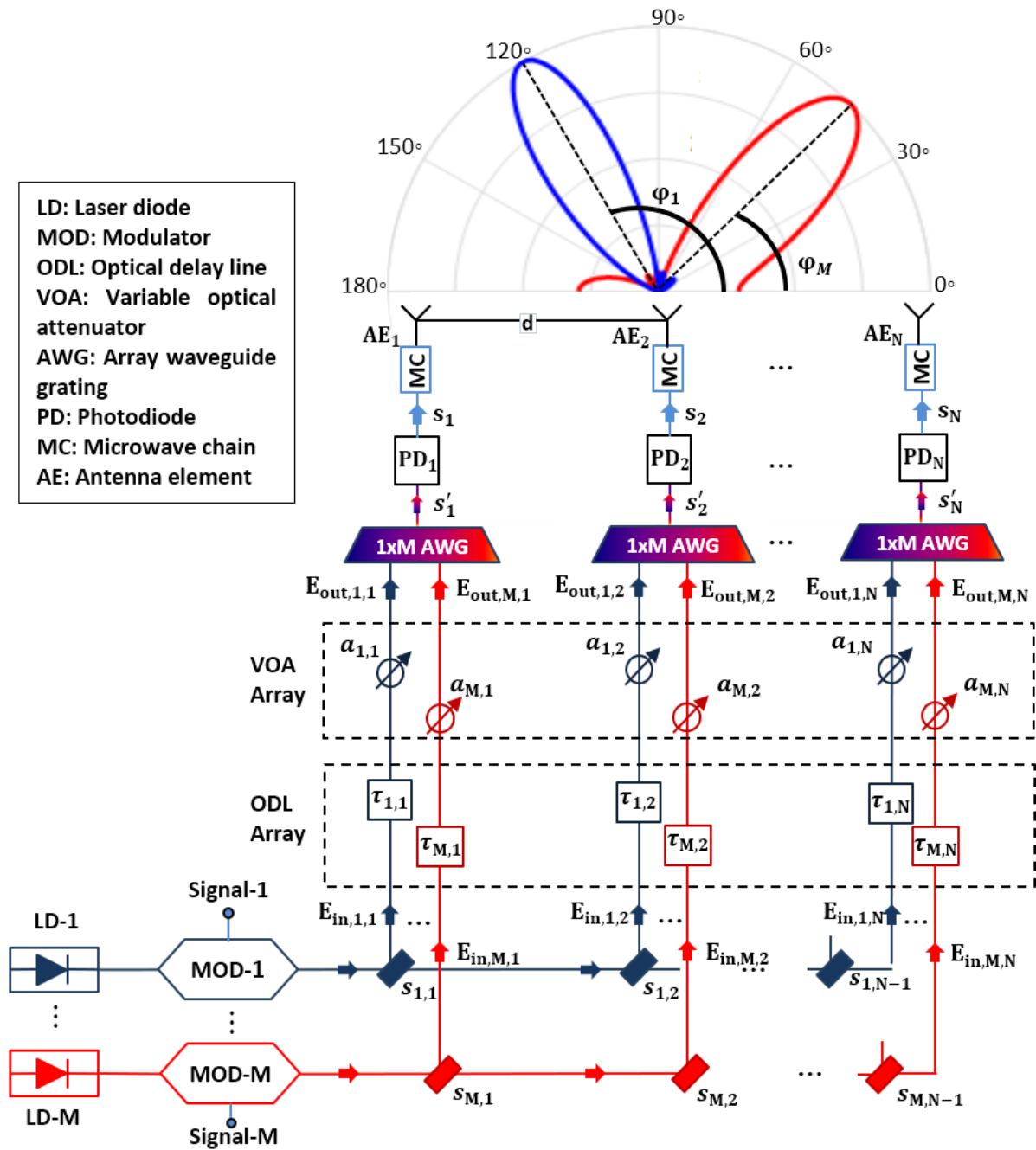


Figure 4.1: Layout of the proposed $M \times N$ OBFN operating (a) in the downlink direction, feeding an N -element antenna, and supporting the formation of M beams.

the non-linear effects. The commercial photodiodes can operate at the linear region even for input optical powers in the order of +30 dBm, supporting in that way the simultaneous detection of multiple optical signals. An alternative solution would be the use of a single photodiode for each optical signal, exiting the OBFN, and the combining of the corresponding microwave signals by means of RF couplers. However, this solution increases significantly the number of the required photodiodes, which results in an increase of the overall cost, size, weight and power consumption of the OBFN. Moreover, it should be noted that the frequency response of the RF components limits their capability to handle microwave signals with high frequencies, without inducing extra losses and causing non-linear effects. On the other hand, in the proposed architecture, the signals are wavelength multiplexed by means of AWGs, which have flat frequency responses and low insertion

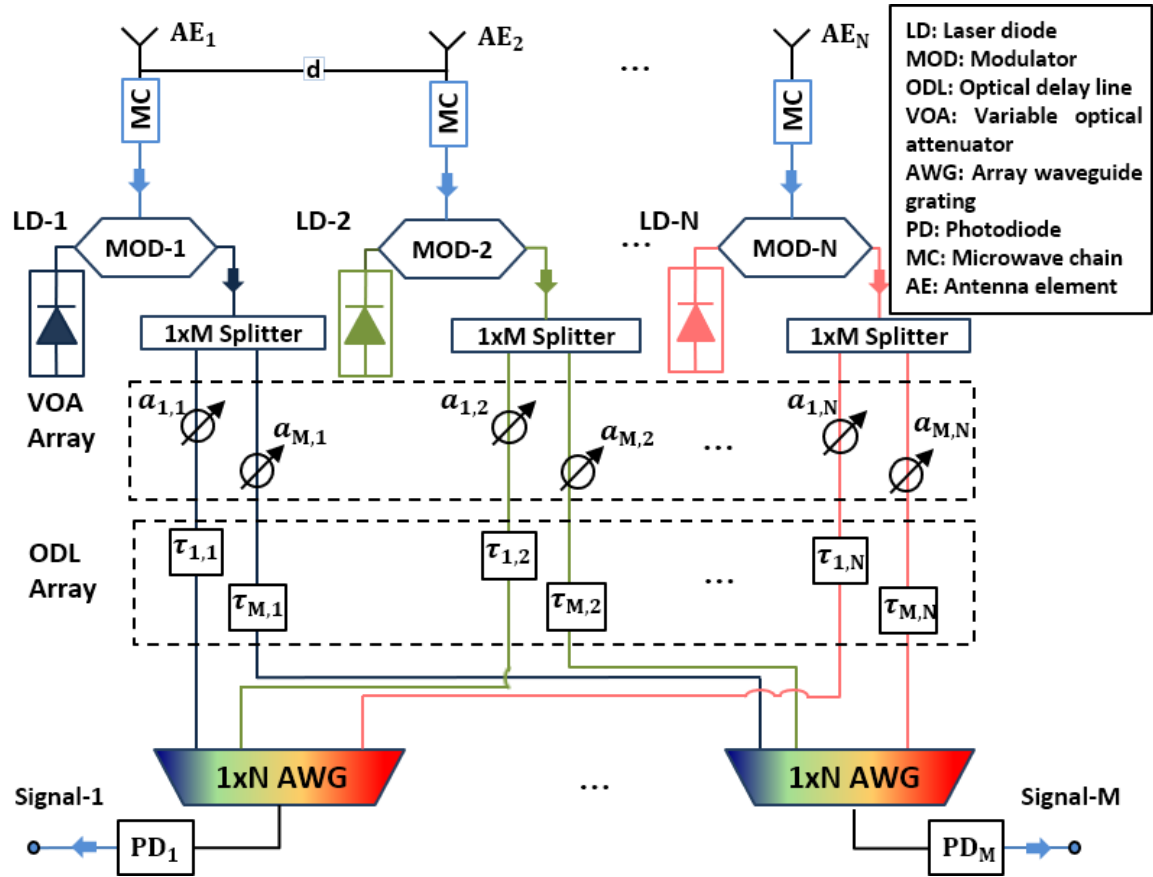


Figure 4.2: Layout of the proposed $M \times N$ OBFN operating in the uplink direction, fed by an N -element antenna array, and forming M independent output microwave signals.

losses, allowing the operation with multiple beams. The signal that excites each AE is the signal at the output of each PD after proper filtering. We can confirm that this excitation signal is a linear superposition of the individual signals that correspond to the different beams and are destined for the specific AE. Thus, no mixing between the beams takes place due to the use of a single PD, and thus no RF interference issues emerge even when the RF signals are at the same frequency. After the wireless transmission of course, RF interference can occur at the position of the final user, if there is an overlap between the radiation patterns of the different beams. However, if these patterns do not overlap, there is no interference at all despite the use of only one PD per AE. To make this clearer, a short mathematical analysis is presented. In order to keep the analysis simple, we take the example of only one AE and only two beams using two optical carriers, each modulated by a single-tone microwave signal. Figure 4.3 presents the corresponding block diagram. The two tones can be either the same or different ones, but they should stay in any case within the microwave band of interest. Assuming that the optical amplitude modulators are biased in their linear regime, the two optical signals $E_{in,1}$ and $E_{in,2}$ at the output of the modulators can be represented as:

$$E_{in,1} = A_1 \cdot [1 + m_1 \cdot \cos(2\pi f_{rf,1}t + \varphi_1)] \cdot \exp[j \cdot (2\pi f_{o,1}t + \varphi_{o,1})] \quad (4.1)$$

$$E_{in,2} = A_2 \cdot [1 + m_2 \cdot \cos(2\pi f_{rf,2}t + \varphi_2)] \cdot \exp[j \cdot (2\pi f_{o,2}t + \varphi_{o,2})] \quad (4.2)$$

where $A_1, A_2, f_{o,1}, f_{o,2}$ and $\varphi_{o,1}, \varphi_{o,2}$ are the amplitudes, the frequencies, and the phases of the two optical carriers and $m_1, m_2, f_{rf,1}, f_{rf,2}$ and φ_1, φ_2 are the amplitude modulation indices, the frequencies and the phases of the microwave signals. It is noted again that $f_{rf,1}$ and $f_{rf,2}$ can be either the same or different but both within the microwave band of interest.

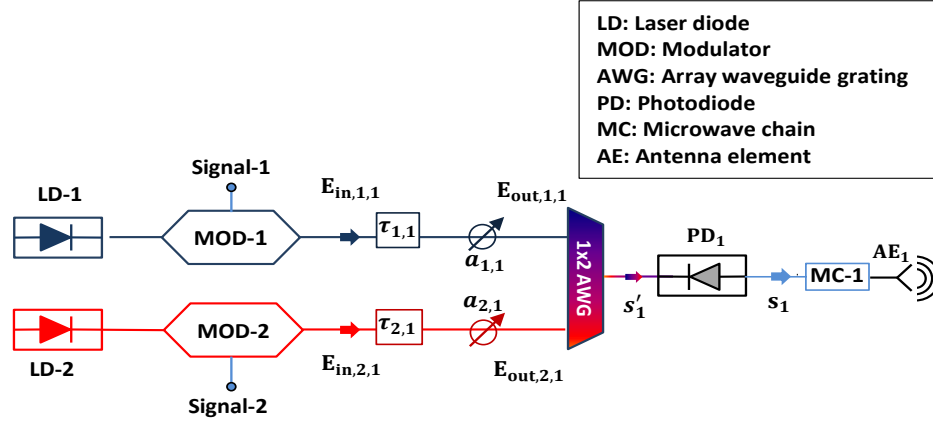


Figure 4.3: Block diagram of the mathematical analysis for proving that the excitation signal after the PD is a linear superposition of the individual signals that correspond to the different beams and are destined to the specific AE.

At the output of the beamforming network, which is represented by the two ODLs and the two VOAs, the signals can be written as:

$$E_{out,1,1} = A_1 \cdot \left[1 + m_1 \cdot \cos[2\pi f_{rf,1}(t - \tau_1) + \varphi_1] \right] \cdot \exp \left[j \cdot [2\pi f_{o,1}(t - \tau_1) + \varphi_{o,1}] \right] \quad (4.3)$$

$$E_{out,2,1} = A_2 \cdot \left[1 + m_2 \cdot \cos[2\pi f_{rf,2}(t - \tau_2) + \varphi_2] \right] \cdot \exp \left[j \cdot [2\pi f_{o,2}(t - \tau_2) + \varphi_{o,2}] \right] \quad (4.4)$$

The optical signals are wavelength multiplexed at the AWG and are fed to the PD. The resultant electrical signal is calculated as follows:

$$s_1 \propto (E_{out,1,1} + E_{out,2,1}) \cdot (E_{out,1,1} + E_{out,2,1})^* \quad (4.5)$$

where the asterisk (*) denotes the complex conjugate. Using eq. (4.3) and (4.4), and making simple calculations we derive the following expression:

$$s_1 \propto |E_{out,1,1}|^2 + |E_{out,2,1}|^2 + 2 \cdot |E_{out,1,1}| \cdot |E_{out,2,1}| \cdot \cos \left[2\pi \cdot [f_{o,1}(t - \tau_1) - f_{o,2}(t - \tau_2)] + (\varphi_{o,1} - \varphi_{o,2}) \right] \quad (4.6)$$

which gets in fact the following much simpler form:

$$s_1 \propto |E_{out,1,1}|^2 + |E_{out,2,1}|^2 \quad (4.7)$$

The reason for the elimination of the mixing product is the incoherent nature of the system, which is in turn due to the use of laser sources at different wavelengths for each beam. As a result, the mixing of the two fields $E_{out,1,1}$ and $E_{out,2,1}$ is averaged out, the average value of the cosine in eq. (4.6) gets null, and the mixing product is eliminated. Making now simple calculations on eq. (4.7) it can be derived that the electrical signal can get the following form:

$$s_1 \propto (DC \text{ terms}) + A_1^2 \cdot m_1 \cdot \cos[2\pi f_{rf,1}(t - \tau_1) + \varphi_1] + A_2^2 \cdot m_2 \cdot \cos[2\pi f_{rf,2}(t - \tau_2) + \varphi_2] + (2f_{rf,1}, 2f_{rf,2} \text{ terms}) \quad (4.8)$$

By using a proper DC block and microwave filters to filter out the generated tones at the high frequencies $2f_{rf,1}$ and $2f_{rf,2}$, the final signal that will be used for the excitation of the AE becomes:

$$s_1 \propto A_1^2 \cdot m_1 \cdot \cos[2\pi f_{rf,1}(t - \tau_1) + \varphi_1] + A_2^2 \cdot m_2 \cdot \cos[2\pi f_{rf,2}(t - \tau_2) + \varphi_2] \quad (4.9)$$

As it can be observed, the final excitation signal is a linear superposition of the two individual signals that correspond to the different beams and are destined for the specific AE, and thus there are no interference issues, meaning that the beams can be steered and operated independently from each other. This conclusion is still valid in the case where $f_{rf,1} = f_{rf,2}$, in the case where the two signals are not simple tones but true signals with spectral content within the same microwave band, and of course in the case where we have more than two beams.

At the final stage, each photocurrent serves as input to a microwave chain (MC) and undergoes a number of processing steps including direct DC blocking, filtering and amplification in order to drive the corresponding AE. Provided that the beams are steered to different directions and their radiation patterns do not overlap, there are not any interference issues arising from the OBFN, even in the case that the beams are within exactly the same spectral band.

In the uplink direction, N independent laser sources, emitting at different wavelengths on the C-band grid and feed N parallel amplitude modulators. The N AEs of the multi-element antenna are excited by the incident wireless waves and generate N microwave signals that drive the modulators after amplification inside a microwave chain. The modulated optical signals are split into M copies before entering the main part of the OBFN architecture, which has the same elements (i.e., ODLs and VOAs) and the same structure as the corresponding part in the case of downlink direction. At the output of this part, the signals corresponding to each beam are combined with the help of an N×1 AWG and are detected by the same PD. Each one of the M generated photocurrents corresponds to an independent wireless beam that is received at the angle defined by the corresponding ODLs of the OBFN.

4.2 Theoretical validation of single-beam, multi-beam, and multicast beamforming

The capability of the proposed optical beamformer to support single-beam, multi-beam, and multicast operation was validated by extensive simulation studies that emulated its system performance in the downlink operation of a wireless link in Matlab environment. Within these studies, the size of the OBFN was selected to be either 2×4 or 2×8 feeding a multi-element antenna array with either 4 or 8 antenna elements.

Single-beam beamforming: In this case, the amplitude of an optical carrier was modulated by a microwave signal at 15 GHz carrying either QPSK, 16-QAM or 64-QAM modulation formats at 1 Gbaud symbol rate. The spectra of the signals were shaped using raised cosine filters with roll-off factor equal to 1. The modulated optical signal was coupled to the first row of the OBFN while the input of the second row was considered null. The relative time-delay and amplitude relationships of the optical signals before the photodetection stage were tuned in accordance with the targeted steering angle and the respective amplitude excitation scheme. At the output ports of the OBFN and after the photodetection stage, the microwave signals fed a multi-element antenna array with isotropic antenna elements (AEs) enabling the transmission over a radio-frequency (RF) channel based on additive white Gaussian noise (AWGN) model. The SNR of the microwave signals after the wireless channel was set at 28 dB. It should be noted that the seed number of the random number generator used in the emulation of the AWGN model is constant for all the simulation studies in order to generate repeatable white Gaussian noise samples. At the other end of the system, a single receiver consisting of an isotropic AE was placed at specific observation angles. Within the following simulation studies and for comparison reasons, the receiver was placed

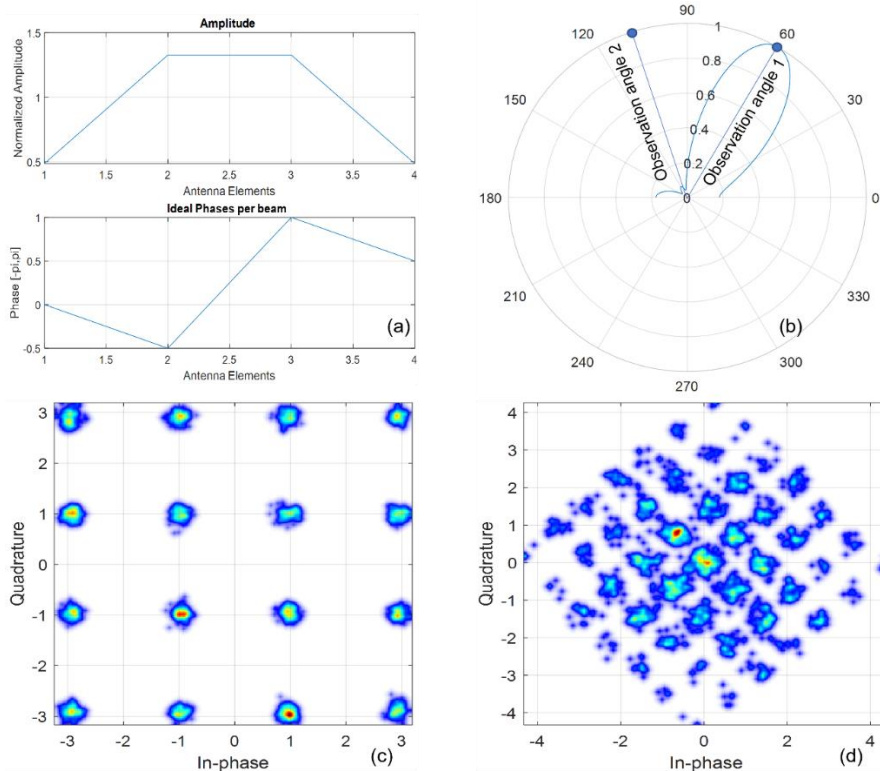


Figure 4.4: Simulation results for single-beam operation of a 2×4 TTD OBFN assuming transmission of a 16-QAM signal at 1 Gbaud symbol rate at 60° . (a) Normalized amplitudes and phases of the excitation signals applying a Gaussian distribution with standard deviation equal to 1.5, (b) calculated array factor, (c) and (d) resulting constellation diagrams at 60° and 110° , respectively.

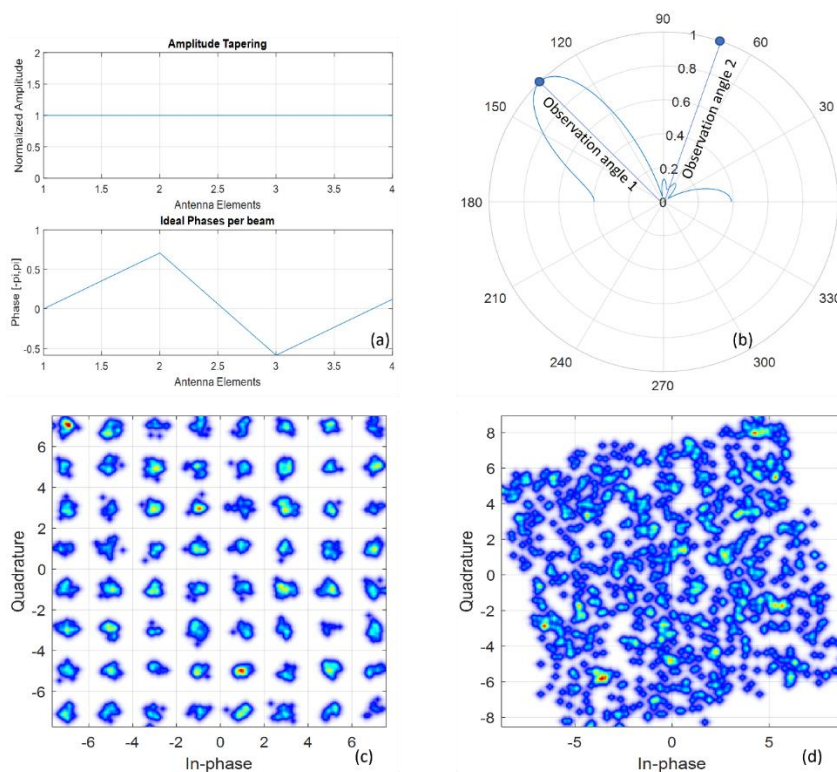


Figure 4.5: Simulation results for single-beam operation of a 2×4 TTD OBFN assuming transmission of a 64-QAM signal at 1 Gbaud symbol rate at 135° . (a) Normalized amplitudes and phases of the excitation signals applying a uniform amplitude distribution, (b) calculated array factor, (c) and (d) resulting constellation diagrams at 135° and 70° , respectively.

successively at the targeted steering angle (Observation angle 1) and at an random angle (Observation angle 2) in order to observe the unwanted signal received in this direction. Finally, at each observation angle, the detected microwave signal was frequency down-converted to the baseband using a local oscillator at 15 GHz and were decoded. Figure 4.4 and Figure 4.5 present the simulation results of two indicative tested cases. More specifically, in the first case which is related to Figure 4.4, the simulation platform was configured to generate and steer a microwave signal carrying 16-QAM modulation format at 60° . The applied amplitude excitation scheme followed a Gaussian distribution with standard deviation equal to 1.5 as it can be seen in Figure 4.4 (a). The calculated array factor is presented in Figure 4.4 (b) and as it can be observed the main lobe is correctly steered at 60° . At the same figure, they are also presented the two observation angles which in this case are 60° and 110° . Figure 4.4 (c) and (d) depict the constellation diagrams at the two observation angles. As observed, at 60° angle the constellation diagram is clear indicating an error free performance while at 110° the constellation diagram is noisy due to the low power of the signal at this direction. In the second case which is related to Figure 4.5, the simulation platform was configured to generate and steer a microwave signal carrying 64-QAM modulation format at 135° with a uniform amplitude excitation scheme. The amplitude and phase of the excitation signals are depicted in Figure 4.5 (a). As it can be observed in Figure 4.5 (b), the main lobe is correctly directed at 135° . Figure 4.5 (c) presents the constellation diagram at 135° while Figure 4.5 (d) presents the constellation diagram at the second observation angle at 70° . As in the first case, the constellation

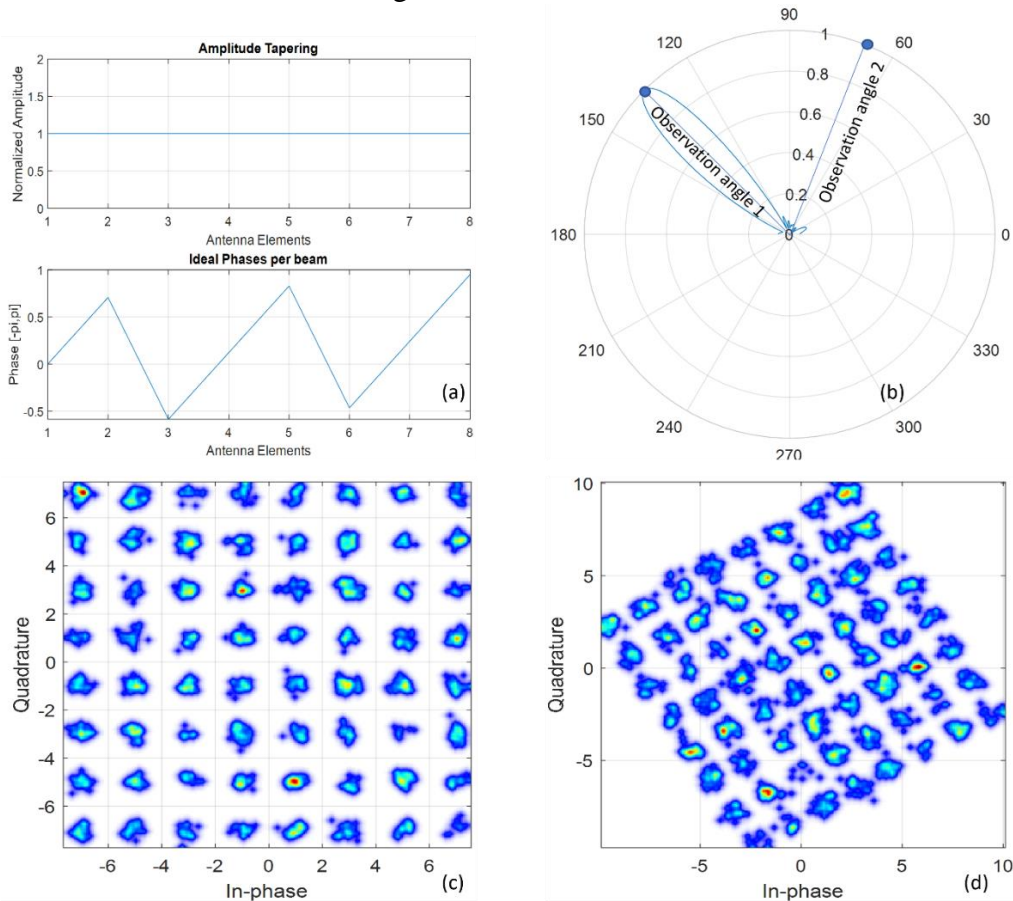


Figure 4.6: Simulation results for single-beam operation of a 2×8 TTD OBFN assuming transmission of a 64-QAM signal at 1 Gbaud symbol rate at 135° . (a) Normalized amplitudes and phases of the excitation signals applying a uniform amplitude distribution, (b) calculated array factor, (c) and (d) resulting constellation diagrams at 135° and 70° , respectively.

diagram at the intended steering angle indicates an error free performance while at the second observation angle the signal too noisy.

In the next simulation case, we considered a 2×8 OBFN which was configured to generate and steer a microwave signal carrying 64-QAM modulation format at 135° with a uniform amplitude excitation scheme, as in the previous simulation case. Figure 4.6 (a)-(d) present the corresponding simulation results. The increase of the number of the antenna elements led to the generation of a narrower beamwidth which dictates that the power of the signal is directed at the intended steering angle. As it can be observed from the constellation diagram presented in Figure 4.6 (c) the signal at 135° remains error-free while at the second observation angle at 70° , illustrated at Figure 4.6 (d), the signal remains noisy and suffers from severe phase noise due to the fact that in this angle the transmitted fields of the antenna array are not combined in phase.

Multi-beam beamforming: In order to facilitate the simulation studies and without loss of generality, the number of the transmitted beams was 2 while the size of the OBFN was 2×4 . Figure 4.7 and Figure 4.8 present the simulation results of two indicative tested cases. More specifically, in the first case which is related to Figure 4.7, the simulation platform was configured to generate and steer a microwave signal carrying QPSK modulation format at 110° and a second microwave signal carrying 16-QAM modulation format at 50° , simultaneously. The applied amplitude excitation scheme for both signals followed a uniform distribution as it can be seen in Figure 4.7 (a).

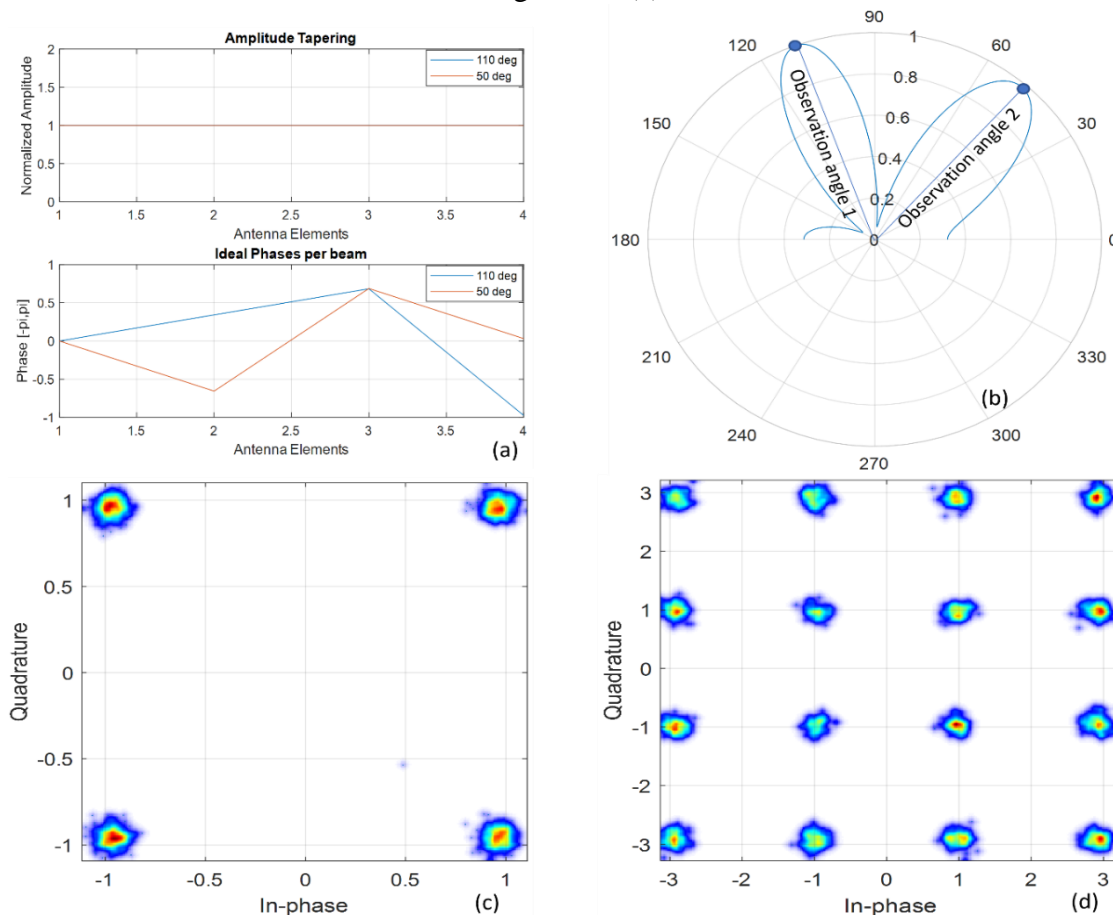


Figure 4.7: Simulation results for multi-beam operation of a 2×4 TTD OBFN assuming transmission of a QPSK signal at 1 Gbaud symbol rate at 110° and a 16-QAM signal at 1 Gbaud symbol rate at 50° . (a) Normalized amplitudes and phases of the excitation signals applying a uniform amplitude distribution, (b) calculated array factor, (c) and (d) resulting constellation diagrams at 50° and 110° , respectively.

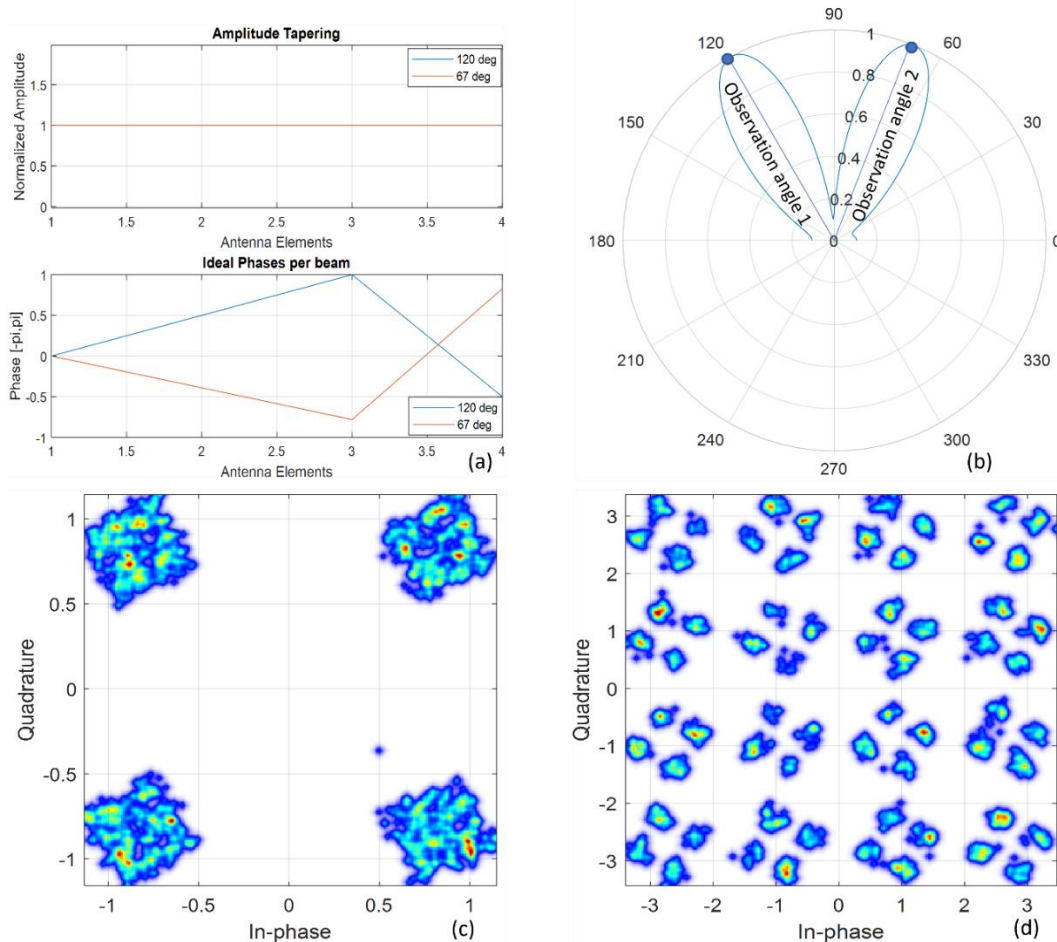


Figure 4.8: Simulation results for multi-beam operation of a 2×4 TTD OBFN assuming transmission of a QPSK signal at 1 Gbaud symbol rate at 120° and a 16-QAM signal at 1 Gbaud symbol rate at 67° . (a) Normalized amplitudes and phases of the excitation signals applying a uniform amplitude distribution, (b) calculated array factor, (c) and (d) resulting constellation diagrams at 120° and 67° , respectively.

The calculated array factor is presented in Figure 4.7 (b) and as it can be observed the main lobes are correctly steered at 110° and 50° . Figure 4.7 (c) and (d) depict the resulted constellation diagrams at the two observation angles. As observed, at both steering angles the constellation diagrams are very clear indicating that the signals have been received at these directions without errors.

In the second case which is related to Figure 4.8, the simulation platform was configured to generate and steer a microwave signal carrying QPSK modulation format at 120° and a second microwave signal carrying 16-QAM modulation format at 67° , simultaneously. The applied amplitude excitation scheme for both signals followed a uniform distribution as it can be seen in Figure 4.8 (a). As it can be observed in Figure 4.8 (b), main lobes are correctly steered at the indented steering angles. Due to the size of the OBFN, the type of the antenna elements, the selected set of angles and also the applied amplitude excitation scheme, the two lobes are interfered to each other as it can be seen in Figure 4.8 (b). Due to this interference, each original constellation point of the QPSK signal now consists of 16 different points, while on the other hand, each original constellation point of the 16-QAM signal consists now of 4 points arranged in the QPSK modulation format. The effect of this interference can easily be observed at the resulting constellation diagrams that are illustrated in Figure 4.8 (c) and (d).

Multi-cast beamforming: In the following simulation study, we validated the inherent capability of the OBFN to support multicast operation, i.e., the transmission of one

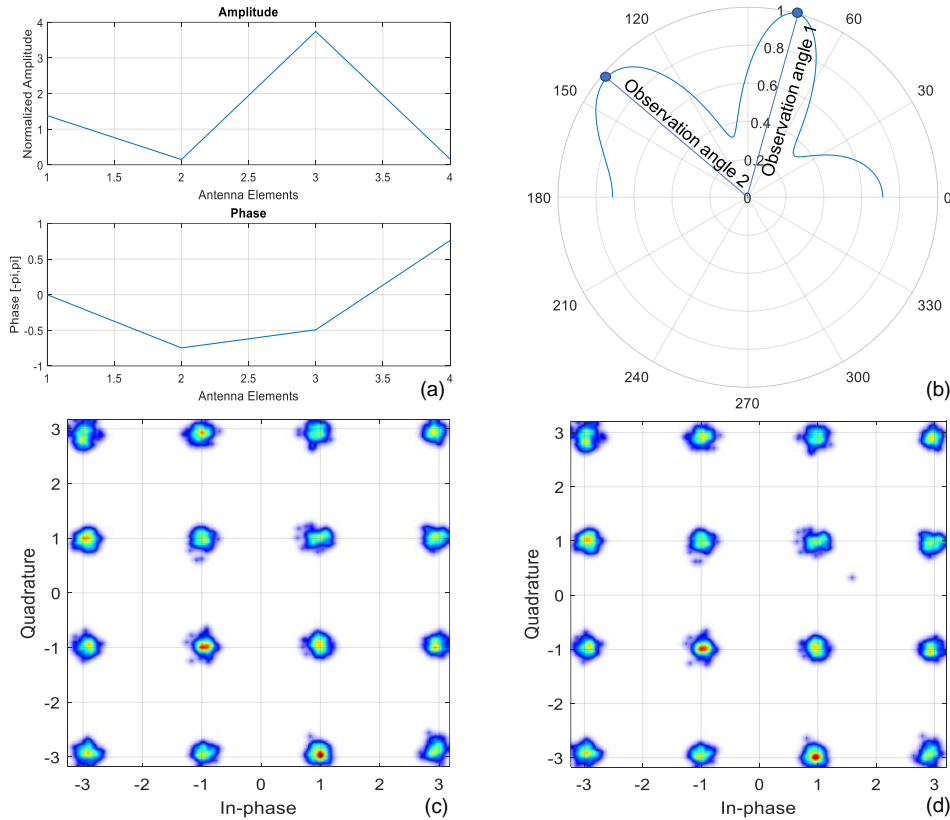


Figure 4.9: Simulation results for multicast operation of a 2×4 TTD OBFN assuming transmission of a 16-QAM signal with 1 Gbaud symbol rate at 75° and 140° . (a) Normalized amplitudes and phases of the excitation signals, (b) calculated array factor, (c) and (d) constellation diagrams at 75° and 140° , respectively.

information signal to multiple and different steering angles simultaneously. Firstly, we considered a 2×4 OBFN and it was configured to generate and steer a microwave signal carrying 16-QAM modulation format with 1 Gbaud symbol rate at 75° and at 140° , simultaneously. The applied amplitude excitation scheme followed a Gaussian distribution with standard deviation equal to 1.5, as it can be seen in Figure 4.9 (a). The calculated array factor is presented in Figure 4.9 (b) and as it can be observed the main lobes are correctly steered at 75° and 140° . Figure 4.9 (c) and (d) present the calculated constellation diagrams at the two observation angles. As observed, at both steering angles the constellation diagrams are clear indicating that the information signal has been successfully transmitted to both directions without errors. As in the case of the multibeam operation, the interference between the lobes of the signals transmitted to different direction could deteriorate the overall system performance. The interference in this case can also be easily observed in the calculated array factors the constellation diagrams.

In order to better explain this interference and illustrate its impact on the array factor and the constellation diagrams, we considered an OBFN configured to generate and steer a microwave signal carrying 16-QAM modulation format with 1 Gbaud symbol rate at 65° and at 140° . In this example, we considered three different combinations of the applied apodization schemes. In particular, firstly, we selected a uniform apodization scheme for both steering angles. Subsequently, we selected a uniform apodization scheme for the beam directed at 65° and a Gaussian scheme with standard deviation equal to 1.5 for the beam directed at 140° and in the last study, we selected a Gaussian apodization schemes for both steering angles with standard deviation equal to 1.5. Figure 4.10 presents the calculated array factors and constellation diagrams for the three different combinations of the applied apodization schemes. Figure 4.10 (a) – (c) refer to the study of considering a uniform apodization schemes for both angles. More specifically, Figure 4.10 (a) illustrates three

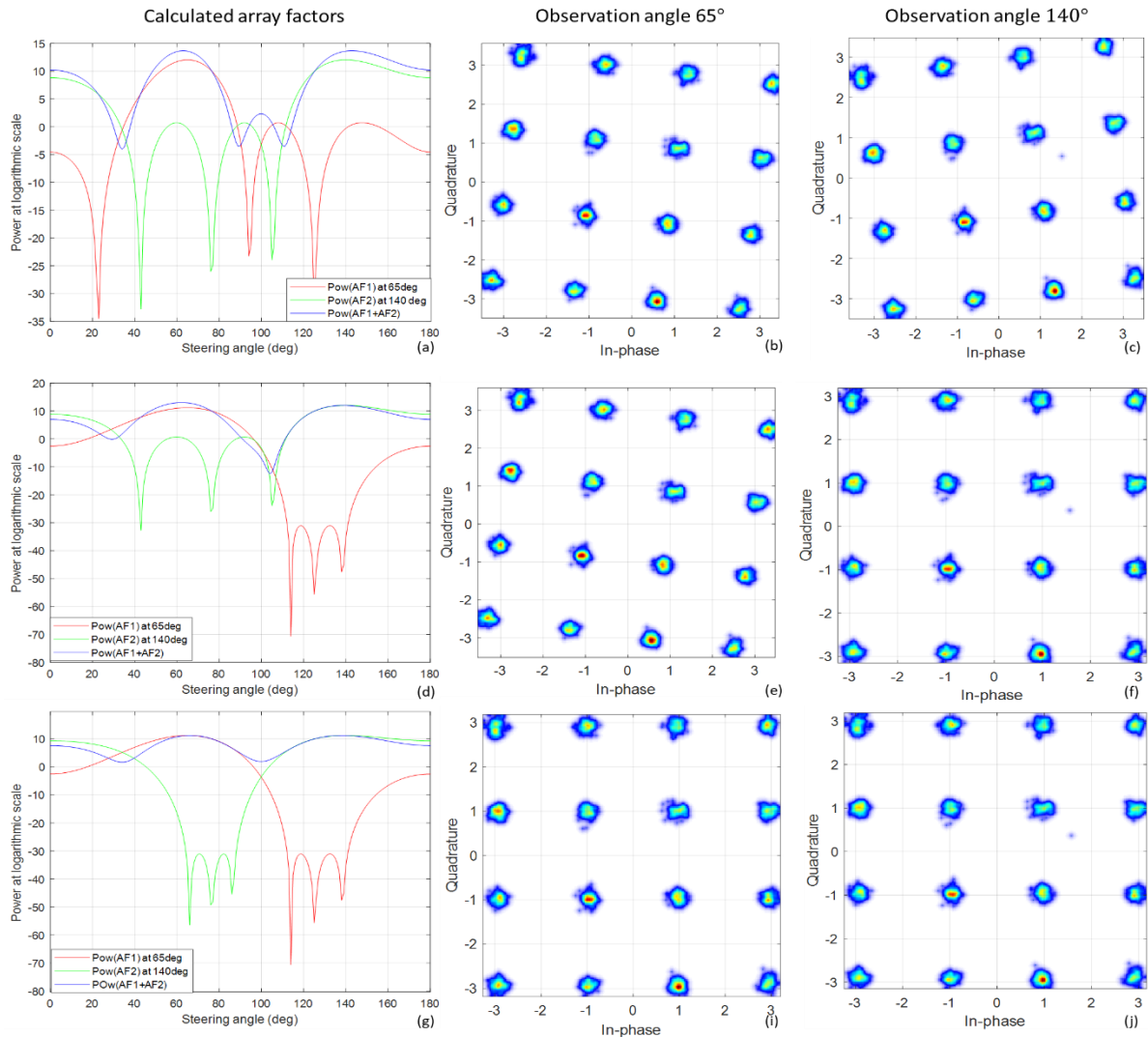


Figure 4.10: Simulation results for multicast operation of a 2×4 TTD OBFN assuming transmission of a 16-QAM signal with 1 Gbaud symbol rate at 65° and 140° for different combination of amplitude apodization schemes. (a) – (c) calculated array factors and constellation diagrams applying a uniform distribution for both steering angles, (d)-(f) and (g)-(j) corresponding results applying a uniform-Gaussian ($\text{std}=1.5$) and a Gaussian-Gaussian ($\text{std}=1.5$) distribution, respectively.

different array factors. With solid red line is illustrated the array factor when the OBFN is configured for single-beam operation, targeting a beam angle at 65° . The solid red line illustrates the array factor when the OBFN is configured for single-beam operation, targeting a beam angle at 140° and with solid red line is illustrated the array factor when the OBFN is configured to support multicast operation at 65° and 140° . Taking into account that the array factor in the case of multicast operation is equivalent to the sum of the array factors calculated for single beam operation for the same targeted steering angles, in Figure 4.10 we can identify the impact of the sidelobes of the array factors as they have been calculated for single-beam operation at 65° and 140° on the array factor in the case of multicast operation. As it can be observed, the peaks of the array factor for the multicast operation (blue line) have an angle offset of the ideal peaks that should be exactly at 65° and 140° due to the presence of strong sidelobes. This angle offset results in a power reduction and in a phase rotation in the constellation diagrams, as it can be seen in Figure 4.10 (b) and (c). As already explained in Chapter 2, the sidelobes can be suppressed if a non-uniform apodization scheme is applied. Figure 4.10 (d) – (f) refer to the study of considering a Gaussian apodization scheme for the beam directed at 65° and a uniform scheme for the

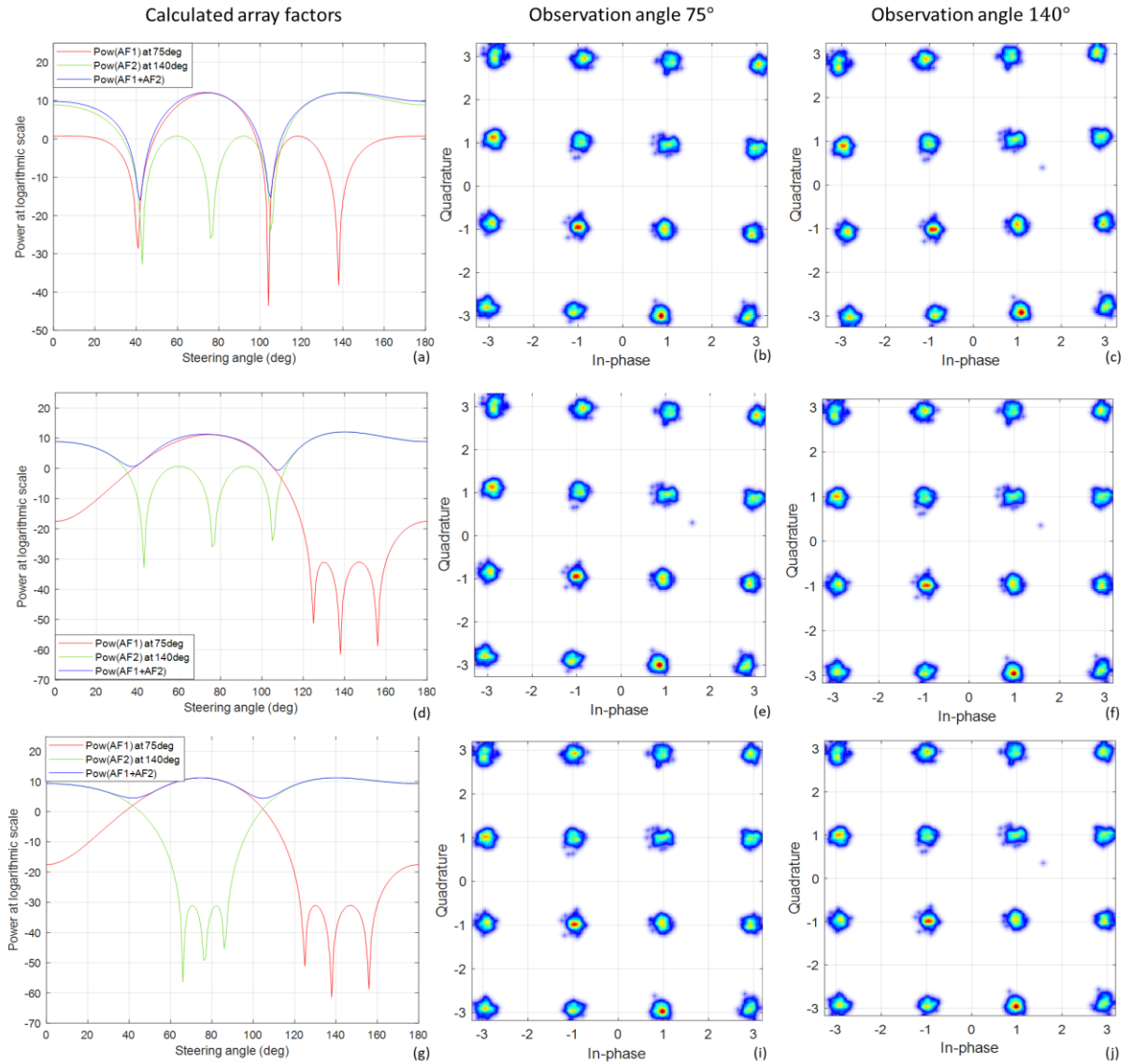


Figure 4.11: Simulation results for multicast operation of a 2×4 TTD OBFN assuming transmission of a 16-QAM signal with 1 Gbaud symbol rate at 75° and 140° for different combination of amplitude apodization schemes. (a) – (c) calculated array factors and constellation diagrams applying a uniform distribution for both steering angles, (d)-(f) and (g)-(j) corresponding results applying a uniform-Gaussian (std=1.5) and a Gaussian-Gaussian (std=1.5) distribution, respectively.

beam directed at 140° . This combination of the apodization schemes results in a significant suppression of the sidelobes of the beam that is directed at 65° , as it can be seen from the array factors presented in Figure 4.10 (d). This outcome is also validated from the constellation diagrams presented in Figure 4.10 (e) and (f) since the signal at 140° has not any phase noise, unlike the signal at 65° which is rotated due to the presence of the sidelobes. The phase noise in both directions can be eliminated if a Gaussian apodization scheme is applied for both angles as it can be observed in Figure 4.10 (g) – (j).

The impact of the sidelobes can be further reduced and eliminated if the selected set of steering angles are located close to the null points of the array factors calculated for single-beam operation for the same angles. As it can be observed in Figure 4.10 (a), (d), and (g), the array factors calculated for the single beam operation targeting 140° have a null point close to 75° . Thus, in order to assess the impact of the sidelobes when the selected steering angles are close to the null points of the equivalent array factors for single beam operation, an additional simulation study was performed, considering the configurations and setups as

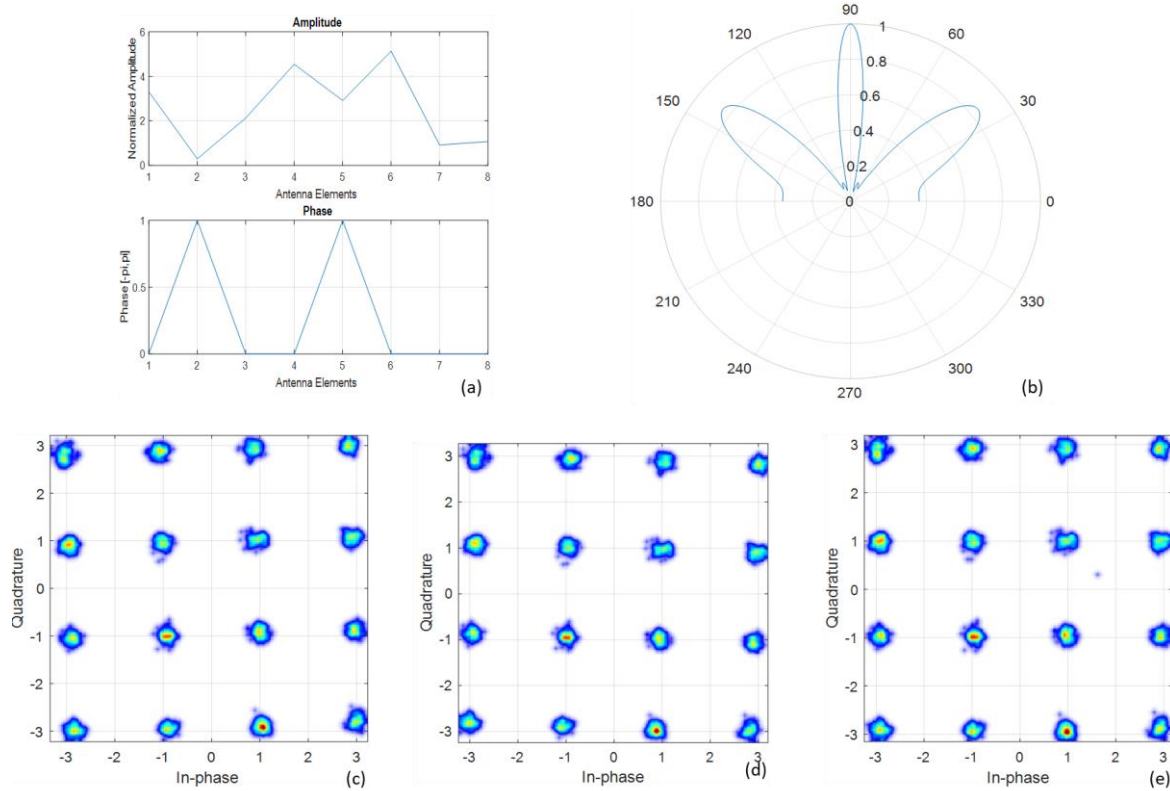


Figure 4.12: Simulation results for multicast operation of a 2×8 TTD OBFN assuming transmission of a 16-QAM signal with 1 Gbaud symbol rate at 45° , 90° , and 140° . (a) Normalized amplitudes and phases of the excitation signals, (b) calculated array factor, (c), (d), and (e) constellation diagrams at 45° , 90° , and 140° , respectively.

In the previous example, but for steering angles equal to 75° and 140° . The simulation results are presented in Figure 4.11. As observed, for all the three different combinations of the applied apodization schemes, the constellation diagrams are clear and do not have any phase noise even for the case of applying a uniform apodization scheme for both angles.

Therefore, from the analysis above, it is evident that the number of the supported steering angles in case of multicast operation can be increased if the impact of the sidelobes is controlled. Figure 4.12 presents the simulation results for multicast operation, targeting three different steering angles and considering a 2×8 OBFN. The selected set of angles was 45° , 90° , and 140° . The apodization scheme for the angles at 45° and 140° followed a Gaussian distribution with standard deviation equal to 1.5 while at 90° a uniform scheme was selected. The normalized amplitude and phase of the excitation signals are presented in Figure 4.12 (a) while the calculated array factor and the constellation diagrams at the three steering angles are presented in Figure 4.12 (b)-(d). As observed, all the three signals exhibit an error-free performance.

4.3 System design and development of experimental testbed

Figure 4.13 presents the experimental setup for the system evaluation of the proposed OBFN architecture in the downlink direction. Without loss of generality, the dimension of the OBFN is limited to 2×4 , meaning that is able to support the generation of two beams and the excitation of four AEs. Provided that a larger number of optical modulators, ODLs, VOAs and PDs is available, the extension to larger OBFN size is straightforward. A 65 GSa/s arbitrary waveform generator (AWG) generates a QPSK signal and a 16-QAM signal at 15 GHz carrier frequency. The two signals correspond to the microwave signals of the two intended beams and drive an EAM and an MZM, respectively. The symbol rate of the

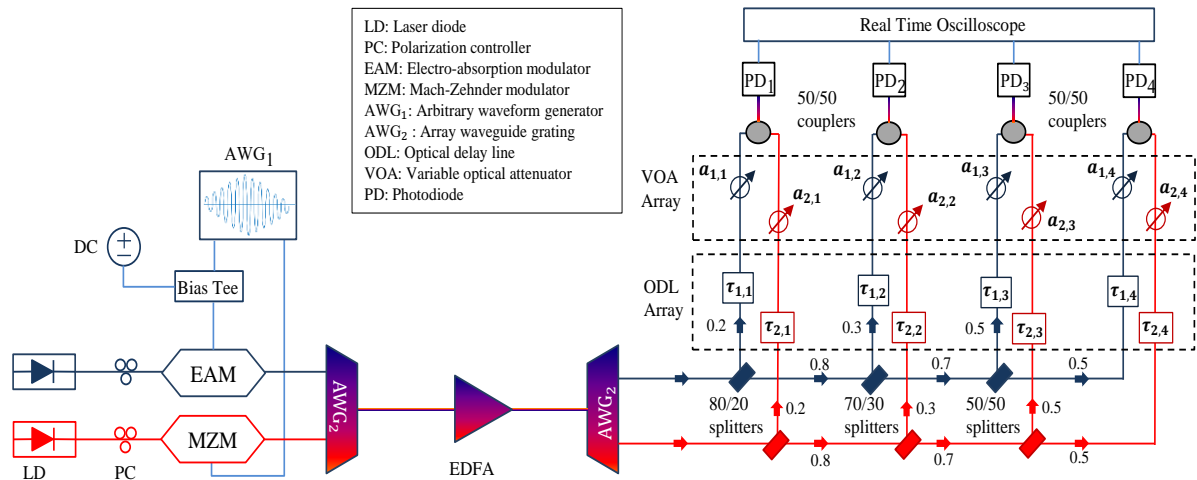


Figure 4.13: Experimental setup for the evaluation of a 2×4 TTD OBFN based on an array of ODLs and an array of VOAs, operating at the downlink direction.

two microwave signals can be either 500 Mbaud or 1 Gbaud, while their bandwidth is limited around their carrier using a pulse shaping filter with roll-off factor equal to 1. The CW signals that are modulated by the EAM and the MZM are generated by two DFB lasers at 1554.94 nm and 1558.17 nm, respectively. Polarization controllers at the input of the modulators adjust the polarization state of the two cw signals in order to optimize the amplitude modulation process. In order to compensate the losses of the modulators, the optical signals at the output of the EAM and the MZM are wavelength multiplexed, amplified by an Erbium-doped fiber amplifier (EDFA) and wavelength demultiplexed by a second AWG.

The two optical signals serve thereafter as inputs to the main stage of the OBFN and generate four copies each. These copies propagate through the ODLs and the VOAs of the OBFN in order to acquire the proper time delay differences and the proper relations between their amplitude levels. The duration of the induced delay by the ODLs is manually controlled by adjusting the position of a prism reflector, which adjusts in turns the optical path difference between the input and output signals. Each ODL is 134 mm long, 58 mm wide and 28 mm height. The insertion losses of both ODLs and the VOAs are 1.5 dB and 0.5 dB, respectively. Taking into account the carrier frequency of the microwave signals (15 GHz) and assuming $\lambda/2$ spacing between the AEs of the multi-element antenna, the total dynamic range of the employed ODLs (0-300 ps) is found with the help of Eq. 2.31 to be sufficient for covering the full $0-180^\circ$ range of steering angles. Moreover, the high resolution of the ODLs (0.2 ps) enables in practice continuous tuning of the time delay differences between the four copies of each signal, and thus continuous angle tuning of each beam. On the other hand, the VOAs of the OBFN are configured for either uniform excitation of the AEs with equal power levels for all copies of the same signal or for Gaussian excitation of the AEs for the power levels of the corresponding copies with respect to the center of the AE array, with standard deviation equal to 1.

Due to the unavailability of additional AWGs at the output of the main part of the OBFN, the time delayed copies of the two signals that are destined to the same AE are combined with the help of 50:50 optical couplers and are detected by a PD array with 15 GHz bandwidth. After this PD array, the generated photocurrents are sampled by a 4-channel 80 GSa/s real-time oscilloscope and stored for off-line processing.

Figure 4.14 presents the key algorithms and methods for the calculation of the radiation field as well as for the proper demodulation of the QAM signals. More specifically, the first algorithm calculates the received field at the intended angles based on the samples of the four excitation signals. The subsequent algorithms treat the calculated fields independently.

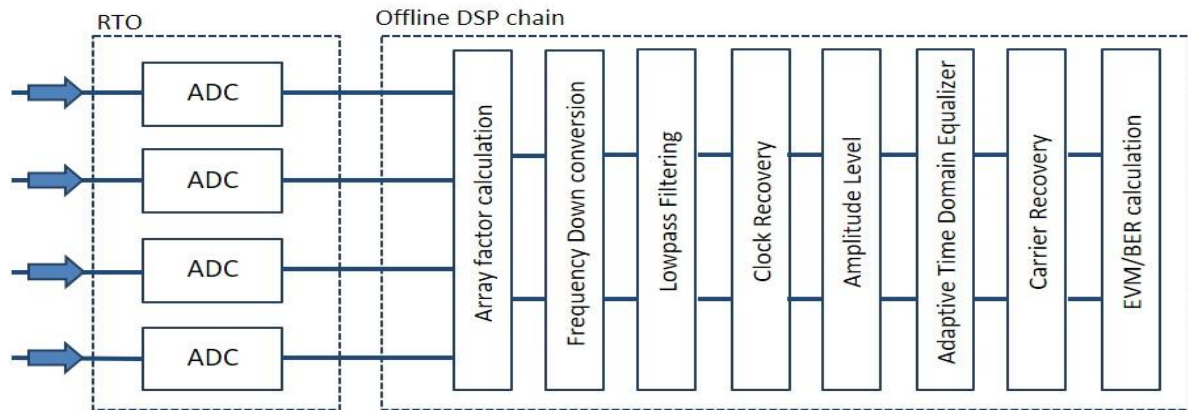


Figure 4.14: Block diagram of the deployed offline DSP chain for the calculation of the array factor of the two beams and the decoding of the mQAM signals.

In more detail, a simple set of DSP algorithms are utilized in order to properly decode and assess the quality of the received signals. First, the signals are frequency down-converted to the baseband using a digital local oscillator at 15 GHz. A sharp low-pass filter with cut-off frequency equal to the baseband bandwidth of the signals is used to filter out the content of the unwanted frequencies. A time recovery (TR) algorithm recovers in turn the symbol rate of the signals and identifies the optimal sampling instants, allowing for minimization of the ISI and providing two samples per symbol. Subsequently, an automatic gain control algorithm based on a closed-feedback loop scales the power of the signal to specific power level depending on the modulation format. Then, an adaptive equalizer converging to each radius of the QAM constellation, is used for the optical channel equalization, while carrier recovery algorithms compensate for frequency and phase offsets. Finally, the processed samples are used for the extraction of the constellation diagram and the calculation of the BER, and thus for the overall assessment of the quality of the beamforming system. More details about the DSP toolbox can be found in the Appendix I.

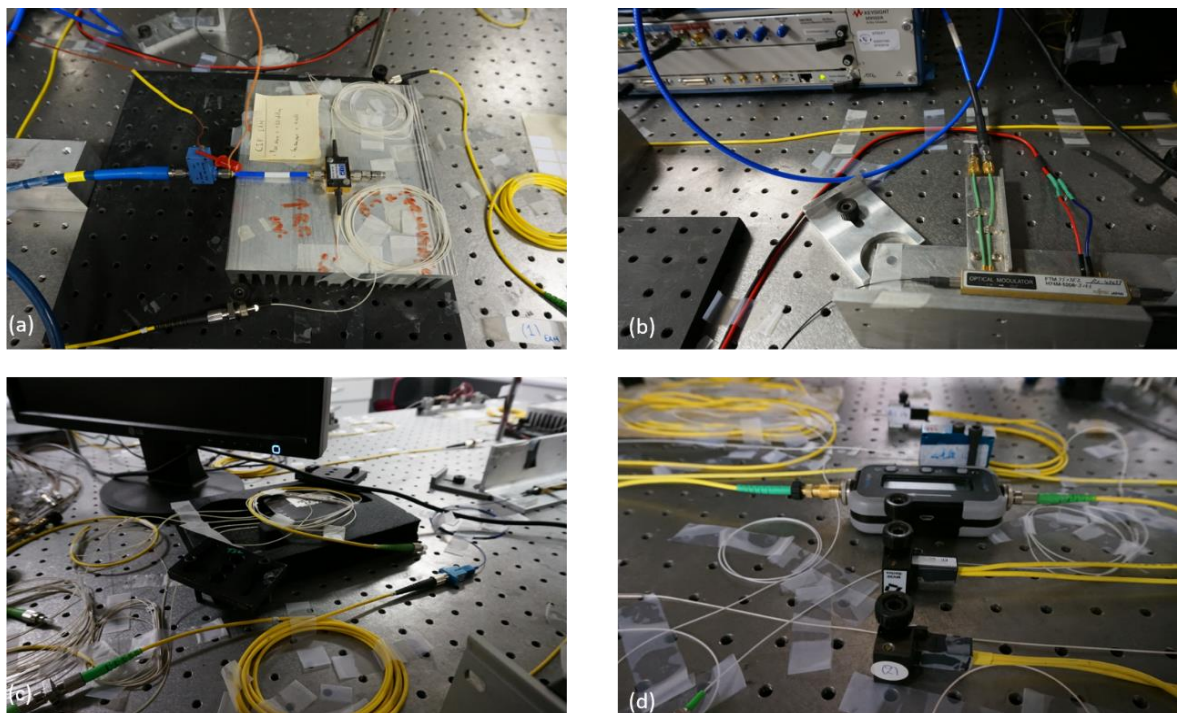


Figure 4.15: key optical components used in the experimental testbed. (a) Electro-absorption modulator, (b) Mach-Zehnder modulator, (c) Arrayed waveguide grating, and variable optical attenuators.

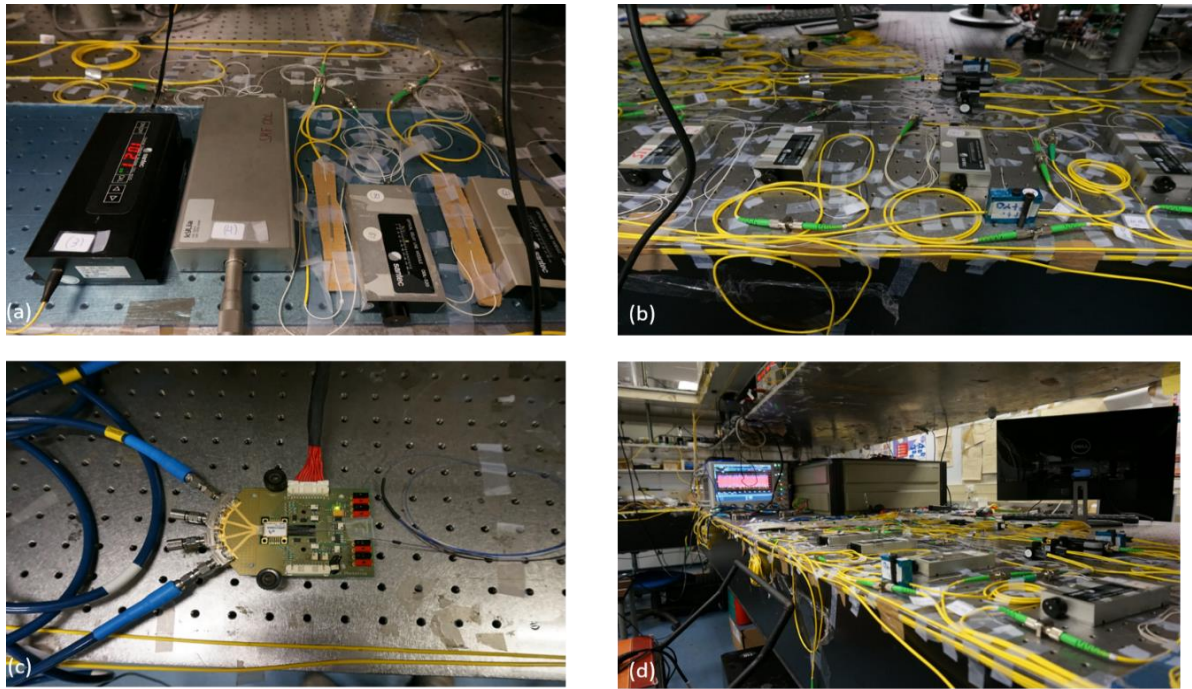


Figure 4.16: Key optical components of the experimental testbed. (a) and (b) Optical delay line arrays, (c) a dual photodetector, and (d) a general aspect of the experimental testbed.

Finally, Figure 4.15 and Figure 4.16 present indicative pictures of the experimental testbed and the key optical components that comprises it.

4.4 Automation of the reconfiguration process

The experimental setup has been further upgraded by automating the reconfiguration process of the ODLs which was a time-consuming process lasting in many cases several minutes. For this purpose, the micrometer heads of six ODLs, three of the ODL array that controlled the direction of the beam generated by the EAM and three from the second ODL array that controlled the direction of the beam generated by the MZM, were replaced by motorized actuators in the form of stepper motors. The other two ODLs, one of each ODL array, remained intact and acted as reference. Therefore, the reconfiguration of the direction of each beam was performed by tuning properly the relative delays between the reference ODL and the other three ODLs which were controlled by the stepper motors.

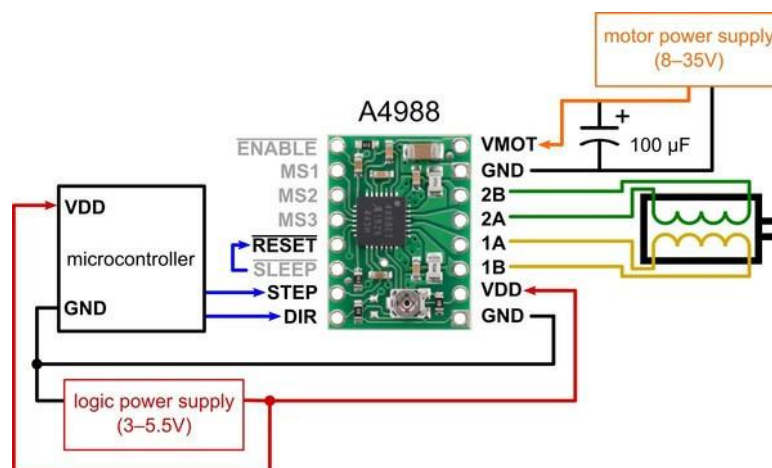


Figure 4.17: Wiring diagram for connecting the Raspberry Pi 3 Model B+ microcontroller to the stepper motor, utilizing an A4988 stepper motor driver carrier.

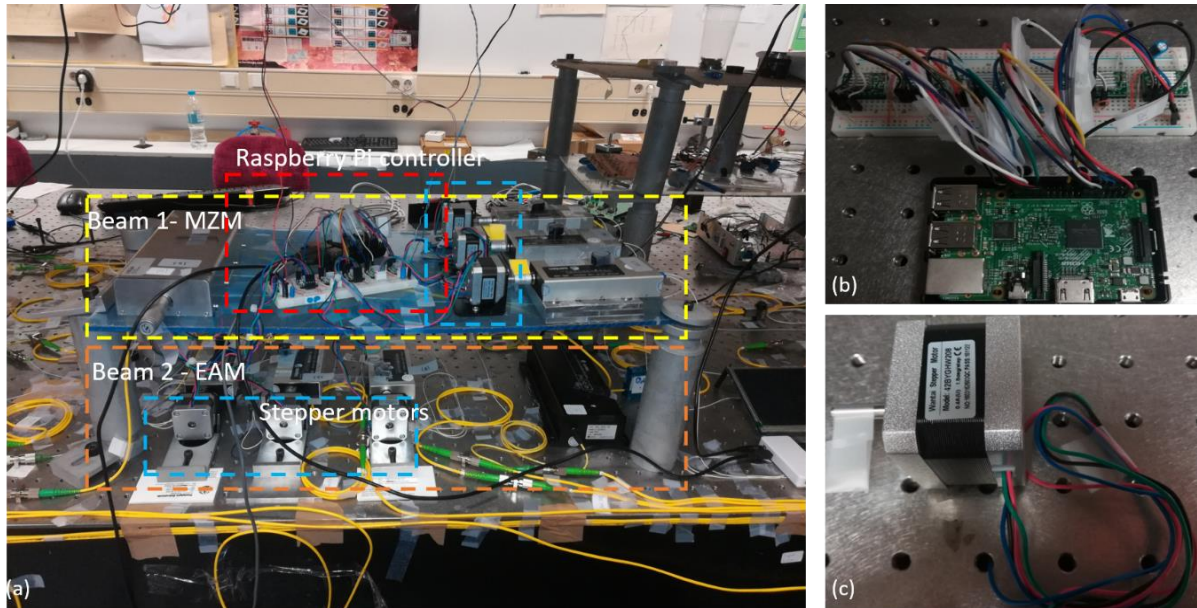


Figure 4.18: (a) Aspect of the experimental setup after automating its reconfiguration procedure, (b) picture of the Raspberry Pi microcontroller and the corresponding electrical driver circuits and (c) a zoom in picture of a stepper motor.

The stepper motors have an angle resolution equal to 1.8 degrees while its holding torque is equal to 2.8 kg.cm. The rotation of the axes of the stepper motors was controlled by six Pololu A4988 stepper motor drivers [1]. These driver units generated the proper enabling signals that controlled the direction and the angle of the rotating axis and thus the induced time delay on the propagating optical signals through the ODLs. Additionally, the stepper motor drivers were controlled by a Raspberry Pi 3 Model B+ [2]. The Raspberry Pi 3 Model B+ is equipped with a 64-bit quad core processor running at 1.4 GHz and 1 GB LPDDR2 SDRAM. This powerful microcontroller was programmed in a Python environment to receive as input the targeted direction as well as the operating microwave frequency of each beam by an end-user, to calculate the time delays that should be applied by the ODLs taking into account their current status and finally, to define the angle steps and the direction each stepper motor. Additionally, the microcontroller could reset the status of the ODLs to their initial operating status and also tune the induced delay with a resolution of 1 ps independently for each ODL for calibration purposes.

The wiring scheme between the Raspberry Pi microcontroller, the drivers and the stepper motors is presented in Figure 4.17. More specifically, the RESET, the STEP and the DIR of each driver were controller by the microcontroller while the stepper motor was controller by

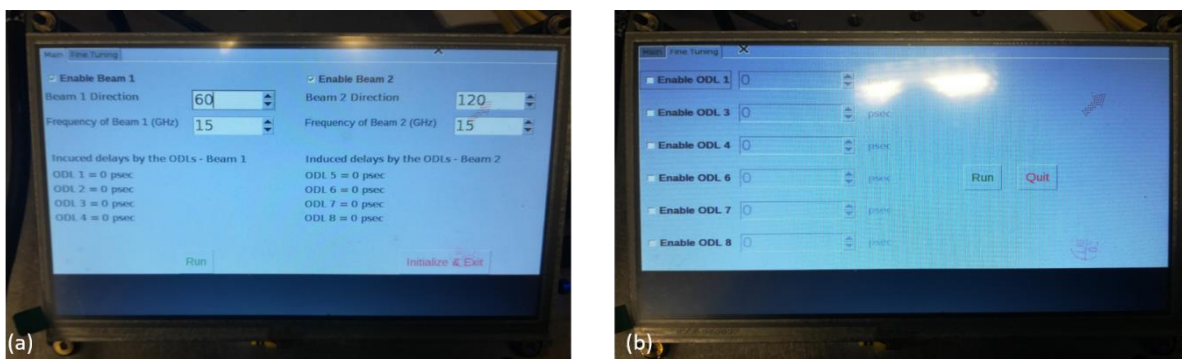


Figure 4.19: Pictures of the graphical user interface developed to facilitate the user to insert the information about the direction and the operating microwave frequency of each beam.

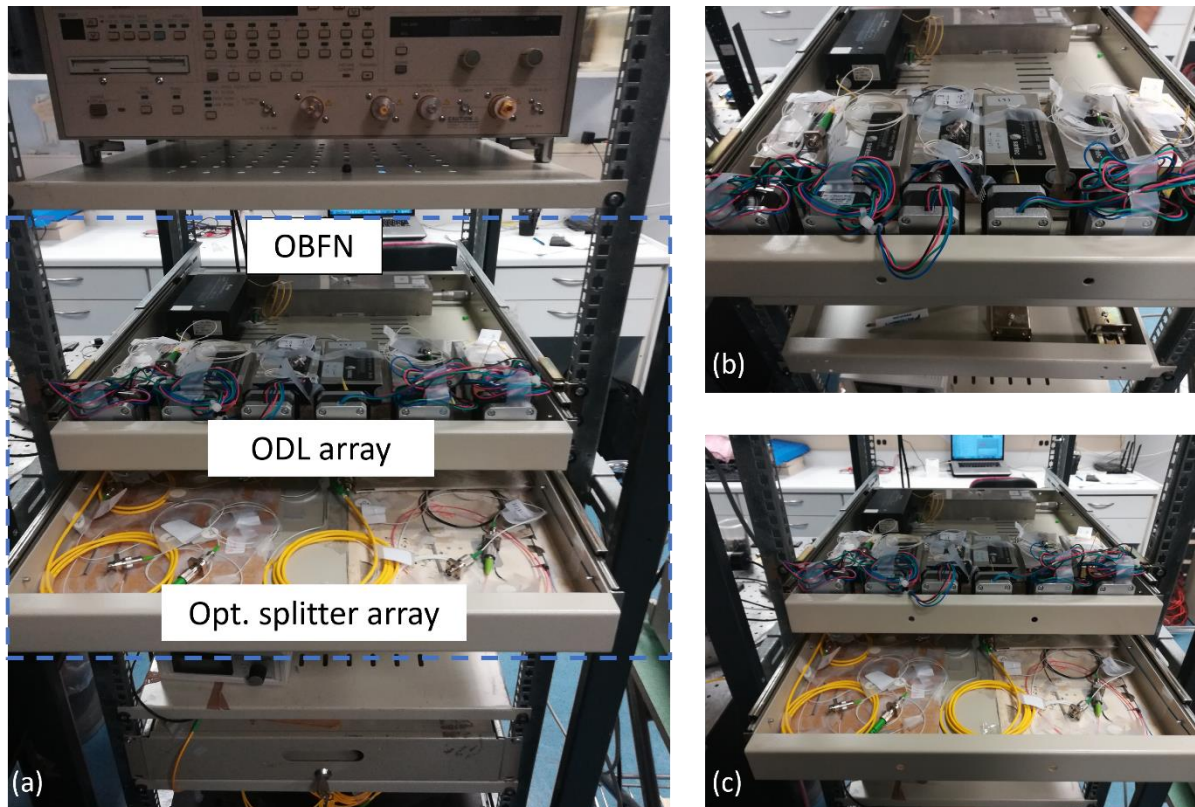


Figure 4.20: Images of the rack-based testbed which will host the whole OBFN. In total three shelves will be used and will host successively the optical splitters, the programmable ODLs, the VOAs and the optical couplers.

four enabling signals provided by the driver (2B, 2A, 1B, and 1A). Figure 4.18(a) presents a picture of the upgraded experimental testbed that supported the automated reconfiguration process. Figure 4.18 (b) and (c) depict the Raspberry Pi microcontroller coupled to the array of the stepper motor drivers and a magnified picture of the stepper motor, respectively.

Moreover, in order to ease the configuration of the OBFN and make it more user-friendly, a 7-inch external touch screen was also used, equipped with a graphical user interface (GUI). The user can enable or disable the beams and set the steering angle of each beam by simply defining the desired direction and the operating microwave frequency. In addition, the user can separately tune each ODL if this was necessary, as shown in Figure 4.19.

As it is presented in Figure 4.16 and Figure 4.19, initially, the experimental testbed was extended over a wide surface of an optical table since the reconfiguration of the ODLs was performed manually and therefore direct access to these optical devices was required. However, after the automation of this procedure, this requirement was eliminated and so, the experimental testbed was mounted on metallic rack occupying three shelves (3U), resulting in a very compact form. Figure 4.20 presents indicative pictures of the first two shelves that host the optical splitters and the array of the ODLs.

4.5 Experimental performance evaluation for single-beam beamforming

Following the theoretical validation of the proposed optical beamforming network for different operating modes (single-beam, multi-beam, and multicast) and the preparation of the experimental testbed, the next step involves the experimental validation of its principle of operation utilizing modulated microwave signals. Table 5 summarizes the cases that have been experimentally investigated in case of single-beam operation and presents the selected modulation format, the intended steering angle as well as the amplitude apodization scheme of the beam.

For the purposes of this measurement campaign, only the MZM was utilized since the scope of this study was to experimentally validate the inherent capability of the proposed OBFN to support beam steering from 40° to 140° for microwave signals modulated at 15 GHz with QPSK and 16-QAM modulation formats and symbol rates at 1 Gbaud. The evaluation of the OBFN was performed by calculating the BER of the demodulated microwave signals after the photodetection stage. The optical power of the signals incident to the photodiode array was varied from 0 dBm down to -14 dBm with a step of 2 dB.

Table 5: Experimental use cases in single-beam beamforming

Case no.	Beam 1 modulation format	Beam 1 steering angle	Symbol rate (Gbaud)	Amplitude apodization function
1	QPSK/16-QAM	140°	1	Uniform
2	QPSK/16-QAM	120°	1	Uniform
3	QPSK/16-QAM	105°	1	Uniform
4	QPSK/16-QAM	90°	1	Uniform
5	QPSK/16-QAM	75°	1 <td Uniform	
6	QPSK/16-QAM	60°	1	Uniform
7	QPSK/16-QAM	40°	1	Uniform

Figure 4.21 presents as an indicative example of the polar diagram of the for the second experimental case and the constellation diagrams of the two decoded signals at 120° and 40° for -3 dBm received optical power at each one of the four PD.

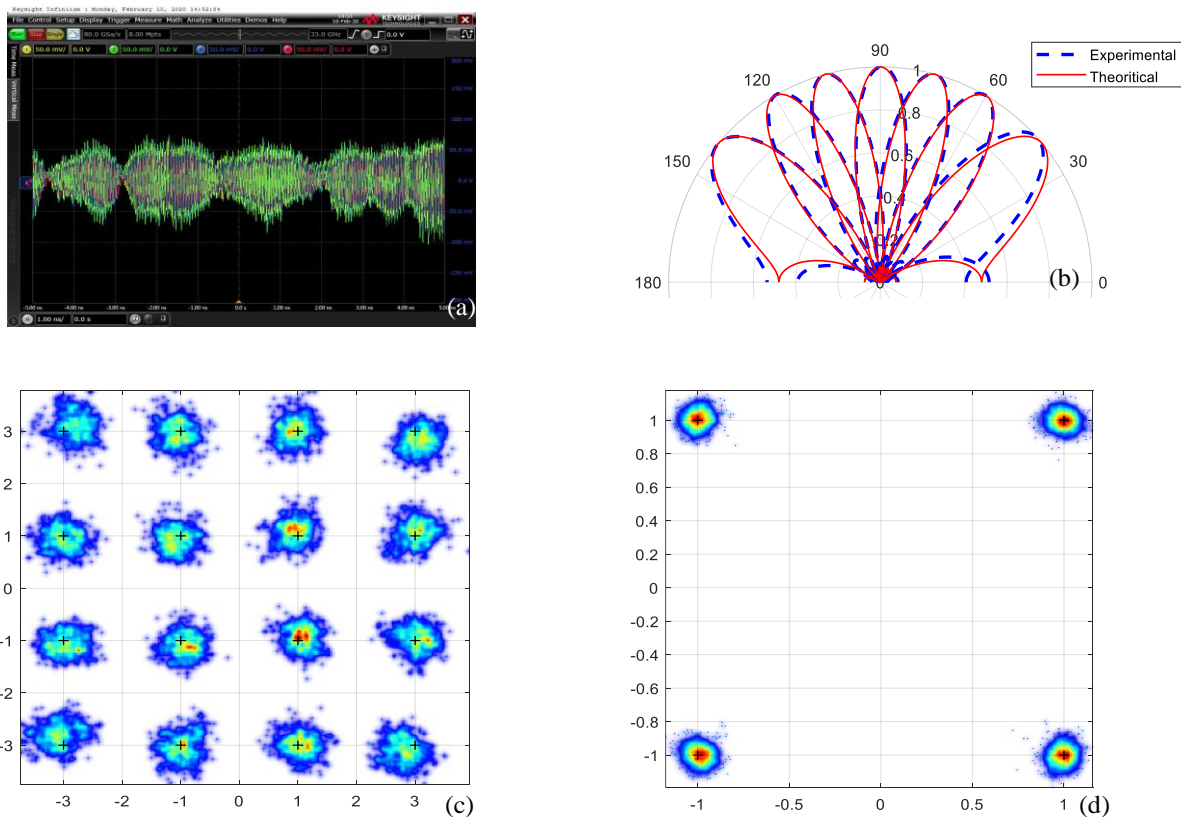


Figure 4.21: (a) Screenshot captured at the real-time oscilloscope presenting the four 16-QAM electrical signals with 1 Gbaud symbol rate after the photodetection stage for case 2. (b) Polar diagrams for all the cases operating with microwave signals with central frequencies at 15 GHz, (c) and (d) indicative constellation diagrams of the demodulated signals of case 6 and with modulation format 16-QAM and QPSK, respectively.

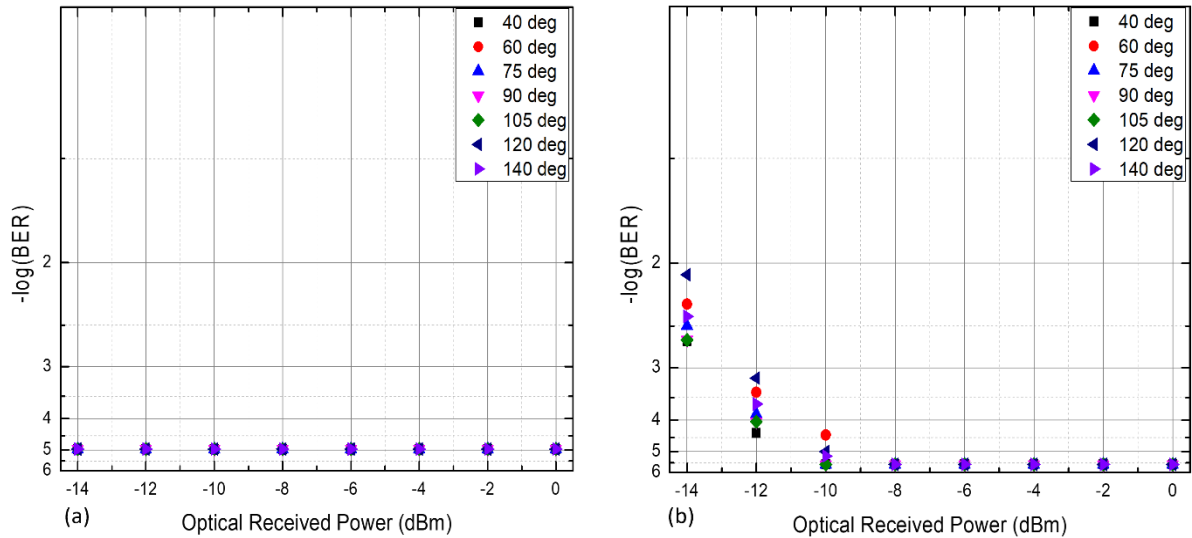


Figure 4.22: BER curves for all the experimental cases operating (a) with QPSK and (b) 16-QAM modulation formats.

Figure 4.22 depicts the BER curves for all the experimental cases with regards to the optical received power of the signal incident to the photodiodes. As observed, for all the experimental cases, an error free performance was achieved. More specifically, for the case of operating with QPSK modulation format, the BER curves of the decoded signals remained flat independently of the optical received power for all the different steering angles. On the other hand, in case of operating with 16-QAM modulation format, the BER curves remained below 10^{-3} for optical received powers down to -12 dBm. The increase of BER values for higher values is due to the decrease of the SNR of the detected electrical signals. Moreover, it should be noted that the BER should be in principal independent of the targeting steering angle as in the demodulation stage of the microwave signals, four ideal isotropic antennas had been considered which emits uniformly in all directions.

4.6 Experimental performance evaluation for multi-beam beamforming

Table 6 outlines the cases that have been experimentally investigated in case of multi-beam operation and summarizes the modulation format, the intended steering angle and the excitation type for each one of the two beams. Figure 4.23 presents as an example the polar diagram of the calculated microwave field for the second experimental case and the constellation diagrams of the two decoded signals at 120° and 45° for -3 dBm received optical power at each one of the four PD.

Table 6: Experimental use cases in multi-beam beamforming

Case no.	Beam 1 modulation format	Beam 2 modulation format	Beam 1 steering angle	Beam 2 steering angle	Symbol rate (Gbaud)	Amplitude apodization function
1	QPSK	16-QAM	135°	60°	1/0.5	Uniform/Gaussian
2	QPSK	16-QAM	120°	45°	1/0.5	Uniform/Gaussian
3	QPSK	16-QAM	75°	150°	1/0.5	Uniform/Gaussian
4	QPSK	16-QAM	60°	105°	1/0.5	Uniform/Gaussian

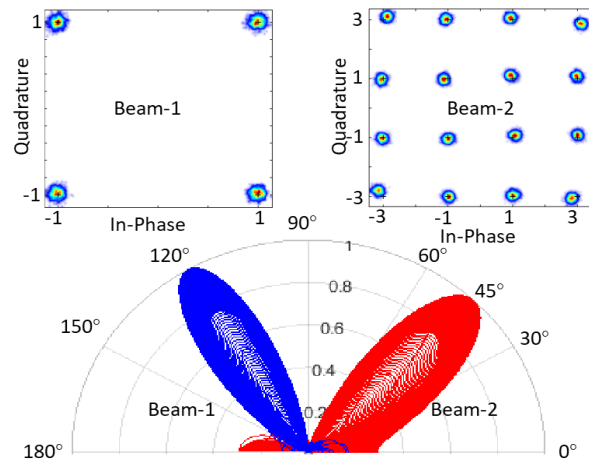


Figure 4.23: (Bottom) Polar diagram of the second experimental case assuming a linear antenna array with 4 omnidirectional AEs. (Top) The corresponding constellation diagrams of the two beams for -3 dBm received optical power.

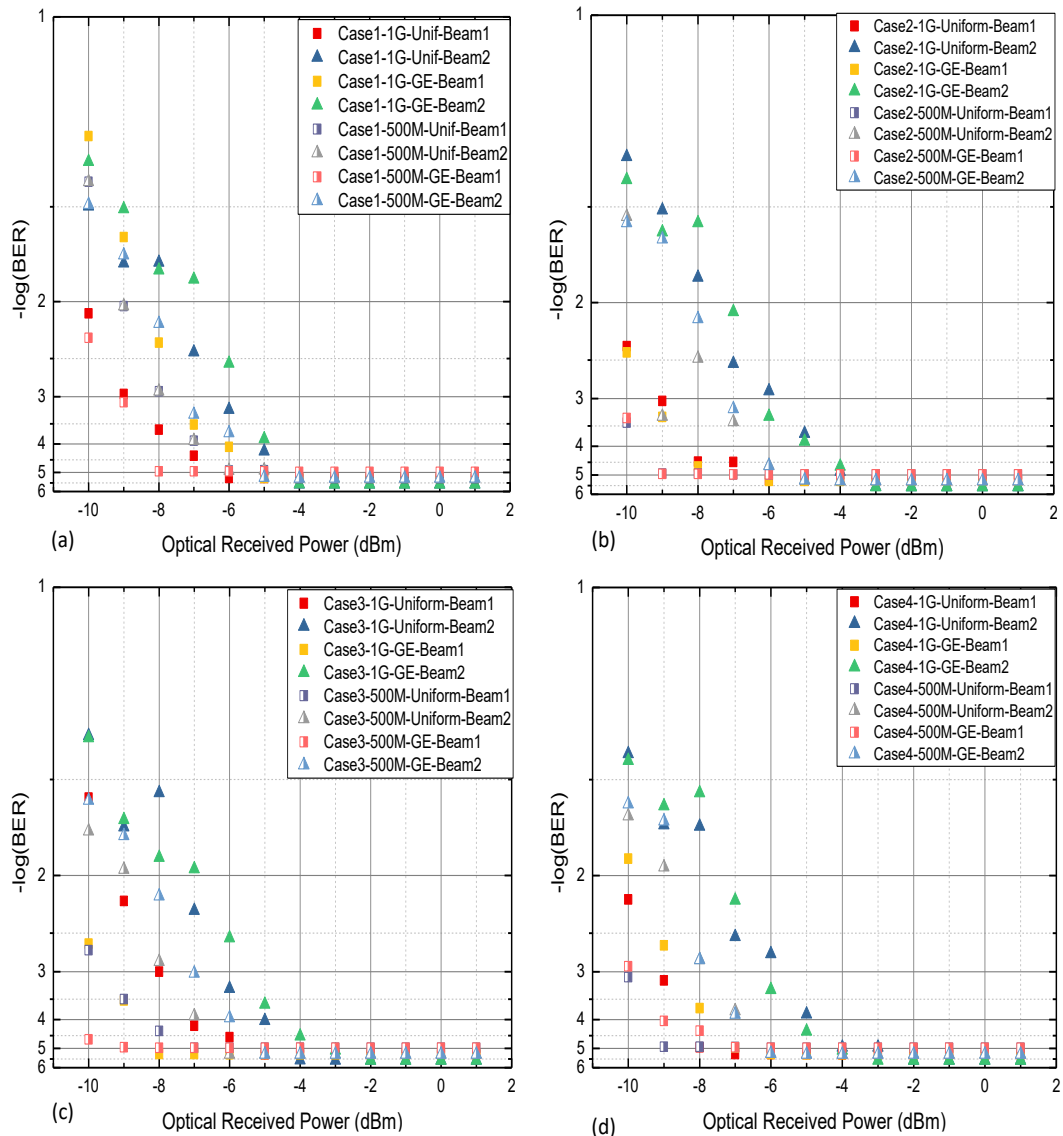


Figure 4.24: (a) – (d) BER curves as a function of the optical received power at the photodiode array in case of operating the 2×4 OBFN in multi-beam operation for the experimental cases 1, 2, 3, and 4 of Table 6, respectively.

Figure 4.24 summarizes the BER measurements for all investigated cases as a function of the received optical power at the PDs of the setup. As observed, in all cases the BER of the decoded signals at the intended angles can easily get below 10^{-3} for received optical power higher than the -5 dBm, validating the intrinsic potential of the proposed OBFN architecture for multi-beam operation. Additionally, in all experimental cases, the BER curves that correspond to the signals with 1 Gbaud symbol rate are higher than the corresponding BER curves of the signal with 500 Mbaud symbol rates. This is absolutely consistent with the theory since as the symbol rate of a signal is increased higher SNR is required to achieve a specific BER value.

4.7 Experimental performance evaluation for multicast beamforming

Table 1 outlines the cases that have been experimentally investigated summarizing the modulation format and the intended steering angles. Figure 5 summarizes the corresponding BER measurements for all cases with respect to the optical received power before the photodetection stage, as well as the reference BER measurements when each signal is transmitted individually to one steering angle (single-beam operation). As observed, in all cases, the BERs remain below 10^{-3} for received optical power higher than -4 dBm, validating the potential of this OBFN architecture for multicast operation. Especially when transmitting a QPSK signal, the degradation imposed on the signal due to the coexistence of multiple beams remains negligible, validating the OBFN's proof of concept.

Table 7: Experimental Use Cases in Multicast beamforming

Case index	Modulation format	Steering angles	Apodization function
1a	QPSK	[75°, 140°]	[Gaussian, Gaussian]
1b	16-QAM	[75°, 140°]	[Gaussian, Gaussian]
2a	QPSK	[40°, 90°, 140°]	[Gaussian, Uniform, Gaussian]
2b	16-QAM	[40°, 90°, 140°]	[Gaussian, Uniform, Gaussian]

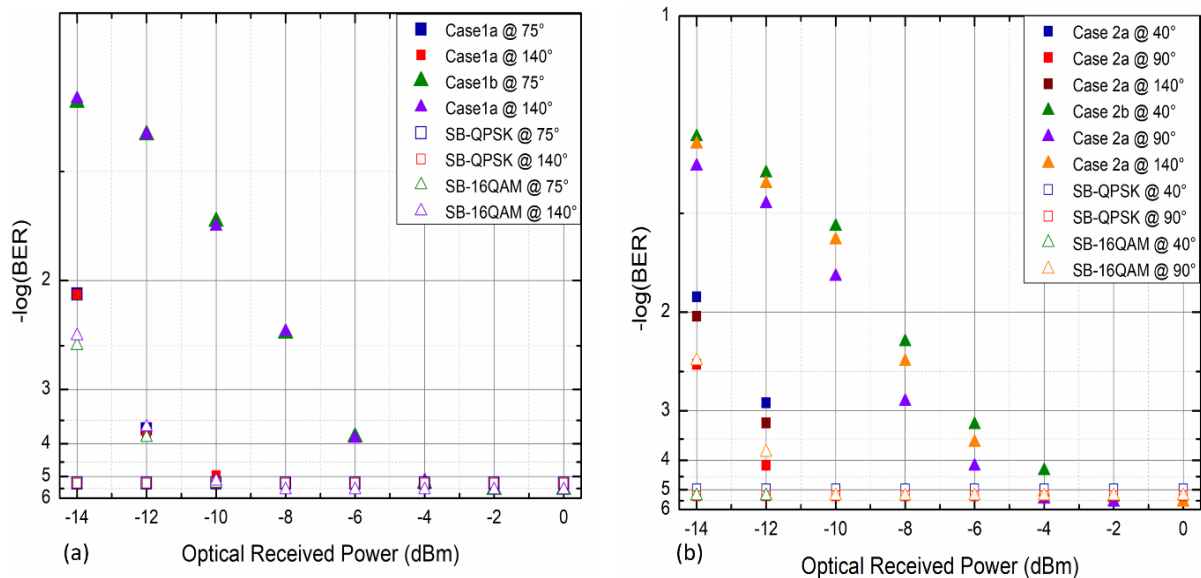


Figure 4.25: (a) and (b) BER curves as a function of the optical received power at the photodiode array in case of operating the 2×4 OBFN in multicast operation for the experimental cases 1a, 1b and 2a, 2b of Table 2, respectively.

Conclusions of Chapter 4

In this chapter, an OBFN architecture that can support single-beam, multi-beam and multicast operation with continuous tuning of the beam angles was proposed. The architecture is based on a number of ODLs for introduction of time delays to the copies of the signals that correspond to different wireless beams and different AEs. First, its principle of operation was validated through extensive simulation studies, indicating that an error-free operation for all three modes is feasible for microwave signals at 15 GHz carrying QPSK and 16-QAM modulation formats at 1 Gbaud symbol rates and with different apodization schemes. Subsequently, a 2×4 TTD-OBFN was developed using commercial off-the-shelf optical modulators, optical delay lines, optical attenuators, optical couplers and photodiodes. The OBFN architecture was capable of forming up to two beams and feeding up to four AEs and has been operated in the downlink direction using as inputs optical signals that are modulated by 15 GHz microwave signals with QPSK and 16-QAM formats and symbol rates equal to 0.5 and 1 Gbaud. The processing of the electrical signals at the output of the OBFN, the calculation of the expected radiation patterns, and the BER measurements of the decoded signals at the intended beam angles validated the potential of the proposed OBFN architecture for single-beam, multi-beam and multicast beamforming operation with broadband wireless signals.

The scalability is undoubtedly an important parameter of an OBFN architecture for its use in practical applications. Our OBFN architecture follows the expected scaling laws: in the downlink direction requires a number of laser diodes and optical modulators equal to the number of the independent beams, a number of photodiodes equal to the number of the antennas elements, and a number of ODLs and optical attenuators equal to the product of the independent beams times the number of the antenna elements. In the uplink direction, it requires a number of laser diodes and optical modulators equal to the number of the antenna elements, a number of photodiodes equal to the number of the independent beams, and a number of ODLs and optical attenuators equal to the product of the independent beams times the number of the antenna elements. The implementation of the setup using bulk optical components increases the size, weight and cost of the OBFN and limits its practical potential to scale to large beam numbers and large antenna arrays. However, photonic integration technology can enable the replacement of the bulk components by photonic integrated circuits, which can enable in turn significant reduction in the size, weight and cost of the OBFN and significant increase in the scale of the OBFN (in terms of number of optical components, and thus in terms of accommodated beams and antenna elements). Leveraging the recent technology advancements of the photonics integrated circuit technology, the following chapters present integrated OBFN architectures that can support continuous tuning of the beam angles and can be efficiently scaled to support several antenna elements.

References of Chapter 4

- [1] <https://grobotronics.com/stepper-motor-42byghw208-2.6kg.cm.html>
- [2] <https://www.raspberrypi.org/products/raspberrypi-3-model-b/>
- [3] <https://www.pololu.com/product/1182>

Chapter 5 - A 1×4 fully integrated true time delay optical beamforming network based on tunable micro-ring resonators

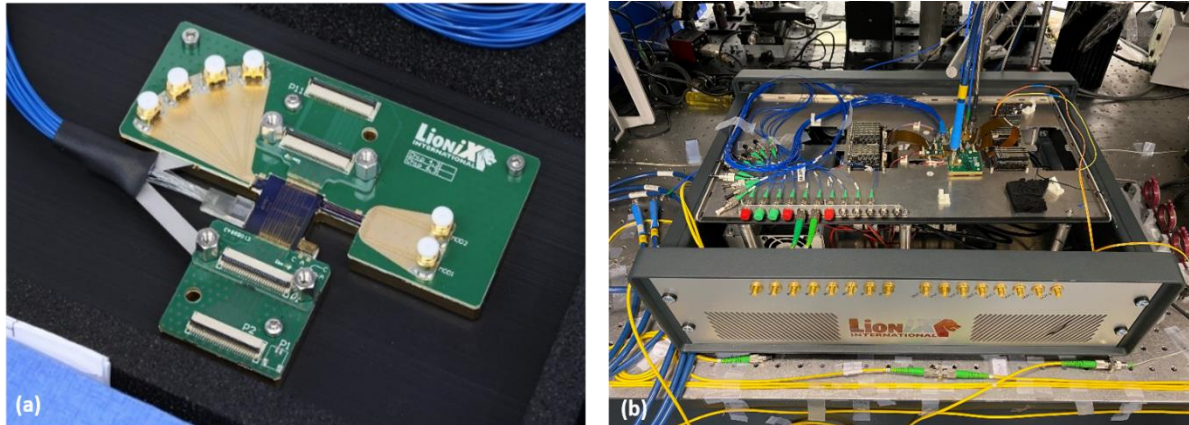


Figure 5.1 Picture of the (a) 1×4 InP-TriPleX OBFN-PIC and (b) assembled OBFN-PIC with the driving electronics.

In this chapter, a fully integrated 1×4 TTD-OBFN on the InP and TriPleX platforms is presented and experimentally evaluated. It can support the generation and steering of a single microwave beam with central frequencies up to 40 GHz over a continuous set of angles. The integrated InP components are a pair of high-speed phase modulators and a quad array of photodetectors, whereas the TriPleX platform hosts a single-sideband full carrier optical (SSBFC) filter and four OTTDLs with thermally tunable MRRs. Moreover, a high-power external cavity laser is also part of the PIC consisting of an InP gain section and an external cavity in the TriPleX part of the circuit. Figure 5.1 illustrates the packaged OBFN-PIC as well as the electronic driving units. It is of 16 mm × 19 mm size, and includes 21 fiber pigtailed, 6 RF connectors, and four connectors for flat electrical cables to control the 79 heating electrodes of the circuit.

5.1 Photonic integration platforms and key optical components

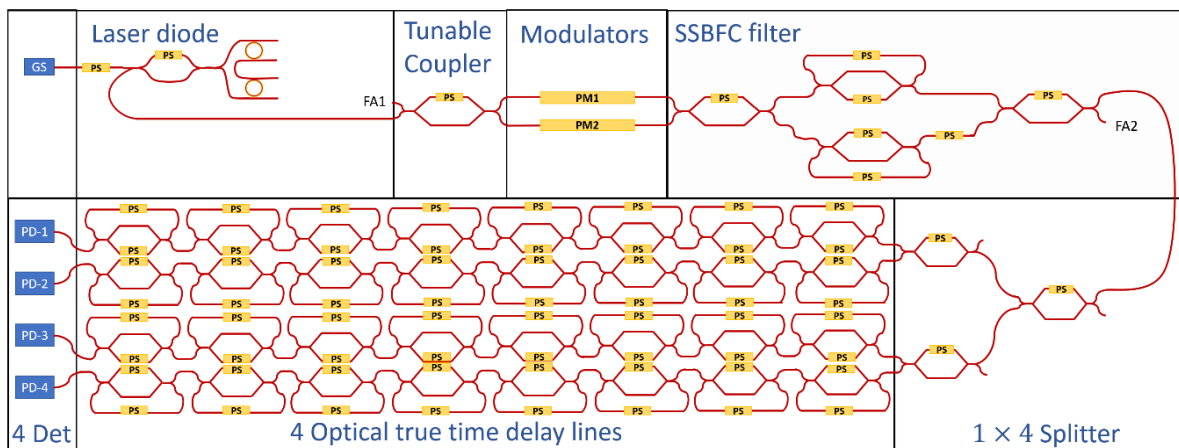


Figure 5.2 : Layout of the fully hybrid integrated 1×4 OBFN-PIC. It comprises a hybrid InP-TriPleX external cavity laser, two InP phase modulators, a TriPleX SSBFC filter followed by a 1×4 splitter, and four OTTDLs based on 8 MRRs each, and four InP photodetectors

The schematic of the 1×4 OBFN-PIC is presented in Figure 5.2. By combining two powerful and complementary photonic integration platforms, i.e., the TriPleX and InP, the optical chip accommodates a fully functional MWP system including a continuous tuning

TTD-OBFN. The following paragraphs present the main characteristics and key integrated optical components of the two PIC platforms.

5.1.1 TriPleX platform

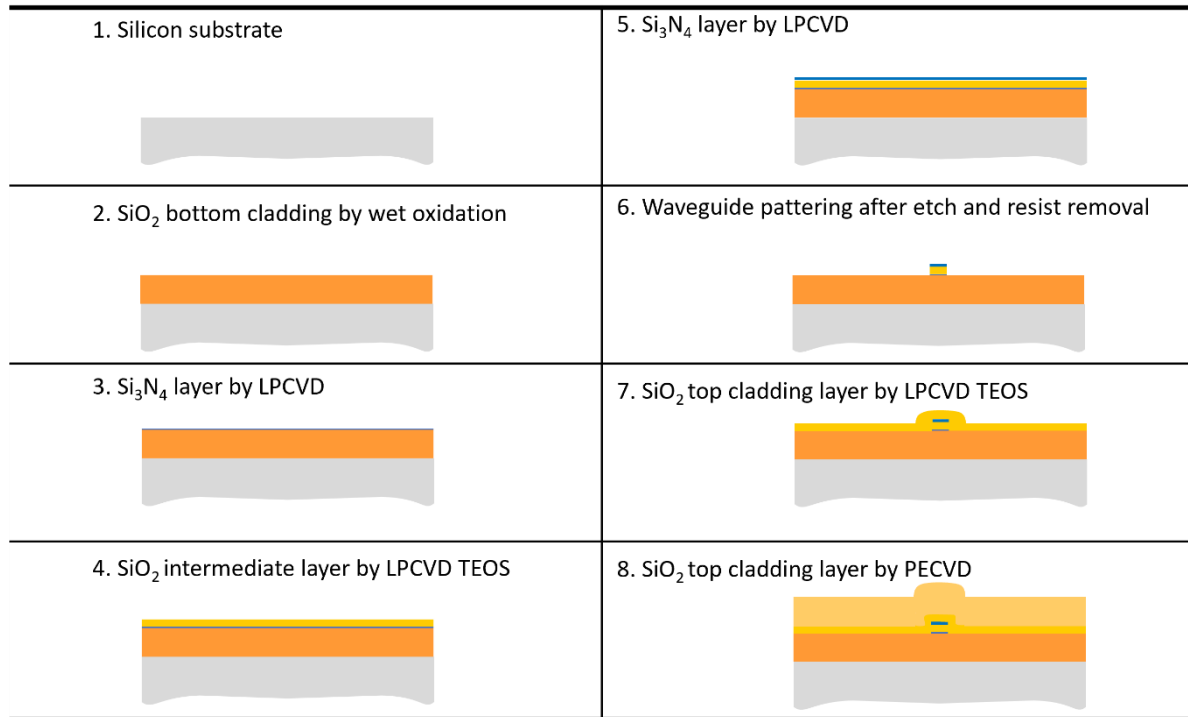


Figure 5.3: Generic process flow for the fabrication of the ADS waveguide geometry [1].

TriPleX platform includes a family of waveguide geometries that is based on an alternating layer stack consisting of two materials: Si₃N₄ (silicon nitride) and SiO₂ (silicon dioxide) that have refractive indices of about 1.98 and 1.45, respectively, at 1.55 μm wavelength [1]. Most commonly used substrate is a single crystal silicon, for some applications fused silica glass substrates have been used too. Thanks to its versatility, TriPleX can accommodate different waveguide geometries such as the box shell, single-stripe, symmetric double-stripe, and asymmetric double-stripe (ADS) [1].

In our specific prototype the ADS waveguide geometry has been selected. The ADS consists of two parallel stripes of Si₃N₄ with different thickness at the top on top of each other, separated by an intermediate SiO₂ layer. The lower Si₃N₄ layer of the ADS geometry allows for optimization of coupling to external components such as fibers and/or active materials without adjusting its thickness, while the upper Si₃N₄ stripe thickness can be optimized for a target bending radius and is removed completely (tapered down to zero thickness) elsewhere in the circuit. The thickness for the upper Si₃N₄ stripe of 175 nm has been chosen to give the ADS geometry an effective index of 1.535, a group index of 1.77 and a mode-field size equal to $MFD_{x \times y} = 1.5 \times 1.2 \mu\text{m}$. Compared to the single-double stripe waveguide geometry, the ADS requires less fabrication steps, going with higher yield and even better optical characteristics. Propagation loss values on ADS waveguides are reproducibly measured equal to 0.1 dB/cm.

The general process flow is presented schematically in Figure 5.3. The highest quality SiO₂ layer results from wet thermal oxidation of single-crystal silicon substrates to create an SiO₂ layer (steps 1, 2), typically at temperatures equal to or above 1000 °C. Low-pressure chemical vapor deposition (LPCVD) is used for the Si₃N₄ layers and, where thermal oxidation is not applicable, also for the SiO₂ layer. For the latter process, the gas tetraethylorthosilicate (TEOS) is used. LPCVD deposition results in high quality layers,

shows very good layer uniformity, both in thickness and in refractive index, good step coverage because of conformal growth, and the layer is deposited on both sides of the substrate at the same time (step 3, 4, 5, and 7). The top cladding thicknesses is deposited using another deposition technique: plasma-enhanced chemical vapor deposition (PECVD). Typical deposition temperatures are between 300 °C and 400°C. This growth technique is directional, and as the substrate has to lie down on a bottom electrode (for the generation of the plasma), this type of film is deposited on one side of the substrate. Besides the optical quality and the surface roughness of the used deposition techniques, another factor that is important for low-loss propagation of light is the sidewall roughness or line edge roughness, which is determined by the details of the photolithographic process and the etching technique that is used for the waveguide definition (steps 6) [2]. Thanks to the low roughness of Si₃N₄ waveguides, a wide variety of optical components can be designed and integrated in the platform. The paragraphs below describe principle of operation of the optical components that have been integrated in the PIC.

MZI based tuneable coupler:

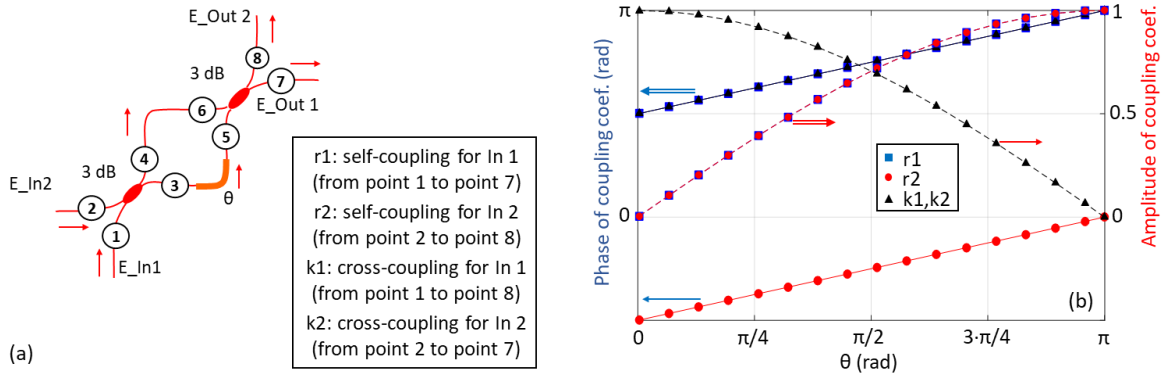


Figure 5.4: (a) Layout of the MZI, serving as coupler inside the Blass matrix, and definition of its coupling coefficients and (b) dependence of the phase and amplitude of the self- and cross-coupling coefficients of the MZI as a function of the phase shift θ in the lower arm.

The routing of the optical signals in the PIC is performed utilizing MZI-based tuneable couplers. We take as an example the MZI shown in the example of Figure 5.4 which has a phase shifter in its lower arm and we assume that an optical field E_{In1} with a single optical frequency f_0 and amplitude E_0 enters the MZI from the first port (point 1). The first 3-dB coupler splits this field into two parts that appear at points 3 and 4. The fields propagate along the two arms, arrive at points 5 and 6, and they are combined coherently at the second 3-dB coupler. Using phasors for this representation, and assuming that the length of the two arms is exactly the same, the optical fields at the first and the second output port of the MZI (points 7 and 8, respectively) can be represented as:

$$E_{Out1} = \frac{E_0}{2} [\exp(j \cdot \theta) - 1] \quad (5.1)$$

$$E_{Out2} = \frac{E_0}{2} \exp\left(j \cdot \frac{\pi}{2}\right) \cdot [\exp(j \cdot \theta) + 1] \quad (5.2)$$

where φ_1 the phase shift, which is applied to the propagating field by the phase shifter inside the upper arm of the MZI. By taking the ratio of these fields over the input field, we derive the expressions of the self-coupling (r_1) and the cross-coupling coefficient (k_1) in the case of input from the first input port (point 1).

$$r_1 = \frac{1}{2} [\exp(j \cdot \theta) - 1] \quad (5.3)$$

$$k_1 = \frac{1}{2} \exp\left(j \cdot \frac{\pi}{2}\right) \cdot [\exp(j \cdot \theta) + 1] \quad (5.4)$$

Making the same calculations in the case of input from the second input port (point 2), we derive again the output fields at points 8 and 7, and thus the corresponding self-coupling (r_2) and cross-coupling coefficient (k_2) in this second case:

$$r_2 = \frac{1}{2} \cdot [1 - \exp(j \cdot \theta)] = -r_1 \quad (5.5)$$

$$k_2 = \frac{1}{2} \cdot \exp\left(j \cdot \frac{\pi}{2}\right) \cdot [\exp(j \cdot \theta) + 1] = k_1 \quad (5.6)$$

As observed in the equations (5.3) – (5.6), the sign of the self-coupling coefficient of the MZI depends on the input port, whereas the cross-coupling coefficient remains the same in either case. Figure 5.4 (b) presents the plots of the amplitude and the phase of the self- and cross-coupling coefficients in the two cases as a function of the phase shift θ in the lower arm of the MZI and reveals the interrelation of these parameters. As θ increases from 0 to π rad, the amplitude of the self-coupling coefficients increases from 0 to 1, whereas the amplitude of the cross-coupling coefficients drops from 1 to 0. Provided that the MZI can be considered as lossless, the sum of the squares of the amplitudes is equal to 1 for both pairs of self- and cross-coupling coefficients and for every value of θ :

$$|r_1|^2 + |k_1|^2 = 1 \text{ and } |r_2|^2 + |k_2|^2 = 1 \quad (5.7)$$

On the other hand, as θ increases from 0 to π rad, the phase of the first self-coupling coefficient (r_1) and the phases of the two cross-coupling coefficients increase in a linear way from $\pi/2$ to π rad, while the phase of the second self-coupling coefficient trails behind by π rad. From a practical point of view, the extinction ratio (ER) of the optical power between the two output ports cannot be infinitely large, implying that the self- and cross-coupling coefficients of the MZI cannot be extremely close to 0 or 1. Assuming again that the input optical field enters the MZI from the first input port, the ER can be defined as:

$$ER = 10 \cdot \left(\frac{|r_1|^2}{|k_1|^2} \right) \quad (5.8)$$

Taking a typical ER limit of 27 dB and working with (5.7) and (5.8), the maximum value of $|r_1|$ and the minimum value of $|k_1|$ are found to be close to 0.999 and 0.045, respectively. It is noted that the same maximum and minimum values apply to $|k_1|$ and $|r_1|$ in the opposite way, if the input signal is switched to the other output port, as well as to the second pair of coupling coefficients $|r_2|$ and $|k_2|$, if the input signal enters the MZI from the second input port.

Asymmetric Mach-Zehnder interferometer: A well-known waveguide-based optical filter is the asymmetric Mach-Zehnder interferometer (aMZI), shown in Figure 5.5. In an aMZI, the incoming signal is split into paths thanks to the first tunable coupler. In an aMZI, the incoming signal is split into paths thanks to the first tunable coupler. As it is analyzed in the previous paragraph, the transfer function of the tunable coupler can be expressed as follows:

$$H_{TC,1} = \begin{bmatrix} r_1^1 & k_1^1 \\ k_2^1 & r_2^1 \end{bmatrix} \quad (5.9)$$

, where the coupling coefficients $r_1^1, k_1^1, r_2^1, k_2^1$ are given by the equations (5.3)-(5.6).

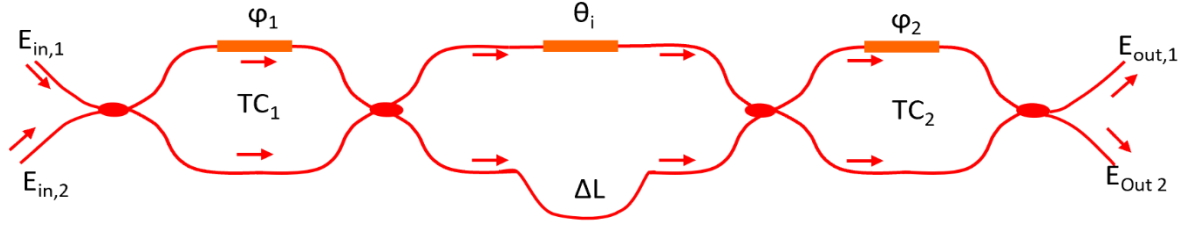


Figure 5.5: Layout of an asymmetric Mach-Zehnder interferometer, designed with ΔL path length difference between the upper and the lower branches.

The output ports of the first tuneable coupler are connected to a second tuneable coupler through two optical paths. The signal propagating into the bottom path is delayed with respect to the other by a time delay expressed as:

$$T_d = \Delta L \cdot \frac{n_g}{c} \quad (5.10)$$

, where n_g is the group refractive index of the optical waveguide, c the velocity of light in vacuum and, ΔL the path length difference. On the other hand, into the upper path an optical phase shifter is integrated to control the phase of the propagating signals. The transfer matrix of the two paths can be written as follows:

$$H_{\text{paths}} = \begin{bmatrix} \exp(j \cdot \theta) & 0 \\ 0 & \alpha \cdot \exp(j \cdot 2\pi \cdot \nu \cdot T_d) \end{bmatrix} \quad (5.11)$$

, where θ is the induced phase by the phase shifter at the upper branch and α is the transmission coefficient considering the loss along the differential path. The signals propagating into the two paths are coherently combined through a second tuneable coupler with a transfer function expressed as:

$$H_{\text{TC},2} = \begin{bmatrix} r_1^2 & k_1^2 \\ k_2^2 & r_2^2 \end{bmatrix} \quad (5.12)$$

, where similarly to the first tuneable coupler, the coupling coefficients r_1^2 , k_1^2 , r_2^2 , k_2^2 are given by the equations (5.3)-(5.6). The coherent interference of the two signals at the output ports of the second tuneable coupler leads to a sinusoidal frequency response. Its frequency spectral range (FSR) which is defined as the frequency distance of two adjacent resonances is inversely proportional to the path length difference. By combining equations (5.9) - (5.12) the transfer function of the aMZI shown in Figure 5.5 can be expressed as follows:

$$H_{\text{aMZI}} = H_{\text{TC},1} \cdot H_{\text{paths}} \cdot H_{\text{TC},2} \quad (5.13)$$

$$H_{\text{aMZI}} = \gamma \cdot \begin{bmatrix} r_1^1 & k_1^1 \\ k_2^1 & r_2^1 \end{bmatrix} \cdot \begin{bmatrix} \exp(j \cdot \theta) & 0 \\ 0 & \alpha \cdot \exp(j \cdot 2\pi \cdot \nu \cdot T_d) \end{bmatrix} \cdot \begin{bmatrix} r_1^2 & k_1^2 \\ k_2^2 & r_2^2 \end{bmatrix}$$

, where γ the coefficient taking into account the waveguide loss and the phase contribution of the common path. Therefore, the electrical field at the output of the second tuneable couplers can be expressed as follows:

$$\begin{bmatrix} E_{\text{out},1} \\ E_{\text{out},2} \end{bmatrix} = H_{\text{aMZI}} \cdot \begin{bmatrix} E_{\text{in},1} \\ E_{\text{in},2} \end{bmatrix} \quad (5.14)$$

Assuming $E_{\text{in},2} = 0$, the output electrical fields of the aMZI are expressed as:

$$\begin{bmatrix} E_{out,1} \\ E_{out,2} \end{bmatrix} = \begin{bmatrix} r_1^1 \cdot r_1^2 \cdot \exp(j \cdot \theta) + k_1^1 \cdot k_2^2 \cdot \alpha \cdot \exp(j \cdot 2\pi \cdot \nu \cdot T_d) \\ k_2^1 \cdot r_1^2 \exp(j \cdot \theta) + r_2^1 \cdot k_2^2 \cdot \alpha \cdot \exp(j \cdot 2\pi \cdot \nu \cdot T_d) \end{bmatrix} \cdot E_{in,1} \quad (5.15)$$

Figure 5.6 (a) presents an indicative transmission response of the two output ports of an aMZI, considering that the phase shifters of both tunable couplers are set to $\pi/2$, the phase shifter of the upper path set to 0, and neglecting the propagation loss ($\gamma=\alpha=1$). The aMZI introduces significant attenuation at the resonance frequencies which depends on the ER of the two tunable couplers. Under the same assumptions, Figure 5.6 (b) presents the phase responses of the electrical fields at the output ports. As it can be observed, an abrupt π phase shift is introduced at the resonance frequencies. The resonance frequencies are tuned by the phase shifter integrated into the upper path of the aMZI (θ). Figure 5.7 presents the equivalent transmission and phase spectra for $\theta = 0, \pi/4$, and $\pi/2$.

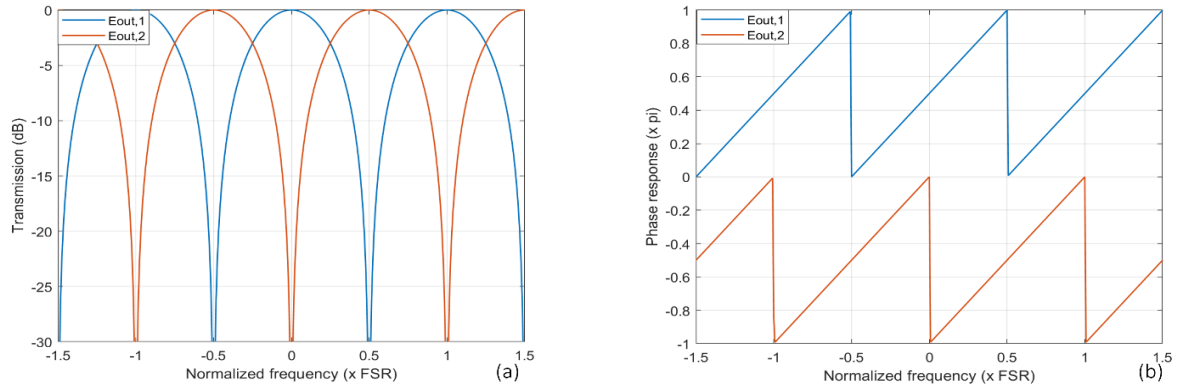


Figure 5.6: (a) Power transfer functions and (b) phase response of the two output ports of an aMZI with respect to the normalized frequency.

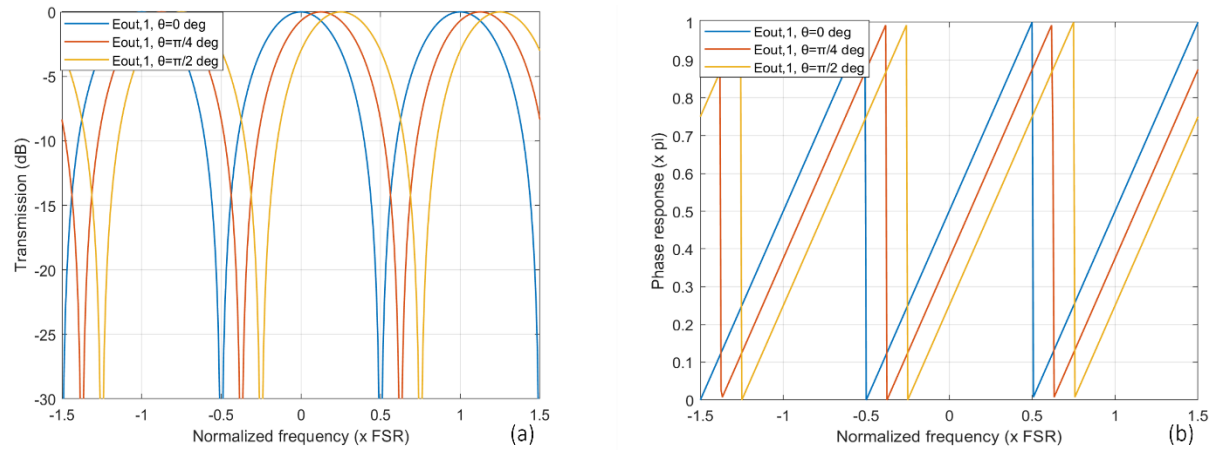


Figure 5.7: Power transfer functions and (b) phase response of the two output ports of an aMZI with respect to the normalized frequency and $\theta = 0, \theta = \pi/4$, and $\theta = \pi/2$.

Micro-ring resonator: Figure 5.8 illustrates a schematic of the thermo-optical tunable MRR. It is implemented as a balanced MZI, which one output port is fed back to the input port, forming a feedback loop mechanism. The operation of the MRR is controlled by two thermal phase shifters, which reside in one of the arms of the MZI and in the feedback loop waveguide, respectively. The phase shifter in the MZI arm controls the self- (r) and cross-coupling coefficient (k) of the MZI, as already described in paragraph 5.1.1.2 and thus the power of the optical signal coupled to the feedback loop waveguide, whereas the second phase shifter controls its optical phase (φ). The feedback loop waveguide couples the output field E_{out2} back to the input port (2).

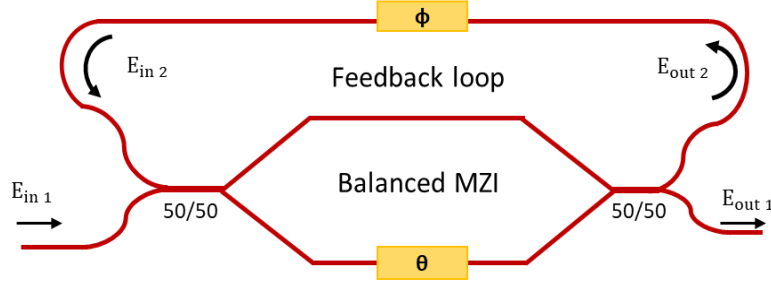


Figure 5.8: Layout of a micro-ring resonator, implemented as a balanced MZI.

The relation between the E_{out2} and E_{in2} is given by the following equation:

$$E_{in2} = a_r \cdot \exp(-j \cdot \varphi) \cdot E_{out2} \quad (5.16)$$

, where a_r the single-pass amplitude and φ the additional phase shift introduced by the phase shifter in the feedback loop waveguide. Using the equation (5.1) and (5.2), the ratio of the transmitted and incident field in the MRR as can be expressed as:

$$\begin{aligned} H_{MRR} &= \frac{E_{out1}}{E_{in1}} \\ &= \frac{r_2 - r_1 r_2 a_r \cdot \exp(-j \cdot \varphi) \cdot \exp\left(-j \cdot 2\pi \cdot \frac{v}{FSR}\right) + \kappa_1 \kappa_2 a_r \cdot \exp(-j \cdot \varphi) \cdot \exp\left(-j \cdot 2\pi \cdot \frac{v}{FSR}\right)}{1 - r_1 \cdot a_r \cdot \exp(-j \cdot \varphi) \cdot \exp\left(-j \cdot 2\pi \cdot \frac{v}{FSR}\right)} \\ &= \frac{r_2 - (r_1 r_2 a_r - \kappa_1 \kappa_2 a_r) \exp(-j \cdot \varphi) \cdot \exp\left(-j \cdot 2\pi \cdot \frac{v}{FSR}\right)}{1 - r_1 \cdot a_r \cdot \exp(-j \cdot \varphi) \cdot \exp\left(-j \cdot 2\pi \cdot \frac{v}{FSR}\right)} \\ &= \frac{r_2 - \exp(-j \cdot \theta) \exp(-j \cdot \varphi) \cdot \exp\left(-j \cdot 2\pi \cdot \frac{v}{FSR}\right)}{1 - r_1 \cdot a_r \cdot \exp(-j \cdot \varphi) \cdot \exp\left(-j \cdot 2\pi \cdot \frac{v}{FSR}\right)} \end{aligned} \quad (5.17)$$

, where v the optical frequency of the propagating signal and FSR the free spectral range of the micro-ring resonator. The ring is on resonance when the detuning phase, φ , is a multiple of 2π , or when the wavelength of the light fits a whole number of times inside the optical length of the feedback loop waveguide:

$$\lambda_{res} = \frac{n_{eff} \cdot L}{m}, m = 1, 2, 3, \dots \quad (5.18)$$

where n_{eff} and L the effective refractive index and the length of the feedback loop waveguide. The power transfer function of the MRR can be calculated by squaring equation (5.17). As an example, Figure 5.9 presents the power transmission and phase spectra of a single MRR under different system parameters which are summarized in Table 8.

Table 8: Simulation parameters for the transmission and phase spectra of an MRR presented in Figure 5.9

Case number	θ	φ	$ r_{1,2} $	$ \kappa_{1,2} $	α
1	0.79π	-0.9π	0.948	0.317	0.99
2	0.61π	-0.81π	0.819	0.575	0.99
3	0.24π	-0.62π	0.361	0.933	0.99
4	0.61π	$-0.81 \pi + \pi/2$	0.819	0.575	0.99

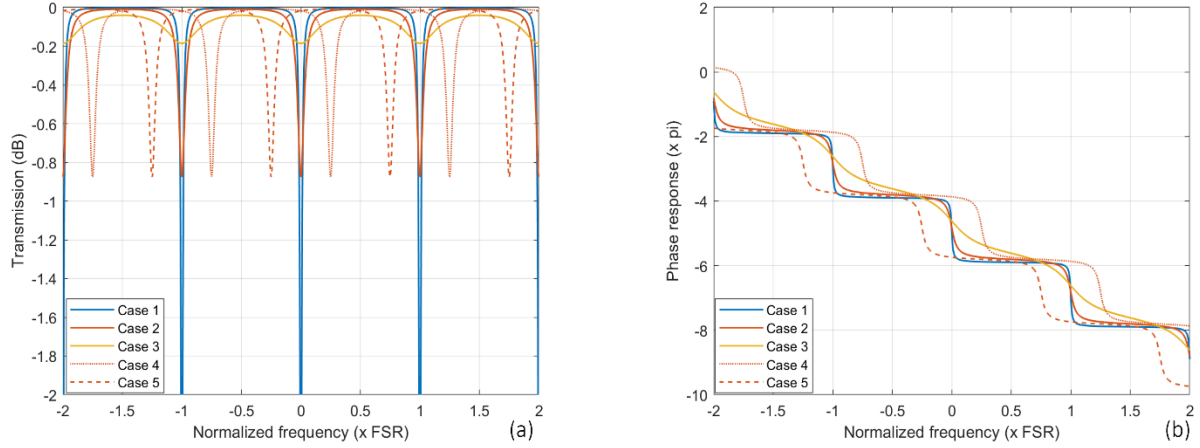


Figure 5.9 (a) Power and phase transmission spectra of a MRR under different configurations.

Additionally, to the power transfer function, a micro-ring resonator can be described by certain figure of merits, such as the finesses, F , and quality factor Q which are expressed as follows:

$$F = \frac{\text{FSR}}{\text{FWHM}} \quad (5.19)$$

$$Q = \frac{f_0}{\text{FWHM}} \quad (5.20)$$

The finesse is found to represent within a factor of 2π the number of round-trips made by light in the ring before its energy is reduced to $1/e$ of its initial value while Q -factor represents the number of oscillations of the field before the circulating energy is depleted to $1/e$ of the initial energy.

Single sideband full carrier optical filter: Assuming operation with microwave signals with peak-to-peak voltages lower than V_π , the phase modulated optical signal comprises the optical carrier and two sidebands with opposite phase, and with frequency offset dictated by the frequency of the microwave carrier. If this optical signal is incident on a photodiode, the microwave signal cannot pass on the generated photocurrent due to the square-law of the photodetection process and gets lost. To prevent this loss, an SSBFC filter is deployed to suppress one of the two sidebands [3]. The filter comprises an asymmetric MZI having both its arms coupled to an MRR, as it is presented at Figure 5.10. The round-trip length of the MRRs should be twice as large as the inter-arm path length difference of the asymmetric MZI in order to maximize the ER between the passbands and stopbands [3]. Based on the equations (5.9 – 5.18), the transfer function of the SSBFC filter can be expressed as follows:

$$H_{\text{SSBFC}} = \begin{bmatrix} r_1^1 & k_1^1 \\ k_2^1 & r_2^1 \end{bmatrix} \cdot \begin{bmatrix} H_{\text{MRR},1} & 0 \\ 0 & H_{\text{MRR},2} \cdot D \end{bmatrix} \cdot \begin{bmatrix} r_1^2 & k_1^2 \\ k_2^2 & r_2^2 \end{bmatrix} \quad (5.21)$$

, where $H_{\text{MRR},1,2}$ describes the transfer function of the two MRRs with round-trip length twice the inter-arm length difference ($2 \Delta L$) and D describes the transfer function of the inter-arm path length difference given by the following equation:

$$D = a_r \exp(-j \cdot 2\pi \cdot \nu \cdot T_d) \cdot \exp(-j\varphi_3) \quad (5.22)$$

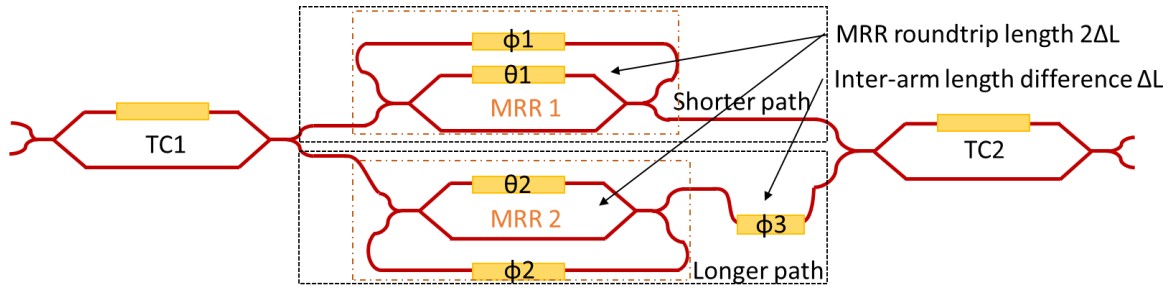


Figure 5.10: Layout of the single-sideband full carrier optical filter consisting of an asymmetrical MZI having each arm side-coupled to a micro-ring resonator.

Table 9: Simulation parameters for the transmission and phase spectra of an MRR presented in Figure 5.11

φ_1	θ_1	φ_2	θ_2	φ_3	α
0.24π	-0.62π	0.61π	-0.81π	1.5π	0.99

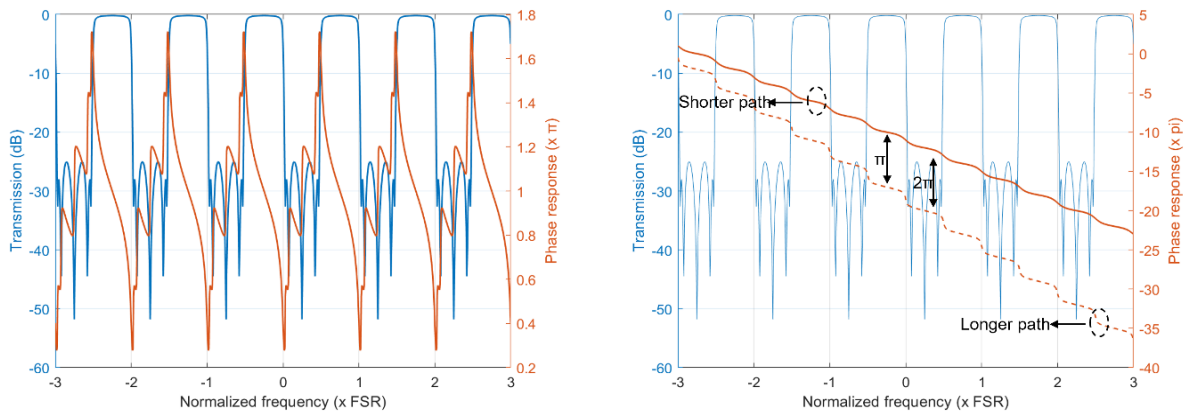


Figure 5.11: (a) Power transfer function and phase response of the SBBFC optical filter and (b) the phase responses of the shorter and longer path without taking into account the phase induced by the two tunable couplers at the input and output

, where T_d the propagation delay due to the inter-arm length difference and φ_3 the additional phase shift induced by the phase shifter integrated in this path. Both tunable couplers at the input and output of the filter are configured to split and combine the power of the propagating optical signals equally. The MRR of the shorter path (MRR1 in Figure 5.10) is set to a low quality factor by coupling a large portion of the light propagated in its companion MZI into the resonator, which means setting k_1 close to 1 ($|k_1|=0.93$). In this case, MRR1 features a weak notch filter effect at its resonance frequencies as depicted in Figure 5.9 (yellow solid line – Case 3), especially when the waveguide propagation loss in the resonator is negligible ($\alpha_r=0.99$). Its frequency dependent phase-shift characteristic is depicted in Figure 5.9 (yellow solid line – Case 3) where a π phase-shift is induced as approaching the resonance frequencies, while nearly linear phase-shift transitions are seen in the regions around the off-resonance frequencies. On the other hand, the MRR of the longer path (MRR2) is set at a high-quality factor ($|k_2|=0.575$). Under this configuration, MRR2 features a strong notch filter effect at its resonance frequencies as depicted in Figure 5.11 (orange solid line – Case 2). Its frequency dependent phase-shift characteristic is depicted in Figure 5.9 (orange solid line – Case 2) where a 2π phase-shift is induced as approaching the resonance frequencies, while nearly linear phase-shift transitions are seen in the regions around the off-resonance frequencies. When the light of the two paths interact with each other a filter characterized by an interleaver transmission pattern is resulted. This

pattern is caused by the constructive and destructive interferences determined by the phase-shift differences between the two interferometer arms.

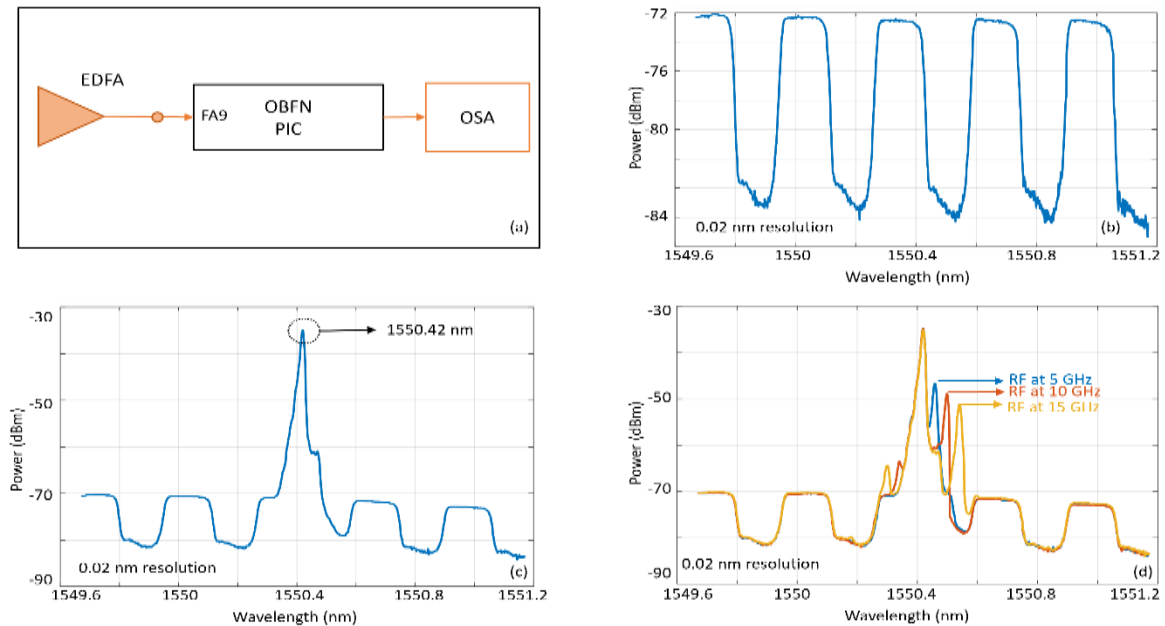


Figure 5.12: (a) Experimental setup for characterizing the performance of the optical filter (SSBFC). A broadband source is coupled to FA 1, passes through PM2 by setting the tuneable coupler at the cross-state and is coupled to the lower input of SSBFC filter (see Figure 5.2) . (b) Measured transfer function at the output of the PIC (FA 2) when the integrated laser source is OFF and (c)-(d) experimental optical spectra when the integrated laser is ON and the generated optical carrier is not modulated by PM1 and when PM1 is driven by a 5 GHz, 10 GHz, and 15 GHz sine waves, respectively.

Figure 5.11 (a) presents the theoretical power transfer function and phase response of the optical filter. As it can be observed, the implemented filter is a fifth-order periodic filter with a stopband attenuation equal to 25 dB while the insertion loss of the passband frequencies is below 0.01 dB. Figure 5.11 (b) presents the phase responses of the two optical paths of the filter without taking into account the accumulated π phase shift induced by the two tuneable couplers at the input and output. Taking into account that the PIC-OBFN is aimed to operate up to 40 GHz, the FSR of the MRRs is set to 20 GHz and the FSR of the asymmetric MZI to 40 GHz.

The configuration of the optical filter was performed by coupling an Erbium-doped fiber amplifier acting as a broadband optical source at FA 1(see Figure 5.2), as it is shown in Figure 5.12 (a). The tuneable coupler was set to couple all the light toward PM2 and thus toward the lower input of the SSBFC filter. The resulting optical spectra were captured by an optical spectrum analyzer that was connected to FA2 (see Figure 5.2). Figure 5.12 (b) presents the power transfer function of the filter. As observed, the passband is 20 GHz, the FSR of the filter is 40 GHz and the stopband ratio close to 12 dB. Figure 5.12 (c) depicts the optical spectra at the output of the optical SSBFC filter when the integrated laser source is ON. In this case, the tuneable coupler before the modulation unit is set to split equally the two input optical signals and thus the optical carrier is coupled at the upper input port of the filter and the broadband signal at the lower. During the following experiments, the central wavelength of the optical carrier is chosen so to corresponds to the edge of the passband in order to suppress the one sideband and pass the other one. Finally, Figure 5.12 (d) depicts the optical spectra when driving the PM1 with 5, 10 and 15 GHz sinusoidal signals. The left sidebands of the optical carrier are suppressed with respect to the right ones by 12 dB, which corresponds to the ER of the filter. It should be noted that the power transfer function of the SSBFC filter is plotted with a half FSR wavelength shift relative to the spectra of the

filtered optical signals. This is due to the fact that the broadband noise source used for the extraction of the optical spectra was coupled to the upper port of the tuneable coupler prior

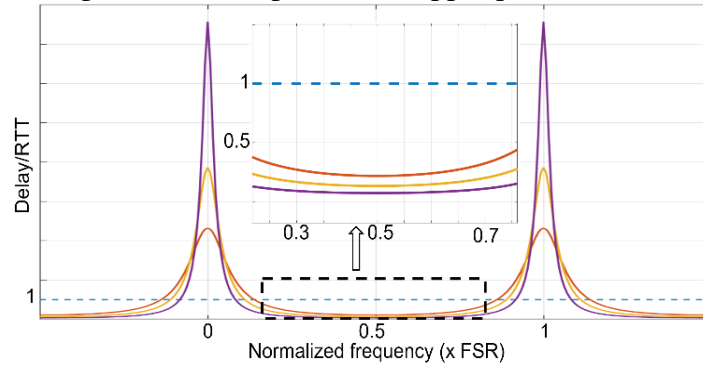


Figure 5.13: Imposed delay by an MRR for different coupling coefficient (k) of the companion MZI.

to the modulator (FA 1 in Figure 5.2), whereas the unmodulated optical carrier was coupled to the lower port.

Optical true-time delay lines: The core part of the demonstrator PIC is the beamforming unit which consists of a set of four OTTDLs. Each OTTDL comprises 8 cascaded MRRs with 22 GHz FSR that can be tuned independently. The round-trip length of the MRRs is 0.8 cm which results to a round-trip loss equal to 0.08 dB. The total true time delay at the output of each OTTDL is the sum of the delay imposed by each MRR. The output signal of the SSBFC filter is fed to the four OTTDLs via a 1×4 splitter based on a combination of three MZIs. The power of the signals at the output of the splitter can be controlled by proper adjustment of the coupling coefficients of the MZIs. Therefore, any difference in the optical propagation losses between the subsequent OTTDLs can be compensated. More importantly, various amplitude tapering schemes can be used for enhanced beam shaping. In order to steer a microwave beam to an intended angle (θ), the total time delay imposed by each OTTDL is given by Eq. 2.31. The thermal crosstalk between the MRRs remains as low as -17 dB by maintaining a distance of 250 μm between the heating electrodes and the adjacent optical waveguides.

The group delay (GD) induced by the MRR on the propagating optical field can be expressed as the derivative of the phase of H_{MRR} to the optical angular frequency. The normalized group delay (GD_N) is given by the following equation:

$$\text{GD}_N = \frac{d \arctan \left(\frac{\text{Im}(H_{\text{MRR}})}{\text{Re}(H_{\text{MRR}})} \right)}{d\phi} \quad (5.12)$$

Figure 5.13 depicts the delay normalized to the round-trip time (RTT) imposed by a single MRR over one free spectral range (FSR) as a function of the coefficient k . In the case of k equal to 1 (blue-dashed line), the delay is unitary and the MRR operates as a simple time delay line without spectral selectivity. In the other cases, the k falls within the range $k_c \leq k \leq 1$, where k_c represents the value of k in the case of critical coupling. As observed, delays that are multiple to the RTT can be imposed at the resonance frequencies, whereas delays equal to a fraction of the RTT can be introduced at frequencies off-resonance. Therefore, the continuous tuning of both phase shifters provides direct control on the quality (Q)-factor of the MRR and on the true time delay imposed by the MRR on the optical signal [4], [5].

5.1.2 InP platform

Indium phosphide is the most advanced platform for high-performance large-scale PICs allowing the monolithic integration of all the required active components (e.g., lasers,

semiconductor optical amplifiers (SOAs), modulators, photodetectors), and passive components (e.g., waveguide interconnects, filters, couplers), thus enabling complex single-

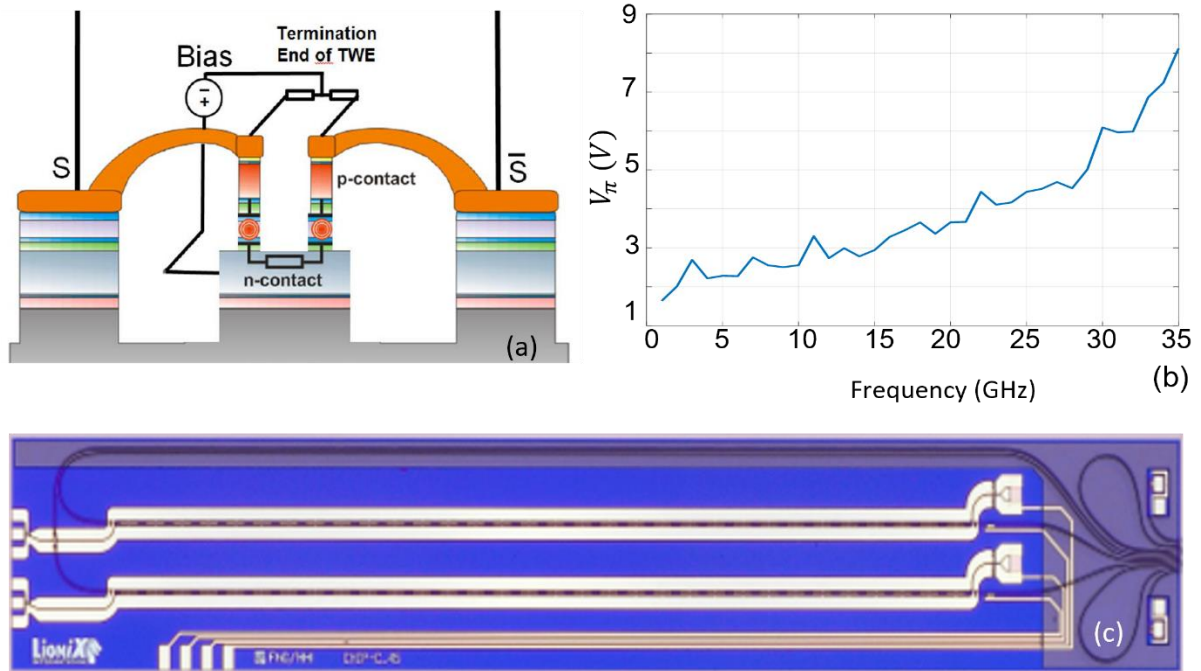


Figure 5.14: Cross section and equivalent electrical circuit of the InP phase modulator, (b) its measured half-wave voltage, V_{π} as function of the modulation microwave frequency, and (c) a picture of fabricated InP PIC.

chip implementations of advanced transmitters and receivers [6]. However, due to its inherent high propagation loss ($\sim 0.3/\text{mm}$), InP is widely used mainly only for the active components while the passive components are usually integrated in low-propagation loss platform like TriPleX. The following paragraphs describe the active components that have been integrated in the demonstrating OBFN-PIC.

Optical phase modulator: In the modulation unit, the microwave signal that will be processed by the OBFN-PIC is frequency up-converted and brought to the optical domain via the phase modulation of the optical carrier generated by the integrated laser source. The principle operation of the phase modulator (PM) is described in paragraph 3.2. The electrodes of the specific phase modulator are carefully designed for traveling-wave (TW) interaction. The operation of a TW modulator is the distributed interaction over a region in space between electrical and optical signals propagating in a transmission line and in a waveguide, respectively. Figure 5.14(a) depicts the cross section and equivalent circuit of the InP PM. The optical waveguide is fabricated between different InP based layers that form n- and p-contacts. The PM is biased with a negative biased up to -8 V while specific electrodes (S) transfer the microwave signal close to the optical waveguide. In our PIC, two InP phase modulators with 35 GHz 3-dB analog bandwidth have been integrated for redundancy purposes although only one is required. Figure 5.14 (b) presents the measured V_{π} as a function of the modulation frequency. As observed, the V_{π} is below 3 V for frequencies up to 10 GHz and increases to 8.1 V at 35 GHz. In a microwave photonics link such in our case, the half-wave voltage frequency response, $(V_{\pi}(f))$, dictates the power of the microwave tones after the photodetection stage, for a given optical and RF input power. More specifically, the relationship between the power of the fundamental microwave tone, P_{Ω} , and the $V_{\pi}(\Omega)$ can be expressed as follows:

$$P_{\Omega} \sim J_1 \left(\frac{V_{\text{rf}}(\Omega)}{V_{\pi}(\Omega)} \cdot \pi \right)^2 \quad (5.13)$$

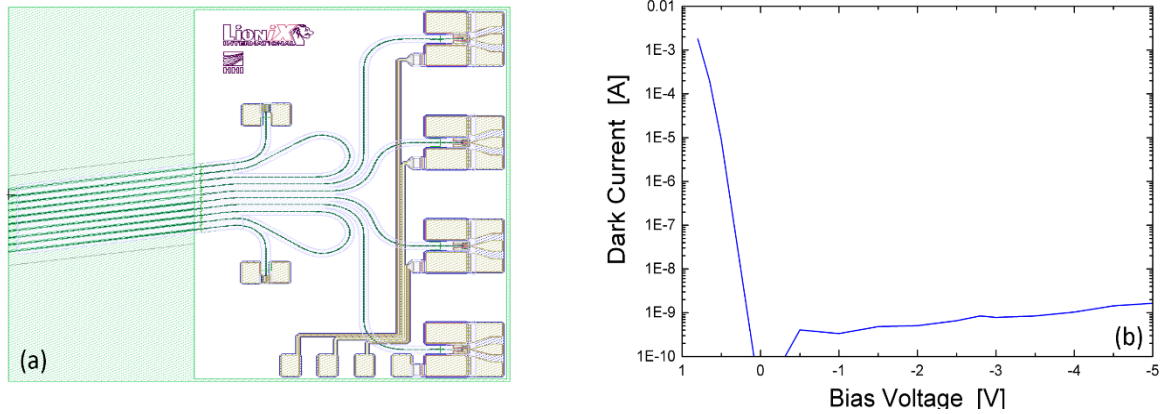


Figure 5.15: (a) Layout of the quad InP photodiode array and (b) the measured dark current of the photodiodes as a function of the bias voltage.

, where J_1 the Bessel function of the first kind and V_{rf} the amplitude of the input microwave signal. The power of the signal at the fundamental frequency is maximized when the voltage ratio $\frac{V_{rf}(\Omega)}{V_{\pi}(\Omega)}$ is equal to 0.58. At this point, the 1st-order Bessel function of the first kind is maximized and so is the power of the fundamental tone.

Within our experiments, this voltage ratio takes values from 0 to below 0.58. In this range, J_1 is a monotonic function, meaning that a decrease of the voltage ratio leads to a decrease to the power of the fundamental tone. Therefore, it can be concluded that for a given V_{rf} , increasing $V_{\pi}(\Omega)$ reduces the power of the fundamental tone and thus the link gain. The two optical phase modulators exhibit a slightly different RF performance in terms of V_{π} over the operating frequency range which also results to slightly different link gains. The reason for this difference is manifold since it depends on the fabrication and also the packaging procedure. Consequently, for the system experiments, the phase modulator 1 (PM1 in Figure 5.2 of the manuscript) was selected over PM2. The InP chip is butt-coupled to the TriPleX platform and the average insertion loss per facet is 4.9 dB.

Photodetector: An InP quad photodetector array is used for the conversion of the microwave signals from the optical back to the RF domain. The analog bandwidth of the photodiodes is more than 40 GHz, while their responsivity is 0.8 A/W. The average insertion loss between the TriPleX platform and InP detector chip is 2 dB per facet. A waveguide break at the optical path of the bottom photodiode (PD 4), adds significant losses that render this photodiode unable to detect the optical signal from the corresponding OTTDL. Therefore, in our experimental testing, only the top three PDs and OTTDLs were utilized.

5.1.3 InP-TriPleX integration

The hybrid integration between InP and Si_3N_4 platforms has been optimized over the last years and has successfully led to the demonstration of powerful optical components such as hybrid InP- Si_3N_4 optical lasers. The minimization of the return loss has been the subject of extensive studies that resulted in the development of a solid set of design rules. An important design rule is that all the individual photonic chips should have angled facets. The angle is chosen such that, for the mode refractive index of the specific waveguides, the reflection coefficient is minimized. Moreover, adiabatic mode converters are integrated on the Si_3N_4 chips at the interfaces with the InP chips in order to achieve a mode profile matching between the platforms and minimize the coupling loss. Additionally, all the interfaces of the InP chips are fabricated with anti-reflection coating that matches the

refractive index of the TriPleX platform. Therefore, the actual value of the return loss is expected to be negligible and indeed, during the characterization of the OBFN-PIC, we did

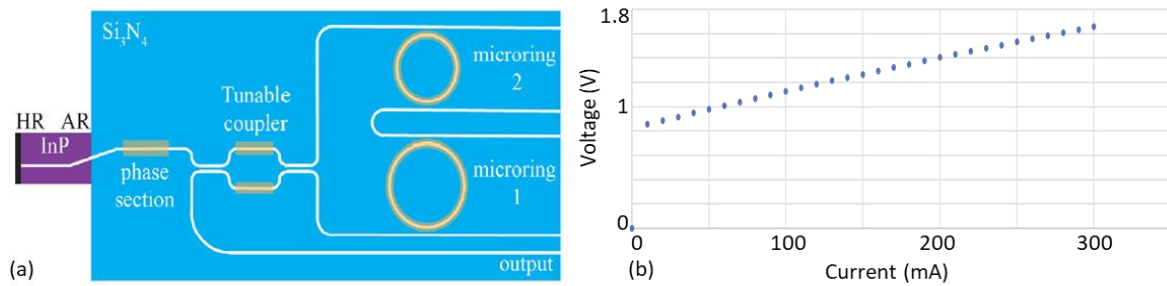


Figure 5.16 (a) Schematic view of the WECL and (b) its characteristic I-V curve.

not observe any Fabry-Perot resonance. Leveraging the hybrid InP-TriPleX integration, the demonstrated OBFN-PIC hosts a powerful waveguide external cavity laser which was used for the generation of the optical carrier.

Hybrid InP-TriPleX waveguide-based external cavity laser: The WECL comprises an InP semiconductor optical amplifier as the gain section (GS) and an extended cavity implemented in the TriPleX platform. Figure 5.16 (a) presents the schematic view of the laser. The semiconductor chip is fabricated by the Fraunhofer Heinrich Hertz Institute and contains a multi-quantum well active waveguide based on InP. To reduce undesired reflections at the interface between the two chips, an anti-reflection coating is applied to the facet and the waveguide is tilted by 9° with respect to the facet normal. The function of the TriPleX chip is to provide frequency selective feedback and to increase the effective cavity length for linewidth narrowing. The frequency selective filter is implemented using two sequential racetrack shaped MRRs, in a Vernier configuration placed inside a loop mirror. The MRRs have a circumference of 787 and 813 μm , respectively. Although the bandwidth of the InP gain chip is larger, this free-spectral range is sufficient to obtain single mode lasing over a large part of the gain bandwidth. Both rings are symmetric and are designed for a power coupling coefficient to the bus waveguides. To control the phase of the circulating light and to compensate phase changes when tuning any other element, a phase section is added to the bus waveguide. Typically, the phase section is set to provide maximum feedback for a single longitudinal mode of the laser cavity, which restricts laser oscillation to a single wavelength and provides maximum output power. A tunable coupler, implemented as a balanced MZI, is used to couple the circulating light out of the laser cavity. The tuning of the WECL is implemented via resistive heaters placed above the rings, the phase section and the output coupler. Figure 5.16 (b) presents the characteristic I-V curve of the WECL. As it can be observed, the power consumption is almost 0.4 W for currents around 260 mA. The typical output power of the laser measured at the fiber array port after the optical filter (FA 2 in Figure 5.2) is 10 mW.

5.2 Experimental performance evaluation of the OBFN-PIC

The experimental evaluation of the PIC was performed into two successive stages. Firstly, the link gain, noise figure, SFDR₃ are measured by performing single-tone or two-tones experiments with the generation of pure sine waves with frequencies from 0.04 GHz up to 40 GHz. At the second stage, the PIC was characterized under different beamforming configurations, utilizing modulated microwave signals with central frequencies either 5 GHz or 10 GHz. The baseband information signal was modulated into the microwave carriers, employing either QPSK or 16-QAM modulation formats. The evaluation of the OBFN-PIC was based on the calculation of the EVM and BER of the detected microwave signals after

the photodetection stage. The following paragraphs present in detail the several experimental setup as well as the experimental results of both stages.

Sweeping single-tone from 40 MHz to 40 GHz

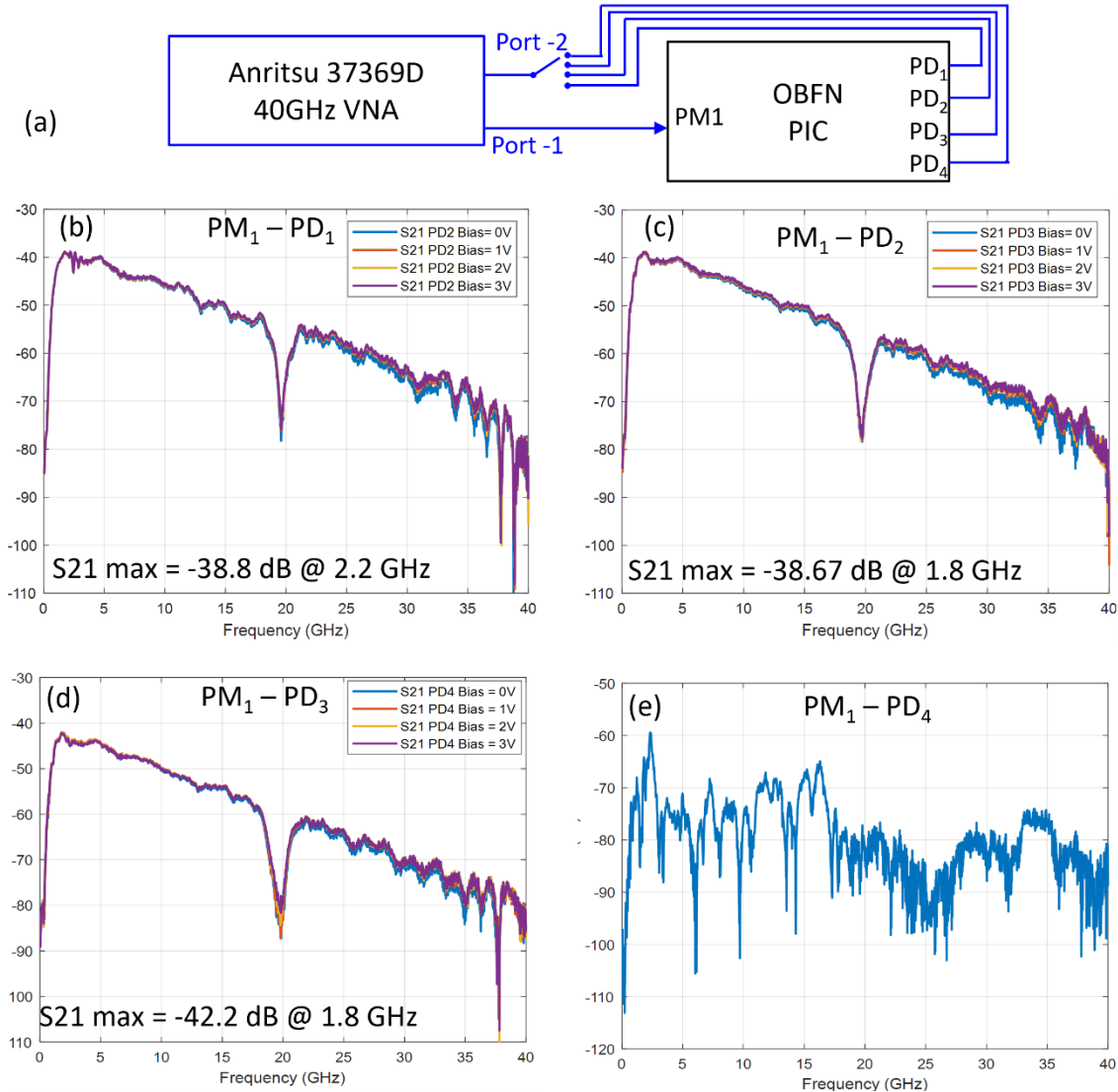


Figure 5.17: (a) Experimental set-up for measuring the link gain of the four independent MWP links (PM1-PD1, PM1-PD2, PM1-PD3, and PM1-PD4) of the PIC-OBFN and (b) – (d) the link gains spectra of the MWP links for biasing voltages of the photodiodes from 0 V up to -3 V.

5.2.1 Link gain

As it was described in Chapter 3, the link gain indicates the gain (or loss) imposed by a microwave photonics system on the power of the input microwave signal as a function of its frequency. Therefore, the link gain from the input of the PM₁ at the output of each PD can be expressed as the magnitude of the forward transmission parameter S_{21} . The measurement of the S_{21} coefficient was performed using a 2-port calibrated Vector Network Analyzer (VNA) with 40 GHz 3-dB analog bandwidth. The output port of the VNA was connected to the PM₁ and generated sinewaves with frequencies varying from 0.04 GHz to 40 GHz while the input port was connected successively to the four PDs. During these measurements, the central wavelength of the unmodulated optical carrier was located at the edge of the passband of the SSBFC filter, while all the companion MZIs of the MRRs of the OTTDLs

were set at k equal to 1. Figure 5.17 shows the link gain for the microwave photonics links PM_1 - PD_1 , PM_1 - PD_2 , PM_1 - PD_3 and PM_1 - PD_4 , taking also into account the propagation loss induced by the printed circuit boards. The maximum link gain of the PM_1 - PD_1 link is -36.98 dB at 2.6 GHz while the link gain of the PM_1 - PD_2 link is -37.23 dB at 4.6 GHz and of the PM_1 - PD_3 link is -39.39 at 2 GHz. Due to a small tilt between the bottom part of the InP PD chip and TriPLeX chip, high coupling loss was measured for the fourth PD which was located at the bottom part of the InP chip. Therefore, the fourth microwave photonics link between PM_1 and PD_4 was dominated by the noise as a result this link was not used for the rest of the experiments. As observed, while increasing the operating frequency, the link gain decreases mainly due to the frequency response of the phase modulator and the PDs, and the increase of the V_π . For microwave frequencies below 1 GHz, between 18 and 21 GHz, and above 39 GHz, the SSBFC filter allows both sidebands of the modulated optical signal to pass through, imposing significant losses.

5.2.2 Noise figure and spurious free dynamic range

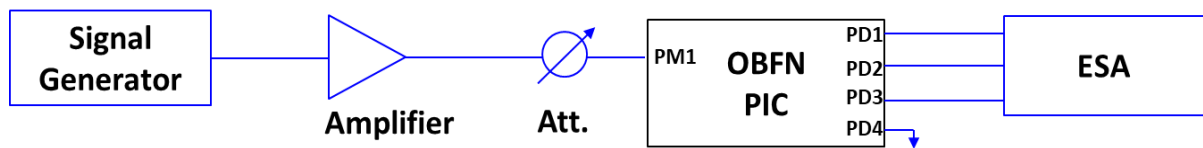


Figure 5.18: Experimental set-up for measuring the noise figure of the OBFN-PIC at 5 GHz and 10 GHz carrier frequencies.

As analysed in paragraph 3.4, the NF describes the degradation of the SNR caused by the microwave photonics system. Figure 5.18 presents the experimental setup for measuring the NF of the of the microwave links of the PIC-OBFN. By using a 50 GHz electrical spectrum analyzer and terminating the input of the PM_1 with a 50-ohm load terminator, we found the noise power density at the outputs of the photodiodes equal to -171.75 dB/Hz, which corresponds to the minimum detectable power density by our equipment. Therefore, the NF can be calculated at different frequencies, replacing the value of the link gain from Figure 5.17, and considering the temperature equal to 30°C. Indicatively, the NF of the PM_1 - PD_1 link at 5 and 10 GHz was equal to 42.19 dB and 47.48 dB, respectively. Without the limitation imposed by the equipment, the actual value of the NF could be even lower. Taking into account that the amplitude of the photocurrents was below 0.3 mA, it can be assumed that our system is limited only by the thermal noise, and thus the impact of the other noise sources is negligible [7]. In this case, P_N is equal to the thermal noise and the NF at 5 GHz and 10 GHz is 38.28 dB and 41.95 dB, respectively.

Two tones at 4.9 (9.9) GHz and 5.1 (10.1) GHz

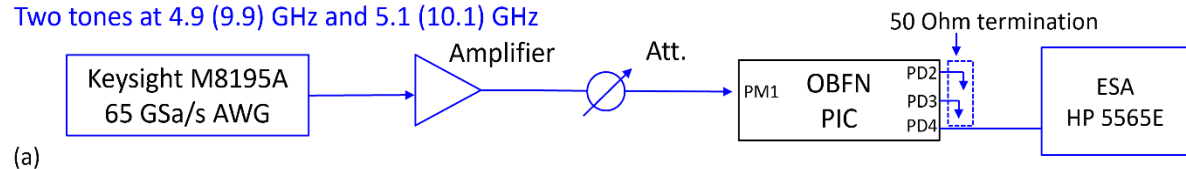


Figure 5.19: Two-tone experimental set-up for measuring the $SFDR_3$ of the OBFN-PIC.

Following the analysis of paragraph 3.4, the n th-order SFDR defines the range of input powers over which the output fundamental tone is above the noise floor whilst all n th-order intermodulation distortion tones are less than or equal to the noise floor. The OIP_n can be calculated measuring the power of the fundamental and distortion tones at the same input power [7]. As shown in Figure 5.19, a standard two-tone experiment was carried out at the PM_1 - PD_1 link. The pair of tones was centered around 5 or 10 GHz with a 200 MHz frequency interval in either case. The OIP_2 and OIP_3 around 5 GHz are -32.8 dBm and -38.8 dBm, respectively and around 10 GHz are -38.3 dBm and -40.6 dBm, respectively.

Assuming a noise floor equal to the thermal noise at 30°C, the SFDR₂ and SFDR₃ around 5 GHz are 70.5 dB·Hz^{1/2} and 89.9 dB·Hz^{2/3}, respectively whereas around 10 GHz are equal to 67.7 dB·Hz^{1/2} and 88.8 dB·Hz^{2/3}, respectively.

5.2.3 System evaluation

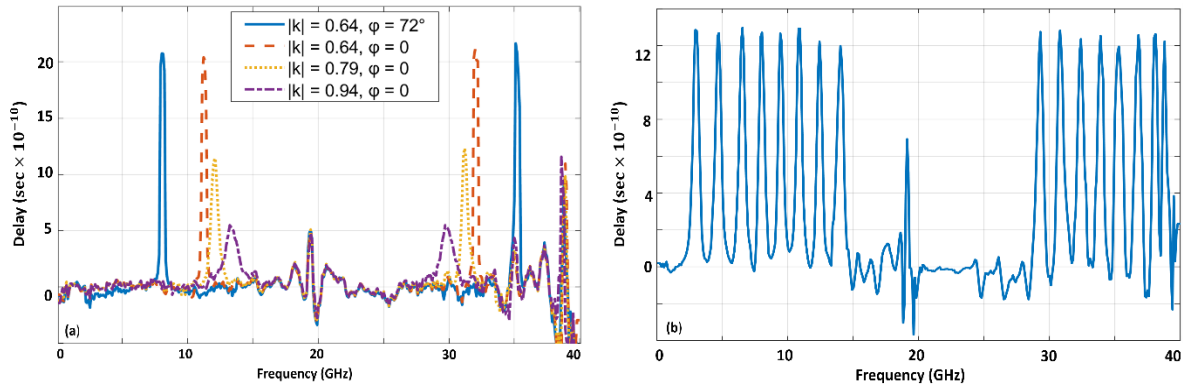


Figure 5.20: (a) Imposed delay by one MRR for different coupling coefficients of the MZI and phase shifts on the feedback loop waveguide and (b) imposed delay by the OTTDL that corresponds to PD1, setting all the MRRs at adjacent resonance frequencies.

The delay imposed by each OTTDL was measured using the VNA which calculates the delay from the derivative of the phase of the forward transmission coefficient, S_{21} , with respect to the frequency. Figure 5.20 shows the imposed delay by a single MRR of the (GHz). The frequency separation between two delay peaks, that correspond to the same MRR, is not dictated only by its FSR but also by the minimum frequency offset between the optical carrier and its resonance frequency that falls within the passbands of the optical filter. Considering that the FSR of the MRR is constant, by shifting the resonance frequencies of the MRRs with respect to the optical carrier, we can define the number as well as the frequency of the delay peaks.

In order to explain this dependency, we take as an example four indicative cases where the optical carrier is modulated by pure sinewaves. In the first case, we assume the optical carrier is modulated by an 8 GHz sinewave. Figure 5.21 (a-I) presents the optical spectrum after the modulation stage. Moreover, we assume that the optical carrier is placed at the edge of the passband of the optical filter, as it is depicted in Figure 5.21 (a-II). Due to the frequency response of the optical filter, only one of the two sidebands of the sinewave passes through the filter without being suppressed. In our example, this sideband is located at -8 GHz with respect to the optical carrier. After the photodetection stage, this sideband will generate the equivalent frequency tone at 8 GHz. With these settings, we further assume that a single MRR of the OBFN is set on-resonance at -8 GHz and imposes a delay OTTDL that corresponds to PD1 for different cross-coupling coefficients of the companion MZI, and for different phase shifts applied in the feedback loop waveguide. Each MRR of the OTTDLs can impose up to two delay peaks within the operating RF bandwidth (0-40

peak at this frequency. Taking into account that the FSR of the MRR is 22 GHz, the adjacent resonance frequencies (± 22 GHz) correspond to frequencies that fall within the stopbands of the filter. However, as it can be observed in Figure 5.21 (a-III), the resonance frequency of the MRR that is two FSRs away (+44 GHz) falls within the passband of the filter. The frequency of this resonance with respect to the optical carrier is 36 GHz. Therefore, a delay peak at 8 GHz with respect to the optical carrier will also impose a delay peak at 36 GHz. In this case, the frequency distance, Δf , between the two peaks can be expressed as follows:

$$\Delta f [\text{GHz}] = 2 \cdot (\text{FSR}_{\text{MRR}} - |f_{\text{off}}|_{\text{min}}), \quad \text{for } 4 \text{ GHz} \leq |f_{\text{off}}|_{\text{min}} < 20 \text{ GHz} \quad (5.14)$$

where $|f_{\text{off}}|_{\text{min}}$ the minimum frequency offset between the resonance frequencies of the MRR that falls within the passband of the filter and the optical carrier. Equation 5.14 is valid only for $4 \text{ GHz} \leq |f_{\text{off}}|_{\text{min}} < 20 \text{ GHz}$.

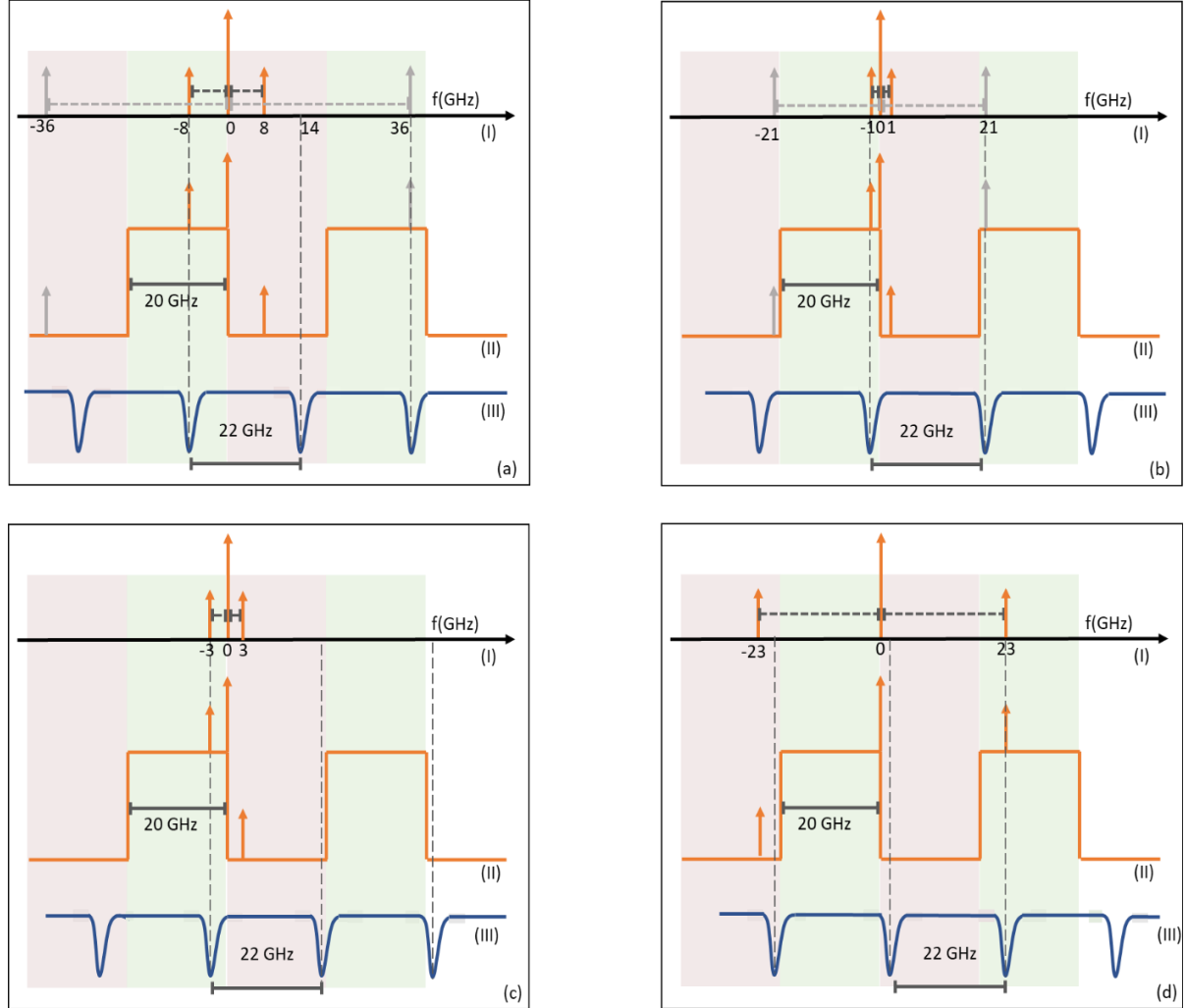


Figure 5.21: Optical spectra of the (I) modulated optical signal, (II) the transfer function of the optical filter, and (III) the power transmission of a single MRR, for driving frequencies (a) 8 GHz, (b) 1 GHz, (c) 3 GHz, and (d) 23 GHz.

Respectively, as a second example, in Figure 5.21(b), we assume the optical carrier is modulated by a 1 GHz sinewave. Following the same analysis, it can be calculated that also in this case a second delay peak will be generated at 21 GHz and the frequency distance of the two delay peaks can be expressed as follows:

$$\Delta f [\text{GHz}] = (\text{FSR}_{\text{MRR}} - 2 \cdot |f_{\text{off}}|_{\text{min}}), \quad \text{for } 0 \text{ GHz} \leq |f_{\text{off}}|_{\text{min}} < 2 \text{ GHz} \quad (5.15)$$

This equation (5.15) is valid only for $0 \text{ GHz} \leq |f_{\text{off}}|_{\text{min}} < 2 \text{ GHz}$. In all the other cases, each MRR imposes a single delay peak whose frequency is defined only by the $|f_{\text{off}}|_{\text{min}}$. For example, Figure 5.21(c) and (d), present the cases where the optical carrier is modulated by 3 GHz and 23 GHz, respectively. As observed in both cases, only one resonance frequency of the MRR passes through the optical filter and thus it imposes one delay peak at frequency dictated by the $|f_{\text{off}}|_{\text{min}}$.

To summarize, the relative minimum frequency offset between the resonance frequencies of the MRR that falls within the passband of the filter and the optical carrier defines whether we will observe one or two delay peaks within the operating frequency range. Taking into account that the resonance frequencies of the MRRs depend on both the cross-coupling coefficient and the phase shifter in the loop waveguide, the delay spectra presented in Figure 5.21 is dictated by Equation 3.

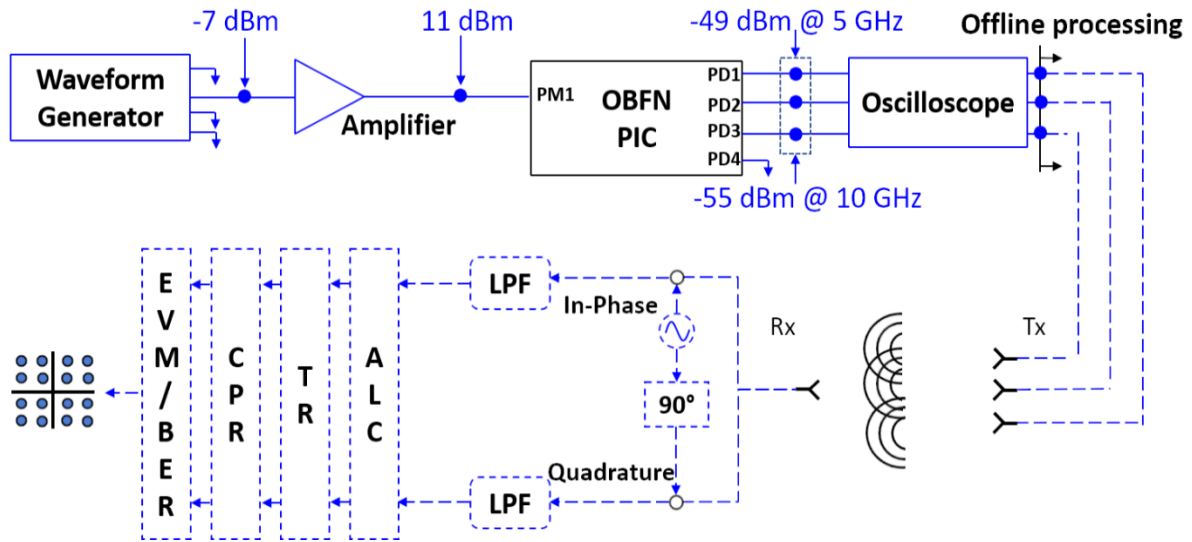


Figure 5.22: Experimental setup for the system evaluation of the OBFN-PIC using QAM modulated signals at 5 GHz and 10 GHz. It consists of a measuring part (blue solid lines) and a virtual part (blue dashed lines).

Table 10: Modulation and beamforming parameters of the evaluation cases.

	Format	Symbol rate (Mbaud)	RF carrier (GHz)	Pulse shaping	Roll-off factor	Beam angles (°)
Case 1	QPSK	500	5	Raised Cosine	1	45, 60, 70, 90, 110, 120, 135
Case 2	16-QAM	500	5	Raised Cosine	1	
Case 3	QPSK	500	10	Raised Cosine	1	

Figure 5.21 presents on the other hand the time delay that is imposed by the same OTTDL, when all of the eight MRRs are tuned at adjacent resonance frequencies. The extra delay peaks and delay ripple around 19 GHz and 39 GHz are due to the optical filter. As it is analyzed in [3], the optical filter imposes an equal delay at the frequencies falling within the passband, but at the frequencies that correspond to the transitions between the passbands and stopbands a delay ripple is imposed. In our case, this transition of the optical filter is located at around 19 GHz and 39 GHz with respect to the optical carrier. This delay ripple does not affect the system performance because at these frequency ranges both sidebands of the optical modulated signals experience almost the same attenuation from the optical filter and as a result the microwave signal cannot pass on the generated photocurrent due to the square-law of the photodetection process and gets lost.

The beamforming capabilities of the OBFN-PIC are demonstrated by emulating a wireless system that operates in the downlink direction. In this system, the output microwave signals of the OBFN-PIC are emitted by a 3-element antenna array that forms a single beam directed to a single user. Figure 5.22 presents the experimental setup for the performance evaluation of the OBFN-PIC utilizing high-order QAM microwave signals. It consists of a measuring part that includes the actual experimental testbed and a virtual part that includes the offline processing steps. More specifically, in the measuring setup a 65 GSa/s arbitrary

waveform generator produces either QPSK or 16-QAM microwave signals at 5 or 10 GHz carrier frequency. The symbol rate of the microwave signals is set at 500 Mbaud, while their spectral content is confined around their microwave carrier using a raised-cosine pulse shaping filter with roll-off factor equal to 1. The microwave signals are amplified up to 11 dBm by a broadband and low-noise amplifier to drive the PM₁. In the OBFN-PIC, the external cavity laser emits a continuous wave signal with central wavelength at 1550.42 nm, which is fed via the tunable coupler to the PM₁. The modulated optical signal is subsequently processed by the SSBFC filter, which is configured to have flat passbands and stopbands with ER and FSR equal to 12 dB and 40 GHz, respectively. At the output of the filter, the signal is equally split into three copies that are coupled to the upper three OTTDLs of the OBFN. The signals at the output of the OBFN are detected by the PD array and are sampled by a 4-channel real-time oscilloscope with 70 GHz analog bandwidth and 256 GSa/s sampling rate, within a 200 μ sec time window. As a result of this sampling process, three vectors consisting of 51.200.000 samples each, are acquired and stored in the internal memory of the oscilloscope.

Within the virtual part, the stored samples are further processed offline for the calculation of the radiated field assuming that the detected signals are transmitted by a linear 3- element antenna array with omnidirectional AEs. The spacing between successive AEs is set at $\lambda/2$. For each experimental case, it is also assumed that a single omnidirectional antenna is placed at a specific nominal beam angle and acts as the receiving antenna to detect the radiated field. The calculated microwave field is down-converted to the baseband using a local oscillator at the carrier frequency and is analysed back into its in-phase and quadrature

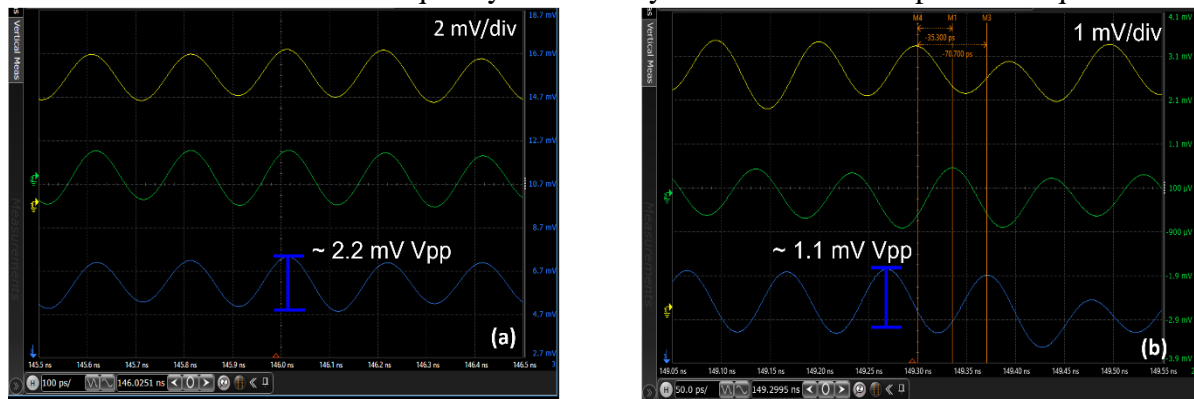


Figure 5.23: Indicative microwave waveforms with central frequencies at 5 GHz (a) and 10 GHz (b) as they were captured at the oscilloscope while the OBFN was configured to steer the 5 GHz signal at 90° and the 10 GHz signal at 45°.

components. Finally, a sharp low-pass filter (LPF) with 500 MHz 3-dB bandwidth is applied to each component to filter out the unwanted spectral content at higher frequencies.

A standard set of DSP algorithms is utilized to properly decode and evaluate the quality of the received baseband signal. First, an amplitude level correction algorithm normalizes the power of the signal to a specific power level dictated by the modulation format. Next, a time recovery algorithm estimates and removes the timing error offset that is inevitably generated, since the waveform generator and the oscilloscope are not synchronized. Subsequently, the carrier phase recovery algorithm removes the phase noise that it is introduced by the waveform generator and the oscilloscope. Finally, the acquired samples are used for the construction of the constellation diagrams and the calculation of the EVM and the BER in order to evaluate the beamforming performance and the overall quality of the transmission system. Table 10 summarizes the three cases that have been experimentally investigated, presenting for each one of them the corresponding modulation format, the symbol rate, the carrier frequency, the type of the pulse shaping filter and the selected roll-

off factor for the generation of the microwave signals, as well as the set of the intended beam angles.

The average power consumption of the OBFN-PIC in these experimental cases was 17.5 W. The sources of the power consumption are the external cavity laser and the thermal phase shifters, which require almost 300 mW each for π phase shift.

The initial adjustment of the group time delays in each OTTDL was realized utilizing pure sinusoidal waves at either 5 or 10 GHz, depending on the experimental case. As an example, Figure 5.23 (a) presents two microwave waveforms as captured at the oscilloscope and correspond to Case 1 (central frequency at 5 GHz) for steering angle 90° and Case 3 (central frequency at 10 GHz) for steering angle 45° . As it can be observed, in Figure 5.23(a), the three waveforms have the same amplitude and are time-synchronized in order to achieve 90° steering angle while in Figure 5.23(b) the waveforms are delayed to each other by 35.3 ps which based on equation (2.24) will lead to a steering angle equal to 45° . It should be noted that between the signals in the two cases have different amplitudes due to frequency response of our microwave photonics links, as it can be easily seen in Figure 5.23, which presents the link gain of the links with respect the microwave frequencies.

The delay resolution depends mainly on the minimum phase shift that can be achieved by the phase shifter placed inside the companion Mach-Zehnder interferometer of each MRR and controls its quality factor (Q-factor). The phase shifter is controlled by applying voltage signals on the heating electrode placed on top of the optical waveguide. Due to the thermo-optic effect, the resultant phase shift ($\Delta\phi$) is proportional to the square of the applied signal and thus the minimum phase shift that can be achieved depends not only on the voltage

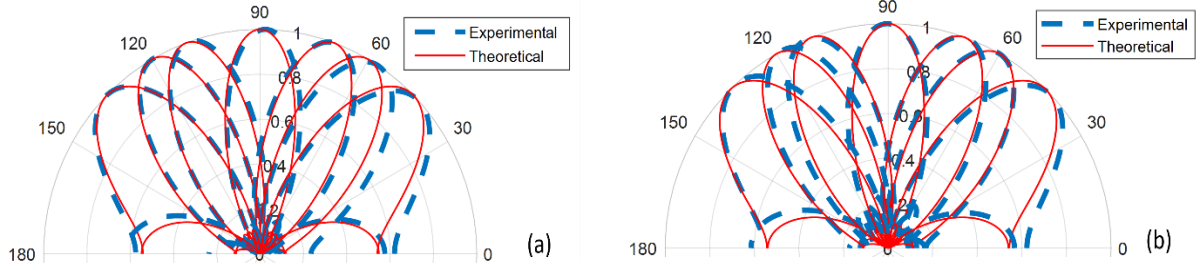


Figure 5.24: Theoretical and experimental average array factors after configuring the OBFN PIC to operate with sine waves with central frequencies at (a) 5 GHz and (b) 10 GHz. Target beam angles were 45°, 60°, 70°, 90°, 110°, 120° and 135°.

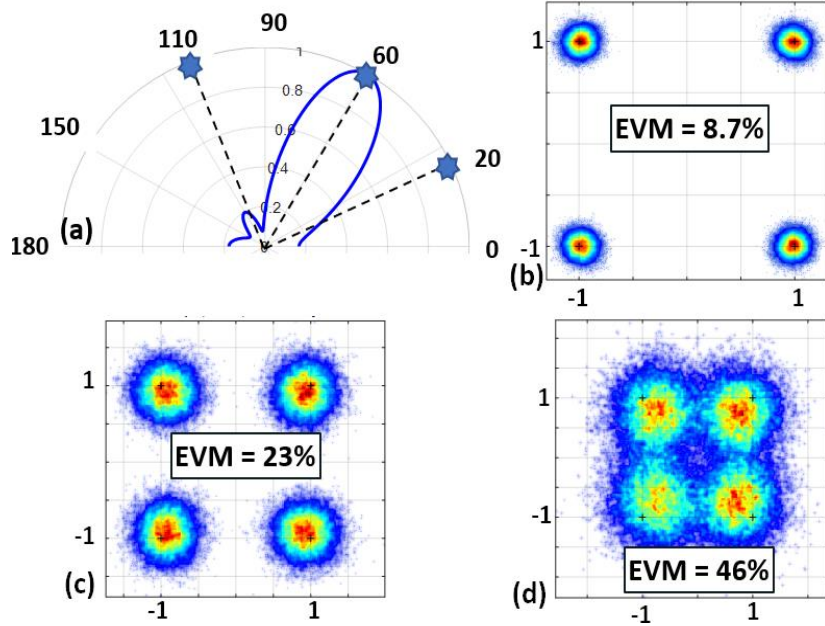


Figure 5.25: (a) Array factor of the 500 Mbaud QPSK signal modulated with a 10 GHz microwave carrier and steered at 60°. (b)-(d) Constellation diagrams of the received signal at the observation angle 60°, 20° and 110°, respectively.

resolution (V_{res}) of the driving circuits but also on the current voltage state (V_{curr}), as it is described from the following equation:

$$\Delta\varphi \propto V_{upd}^2 - V_{curr}^2 \xrightarrow{V_{upd}=V_{curr} \pm V_{res}} V_{res}^2 \pm 2 \cdot V_{curr} \cdot V_{res} \quad (5.16)$$

Therefore, the resolution of the imposed delays is lower when operating in higher voltages and vice versa. Given that within our experimental testbed, the voltage resolution of the driving circuit is 0.001 V, it can be calculated that the minimum delay shift for a single MRR at either on-resonance (long delays) or off-resonance frequencies (short delays) is well below the pico-second regime. At the maximum delay settings a single OTTDL (8 MRRs) imposes 1900 ps delay over almost 600 MHz bandwidth with a delay ripple equal to 1 ps. The delay resolution for this given delay ripple is only 1 ps.

Figure 5.24 depicts the time average array factors based on the samples acquired from the oscilloscope, when the OBFN-PIC is configured to operate with sinusoidal waves at 5 and 10 GHz, as well as the corresponding theoretical values for all intended beam angles. Despite some slight angle deviation, which is mainly due to the impact of the noise power, the experimental and the theoretical array factors are in good agreement.

In addition to these initial tests, we validate the inherent capability of the OBFN to improve the SNIR at a desired direction, utilizing modulated microwave signals. In order to

do that, the OBFN-PIC was configured to steer a 500 Mbaud QPSK signal at 10 GHz to 60° beam angle. Figure 5.25 (a) shows the array factor as calculated using the samples acquired from the oscilloscope. As observed, the main lobe of the beam is directed to the intended direction, validating that the imposed delays by the three OTTDLs of the OBFN were chosen correctly. Figure 5.25 (b)-(d) present the reconstructed constellation diagrams at 60° , 20° and 110° . The constellation diagram at 60° is clear and indicates an error-free performance, whereas the constellation diagrams at 20° and 110° are both noisy due to the low signal power propagating to the corresponding directions.

As it was explained in Chapter 2, the intensity of the radiated field at each direction is the product of the square absolute value of the array factor with the radiation pattern of a single antenna element of the array. Within our system experiments, we assumed that the signals are transmitted by a linear 3-element antenna array formed by omnidirectional antenna elements. The type of the antenna elements simplified the calculation of the radiated field because an omnidirectional antenna radiates equal power in all azimuthal directions and thus, the radiation direction is dictated only by the array factor. For a given antenna array, the array factor is controlled only by the beamforming network and is maximized only at the angles that correspond to the delays imposed by the optical beamforming network. Ideally, if we further consider that the beamforming network does not introduce losses when the signals are delayed, the intensity at the maximum transmission direction (peak of the beam) is always constant and it does not depend on the selected beam angle. If within our calculations, we had considered directional antenna elements instead of the omnidirectional, we should have expected the angles that are closer to 90° to have a higher radiation intensity and thus, to exhibit a better system performance in terms of EVM and BER.

Figure 5.26 presents the constellation diagrams for all the experimental cases and every steering beam angle. In each diagram, the calculated EVM values based on the symbols that have been processed are shown as insets. More specifically, in case 1, the EVM ranges from 4.7% up to 6.4 % measured at 70° and 110° nominal beam angles, respectively. Similarly, in case 2 the lowest EVM is 7.1% at 90° and the highest 7.8% at 70° , while in case 3 the lowest is 7.6% at 90° and the highest 8.7% at 135° . As it can be observed, the EVMs for each case seems to depend on the steering angle. This would be valid if the beamforming network would induce significantly higher losses for imposing larger delays. However, when our OBFN-PIC imposes larger delays via the elongation of the optical paths, the additional losses are negligible and do not affect practically the power of the signals generated after the photodetection stage thanks to the ultra-low propagation characteristics of the TriPleX platform (0.1 dB/cm). Taking also into account that the OBFN-PIC is thermal-noise limited, the resultant SNRs and therefore the EVMs are dictated by the noise

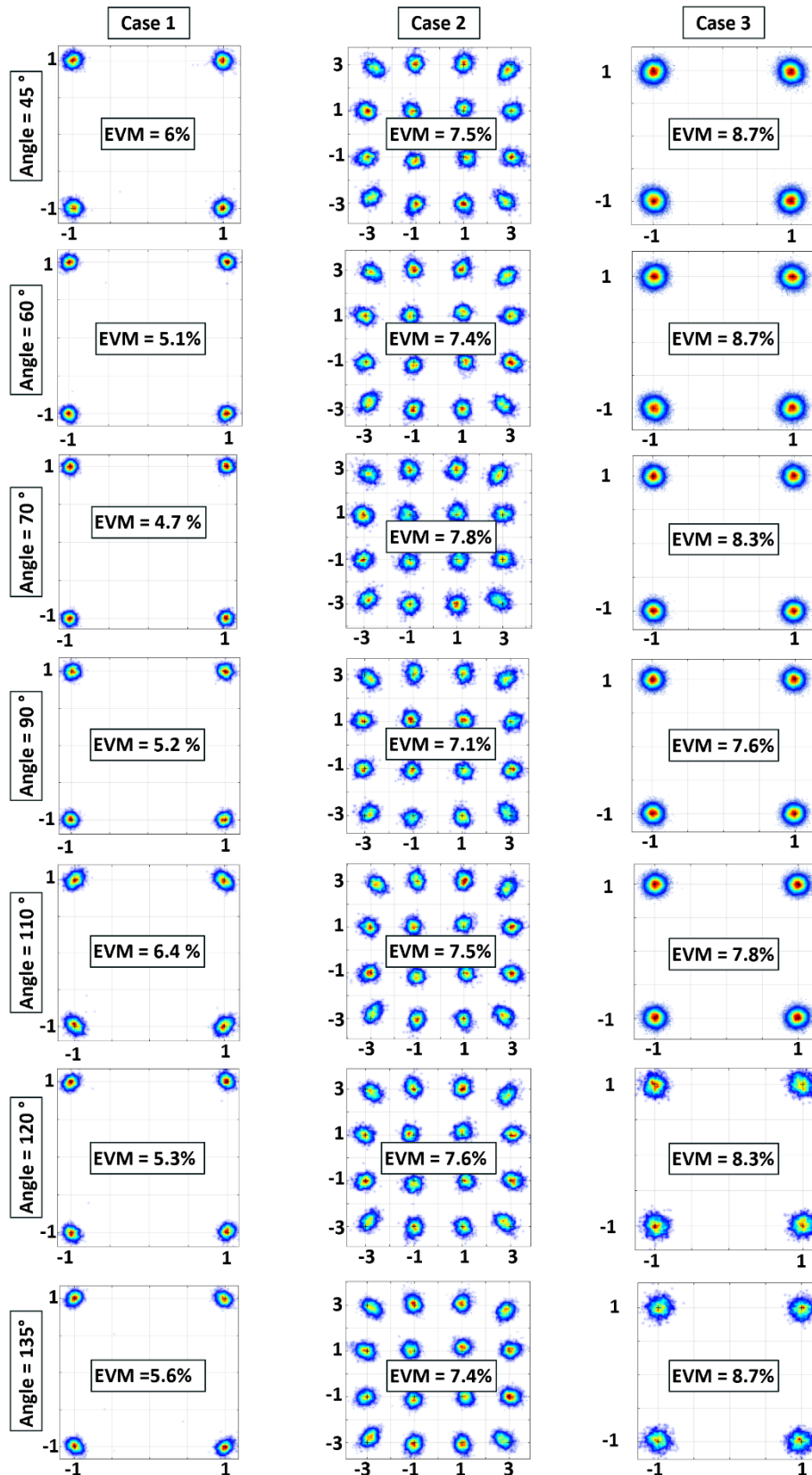


Figure 5.26: Reconstructed constellation diagrams for each experimental case. As insets are shown the calculated EVM values.

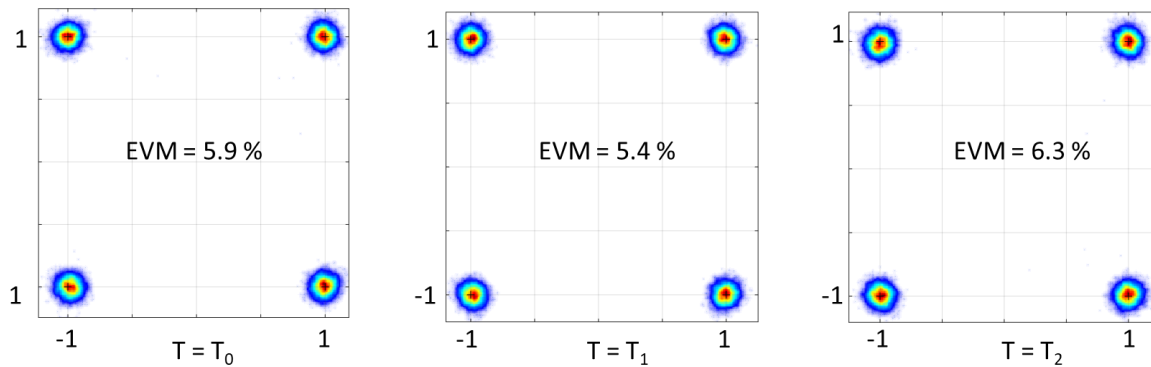


Figure 5.27: Constellation diagrams and the calculated EVMs for the case of steering a 500 Mbaud microwave signal modulated around a 5 GHz carrier at 45° , sampled and stored by the oscilloscope at different time instants.

power spectral density of the oscilloscope. In the analysis presented in the paragraph 5.3.2 regarding the measurement of the noise figure, it was concluded that the OBFN-PIC was thermal-noise limited. Within the system experiments, the operating temperature of the OBFN-PIC was stabilized to 30°C using Peltier elements with an accuracy better than 0.0012°C . As a result, the noise power spectral density of the OBFN-PIC was equal to -173.78 dBm/Hz , constant with respect to the observation time window. Therefore, the fluctuation of the EVMs was due to the noise induced by the real-time oscilloscope (RTO) used for sampling and storing the signals after the photodetection stage. In order to reduce the impact of the induced noise and the EVM fluctuation, in all the experimental cases and for all the channels of the RTO, we limited the measuring analog bandwidth to 12 GHz. At these settings, and by terminating the channels of the RTO with 50-ohm loads, we measured the average and standard deviation of the AC RMS value of the noise in over 10^7 acquisitions equal to $179.41\text{ }\mu\text{V}$ and $18.35\text{ }\mu\text{V}$, respectively. After this observation time window, both parameters fluctuated at the fourth decimal digit.

In order to assess the impact of the oscilloscope noise on the EVM, we configured the OBFN to steer a 500 Mbaud signal modulated around a 5 GHz carrier at 45° and we sampled the signals after the photodetection stage using the oscilloscope, at different observation times with a time interval in the order of few seconds. Within this experimental case, the OBFN was imposing 0 delay at the first path, 70.7 ps at the second path and 141.4 ps at the third path. The delay of the third path corresponds to the maximum delay imposed by the OBFN-PIC during the system experiments. Figure 5.27 presents the constellation diagrams and the corresponding EVMs after the offline processing. As observed, even though the configuration settings of the OBFN are stable (laser optical power, operating temperature, and delay settings), the EVM fluctuates by almost 1%. Despite this small fluctuation, the system has an error-free performance since no errors were detected. In order to minimize this fluctuation and considering that the noise power is dictated by the measuring bandwidth, in all the experimental cases the measuring bandwidth of the oscilloscope was limited at 12 GHz. Therefore, for a given operating microwave frequency, the OBFN can be successfully configured to any arbitrary beam angle without deteriorating the overall transmission performance.

Within the system experiments, the maximum delay was 141.4 ps, imposed at the $\text{PM}_1\text{-PD}_1$ link, and corresponds to the case 1 for beam angle at 135° . At these delay settings, the link gain of the $\text{PM}_1\text{-PD}_1$ link at 5 GHz was -38.53 dB , reduced by 0.25 dB compared to the corresponding value of the link gain curve, shown in Fig. 6. Furthermore, the NF at the same frequency was 38.53 dB while the SFDR_3 was $89.7\text{ dB}\cdot\text{Hz}^{2/3}$.

Finally, it should be noted that the increase of the EVM from the case 1 to the case 3 is due to the fact that the OBFN-PIC has higher NF in the frequency region around 10 GHz

compared to the region around 5 GHz, and consequently a lower SNR is achieved in case 3. In all cases, no errors were detected and as a result the calculated BER for cases 1 and 3 is equal to $5 \cdot 10^{-6}$ and $2.5 \cdot 10^{-6}$ for case 2, validating the beamforming potential of the demonstrated OBFN-PIC.

Conclusions of Chapter 5

In this chapter, the system demonstration of a 1×4 OBFN-PIC based on the hybrid integration of InP components in a TriPleX platform was reported. The prototype is a fully integrated and flexible optical signal processor in a very compact form that can handle and process high-frequency microwave signals purely in the optical domain. Compared to other state-of-the-art integrated optical beamformers, the reported OBFN-PIC stands out due to the co-integration of InP components that can support the generation, modulation, and detection of optical signals on-chip with a TriPleX processing unit that can induce continuously tunable true time delay into four optical paths. More specifically, the OBFN-PIC comprises a hybrid external cavity laser, two InP phase modulators, a TriPleX SSBFC optical filter, four TriPleX OTTDLs based on tunable MRRs, and four InP photodetectors. Thanks to the integration of the high-bandwidth modulators and photodiodes as well as of the eight cascaded MRRs in each OTTDL, the OBFN-PIC can process microwave signals with central frequencies up to 40 GHz and impose continuously tunable time delays over wide operating bandwidths without deteriorating the system performance. To the best of our knowledge, we provided for the first-time a concrete analysis of the system performance of a fully integrated OBFN-PIC. In specific, we have experimentally evaluated the performance of the OBFN-PIC to process microwave signals, by measuring the link gain for operating frequencies from 0.04 GHz up to 40 GHz, and the NF as well as the SFDR_{2,3} at 5 and 10 GHz. The maximum link gain was -36.98 dB measured at 2.6 GHz. The NF was calculated to be equal to 38.28 dB and 41.95 dB at 5 GHz and 10 GHz, respectively, and the SFDR₂ and SFDR₃ around 5 GHz were 70.5 dB·Hz^{1/2} and 89.9 dB·Hz^{2/3}, respectively, whereas around 10 GHz were 67.7 dB·Hz^{1/2} and 88.8 dB·Hz^{2/3}, respectively. Furthermore, using 500 Mbaud QAM signals at 5 and 10 GHz as input signals and an experimental setup that emulates the operation of the OBFN-PIC in the downlink direction of a wireless system, we have evaluated the EVM and BER performance of the decoded signals for beam angles ranging from 45° to 135°. In all cases, error-free performance has been successfully achieved. The average power consumption has been equal to 17.5 W.

References of Chapter 5

- [1] C. G. H. Roeloffzen et al., "Low-Loss Si₃N₄ TriPleX Optical Waveguides: Technology and Applications Overview," in *IEEE Journal of Selected Topics in Quantum Electronics*, vol. 24, no. 4, pp. 1-21, July-Aug. 2018, Art no. 4400321, doi: 10.1109/JSTQE.2018.2793945.
- [2] K. Worhoff, R. G. Heideman, A. Leinse, and M. Hoekman, "TriPleX: A " versatile dielectric photonic platform," *Adv. Opt. Technol.*, vol. 4, no. 2, pp. 189–207, 2015.
- [3] L. Zhuang, M. Hoekman, R. M. Oldenbeuving, K. Boller and C. G. H. Roeloffzen, "CRIT-Alternative Narrow-Passband Waveguide Filter for Microwave Photonic Signal Processors," in *IEEE Photonics Technology Letters*, vol. 26, no. 10, pp. 1034-1037, May15, 2014, doi: 10.1109/LPT.2014.2312718.
- [4] S. G. Hailu, and S. L. Lee. "Tunable Optical Delay Line Based on a Racetrack Resonator with Tunable Coupling and Stable Wavelength." *Applied Sciences* 9.24 (2019): 5483.
- [5] C. Kouloumentas, C. Tsokos, P. Groumas, L. Gounaridis, A. Raptakis, E. Mylonas, E. Andrianopoulos, K. Wörhoff, K. Ławniczuk, A. Leinse, H. Avramopoulos, "Multi-Rate and Multi-Channel Optical Equalizer Based on Photonic Integration," in *IEEE Photonics Technology Letters*, vol. 32, no. 23, pp. 1465-1468, 1 Dec.1, 2020, doi: 10.1109/LPT.2020.3035506.
- [6] H. Zhao et al., "High-Power Indium Phosphide Photonic Integrated Circuits," in *IEEE Journal of Selected Topics in Quantum Electronics*, vol. 25, no. 6, pp. 1-10, Nov.-Dec. 2019, Art no. 4500410, doi: 10.1109/JSTQE.2019.2908788.
- [7] V. J. Urick, K. J. Williams, and J. D. McKinney. "Fundamentals of microwave photonics." John Wiley & Sons, 2015.

Chapter 6 - System design, development, and baseline characterization of integrated optical beamforming network based on Blass matrix architecture

In this Chapter, a solid background for the design and operation of a multi-beam optical beamforming network based on Blass matrix is provided via a mathematical analysis and extensive simulation studies. More specifically, the analysis starts from the processing steps that are necessary for the microwave photonics signals at the input and output of the Blass matrix and a simple design and an algorithm for the configuration of the matrix, taking into account the properties of the MZIs as tunable optical couplers is proposed. Afterwards, the multi-beam capability of the beamforming network is validated and the impact of the beam squinting effect which is inherent to this design is evaluated as a function of the symbol rate, modulation format and pulse shaping of the signals. Assuming operation with QAM signals at 28.5 GHz, it is proven through EVM calculations that the beam squinting effect is not critical in typical cases, where the symbol rate remains below 3 Gbaud. Moreover, the additional frequency dependence of the proposed beamforming network due to inevitable asymmetries of the MZIs and length variations of the waveguides inside the Blass matrix, and the additional impact of imperfections is investigated with respect to the couplers inside the MZIs and the phase shifters inside the Blass matrix. In all cases, the impact of the asymmetries and the imperfections remains negligible for realistic fabrication and operation conditions.

Within the framework of the European funded project, ICT-HAMLET, the first-ever fully integrated optical beamforming networks based on the Blass-matrix architecture were designed, fabricated, and evaluated. The outcome of HAMLET project was the fabrication of a 2×2 and an 8×8 optical beamforming networks based on the hybrid integration of the InP, PolyBoard and TriPleX photonic platforms while the optical beam forming networks themselves were based on PZT-based phase actuators to enable their fast and low-power tuning. Both prototypes are extensively characterized in lab settings and the main individual building blocks are evaluated. However, due to the complexity of the integration of these systems, their system characterization could not be assessed. Nevertheless, the lessons learned from these testing campaigns have been used as the starting points for the design and fabrication of the next generation of optical beamforming networks based on the Blass-matrix which is currently being developed by the successor of HAMLET, TERAWAY.

6.1 Operating principle and design of optical Blass matrix beamforming network

Before going into the details of the Blass matrix design, we explain below the mechanism and the required processing steps for getting significant phase shift in the microwave domain via a corresponding phase shift in the optical domain.

Carrier suppression and re-insertion concept and relation between optical and microwave phase shifts: We take as example a simple signal y_{in} with two frequency tones at f_1 and f_2 , which fall within the frequency band of interest in the microwave or mm-wave regime:

$$y_{in}(t) = M_1 \cos(2\pi f_1 t + \varphi_1) + M_2 \cos(2\pi f_2 t + \varphi_2) \quad (6.1)$$

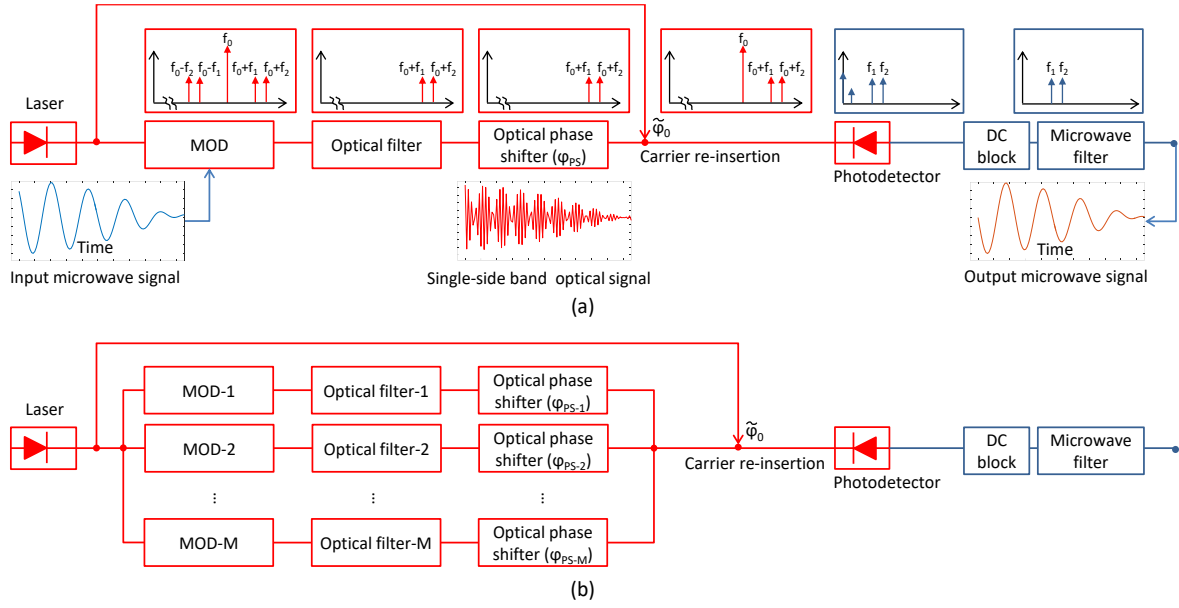


Figure 6.1: (a) Block diagram for the introduction of a phase shift on a microwave or mm-wave signal via the introduction of the same phase shift in the optical domain. The processing steps are based on microwave photonics techniques with optical carrier suppression, SSB propagation and carrier re-insertion. (b) Block diagram for the extension of the same concept to the case of multiple microwave signals carried by optical waves with the same optical carrier. At the end of the processing chain, the output signal is the sum of the input microwave signals, each with an independently selected phase shift.

, where M_1 , M_2 , φ_1 and φ_2 the amplitudes and the phases of the two tones, respectively. This microwave signal can modulate the amplitude of an optical carrier with frequency f_0 , resulting in an optical signal, which can be represented in turn as:

$$x_{in}(t) = A \cdot [1 + M_1 \cos(2\pi f_1 t + \varphi_1) + M_2 \cos(2\pi f_2 t + \varphi_2)] \cdot \exp[j \cdot (2\pi f_0 t + \varphi_0)] \quad (6.2)$$

, where A an amplitude factor and φ_0 the phase of the optical carrier. When this signal passes through an optical phase shifter, it acquires a phase shift φ_{PS} , which adds to φ_0 inside the exponential of Eq. 6.2. Unfortunately, if this signal is incident on a PD, the phase shift cannot pass on the generated photocurrent due to the square-law of the photodetection process, and thus it gets lost [1]. In order to prevent this loss and make this method useful for beamforming applications, certain processing steps are needed. As shown in Figure 6.1 after modulation the optical signal should pass through an optical filter to filter out its carrier and one of its side-bands, allowing for single-sideband (SSB) propagation through the optical phase shifter. At the output of the phase shifter, a copy of the carrier should be re-inserted in order to enable the beating process at the photodetector and to generate a photocurrent with a phase shift in the microwave domain as large as the phase shift in the optical domain. The details of this carrier suppression, SSB operation and carrier re-insertion process are better explained via the following equations. Using the exponential expression of cosine in Eq. 6.2, the optical signal can be represented as:

$$x_{in}(t) = A \cdot \exp[j \cdot (2\pi f_0 t + \varphi_0)] + \frac{A \cdot M_1}{2} \exp[j \cdot [2\pi(f_0 - f_1)] \cdot t + \varphi_0 - \varphi_1] + \frac{A \cdot M_2}{2} \exp[j \cdot [2\pi(f_0 - f_2)] \cdot t + \varphi_0 - \varphi_2] + \frac{A \cdot M_1}{2} \exp[j \cdot [2\pi(f_0 + f_1)] \cdot t + \varphi_0 + \varphi_1] + \frac{A \cdot M_2}{2} \exp[j \cdot [2\pi(f_0 + f_2)] \cdot t + \varphi_0 + \varphi_2] \quad (6.3)$$

Without loss of generality, we assume that the filter blocks the carrier and the lower side band, and allows for the propagation of only the upper side band, which is mathematically described by the last two lines in (6.3). At the output of the optical phase shifter, this SSB signal is written as:

$$x_{ps}(t) = \frac{A \cdot M_1}{2} \exp[j \cdot [2\pi(f_0 + f_1)] \cdot t + \varphi_0 + \varphi_1 + \varphi_{ps}] + \frac{A \cdot M_2}{2} \exp[j \cdot [2\pi(f_0 + f_2)] \cdot t + \varphi_0 + \varphi_2 + \varphi_{ps}] \quad (6.4)$$

Finally, after carrier re-insertion the optical signal becomes:

$$x_{out}(t) = \tilde{A} \cdot \exp[j \cdot (2\pi f_0 t + \tilde{\varphi}_0)] + \frac{A \cdot M_1}{2} \exp[j \cdot [2\pi(f_0 + f_1)] \cdot t + \varphi_0 + \varphi_1 + \varphi_{ps}] + \frac{A \cdot M_2}{2} \exp[j \cdot [2\pi(f_0 + f_2)] \cdot t + \varphi_0 + \varphi_2 + \varphi_{ps}] \quad (6.5)$$

, where \tilde{A} and $\tilde{\varphi}_0$ the new amplitude and the new phase of the optical carrier, which are different in the general case from A and φ_0 . When this signal is incident on a photodetector, the generated photocurrent $y_{out}(t)$ is by default proportional to the square of the $x_{out}(t)$ amplitude, and it can be described as:

$$y_{out}(t) \propto x_{out}(t) \cdot x_{out}^*(t) \quad (6.6)$$

, where $x_{out}^*(t)$ the complex conjugate of $x_{out}(t)$. Using the expression in Eq. 6.5, $y_{out}(t)$ can be calculated as a sum of direct current terms and exponential terms at $\pm f_1$, $\pm f_2$ and $\pm(f_1 - f_2)$. Using now the standard expression of cosine, and assuming the use of a proper coupling scheme to block the DC terms and the use of a microwave filter to block the low-frequency terms at $\pm(f_1 - f_2)$, the microwave signal at the output of the photodetector can be represented as:

$$y_{out}(t) \propto \tilde{A} \cdot A \cdot M_1 \cdot \cos[2\pi f_1 t + \varphi_0 - \tilde{\varphi}_0 + \varphi_1 + \varphi_{ps}] + \tilde{A} \cdot A \cdot M_2 \cdot \cos[2\pi f_2 t + \varphi_0 - \tilde{\varphi}_0 + \varphi_2 + \varphi_{ps}] \quad (6.7)$$

As observed in Eq. 6.7, both frequency components of the output microwave signal have acquired an additional phase shift φ_{ps} , which is equal to the optical phase shift of the upper side band, and thus it is adjustable via the optical phase shifter of the setup. The same conclusion can be extended to the case of an optical wave that carries an actual signal with continuous spectral content within a frequency band. To our specific interest in this work, it can be also extended to the case of multiple optical waves that have the same optical carrier, but carry different microwave signals and undergo different phase shifts, as shown in Figure 6.1b More specifically, it can be shown that the microwave signal that is derived after the combination of the individual upper side bands, the carrier re-insertion, the photodetection and the use of a DC block and a microwave filter, is the sum of the input microwave signals, each with an additional phase shift that is equal to the optical phase shift of its corresponding optical signal. This principle is the basis for the design and configuration of an optical Blass matrix beamforming network, as explained in the next paragraph.

Finally, it should be noted that it is not possible to obtain the same results in the case of double-side band operation. Following the same analysis, it can be shown that the presence of both side-bands in the optical domain results in phase shifts to opposite directions in the microwave domain after the carrier re-insertion and photodetection process, affecting the beamforming performance. In order to overcome this problem, working with SSB optical signals proves to be mandatory.

Layout of optical Blass matrix beamforming network: Figure 6.2 presents the layout of an optical Blass matrix beamforming network feeding N AEs and supporting the formation

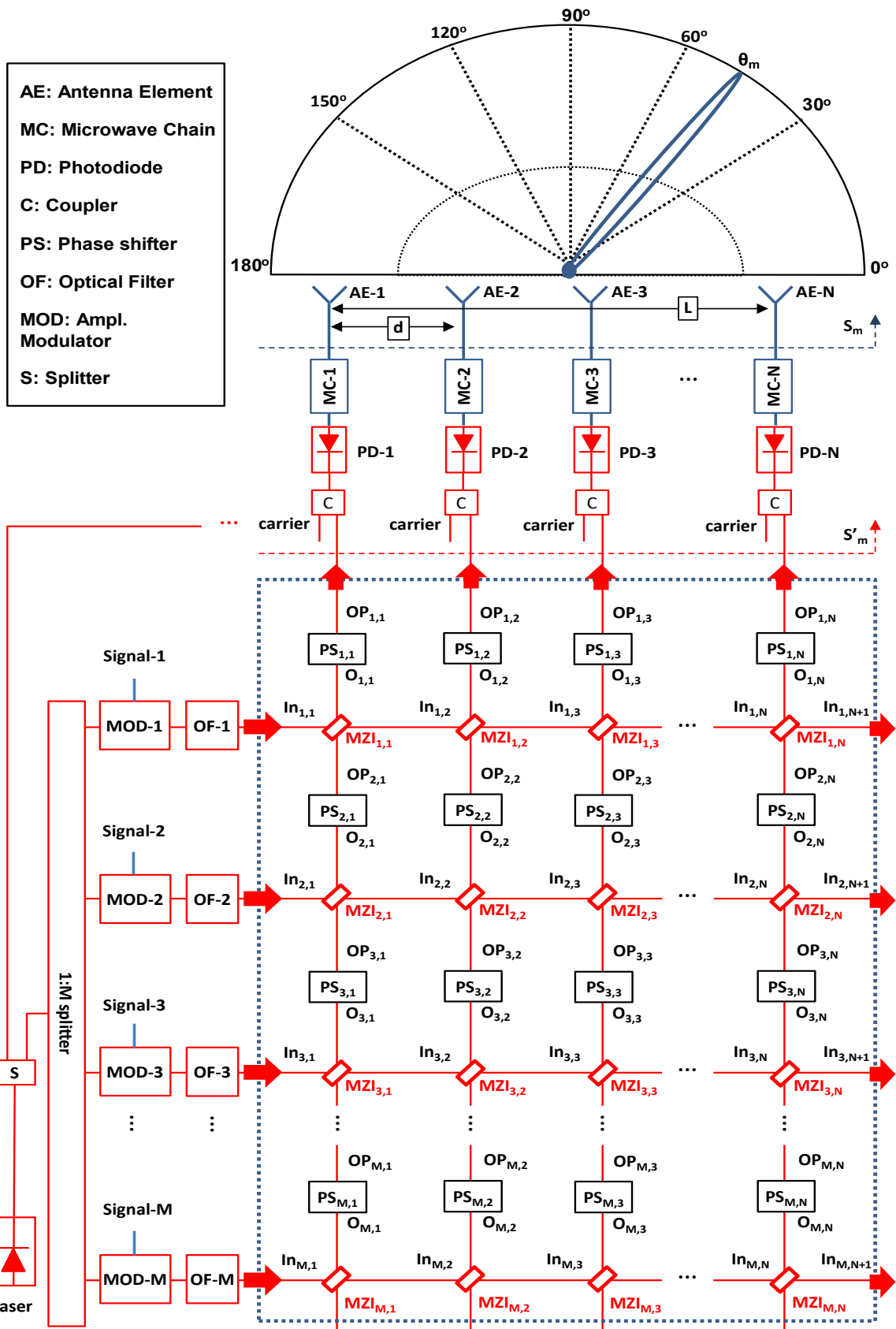


Figure 6.2: Layout of optical beamforming network based on Blass matrix feeding N antenna elements and supporting operation with up to M wireless beams.

of M independent beams. In this layout, an optical carrier is generated by a laser source and is split into two parts. The first part is reserved and bypasses the Blass matrix in order to be used during the carrier re-insertion process. The second one is further split into M parts in order to feed an amplitude modulator array driven by M independent microwave or mm-wave signals. At the output of this array, each optical signal passes through an optical filter in order to filter out its optical carrier and its lower side-band. This filter should be highly selective featuring very sharp transitions between its stop and pass bands. On a real integrated circuit, it can be implemented as an MZI with micro-ring resonators inside its arms and with proper phase shifters, which will allow for controlling the frequency allocation of its periodic stop- and pass-bands. After the filter, the upper side-band of each signal enters the Blass matrix from the corresponding input port. The Blass matrix consists of horizontal and vertical waveguiding lines (M rows and N columns) that are cross-connected by means of MZIs, which facilitate the splitting of each input signal into multiple parts that follow different light paths. Different subsets of these parts are destined for different AEs. The parts that belong to the same subset are split and finally recombined in a coherent way using a subgroup of MZIs that form a larger nested MZI. At the same time, the MZIs enable signals from different input ports to be combined in a coherent way again and be routed to the output ports on the top. Provided that the implementation of the Blass matrix is based on the use of a photonic integrated circuit, this coherent combination is stable and reconfigurable. The corresponding weights are adjusted by the coupling coefficients of the MZIs and the phase shifts that are induced by the phase shifters above each MZI. The signal at each output port on the top is recombined with part of the optical carrier, and is subsequently detected by a PD. Finally, each generated photocurrent enters the subsequent microwave chain and undergoes a number of processing steps including DC blocking, filtering and amplification in order to drive the corresponding AE of the multi-element antenna. It should be noted that part of the optical power that enters the Blass matrix gets inevitably lost, even in the case of ideal MZIs. The reason for this loss is that part of the optical power finds its way out of the Blass matrix not from the output ports on the top, but rather from the ports on the right side of the matrix. From the analysis so far, it is evident that the key building block of an OBFN based on a Blass matrix architecture is the MZI. The principle of operation of such an ideal MZI, working as tuneable coupler has been already presented in Chapter 5.1 and thus, it will not be repeated in this Chapter. For the reader convenience, we just repeat the mathematical Eq. 5.3 – 5.6. :

$$r_1 = \frac{1}{2} [\exp(j \cdot \theta) - 1] \quad (6.8)$$

$$k_1 = \frac{1}{2} \exp\left(j \cdot \frac{\pi}{2}\right) \cdot [\exp(j \cdot \theta) + 1] \quad (6.9)$$

$$r_2 = \frac{1}{2} \cdot [1 - \exp(j \cdot \theta)] = -r_1 \quad (6.10)$$

$$k_2 = \frac{1}{2} \cdot \exp\left(j \cdot \frac{\pi}{2}\right) \cdot [\exp(j \cdot \theta) + 1] = k_1 \quad (6.11)$$

In the following analysis, we retain the new notation of the above equations.

6.2 Configuration of optical Blass matrix

The configuration of the optical Blass matrix involves the proper tuning of its phase shifters $PS_{m,n}$ and its couplers $MZI_{m,n}$ in order to generate the intended number of wireless beams and steer them to the desired directions. The configuration process is very similar to

the process described in [2] for the case of a microwave Blass matrix, but it takes now into account the specifics of the optical implementation. It uses as an example the case of the linear antenna of Figure 6.2, and starts from the calculation of the excitation signal for each AE and each intended beam, based on the theory of multi-element antennas [3]. This linear antenna has N AEs with a distance d between them, which is equal to half the wavelength of the microwave carrier. Assuming that it can steer the beam at the azimuthal plane, the signal that should excite the n -th AE in order to form a beam at an angle θ can be written as [3]:

$$s_{m,n} = |s_{m,n}| \cdot \exp(j\alpha_{m,n}) = |s_n| \cdot \exp[-j \cdot (n - 1) \cdot k_c \cdot d \cdot \cos\theta] \quad (6.12)$$

, where $|s_n|$ and α_n the amplitude and phase of the excitation signal, n the order of the AE inside the array ($n = 1..N$), and k_c the wavenumber that corresponds to the carrier of the wireless signal. For uniform excitation, the amplitude is the same for all AEs and can be written in a normalized form as $1/\sqrt{N}$ so that the total excitation power is unity. For Gaussian apodization on the other hand, the amplitude follows a Gaussian distribution around the center of the array with standard deviation σ that depends on the intended degree of side-lobe suppression [4]. Again, the amplitudes can be normalized so that the total excitation power is still unity.

Following the methodology in [2], we can now extend the representation of Eq. 6.12 to the multi-beam case. Assuming a common carrier frequency for all intended beams, we can write the signal that should excite the n -th AE in order to have the direction of the m -th beam at angle θ_m , as follows:

$$s_{m,n} = |s_{m,n}| \cdot \exp(j\alpha_{m,n}) = |s_{m,n}| \cdot \exp[-j \cdot (n - 1) \cdot k_c \cdot d \cdot \cos\theta_m] \quad (6.13)$$

Using this representation, we can now organize the individual excitation signals in an excitation matrix \tilde{S} with dimensions $M \times N$ as follows:

$$\tilde{S} = \begin{bmatrix} S_1 \\ S_2 \\ S_3 \\ \dots \\ S_M \end{bmatrix} = \begin{bmatrix} S_{1,1} & S_{1,2} & S_{1,3} & \dots & S_{1,N} \\ S_{2,1} & S_{2,2} & S_{2,3} & \dots & S_{2,N} \\ S_{3,1} & S_{3,2} & S_{3,3} & \dots & S_{3,N} \\ \dots & \dots & \dots & \dots & \dots \\ S_{M,1} & S_{M,2} & S_{M,3} & \dots & S_{M,N} \end{bmatrix} \quad (6.14)$$

Within this matrix, each row gives the excitation vector S_m ($m=1\dots,M$) of the corresponding beam, whereas each column describes the signals that have to be superimposed in order to appropriately excite the corresponding AE and enable the beamforming of all intended beams.

Based now on the analysis of the previous paragraph, regarding the relation between the optical SSB signal and the generated microwave signal after carrier re-insertion, photodetection, DC rejection and microwave filtering, we can correlate in a direct way each excitation vector S_m with a new vector S'_m . The latter describes the set of the optical SSB signals $[s'_{m,1} \ s'_{m,2} \ s'_{m,3} \ \dots \ s'_{m,N}]$ that should be present at the output ports of the optical

Blass matrix in order to get the desired excitation vector S_m at the end. More specifically, by comparing the expression of the optical SSB signal in Eq. 6.4 with the microwave signal in Eq. 6.7, it is evident that the amplitude and phase relation between the elements of S_m will be exactly the same with the relation between the elements of S'_m , provided that the part of the optical carrier that is re-inserted has the same amplitude and the same phase for all AEs. In this way, the problem of setting the necessary amplitude and phase for the excitation signals $s_{m,n}$ based on the phasor expression of Eq. 6.14, translates into a problem of ensuring the same amplitudes and phases for the optical SSB signals $s'_{m,n}$ based on the same expression:

$$s'_{m,n} = |s'_{m,n}| \cdot \exp[-j \cdot (n - 1) \cdot k_c \cdot d \cdot \cos\theta_m] \quad (6.15)$$

Clearly, the phasor in Eq. 6.9 implies a wave with the same frequency as the wireless carrier f_c , whereas the phasor in Eq. 6.15 implies an optical wave with frequency $f_o + f_c$, where f_o the frequency of the optical carrier. However, in both expressions, the wavenumber k_c is associated with the wireless carrier.

As illustrated in Figure 6.2, we represent the optical signal that enters the $MZI_{m,n}$ from the left side as $E_{In_{m,n}}$, the optical signal that leaves the $MZI_{m,n}$ and enters the phase shift $PS_{m,n}$ as $E_{O_{m,n}}$, and the optical signal that leaves the phase shifter $PS_{m,n}$ and propagates further to the top as $E_{OP_{m,n}}$. With this convention, the input signals of the matrix are written as $E_{In_{m,1}}$, the signals that leave the matrix and enter the carrier re-insertion stage as $E_{OP_{1,n}}$, and the signals that get lost at the output ports on the right as $E_{In_{m,N+1}}$.

The steps for the configuration of the Blass matrix are summarized below having as reference the layout and the mathematical notation employed in Figure 6.2:

Step 1: Based on the input data regarding the angles θ_m and the type of excitation (uniform or Gaussian) for each beam, we calculate the vectors S'_m using the basic relation of Eq. 6.15 and a normalized form for the $|s'_{m,n}|$ so that the total power of each vector is unity.

Step 2: We define the maximum ER of the MZIs of the matrix.

Step 3: We also define ΔP as the excess signal power that we have to launch into the Blass matrix in order to ensure full flexibility in its configuration, including flexibility in the configuration of the MZIs in the last column of it. ΔP represents in fact the power of each input signal that will be wasted during propagation through the matrix, leaving the circuit from the output ports on the right. Given that the total power of each vector S'_m is unity, the use of this excess power means that the launching power of each input signal should be $1 + \Delta P$, making the power efficiency of the Blass matrix equal to $1/(1 + \Delta P)$. The amplitude of each input signal should be written now as:

$$|E_{In_{m,1}}| = \sqrt{1 + \Delta P} \quad (6.16)$$

From a practical point of view, the provision of this excess power for all input signals can be facilitated by using a laser source with higher output power by a factor of $(1 + \Delta P)$ at the expense of higher system power consumption.

Step 4: We start the solution of the matrix with the first row. We consider all input ports to be inactive apart from the first one ($E_{In_{m,1}} = 0$ for $m \neq 1$). Given the vector S'_1 we start the calculation of the coefficients and phase shifts from left to right. In more detail, given the target amplitude $|s'_{1,1}|$ and the input amplitude $|E_{In_{1,1}}|$, we calculate the amplitude of the self-coupling coefficient $|r_{1,1}|$ at $MZI_{1,1}$:

$$|r_{1,1}| = \frac{|s'_{1,1}|}{|E_{In_{1,1}}|} \quad (6.13)$$

Using Eq.6.8, we extract the phase shift ϕ_i inside $MZI_{1,1}$, and we calculate the amplitude and the phase of all coefficients ($r_{1,1}$, $r_{2,1}$, $k_{1,1}$ and $k_{2,1}$) at $MZI_{1,1}$, using Eq. 6.9-6.12. The output signals $E_{O_{1,1}}$ and $E_{In_{1,2}}$ are derived next as:

$$E_{O_{1,1}} = E_{In_{1,1}} \cdot r_{1,1} \quad (6.14)$$

$$E_{In_{1,2}} = E_{In_{1,1}} \cdot k_{1,1} \quad (6.15)$$

Finally, we calculate the phase shift $\phi_{1,1}$ at $PS_{1,1}$ using the following relation:

$$\varphi_{1,1} = \arg\left\{\frac{s'_{1,1}}{E_{O1,1}}\right\} \quad (6.16)$$

, where $\arg\{\cdot\}$ the argument, which is finally transferred within the range $[0, 2\pi]$. We continue to the right, using the output signal $E_{In_{1,2}}$ as the input for the next MZI, and we continue in the same way further to the right in order to calculate all coupling coefficients ($r1_{1,n}$, $r2_{1,n}$, $k1_{1,n}$ and $k2_{1,n}$) and all phase shifts $\varphi_{1,n}$.

Step 5: We continue with the second row. We consider this time all input ports to be inactive apart from the second one ($E_{In_{m,1}} = 0$ for $m \neq 2$), and we start the calculation of the coefficients and the phase shifts again from left to right. For the calculation of the parameters of $MZI_{2,1}$ and $PS_{2,1}$, we use the input signals $E_{In_{1,1}}$ and $E_{In_{2,1}}$, the information about the $MZI_{1,1}$ and $PS_{1,1}$ (from the previous step) and the target signal $s'_{2,1}$. We calculate first the signal $E_{OP_{2,1}}$ that we should use as the second input to the $MZI_{1,1}$, using the following relation:

$$s'_{2,1} = (E_{In_{1,1}} \cdot r1_{1,1} + E_{OP_{2,1}} \cdot k2_{1,1}) \cdot \exp(j \cdot \varphi_{1,1}) \quad (6.17)$$

In Eq. 6.17, $E_{In_{1,1}}$ is zero, and thus the first part of the expression within the parenthesis can be removed. All other parameters are either given or known from the previous step, facilitating the calculation of $E_{OP_{2,1}}$. The amplitude of the self-coupling coefficient $|r1_{2,1}|$ can be found next in a similar way as in Eq. 6.13 using the relation:

$$|r1_{2,1}| = \frac{|E_{OP_{2,1}}|}{|E_{In_{2,1}}|} \quad (6.18)$$

After that point, the amplitude and the phase of the coupling coefficients at $MZI_{2,1}$ and the phase shift $\varphi_{2,1}$ at $PS_{2,1}$ can be calculated in the same way as in the previous step. Having now the full information about the $MZI_{1,1}$ and $PS_{1,1}$ (from the previous step) and the $MZI_{2,1}$ and $PS_{2,1}$ (from the current step), we can derive the output signals $E_{In_{1,2}}$ and $E_{In_{2,2}}$ that continue their propagation to the right:

$$E_{In_{1,2}} = E_{In_{2,1}} \cdot r1_{2,1} \cdot \exp(j \cdot \varphi_{2,1}) \cdot r2_{1,1} \quad (6.19)$$

$$E_{In_{2,2}} = E_{In_{2,1}} \cdot k1_{2,1} \quad (6.20)$$

Using these two signals, the information about the $MZI_{1,2}$ and $PS_{1,2}$ (from the previous step) and the target signal $s'_{2,2}$, we can repeat the same process described above in the current step in order to calculate the coupling coefficients at $MZI_{2,2}$ and the phase shift $\varphi_{2,2}$ at $PS_{2,2}$. In this way, we can continue moving to the right and calculate all coefficients ($r1_{2,n}$, $r2_{2,n}$, $k1_{2,n}$ and $k2_{2,n}$) and all phase shifts $\varphi_{2,n}$.

Step 6: We continue in the same way with the rest of the rows ($m = 3..M$). For each row m and column n , we keep active only the input port of the specific row, and we calculate the parameters of the $MZI_{m,n}$ and $PS_{m,n}$, using the information about the target signal $s'_{m,n}$, the parameters of the $MZI_{m',n}$ and $PS_{m',n}$ in the previous rows ($m' = 1..m-1$), and the expressions of the signals $E_{In_{m'',n}}$ ($m'' = 1..m$) in the previous and the same row. At the end of this process, the parameters of all MZIs and phase shifters of the Blass matrix have been calculated. When having active all input ports, the signals $E_{OP_{1,n}}$ consist of a linear superposition of the signals $s'_{m,n}$, enabling the beamforming of N beams according to the specifications.

Step 7: We check and validate that the amplitudes of all coupling coefficients are meaningful, falling within the expected range (for example between 0.045 and 0.999 for 27 dB ER). In case this is not true, the solution of the mathematical problem has failed due to

the lack of sufficient optical power at the input of the matrix. The configuration steps 3 to 6 have to be repeated using a larger power margin ΔP .

As only an example, Table I presents the implementation of this configuration algorithm, summarizing the amplitude of the coupling coefficients $|r_{1,m,n}|$ and the phase shifts $\varphi_{m,n}$ for a 3×8 optical Blass matrix. In this particular example, the microwave carrier was 28.5 GHz, and the target directions of the three beams were 40° , 85° and 135° . Moreover, the target excitation type was uniform for beam 1, and Gaussian for beams 2 and 3 with standard deviation $L/2$ and $L/4$, respectively, where $L = (N - 1) \cdot d$ the total length of the antenna array. Finally, the employed power margin ΔP was only 0.08. Fig. 5 presents the diagram of the array factor that is obtained, if we use the signals $E_{OP_{1,n}}$ ($n = 1..8$), which emerge at the upper output ports of the matrix, as the basis for the excitation signals of the AEs, as per the description above. As it can be observed in this diagram, the multi-beam beamforming

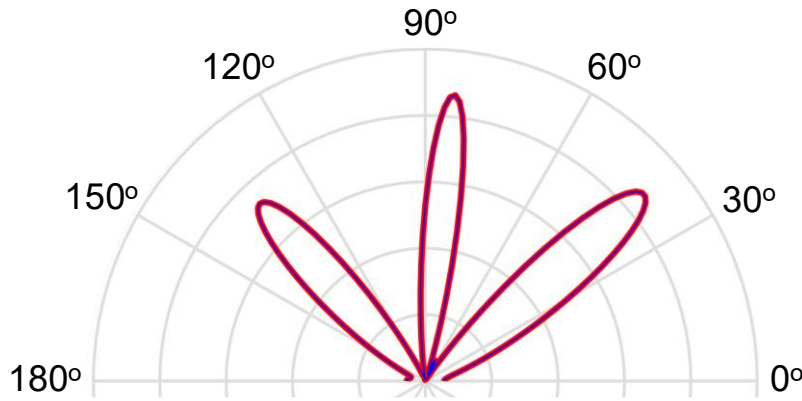


Figure 6.3: Example simulation of an optical Blass matrix beamforming network: Resulting array factor after configuration of a 3×8 Blass matrix for a wireless carrier at 28.5 GHz. Target beam directions were 40° , 85° and 135° , and the type of excitation was uniform for beam 1 and Gaussian for beams 2 and 3.

Table 11: Configuration of MZIs and phase shifters of the 3×8 optical Blass matrix for example of Figure 6.3: Amplitude of self-coupling coefficients and phase shifts.

Amplitude of self-coupling coefficients at $MZI_{m,n}$								
	(1)	(2)	(3)	(4)	(5)	(6)	(7)	(8)
(1)	0.34	0.36	0.39	0.42	0.46	0.52	0.62	0.78
(2)	0.26	0.33	0.39	0.51	0.57	0.58	0.77	0.95
(3)	0.08	0.22	0.42	0.64	0.74	0.74	0.4	0.43
Phase shifts at $PS_{m,n}$ (rad)								
	(1)	(2)	(3)	(4)	(5)	(6)	(7)	(8)
(1)	4.37	0.02	1.93	3.8	5.62	1.09	2.73	4.14
(2)	4.45	0.21	2.38	4.37	6.22	2.04	3.83	4.77
(3)	4.63	1.01	3.36	5.58	1.62	3.80	0.18	3.65

operation of the optical Blass matrix that is achieved is in perfect alignment with the target specifications. It should be noted, however, that our method ensures the optimum configuration of the Blass matrix for operation with the optical frequency $f_o + f_c$, and thus for wireless transmission with the microwave carrier f_c . For any other microwave frequency within the band of interest, the phase relations between the excitation signals are exactly the

same as for f_c . Hence, they do not satisfy the relation of Eq. 6.13 for the wavenumber of the new frequency, leading to the beam squinting effect. Moreover, an additional effect, which is specific to the optical implementation, can be also present degrading further the wireless radiation pattern. This effect is related to the frequency dependence of the amplitude and phase of the coupling coefficients, when there is asymmetry between the arms of an MZI. The next section presents extensive simulation studies that evaluate at first place the impact of the two effects on the beamforming performance of the optical Blass matrix for signals with different symbol rate, modulation format and pulse shaping parameters.

Finally, it should be also noted that the layout of the optical beamformer presented in Figure 6.2 is associated with the downlink direction in a wireless network, where the multi-element antenna transmits the signals to the users. In a true network, a second optical beamformer should be also present associated with the uplink direction allowing for the multi-element antenna to receive signals from the users with maximum gain from specific directions. Figure 6.4 depicts the layout of the corresponding optical beamformer based again on the Blass matrix architecture. In this case, the laser source, the $1 \times N$ optical splitter, the N modulators and the N optical filters are all from the side of the AEs. Each modulator corresponds to a specific AE and is driven by the electrical signal received by this AE. After propagation through the Blass matrix, the M output signals leave the matrix from the output ports on the left side, and propagate further through the carrier re-insertion stage before detection by the M PDs. Each PD corresponds for each intended receiving beam. The basic operating principles, mathematical analysis and steps of the configuration algorithm described above for the downlink direction remain the same also in the uplink case.

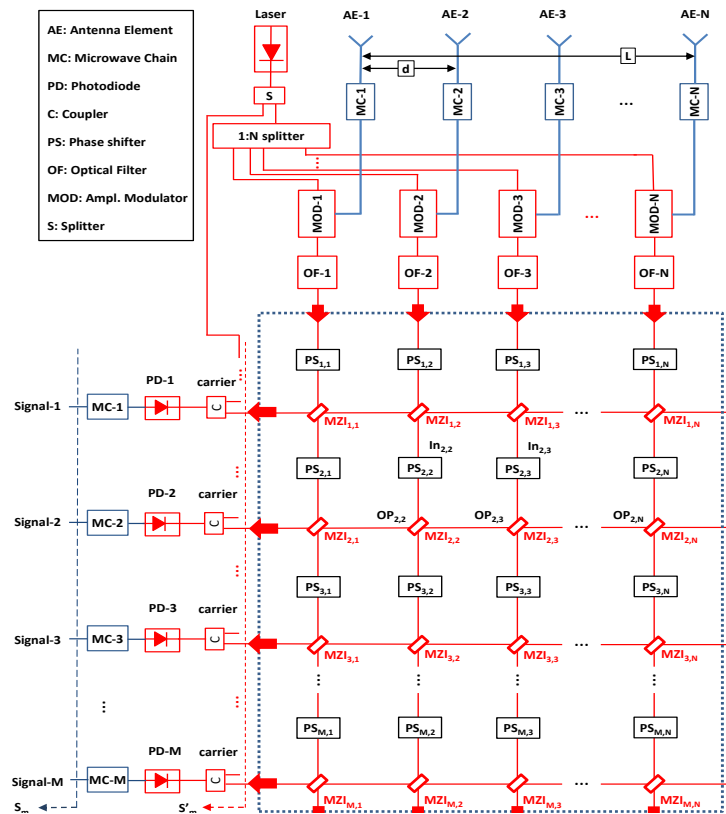


Figure 6.4: Layout of optical beamformer based on Blass matrix supporting operation with up to M beams in the uplink direction in a wireless network.

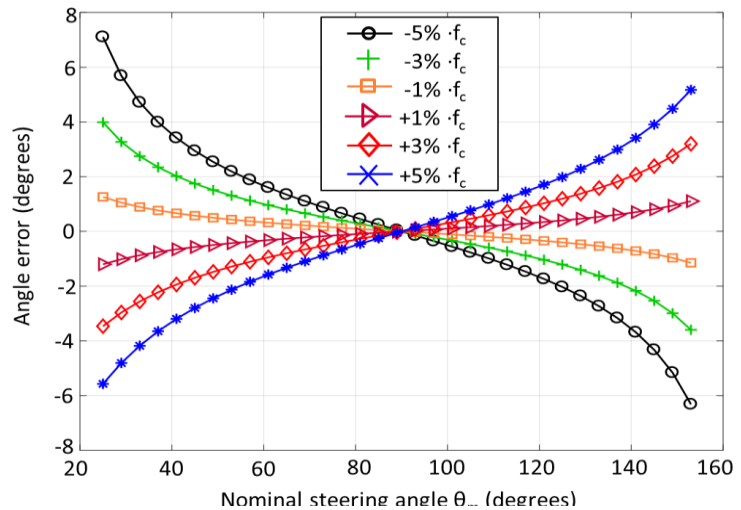


Figure 6.5: Beam squinting effect in optical Blass matrix beamforming network: Error of steering angle compared to the nominal value θ_m as a function of θ_m for different degrees of frequency offset from the nominal frequency f_c .

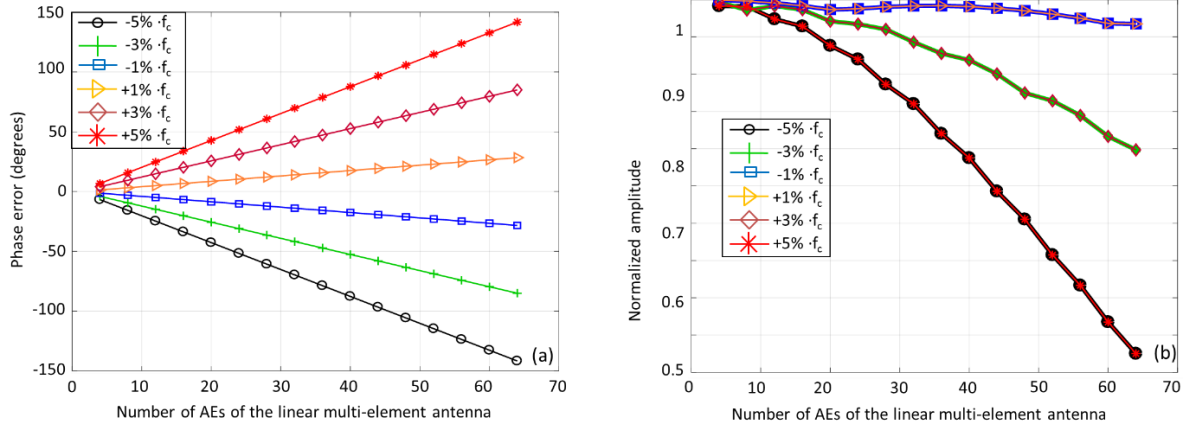


Figure 6.6 (a) Phase offset between the frequency under investigation and the nominal frequency f_c at 60° observation angle, as a function of the number of AEs for different degrees of frequency offset from f_c and (b) amplitude of frequency under investigation at 60° observation angle, as a function of the number of AEs for different degrees of frequency offset from the nominal value f_c . The amplitude is normalized to the corresponding amplitude of f_c at the same observation angle.

6.3 Validation of configuration algorithm and simulation studies

Beam squinting effect: Beam squinting is the effect, where different spectral components of a wireless signal are steered by the beamforming network to angles other than the angle of the carrier frequency f_c . It is present in beamforming networks based on phase shifters that ensure a constant phase relation between the elements of the vector S_m , irrespectively of the exact frequency. As such, it is also present in the optical Blass-matrix network of Figure 6.2 according to the analysis presented in the previous section. Figure 6.5 presents the error in the steering angle that we measure through simulations, when the Blass matrix is configured by our method for the nominal frequency f_c , but the spectral component under investigation has an offset Δf of ± 1 , ± 3 or $\pm 5\%$ with respect to f_c . As observed, the error compared to the nominal value θ_m is very small when θ_m is close to 90° , but it can be very large (i.e. almost 80°) when θ_m deviates significantly from this value. For a receiving device at a certain observation angle, the error of the beamforming network in the steering angle translates into a phase offset and amplitude attenuation of the frequency under investigation with respect to f_c . Figure 6.6(a) and Figure 6.6(b) investigate as an example the case of a receiving device at a moderate observation angle (60°), and present the phase offset and the amplitude attenuation, respectively, as a function of the number of AEs in the linear antenna array. As expected, the deviations that we measure for the same range of Δf (i.e. ± 1 , ± 3 or $\pm 5\%$) are much stronger, when the number of AEs is larger, and thus the beam width is smaller.

The impact of the beam squinting effect can be better assessed via the system evaluation of the beamforming, transmission, and detection process in the case of microwave QAM signals with true spectral content. An input optical signal with optical carrier f_0 , that carries a QAM signal with microwave carrier frequency f_c , can be represented as follows:

$$x_{in}(t) = A \cdot [I(t) \cdot \cos(2\pi f_c t) - Q(t) \cdot \sin(2\pi f_c t)] \cdot \exp[j \cdot (2\pi f_0 t + \varphi_0)] \quad (6.21)$$

, where A an amplitude factor, $I(t)$ and $Q(t)$ the in-phase and quadrature components of the QAM signal, and φ_0 the phase of the optical carrier. Despite the fact that the time dependence of the I and Q components result in a continuum of frequency tones around the carrier frequency f_c , the expression in Eq. 6.21 has the same structure as the expression in (2) that describes the modulation of an optical carrier by two discrete frequency tones. In this sense, the analysis presented in section II connecting in a direct way the optical phase

shift of the optical SSB signal with the microwave phase shift that is obtained after carrier re-insertion, photodetection, DC blocking and microwave filtering can be extended to the case of the optical signal of Eq. 6.21 carrying a microwave QAM signal. This possibility to translate a processing problem in the optical domain into a similar problem in the microwave domain is of high importance for our simulation study, as it eliminates the need for using sampling rates in the Tb/s regime and makes this study feasible with conventional computational resources. It is also important that this translation is realized without loss of information or generality apart from the information that is associated with the impairments (i.e. noise and nonlinearities) of the photodetection and microwave filtering processes. However, the study of these impairments was not within the scope of the present work.

Figure 6.7 presents the setup in MATLAB for the simulation of the communication system considered in this work. At the transmitter side, the symbol generator provides the samples for the I and Q component of the QAM signal that corresponds to each beam (point

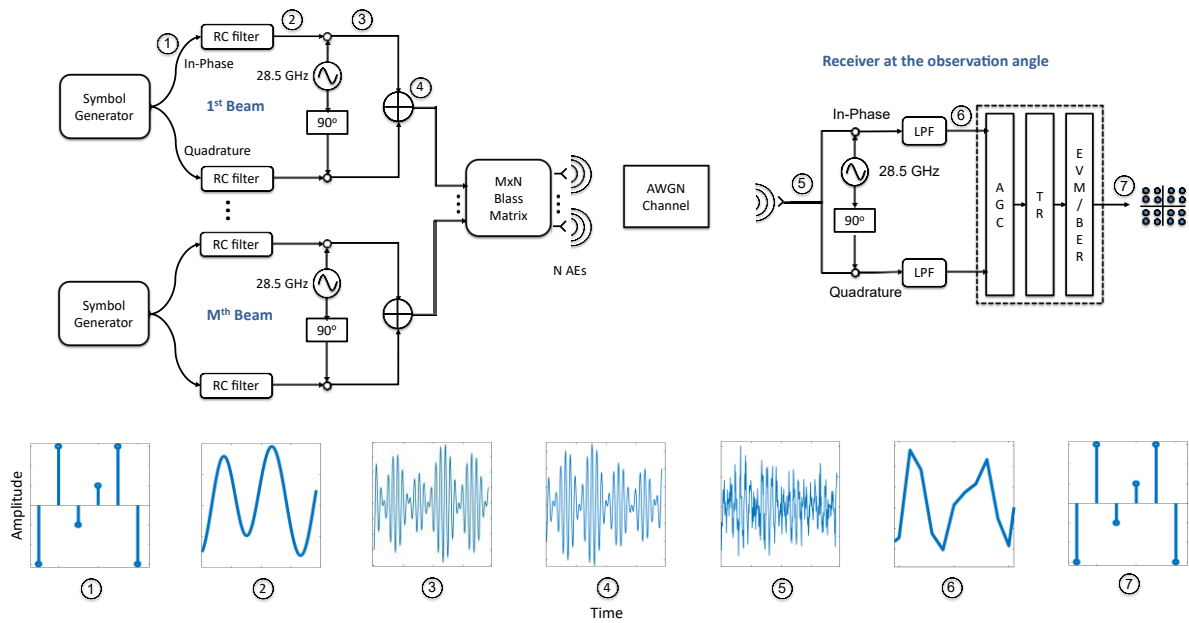


Figure 6.7: Set up for the simulation of a communication system involving the generation of microwave QAM signals, the beamforming process using an $M \times N$ Blass-matrix network, the interaction with an AWGN RF channel model, the signal reception at an observation angle, and the final decoding of the information.

1). Each component undergoes an up- sampling process and passes through a raised cosine (RC) pulse shaping filter, which limits the effective bandwidth of this component, and minimizes any inter-symbol interference effects. More specifically, the resultant bandwidth is given as:

$$BW = (1 + \beta) \cdot f_s / 2 \quad (6.22)$$

, where β is the roll-off factor and f_s the symbol rate of the input signals. At the output of these filters (point 2), the I and Q component are frequency up-converted using a local oscillator at 28.5 GHz, whereas a phase shifter is utilized for the introduction of a 90° phase difference ensuring their orthogonality (point 3). Subsequently, the two components are combined in order to form a microwave QAM signal (point 4) with band-pass bandwidth twice as large as the baseband bandwidth in Eq. 6.22. This QAM signal is now ready for the modulation of an optical carrier in order to form the optical signal that can be optically filtered and processed as a SSB signal by the Blass-matrix network. Based, however, on the previous discussion, this optical modulation stage can be omitted from the simulation chain, allowing for the direct use of the microwave QAM signals as inputs to the Blass matrix.

The Blass matrix itself is configured with the help of the configuration algorithm in the previous section, taking into account the intended direction and excitation type of each wireless beam. At the output ports of the Blass-matrix, the output signals feed the omnidirectional AEs of the linear antenna array, enabling the transmission of the QAM signals over a RF channel based on an AWGN model, which models in an abstract way a variety of noise contributions to the wireless signal. The SNR of the final signal at the receiver is a parameter in our simulations and is appropriately adjusted according to the order of the modulation format.

At the other end of the system, the receiver is placed at a specific observation angle. The microwave field that is calculated in point 5 is down-converted to the baseband, and analysed back into its I and Q components using a local oscillator at 28.5 GHz and a 90° phase shifter. A sharp LPF is also used at each branch in order to filter out the unwanted spectral components with the same cut-off frequency as the effective

Table 12: Modulation and beamforming parameters in a specific operation example of a 3×16 optical Blass-matrix beamforming network.

Beam	Mod. Format	Roll-off factor	Microwave carrier (GHz)	Steering angle (°)	Excitation type	SNR
1	4-QAM	0.5	28.5	40	Uniform	29
2	64-QAM	0.5	28.5	85	Gaussian	28
3	16-QAM	0.5	28.5	135	Gaussian	28

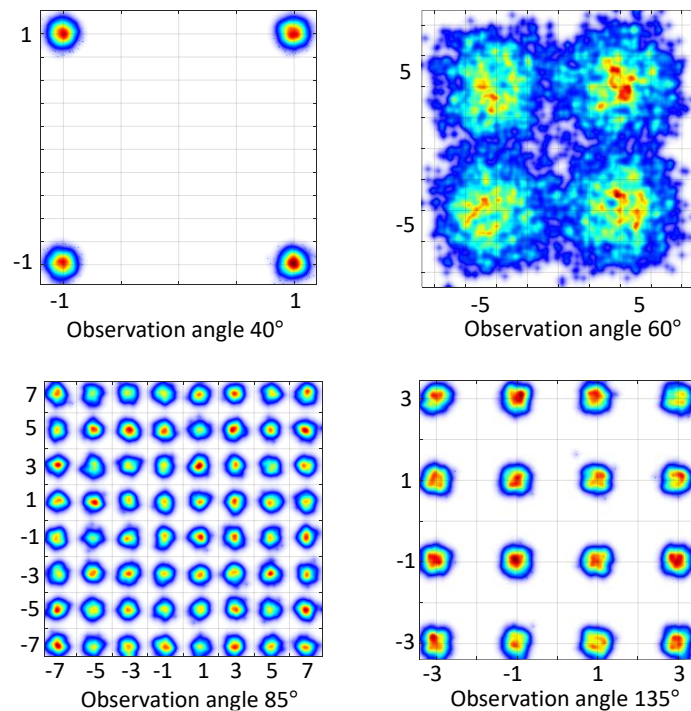


Figure 6.8: Decoded constellation diagrams at 40°, 60°, 85° and 135° observation angles for the multi-beam operation example summarized in Table 12.

baseband bandwidth of the signal (point 6). From that point on, a simple set of DSP algorithms are utilized in order to properly decode and assess the quality of the received signal. First, an automatic gain control algorithm scales the power of the signal to a specific power level, depending on the order of QAM format. Next, a time recovery algorithm recovers the symbol rate of the signal and identifies the optimal sampling instants, allowing for minimization of the ISI and provision of an optimum set of samples at the symbol rate

(down-sampling). Finally, this set is used for the extraction of the constellation diagram, the calculation of the EVM and the BER, and thus for the overall assessment of the quality of the beamforming and transmission system.

Using this simulation setup, we start our study from the re validation of the multi-beam capability of our beamforming network. We use the same example as in Fig. 5, working with a 3×8 Blass-matrix at 28.5 GHz and selecting with our algorithm the proper configuration for beam directions at 40° , 85° and 135° . The power margin is again 0.08, whereas the excitation type is uniform for beam 1 and Gaussian for beams 2 and 3. Unlike the case in Figure 6.3, we do not use here a simple carrier, but a QAM signal for each one of the three beams with 28.5 GHz carrier frequency, 1 Gbaud symbol rate and 0.5 roll-off factor. More specifically, we use a 4-QAM signal for the first beam, a 64-QAM signal for the second one and a 16-QAM signal for the third one. The employed modulation and beamforming parameters are summarized in Table 12. We underline that the purpose of this

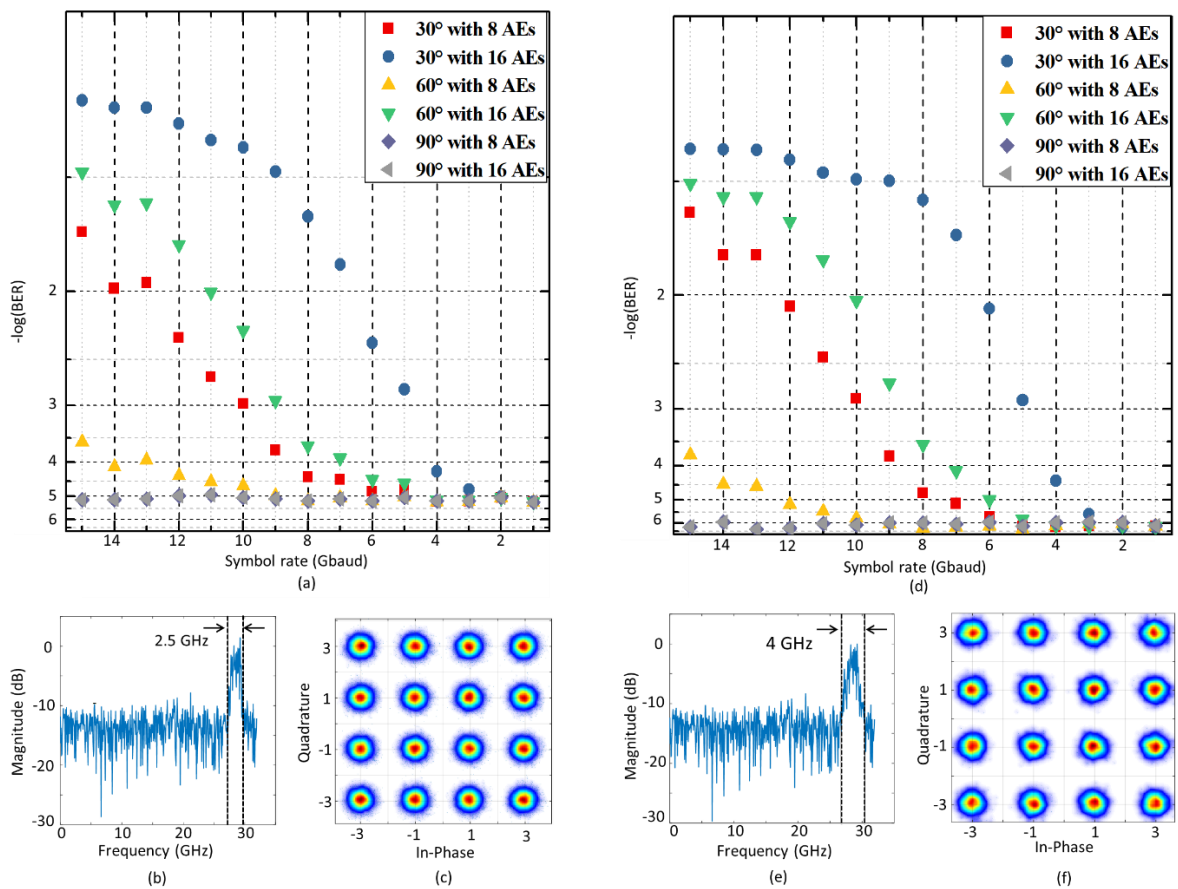


Figure 6.9: (a) Simulated BER as a function of the symbol rate for a 16-QAM signal with roll-off factor equal to 0.25, in the case of an antenna with 8 and 16 AEs, (b) RF spectrum after the AWGN channel for a 2 Gbaud signal and 16 AEs, and (c) the corresponding constellation diagram after the DSP. The SNR is 22 dB in the case of 8 AEs and 25 dB in the case of 16 AEs. (d) Simulated BER as a function of the symbol rate for a 16-QAM signal with roll-off factor equal to 1, in the case of an antenna with 8 and 16 AEs, (e) RF spectrum after the AWGN channel for a 2 Gbaud signal and 16 AEs, and (f) the corresponding constellation diagram after the DSP. The SNR is 22 dB in the case of 8 AEs and 25 dB in the case of 16 AEs.

study is not to compare the system performance in the case of different modulation formats, but to validate again the multi-beam beamforming of our optical Blass matrix design using the different modulation formats as an intuitive way to discriminate between the signals of each beam. We let the three signals get processed by the Blass matrix, and we receive the emitted signal at the nominal angles of 40° , 85° and 135° , as well as at an intermediate angle

of 60° . Fig. 11 depicts the reconstructed constellation diagrams at the four observation angles. As it can be observed, the constellation diagrams at 40° , 85° and 135° are very clear and correspond to the type of QAM signal that was intended to be steered to the specific direction. On the other hand, the constellation diagram for 60° is very blurry and noisy, as it contains normalized contributions from the three QAM signals via the main lobe or the side lobes of the three beams. The four constellation diagrams are in total agreement with the modulation and beamforming parameters of Table 12, and thus confirm the capability of the Blass-matrix of combining multiple inputs and generating the required excitation signals in order to steer these inputs to the target directions.

We focus now on the impact of the beam squinting effect in combination with the modulation parameters and the number of the AEs. In order to make simpler the simulation study, we keep the number of the possible beams equal to 3, but we set active only the third input port, resulting in a single beam under investigation. The excitation of the AEs for this

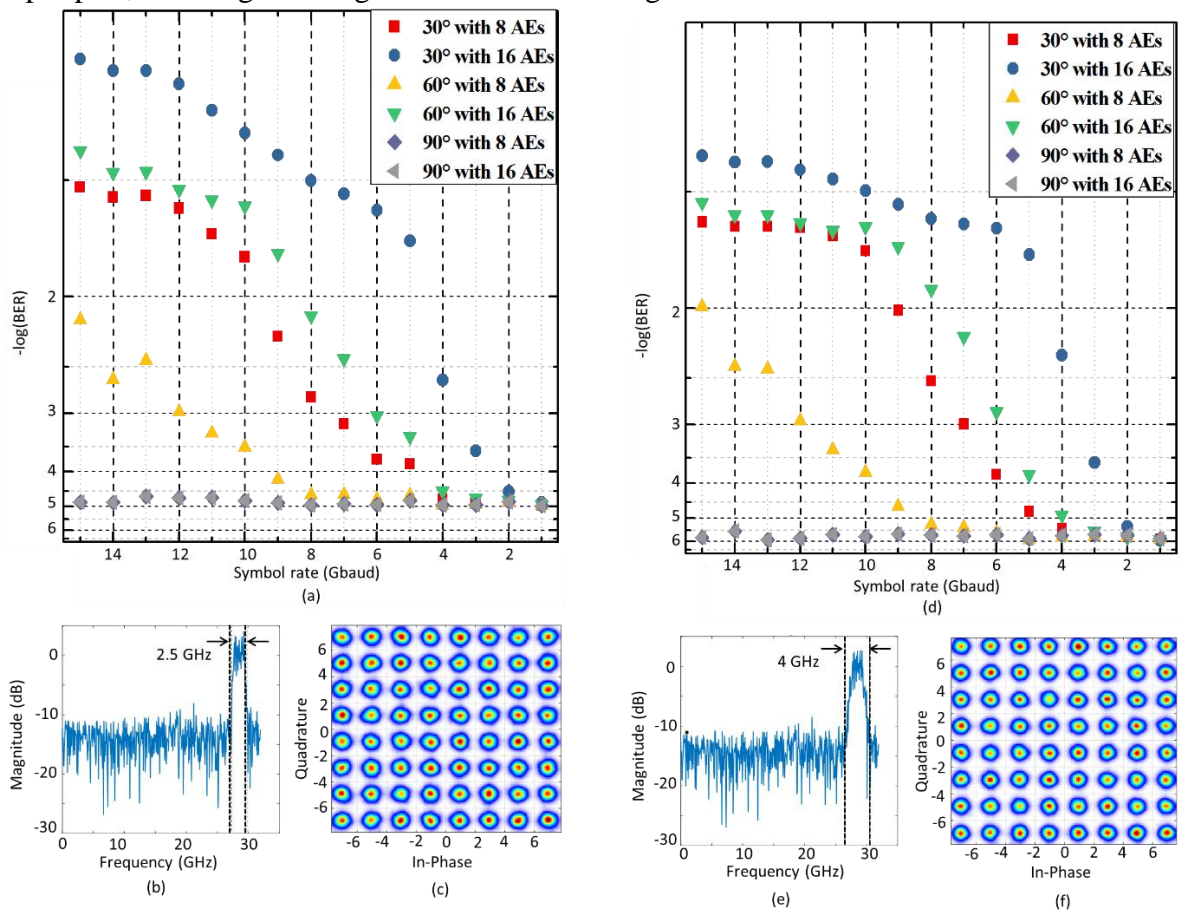


Figure 6.10: (a) Simulated BER as a function of the symbol rate for a 64-QAM signal with roll-off factor equal to 0.25, in the case of an antenna with 8 and 16 AEs, (b) RF spectrum after the AWGN channel for a 2 Gbaud signal and 16 AEs, and (c) the corresponding constellation diagram after the DSP. The SNR is 28 dB in the case of 8 AEs and 31 dB in the case of 16 AEs. (d) Simulated BER as a function of the symbol rate for a 64-QAM signal with roll-off factor equal to 1, in the case of an antenna with 8 and 16 AEs, (e) RF spectrum after the AWGN channel for a 2 Gbaud signal and 16 AEs, and (f) the corresponding constellation diagram after the DSP. The SNR is 28 dB in the case of 8 AEs and 31 dB in the case of 16 AEs.

beam is kept Gaussian with standard deviation $L/4$ as before. The final size of the Blass-matrix is thus 3×8 or 3×16 , depending on the number of AEs in the linear antenna array (either 8 or 16). Although this study corresponds to single-beam operation, the conclusions are general and can be extended in a direct way to the case of multi-beam operation. Figure 6.9(a), Figure 6.9(d), Figure 6.10(a), and Figure 6.10(d) present the calculated BER curves

as a function of the symbol rate for a 16-QAM and a 64-QAM signal, respectively, at 28.5 GHz. The roll-off factor for both formats is 0.25 and 1. The Blass-matrix is combined with a linear array having either 8 or 16 AEs, and it is configured so as to steer the beam at 30°, 60° or 90°. In the case of the 8-element array, the SNR is set at 22 dB for 16-QAM and 28 dB for 64-QAM. In order to take into account the increase in the directivity of the antenna when we go to the 16-element array, the resultant SNR can be approximated by adding 3 dB and setting its value at 25 dB for 16-QAM and 31 dB for 64-QAM. The main reason for the strong dependence of the BER on the symbol rate in almost all cases is the beam squinting effect. This can be easily understood from the fact that for a nominal angle of 90°, where the beam squinting effect is absent by default, error-free operation is achieved for every combination of modulation and antenna parameters including the case of extremely high symbol rates. The small variations of the error-floor between the different diagrams are not associated with the beam squinting effect, but rather with the specifics of the modulation format, pulse shaping and SNR in each case. As however, the nominal beam angle departs from 90°, the impact of the beam squinting effect becomes obvious. This impact is much stronger in the case of the smaller nominal angle (i.e. 30°), higher symbol rates and higher roll-off factor (i.e. $\beta = 1$). The latter has as a result a larger signal bandwidth around the carrier frequency, which leads in turn to larger phase differences between the spectral components of each signal. Moreover, the impact of the beam squinting effect is much stronger in the case of the 16-element array due to the fact that the wireless beam is much thinner. As a result, the large improvement in the BER for low symbol rates in the case of the 16-element array due to the higher SNR is inverted for ultra-high symbol rates due to the dominant role of the beam squinting effect in the case of these rates. This inversion is present both for 30° and 60° beam angles, but it occurs much earlier (i.e. for lower symbol rate) in the case of 30°.

Despite these variations, it should be noted that whatever the combination of the above parameters is, the BER remains lower than 10^{-3} , and thus below the forward error correction (FEC) limit, if the symbol rate remains lower than 3 Gbaud. Since this value is already very high, it indicates the tolerance of the system to the beam squinting effect. The diagrams in the bottom of Figs 12, 13, 14 and 15, depict indicative RF spectra and the decoded constellation diagrams for some of the cases, investigated in this study.

Finally, it should be also noted that the above evaluation results correspond to the case, where the receiver is placed exactly at the nominal angle of the beam. When there is an angle offset, the beam squinting effect acts in combination with the drop in the received power leading to further degradation of the signal quality. For all nominal angles and absolute values of the angle offset, this degradation is smaller when the offset brings the receiver angle closer to the 90°, and larger when it takes it closer to the 0° or 180°.

Frequency dependence and impact of the MZI asymmetry: In the second part of our simulation study, we focus on the impact of the additional frequency dependence, which can be present in our beamforming network. This dependence is associated with the possible asymmetry of the MZIs, and thus it is specific to the optical implementation of the Blass-matrix, which is analyzed in this work. We model this inevitable asymmetry as an additional length ΔL in the upper arm, which can be either positive or negative so as to cover all cases. Using the same notation as in the previous paragraph, we can find again the expressions for the self- and cross-coupling coefficients in the case of inputs from the first and second port as follows:

$$r1 = 1/2 \left[\exp \left(j \cdot \left(\varphi_i + \frac{2\pi \cdot f \cdot \Delta L \cdot n_g}{c} \right) \right) - 1 \right] \quad (6.23)$$

$$k1 = 1/2 \exp(j \pi/2) \left[\exp \left(j \cdot \left(\varphi_i + \frac{2\pi \cdot f \cdot \Delta L \cdot n_g}{c} \right) \right) + 1 \right] \quad (6.24)$$

$$r2 = 1/2 \left[1 - \exp \left(j \cdot \left(\varphi_i + \frac{2\pi \cdot f \cdot \Delta L \cdot n_g}{c} \right) \right) \right] \quad (6.25)$$

$$k2 = \frac{1}{2} \exp \left(j \frac{\pi}{2} \right) \left[\exp \left(j \cdot \left(\varphi_i + \frac{2\pi \cdot f \cdot \Delta L \cdot n_g}{c} \right) \right) + 1 \right] \quad (6.26)$$

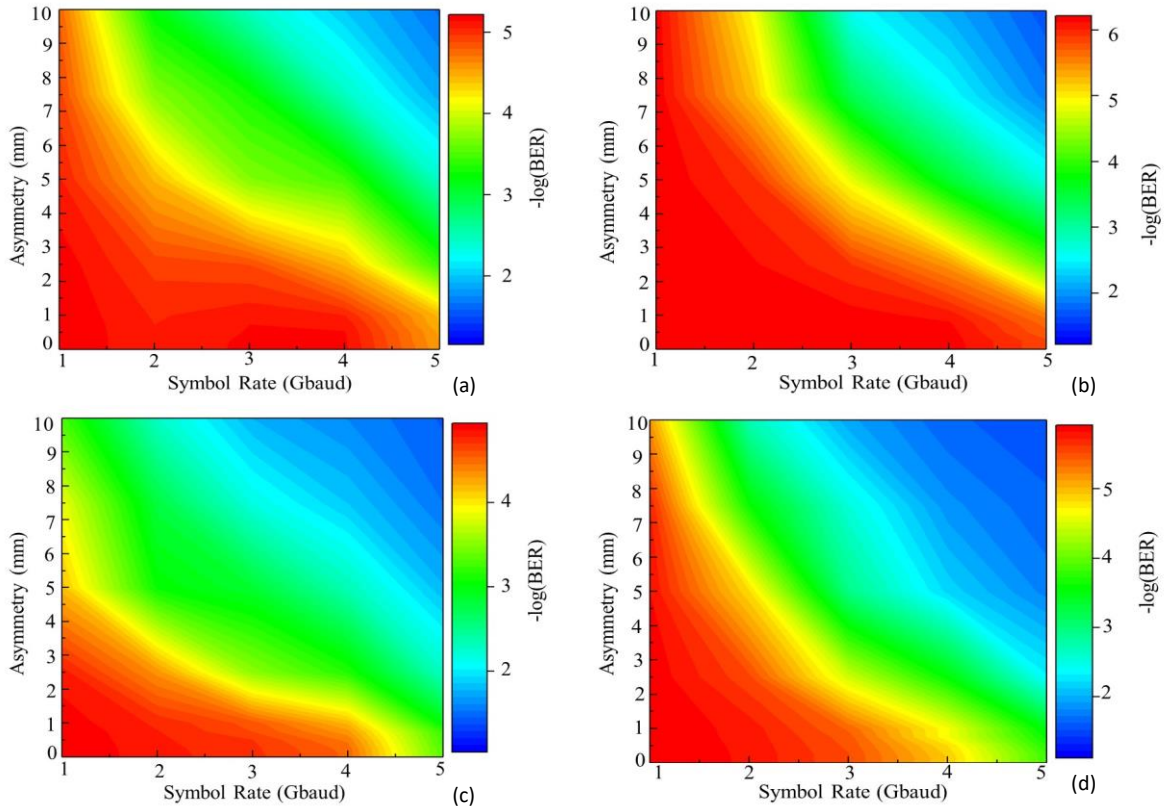


Figure 6.11: (a) BER of decoded 16-QAM signal (roll-off factor 0.25) at 60° observation angle as a function of the symbol rate and the asymmetry of the MZIs (ΔL_{HW}) inside a 4×16 optical Blass matrix. (b) BER of decoded 16-QAM signal (roll-off factor 1) at 60° observation angle as a function of the symbol rate and the asymmetry of the MZIs (ΔL_{HW}) inside a 4×16 optical Blass matrix. (c) BER of decoded 64-QAM signal (roll-off factor 0.25) at 60° observation angle as a function of the symbol rate and the asymmetry of the MZIs (ΔL_{HW}) inside a 4×16 optical Blass matrix. (d) BER of decoded 64-QAM signal (roll-off factor 1) at 60° observation angle as a function of the symbol rate and the asymmetry of the MZIs (ΔL_{HW}) inside a 4×16 optical Blass matrix.

, where f the optical frequency under investigation and n_g the group refractive index of the waveguide, which is supposed to be constant in a first order approximation. As observed in these expressions, the MZI asymmetry ΔL introduces a frequency dependence of the coupling coefficients. As a result, when the input is an optical SSB signal with continuous spectral content around the optical frequency $f_0 + f_c$, its different spectral components will

be subject to different coupling coefficients, when they enter the MZIs inside the Blass-matrix. The algorithm that has been presented in paragraph 6.2 can take into account the MZIs' asymmetry and compensate for it for the optical frequency $f_0 + f_c$, ensuring that the excitation signals for the microwave carrier frequency f_c will have the correct phases and amplitudes. For all other spectral components however, the effect of the MZIs' asymmetry will be present introducing errors in the intended coupling coefficients. Even with this correction, a mechanism for the suppression of the temperature fluctuations should be also present in order to cancel out the thermal drifts that can lead to the reappearance of errors for the f_c . On the other hand, it should be noted that in the absence of compensation of the MZIs' asymmetry for the f_c via corrective adjustment of the phase shifters inside the MZIs, the excitation errors for the f_c will not have a catastrophic effect on the signal, but will result in an additional rotation of the constellation diagram of the wireless signal. However, this rotation can be easily removed using a simple carrier phase recovery (CPR) algorithm in the DSP chain of the receiver.

In order to evaluate the impact of the MZI's asymmetry, we use again the simulation setup of Figure 6.7 for single-beam operation, using a 4×16 Blass matrix with active only its fourth input port. Since the asymmetry of each MZI is random in nature, we use a statistical distribution to assign the asymmetry value to each one of the 64 MZIs in our matrix. Without using real statistics about the fabrication imperfections and tolerances, we use the uniform distribution as a bad case scenario to characterize the asymmetry ΔL of the MZIs. We choose the distribution to be placed around 0, and we use its half-width (ΔL_{HW}) as a free parameter in our study. For example, use of a ΔL_{HW} equal to $10 \mu\text{m}$ imposes that the actual asymmetry of each MZI falls within the $[-10 + 10] \mu\text{m}$ range with a probability that respects the uniform distribution. For each ΔL_{HW} value and each modulation case, we use a Monte Carlo simulation method and repeat the simulation experiment for 200 times in order to calculate the mean BER value of the decoded signal. Four specific cases are studied with QAM modulation at 28.5 GHz, and beam direction at 60° with uniform excitation. These cases involve a 16-QAM signal with roll-off factor 0.25, a 16-QAM signal with roll-off factor 1, a 64-QAM case with roll-off factor 0.25 and a 64-QAM case with roll-off factor 1. The SNR of the channel is 22 dB in the case of the 16-QAM signals and 28 dB in the case of the 64-QAM signals. Finally, the symbol rate serves as a second free parameter in our study ranging from 1 to 5 Gbaud, which is still an ultra-high value for 5G systems operating at 28.5 GHz. In all cases, the configuration algorithm is used in order to compensate for the MZIs' asymmetry for the carrier frequency of 28.5 GHz.

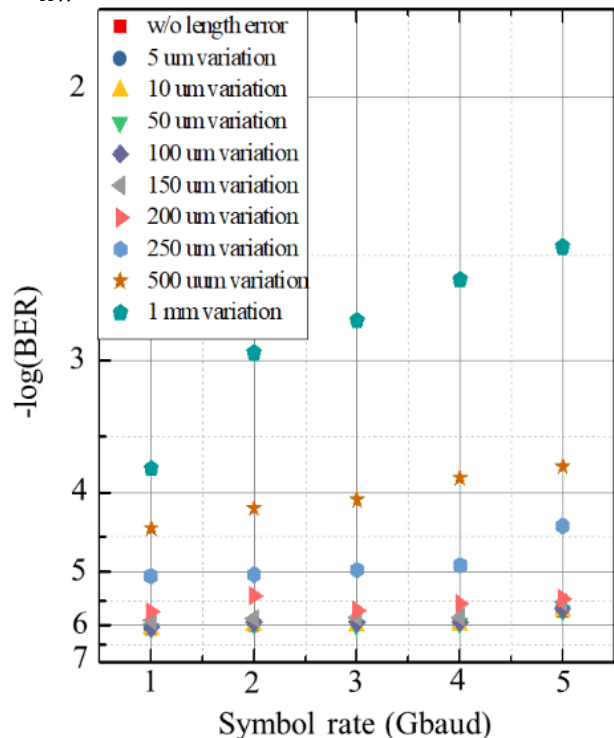


Figure 6.12: BER of decoded 16-QAM signal (roll-off factor 1) at 60° observation angle as a function of the symbol rate and the length variation of the waveguides between successive MZIs (ΔL_{HW}) inside a 4×16 optical Blass matrix.

Figure 6.11(a)-(d) depict the contour plots that correspond to the four cases and the full space of the two free parameters. As observed, the additional dependence of the BER performance on the asymmetry of the MZIs does exist, adding up to the symbol rate dependence due to the beam squinting effect. In a similar way as the beam squinting, this additional dependence gets stronger for signals with wider spectrum, when the symbol rate and/or the roll-off factor is higher. On the other hand, it should be noted that the MZI asymmetry starts having a measurable impact only when the value of the asymmetry becomes unrealistically large (i.e. ΔL_{HW} larger than 500 μm or even 1 mm in Figure 6.11(a)-(d)). Given that in all typical photonic integration platforms, the asymmetry of typical MZI structures is not expected to be larger than 5 μm even in the worst case scenarios, these simulation results confirm that from a practical point of view, the MZI asymmetry cannot be a problem in the optical implementation of the Blass-matrix beamforming concept.

The same concerns regarding the MZIs' asymmetry in an actual implementation can be also extended to the overall structure of the Blass matrix. Every input port is connected to every

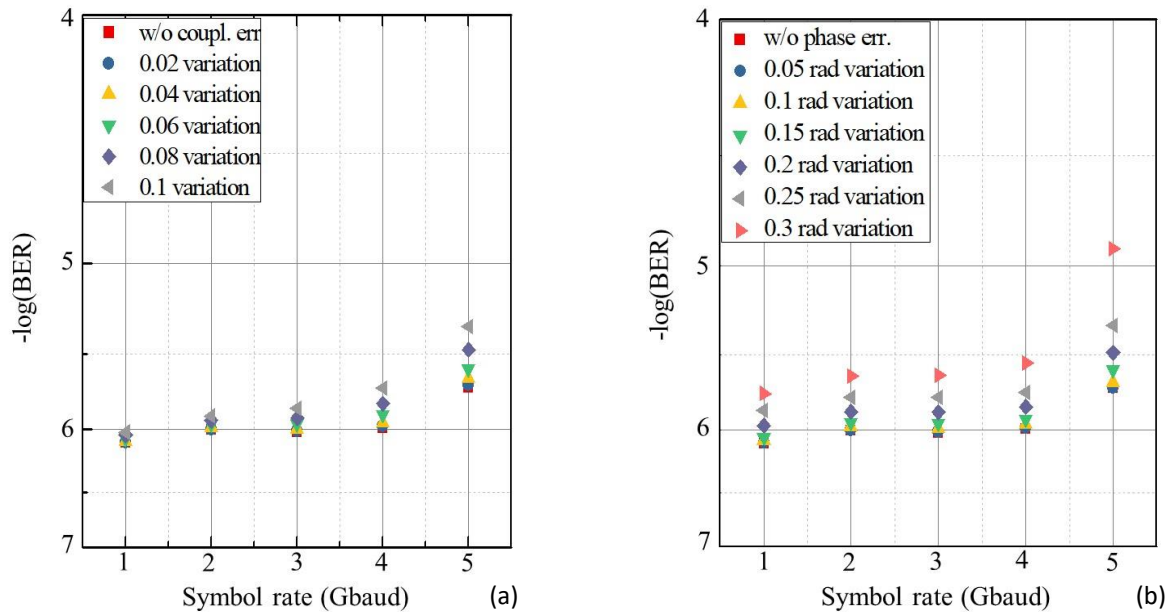


Figure 6.13: (a) BER of decoded 16-QAM signal (roll-off factor 1) at 60° observation angle as a function of the symbol rate and the variation in the power coupling ratio of the couplers inside the MZIs of a 4×16 optical Blass matrix. The variation is described by the half-width of a uniform distribution (ΔCR_{HW}). (b) BER of decoded 16-QAM signal (roll-off factor 1) at 60° observation angle as a function of the symbol rate and the variation in the phase shifts of the phase shifters inside a 4×16 optical Blass matrix. The variation is described by the half-width of a uniform distribution ($\Delta\phi_{HW}$).

output port via a complex interferometer in the form of a nested MZI structure. Longer or shorter paths in the waveguides that interconnect successive MZIs along a row or a column of the matrix result in asymmetries that affect the phases and the amplitudes of the frequencies within the bandwidth of interest in a similar way as the asymmetry of the individual MZIs. In this case however, there is not an obvious way to calibrate out the errors that are generated for the microwave carrier frequency, but there is always the possibility to remove the resultant rotation of the constellation diagram using a CPR algorithm, as explained above. In order to model this effect, we use again a uniform statistical distribution of additional lengths (either positive or negative) for each one of these waveguides between successive MZIs and investigate the impact on the BER. To keep this study short, we consider again the case of a 4×16 Blass matrix with uniform excitation and active only the

fourth input port, but we investigate only the case of a 16-QAM signal with roll-off factor equal to 1, SNR equal to 22 dB and beam direction at 60° . We use again a Monte Carlo method with 200 simulation experiments, and we calculate the mean BER value for each combination of symbol rate and half-width (ΔL_{HW}) of the distribution that corresponds to the additional length of the waveguides. Figure 6.12 summarizes the results for ΔL_{HW} equal to 5, 10, 20, 50, 100, 150, 200, 250, 500 and 1000 μm and for symbol rate up to 5 Gbaud, and reveals that the impact of this length variation is negligible for values of ΔL_{HW} up to 150 μm , which is far beyond the variation we can have in true integrated circuits.

Impact of coupler and phase shifter imperfections: Two more practical aspects of the optical implementation that can have an impact on the system performance are associated with the accuracy in the fabrication of the two couplers inside each MZI and the accuracy in the adjustment of each phase shifter inside the matrix. In the mathematical relations of our analysis in Eq. 6.8-6.11, the two couplers inside each MZI have been supposed to provide a perfect 50:50 power coupling ratio for the input signals. Due to inevitable fabrication imperfections however, their coupling ratios will never be precisely 50:50, but will slightly deviate. In order to model these deviations and investigate their impact on the BER of the signals, we use again a uniform statistical distribution for the coupling ratio of the couplers that are inside the MZIs of the Blass matrix. We also employ the same simulation setup as above based on the 4×16 Blass matrix with active only its fourth port, and investigate the case of a 16-QAM signal with roll-off factor equal to 1, SNR equal to 22 dB and beam direction at 60° . Finally, we use the same Monte Carlo method with 200 simulation experiments and calculate the mean BER for each combination of symbol rate and half-width of the coupling ratio distribution ($\Delta \text{CR}_{\text{HW}}$). Within this simulation setup the total number of MZIs is 64 and thus the total number of the couplers is 128. As observed in Figure 6.13(a), the variation of the coupling ratios has indeed an impact, but this impact is very low for all symbol rates up to 5 Gbaud, if the $\Delta \text{CR}_{\text{HW}}$ is up to 0.04 (i.e. if the coupling ratio varies from 0.46 to 0.54), which is absolutely feasible in all photonic integration platforms today. It is noted that in order to get these BER results, the use of a CPR algorithm at the receiver is necessary.

In a similar way, we model the deviations that will be inevitably present in the actual phase shifts compared to their nominal values due to imperfections in the electronics that drive the phase shifters inside the Blass matrix. In order to model these deviations we employ the same method and simulation setup as before, and use a uniform distribution for the phase shifts of all phase shifters inside the Blass matrix (128 in total) around their nominal values. Figure 6.13(b) summarizes the mean BER for the different combinations of symbol rates and half widths of the phase variation ($\Delta \phi_{\text{HW}}$) and reveals that the impact on the BER performance is very low even for large half widths up to 0.25 rad. Also in this case, the use of a CPR algorithm is necessary in order to cancel out the phase errors for the microwave carrier frequency and remove the additional rotation of the constellation diagram of the signal.

Optical losses: A further issue that can limit the performance of the optical beamforming system is the difference in the optical losses that is always present between the signals that enter the matrix from different input ports and leave it from different output ports. We take as example the 3×4 Blass matrix network shown in Figure 6.14 having distance α between successive rows and distance β between successive columns. These values do not involve only the physical length of the waveguide between the output port – input port of successive MZIs in each dimension, but also the physical length of the MZIs itself. Without special care in this example, the part of any input signal that is directed to the fourth output port

(Output 4) has to propagate over a distance that is longer by 3β compared to the distance covered by the part of the same signal that is directed to the first output port (Output 1). Moreover, the part of the third input signal that is directed to any output port is longer by 2α compared to the distance covered by the part of the first input signal that is directed to the same output port. These differences in the propagation distance translate in a direct way to differences in the optical loss, which can deteriorate the beamforming performance if they are left uncompensated. In order to eliminate these differences, the Blass matrix can be designed as a photonic integrated circuit with additional waveguide lengths at the input and output ports, as shown in Figure 6.14. In this way all optical paths, from any input port to any output port, have the same length, which is equal to $3\alpha + 4\beta$ in this particular example. The same approach can be used for any $M \times N$ Blass matrix in order to make the length of all optical paths equal to $M \cdot \alpha + N \cdot \beta$ and eliminate the differences between the various optical signals.

Even in the absence of any loss difference, the optical loss itself can deteriorate the performance of the Blass matrix via the noise that will be generated during the detection of the optical signal. Having in mind the use of the silicon nitride platform called TriPleX,

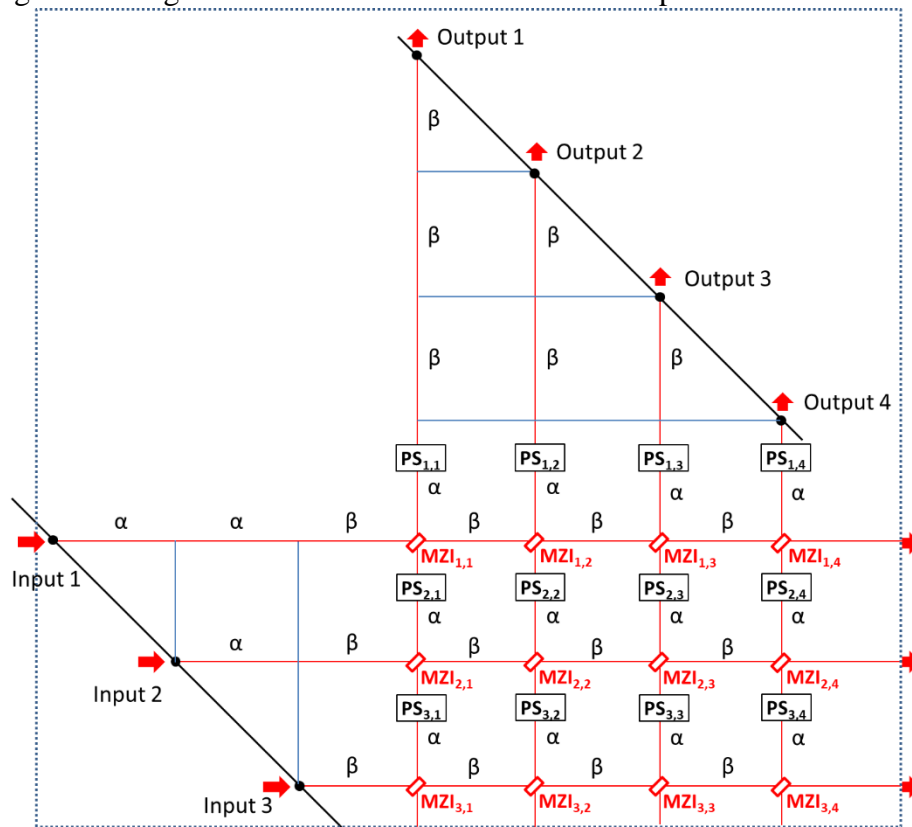


Figure 6.14: Modified layout of the optical Blass matrix ensuring equal path lengths for all input signals propagating towards all possible output ports. In this way the differences in the optical loss that would be otherwise present are eliminated. The example shown in the figure refers to a 3×4 Blass matrix case.

which has been already proposed for optical Blass matrix systems [5], we can derive a handy mathematical formula that associates the propagation loss of each optical signal through the Blass matrix with the size of this matrix. In order to derive this formula, we assume that the distance α and β are both close to 0.7 cm and that the propagation of a signal through an MZI on the TriPleX platform does not entail additional losses apart from the propagation losses over the length of the MZI, which is already taken into account in the calculation of α and β . Taking also into account that the propagation loss on the TriPleX platform is 0.1 dB/cm [6], [7], [8], the loss can be expressed in dB as follows:

$$\text{loss (dB)} = 0.07 \cdot (M + N) \quad (6.27)$$

For the example of Figure 6.14 (3×4 matrix), the loss is found equal to 0.49 dB, whereas for the examples that have been used in the main simulation study (4×8 matrix and 4×16 matrix), equal to 0.84 and 1.4 dB, respectively. It is noted that the calculation in Eq. 6.27 does not include the losses from the optical power that leaves the Blass matrix from the output ports on the right, as described in the presentation of the configuration algorithm. Moreover, it does not include the losses from the amplitude modulators, or the other elements of the beamforming system shown in Figure 6.2 like for example the 1×2 couplers, the 1×M splitter and the optical filters. The final optical power that is incident at each PD depends on the losses of all these elements, as well as on the optical power of the laser source. In order to compensate for these losses and increase the gain of the microwave photonics links, which are represented by the parallel optical paths between the laser source and the PDs, an external (off-chip) laser with high output power can be employed.

Finally, it should be also mentioned that the idea of using paths with equal lengths on the beamforming circuit is not only useful for ensuring the same optical losses in these paths, but also for preventing the formation of unwanted optical filters, which can result in high sensitivity of the circuit in temperature fluctuations and laser frequency drifts. This is especially important for the carrier re-insertion process, where the length of the optical path that brings each part of the optical carrier to the corresponding coupler should be equal to the length of the optical path through the modulators, the optical filters and the Blass matrix. An optical phase shifter will be always necessary to tune the phase of the optical carrier before its coherent addition with the corresponding output of the Blass matrix, but the equality of the optical paths is the key for the long-term stability of the circuit.

6.4 The HAMLET project: Development of the first generation of fully integrated Blass-matrix optical beamformers

The research and innovation project HAMLET, funded by the European Commission under the Horizon 2020 programme [9]-[11], aimed to disrupt the field of 5G networking, by developing a hybrid low-loss and a low-power consuming photonic integration platform, which enables the integration of a large number of photonic structures, providing in that way on-chip analog signal processing functionalities. Work carried out by HAMLET was highly based on the heterogeneous integration of graphene sheets on polymer and PZT layers on low-loss Si₃N₄/SiO₂ platforms, in order to develop fast graphene based electro-absorption modulators and an extensive optical beam forming network based on PZT -based phase actuators. To achieve its goals, the project invested on this hybrid technology for the development transceivers that seamlessly interface the optical fronthaul and radio access at the RAUs of 5G base stations. For the accomplishment of its mission, HAMLET focused on the following objectives:

Objective 1: Development of a simple and reliable methodology for integration of graphene on PolyBoard platform for the production of single and arrayed versions of electro-absorption modulators with high bandwidth (>25 GHz) and low insertion loss (<3 dB).

Objective 2: Development of a simple and reliable methodology for deposition of PZT layers on TriPleX platform for the production of optical phase shifters with sub-μW power consumption and ns response time.

Objective 3: Development of large-scale integrated beamforming networks for multi-element antenna arrays based on PZT-based tuneable elements on TriPleX platform.

Objective 4: Development of a hybrid integration engine for PolyBoard-to-TriPleX integration with large number (>100) of interconnected waveguides and polymer-to-InP integration with long InP component arrays.

Objective 5: Development of a simple integration engine for integration and co-packaging of optical subassemblies with CMOS electronics and MIMO antennas.

Objective 6: Development of hybrid transceivers with integrated optical and wireless sections for remote antenna units used in future 5G networks operating in the 28 GHz band.

Objective 7: Evaluation of the performance of HAMLET transceivers in emulating 5G system environments in terms of system flexibility and throughput.

Objective 8: Exploration of the full range of potential application domains that can take advantage of and/or benefit from HAMLET technology and preparation of a solid roadmap for its commercial uptake in the post-HAMLET era.

Figure 6.15 depicts the artistic layout of the HAMLET transceivers. In particular, the transceiver comprised a very large-scale photonic integrated circuit (VLSPIC) based on

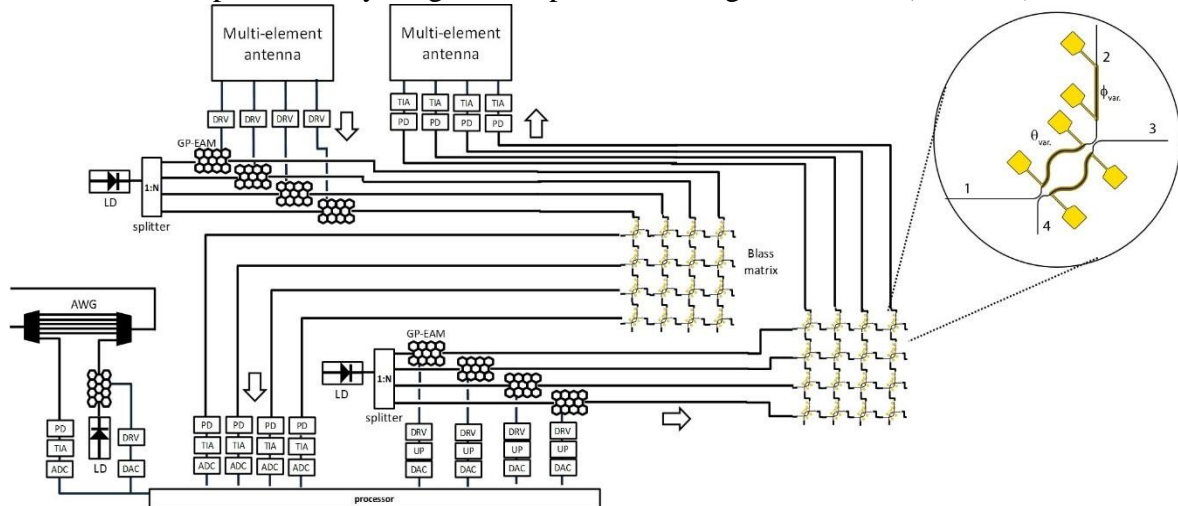


Figure 6.15: Schematic of HAMLET transceiver module (example with 4×4 Blass matrix). Top right: close up of a Blass matrix node showing the 2×2 tuneable coupler and tuneable phase shifter.

the 2D integration engine of HAMLET. Within the network architecture considered, multiple RAUs can be connected to a central office using a DRoF implementation [12], which can rely on a WDM ring at 1550 nm. The transceiver enables both digital and analog processing, and can interact with the optical and wireless domains of the network as follows: In the downlink, the WDM channel intended for the specific RAU can be dropped and detected. After digital-to-analog-conversion and up-conversion to the RF carrier frequency, the data intended for wireless transmission modulate a local optical carrier and generate the analog optical signal. The latter is processed by the Blass-matrix based beamforming network, and the signal replicas with appropriate phase differences are detected by a PD array. Thereafter, the detected signals are amplified by low-noise amplifiers (LNAs) and finally drive the elements of the multi-element antenna array. In the uplink, the RF signals from the elements of the receiving antenna array will drive the GP-EAMs on the PolyBoard. The analog optical signals are processed by a second Blass-matrix beamformer, add up coherently at the output of this network and are detected. The digital data will modulate an optical carrier and will generate a channel that will be added to the incoming WDM signal and will be sent through the ring back to the central office.

Within a period of 42 months, HAMLET developed two types of prototypes. The first one (Precursor-1) involves a 2×2 OBFN based on Blass matrix architecture and can feed up to 2 antenna elements and form up to 2 independent microwave beams. The second prototype (Module-1) involves an 8×8 optical beamforming network based on Blass matrix architecture and can feed up to 8 antenna elements of a multi-element antenna and form up to 8 independent microwave beams. In this way, 8 parallel links to multiple groups of users can be supported while low crosstalk, and substantial increase in the total system capacity is

achieved. Although for the very first time, GP-EAMs have been successfully integrated on PolyBoard, their system performance was not as expected. Therefore, at the modulation stages of both prototypes, InP-EAMs have been used instead of GP-EAMs.

6.5 Baseline characterization of a 2×2 Blass matrix optical beamformer

Figure 6.15 depicts the functional design and a picture of the assembled Precursor-1 prototype which includes a 2×2 optical beamforming network. An InP laser source was responsible for the generation of an optical carrier which subsequently was split into three copies. The two of them fed an InP-EAM and was amplitude modulated by an external RF signal while the other one was routed at the output of the optical beamformer (Carrier Lead

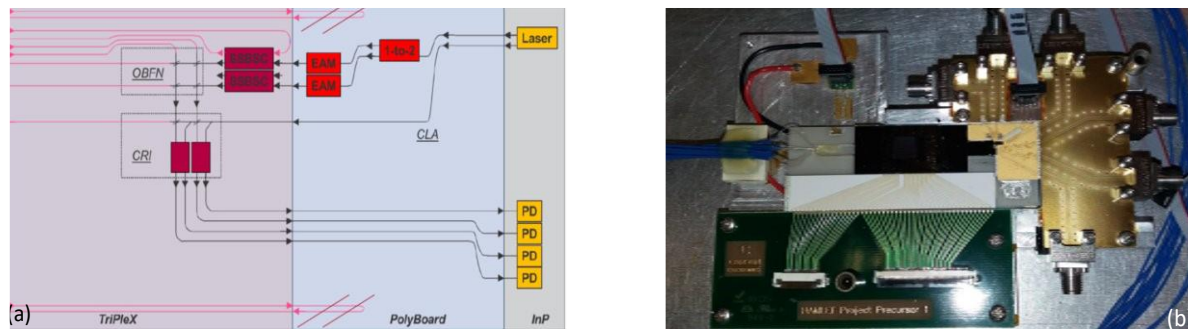


Figure 6.16 (a) Functional layout and (b) picture of the 2×2 fully integrated Blass matrix based optical beamformer.

Around; CLA). Subsequently, the two modulated optical signals were filtered by the on-chip bandpass optical filters, in order to filter out the optical carrier and the one sideband. The outputs of the filters were fed as inputs to the 2×2 optical beamformer which was based on a Blass matrix architecture, employing both PZTs and thermal heaters actuators. At the output of the optical beamformer, the reserved optical carrier was re-inserted (Carrier Re-Insertion; CRI) to the two output signals. Finally, a balanced detection scheme was selected to detect the modulated signals at the photodetectors.

The step-wise testing procedure for the baseline characterization of the precursor included the characterization of the carrier re-insertion process, the characterization of the optical tunable filters, the characterization of the two InP-EAMs and finally the characterization of the 2×2 Blass-matrix optical beamforming network.

The first testing campaign refers to the characterization of the carrier re-insertion process, in which the optical carrier generated from the back side of the on-chip DFB laser, bypasses successively the optical modulation, optical filtering and the beamforming stages and is coherently combined with the optical carrier generated by the front side of the laser which has been used in all the aforementioned stages. The generated optical carrier is coupled through the CLA optical path, highlighted in Figure 6.17 (a), to the CRI stage using a pair of MZIs. Following the same technique, the optical signals processed by the beamforming networks are coupled to the CRI stage using two MZIs. Each MZI includes a pair of PZT and heater actuators to control the power coupling coefficients of the MZIs and one pair for controlling the phase of the optical carrier. For the purposes of this experiment, a Hewlett Packard lightwave multimeter was used to monitor the optical power at the corresponding fiber array (FA) output port. When configuring the PZT/heater actuators for maximum output power at the FA port, the optical power measured at this port for 60 mA of laser diode injection current and for 0 V EAM biasing was -52 dBm, revealing a poor performance in terms of optical power. In this case the optical signal after the carrier re-insertion would exhibit very low optical power deteriorating the performance of the on-chip microwave photonic link.

The next testing campaign refers to the characterization of the on-chip optical tunable filters. The role of the optical filters is to filter out one sideband and the optical carrier of the dual sideband amplitude modulated signal. More specifically, an electrical signal with a microwave carrier f_c modulates the amplitude of the optical carrier f_o , with the help of the EAM, resulting in a dual sideband signal with three distinct spectral components – the optical carrier and the two sidebands at $f_o \pm f_c$. By configuring the optical filter properly in a way that the one sideband falls inside the passband and the optical carrier and the other sideband fall outside, the output signal has only one spectral component at $f_o + f_c$.

To assess the optical filters, a broadband source resulted from an EDFA was used as input to the port F2 in FA [4], which is directly coupled to the input of the top filter and an optical

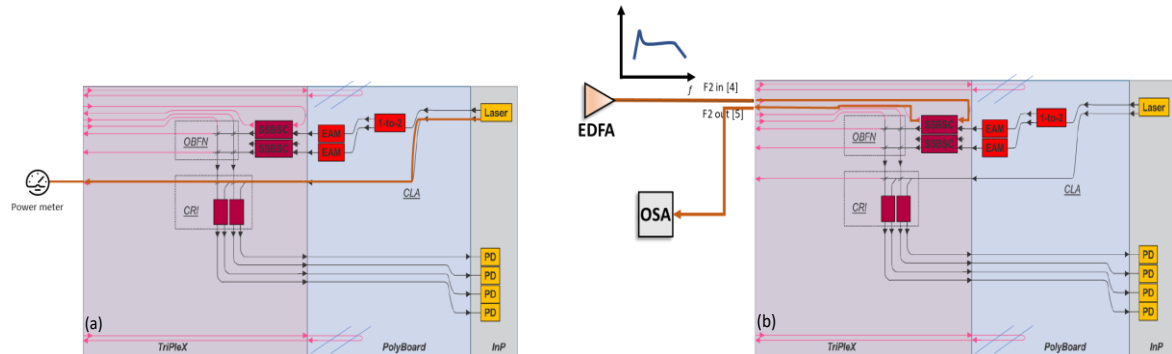


Figure 6.17: (a) Block diagram of the experimental testbed for the static characterization of the carrier reinsertion process by measuring the optical power at the FA port and (b) Block diagram of the experimental testbed for the configuration of the optical tunable SSBSC filter using an ASE broadband light source as input to the top filter.

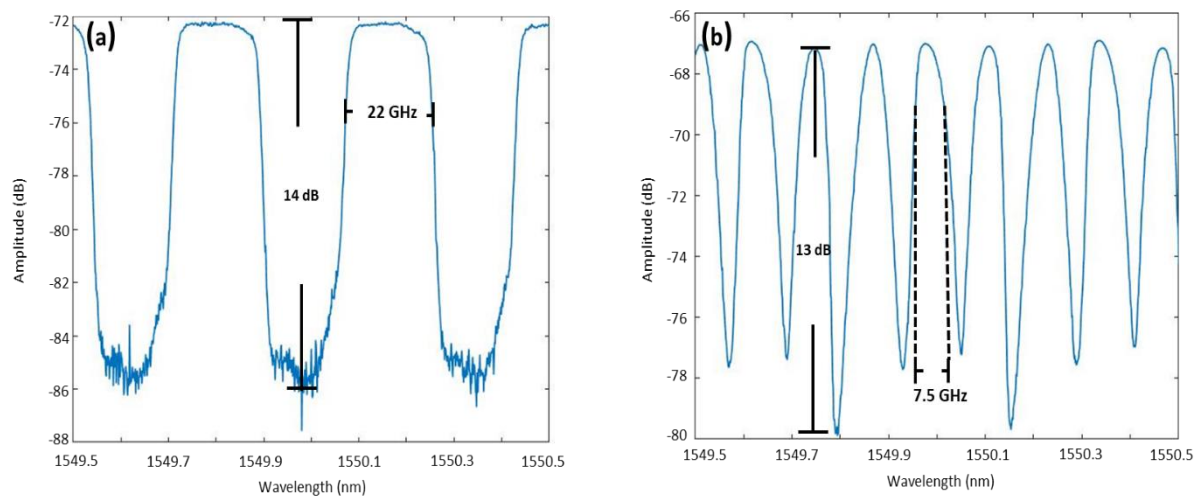


Figure 6.18: Optical spectra of the on-chip tuneable filter for different configurations of the heater elements: (a) 22 GHz passband with 14 dB attenuation at the stopband and (b) 7.5 GHz passband with 13 dB attenuation at the stopband.

spectrum analyser at the output port F2 out FA [5] which is directly connected to the output port of the top filter as it can be seen in Figure 6.17(b). As it can be observed in Figure 6.18, the passband zone of the filter can be varied from 7.5 GHz up to 22 GHz while the attenuation at the stopband in both configurations is around 13 dB and 14 dB respectively. Furthermore, it can be noticed that while the passband zone is increasing, the shape of the transfer function is becoming flatter, meaning that all the frequencies falling inside or

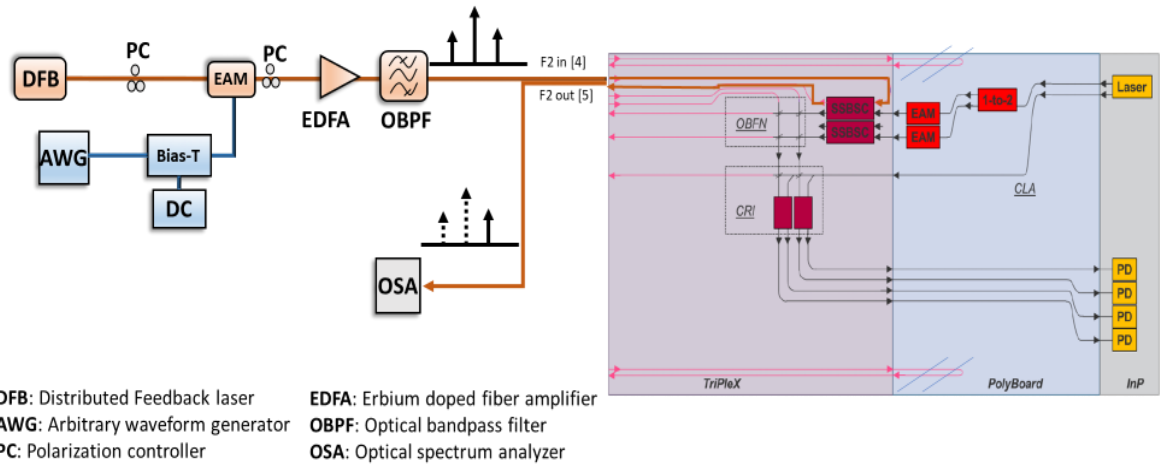


Figure 6.19: Block diagram of the experimental testbed for the characterization of the on-chip tuneable filter.

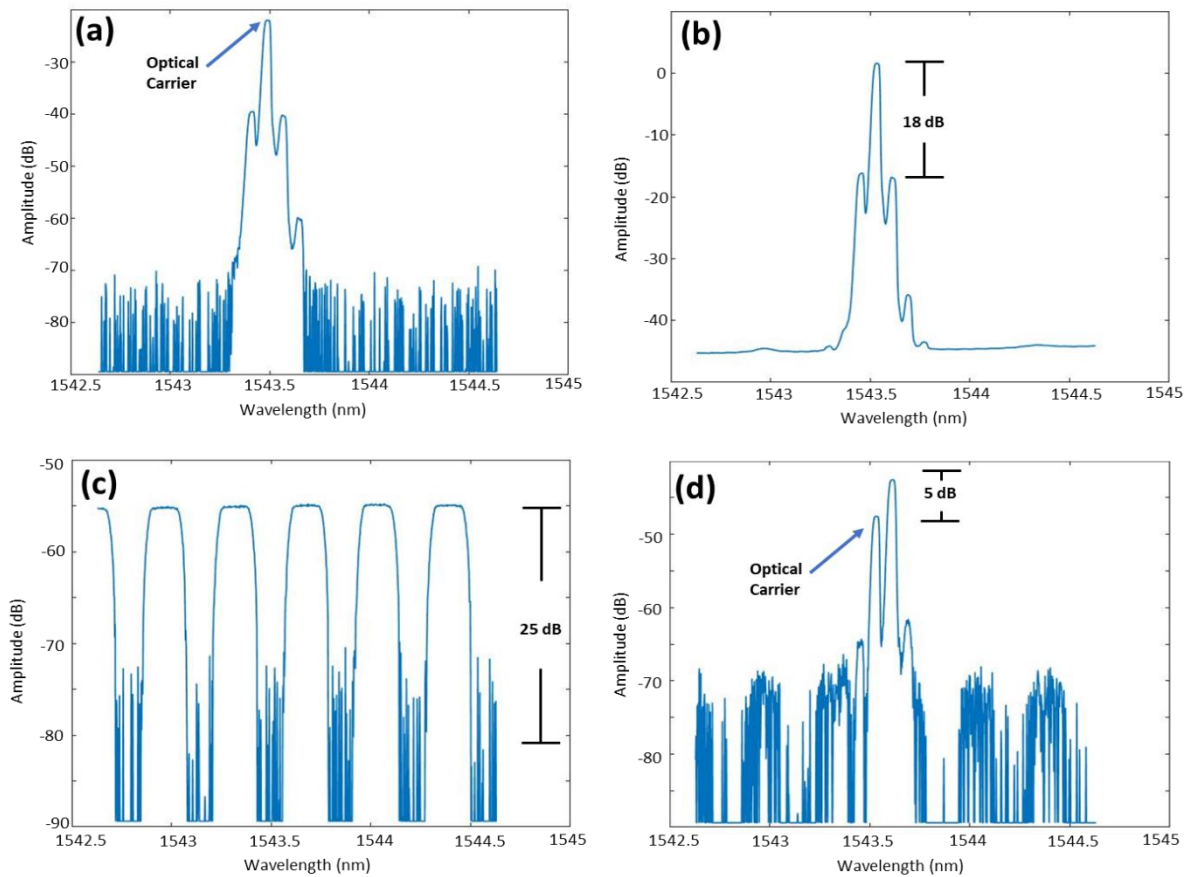


Figure 6.20: Optical spectrum (a) of the amplitude modulated optical carrier by 10 GHz microwave carrier at the input of the module, (b) of the amplified optical signal at the input port (c) of the transfer function of the on-chip optical tuneable filter, (d) of the filtered optical signal with suppressed the one sideband and the optical carrier at the output of the module.

outside of the passband zones are handled by the filter in the same manner. Taking into account that this module should be able to handle microwave signals with microwave carriers at 5 GHz, the optical filters exhibit an exceptional performance of filtering one sideband and the optical carrier of the incoming signal. The performance of the optical filter could be better assessed when dual sideband signals are served as inputs to the optical filters and are filtered instead of broadband sources.

Figure 6.19 presents the experimental testbed which was set up for the purposes of this testing approach. More specifically, a DFB generated an optical carrier whose amplitude is modulated by EAM. The driving signal of the EAM was generated by an arbitrary waveform generator (AWG) which generated a sinusoidal signal at 10 GHz. The bias of the EAM was controlled using a bias tee which combined the sinusoidal signal with a DC component. The generated dual sideband signal was amplified by an EDFA to compensate the insertion losses of the EAM, and consequently was filtered by an external optical filter to reject the out-band noise. The power difference between the carrier and the two sidebands is around 18 dB. It should be noted that the polarization state of the incoming signal is of significant importance because the waveguides on the TriPleX platform are designed for propagations of TE polarized light. Consequently, the polarization controller after the EAM ensures that the input signals have the desirable polarization state. The on-chip filter is configured in a way to filter out the one sideband and suppress the optical carrier. The attenuation at the stopband zone is almost 25 dB. At the output port of the module, an optical signal analyser monitors the filtered optical signal. Figure 6.20 presents the optical spectra of the signals (a) after the EAM, (b) at the input of the module, (c) the transfer function of the on-chip optical filter and (d) the optical spectrum of the output optical signal. It can be observed that the on-chip filter has successfully filtered out one sideband and carrier. The peak power of the sideband is 5 dB greater than the peak power of the optical carrier, validating again the good performance of the optical filter.

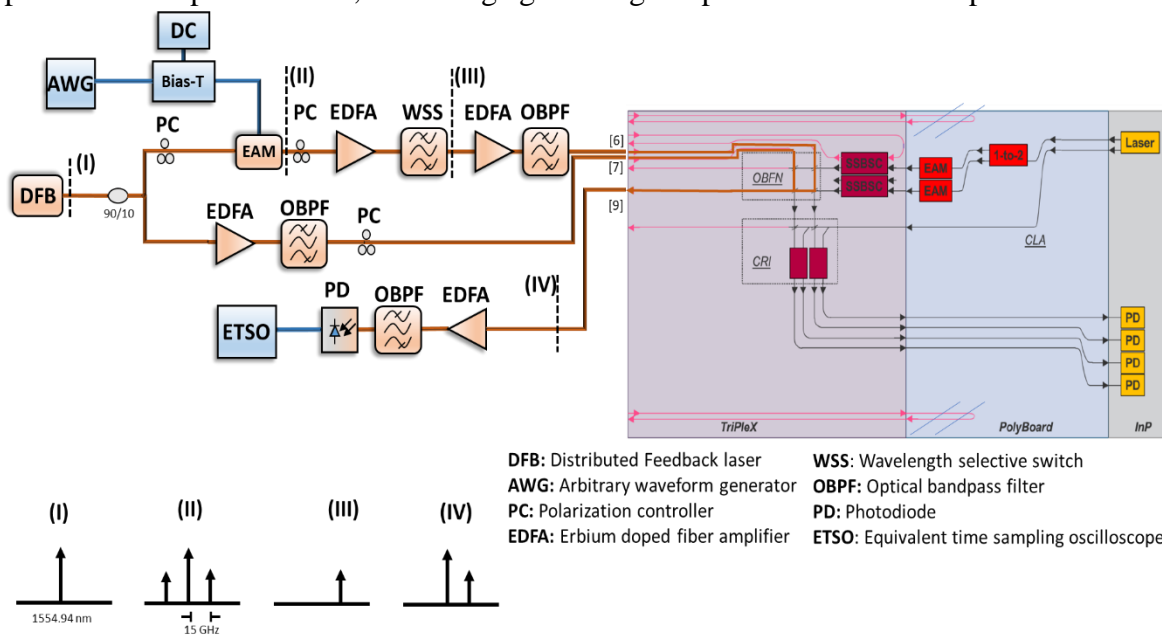


Figure 6.21: Block diagram of the experimental testbed for the validation of the carrier re-insertion concept using external DFB laser, EAM, EDFAs and OBPFs. The insets indicate the optical spectra at each stage of the experiment.

The next test refers to the static characterization of the two InP-EAMs without using microwave signals to modulate the optical carriers. The on-chip InP-laser generates the optical carrier which is split in two light paths using a 3-dB splitter, each one feeding an EAM, as it can be seen in Figure 6.16 (a). The bias voltages of the EAMs were varied from 0 V to -2.5 V with 0.1 V step. In principle, when the bias voltage of the EAM is decreasing the absorption of the EAM is increasing resulting in lower optical power at the output. In this specific study, the optical filters and the beamforming network were configured for maximum optical power at the output port FA [9]. The maximum output optical power was measured at -37.6 dBm when the bias of both EAMs were set at 0 V. However, by

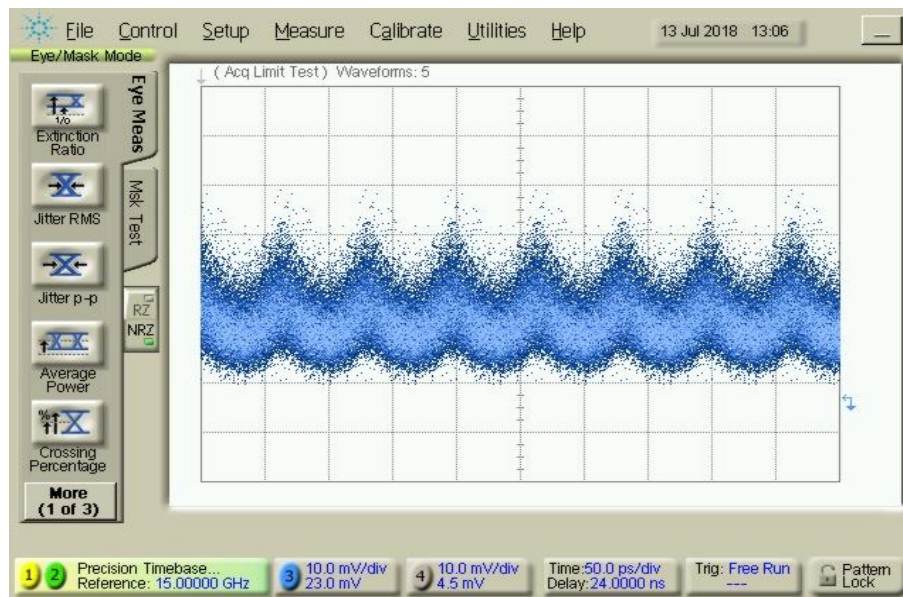


Figure 6.22: Received electrical eye-diagram of the 15 GHz sinusoidal wave, after the combination of the optical carrier and single sideband optical signal within the prototype.

decreasing the bias voltage no significant change in the output power was observed, making it impossible to modulate the optical carriers using microwave signals.

Due to the limitations imposed by the low optical power at the CLA path and the poor modulation performance of the EAMs, the assessment of the beamforming network was impossible using the on-chip laser and the EAMs. For these reasons an extended experimental testbed was set up to validate the fundamental concept of the beamforming network - the translation of a phase shift in the optical domain into the equivalent phase shift in the microwave domain.

Figure 6.21 shown the modified experimental setup for the specific testing. More specifically, a DFB laser generated an optical carrier at 1554.94 nm which was split into two optical paths using a 90/10 optical splitter. The 90 percent of the optical carrier was modulated using a bulk EAM by a microwave sinusoidal signal at 15 GHz generated by an AWG. The dual sideband signal at the output of the EAM was amplified to compensate for the insertion losses of the EAM and subsequently, it was filtered by a wavelength selective switch resulting in a single-sideband signal.

Afterwards, a second amplification stage was deployed to compensate for the insertion losses of the module. Before entering to the module from port [6], an optical filter was used to filter out the out-band noise. On the other optical path, the unmodulated carrier was amplified and filtered before entering to the module from port [7]. In both optical paths polarization controllers were used to correct the polarization states of the incoming optical signal. The optical phase shifters located between the rows of the Blass matrix are controlled in order to define the relative phase difference which will be translated into the microwave domain. Taking advantage of the Mach Zehnder interferometers which constitute the four nodes of the Blass matrix, the optical signals are routed inside the matrix and were combined using an MZI before exiting from the port [9]. At the receiver side, an EDFA and an optical filter are used to amplify the signal and compensate the losses of the module. The detection is performed by means of a single photodiode and the generated electrical signal is directed to an equivalent time sampling oscilloscope. Figure 6.22 depicts the received eye diagram of 15 GHz sinusoidal signal after the combination process. In principle, any relative phase shift between the optical carrier and single sideband optical signal would result in a time shift of the detected sinusoidal signal. However, the use of the very long fibers to connect the bulk components with each other and the use of the also very

long fiber array to couple the optical signals to the module, made it very difficult to stabilize the phase difference between the optical carrier and the single sideband optical signal. On the other hand, in the integrated version of this experiment the relative phase would be stable and controllable enabling the beamforming operation.

6.6 Baseline characterization of an 8×8 Blass matrix optical beamformer

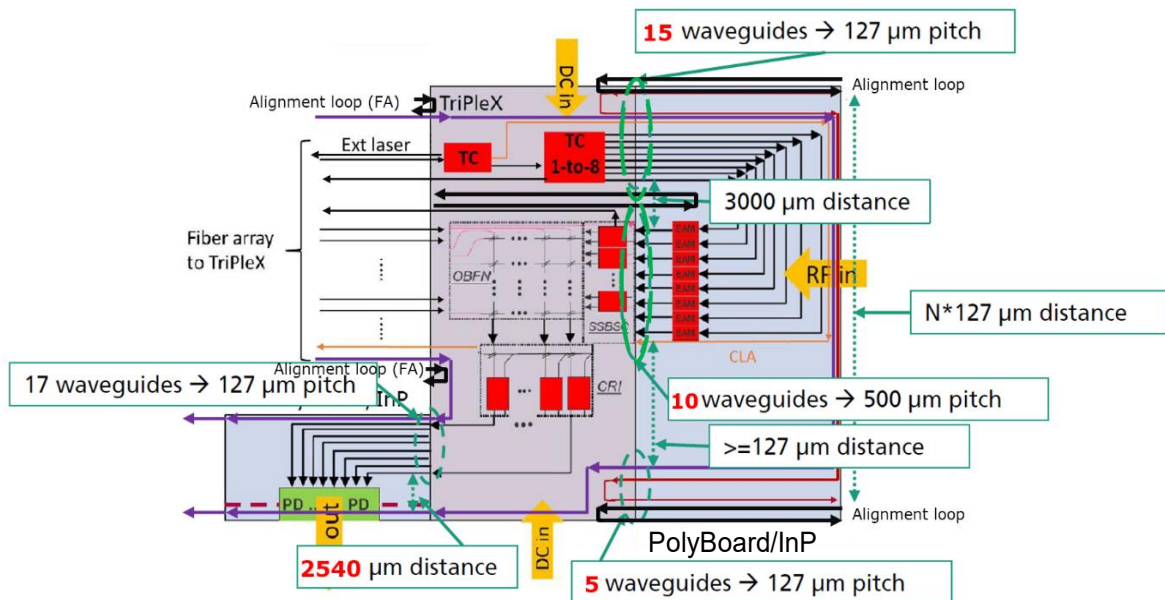


Figure 6.23: Functional layout of the Module-1 consisting of the 2 PolyBoard chips (in blue) with eight InP-EAMs integrated on the PolyBoard chip; and TriPleX chip (in red) with 8x8 multi beam OBFN.

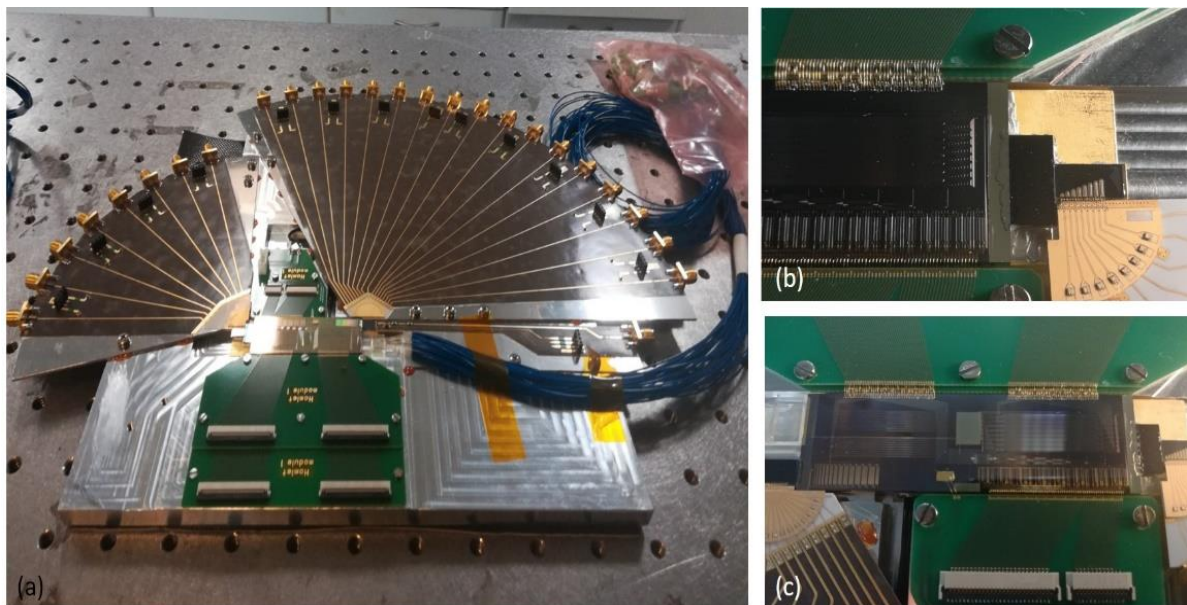


Figure 6.24: a) Picture of the assembled Module-1 prototype that accommodates an array of 8 InP-EAMs and an 8×8 optical beamforming network and (b) & (c) zoom-in pictures of the PolyBoard-InP section and TriPleX chip, respectively.

For the Module-1, it has been agreed to implement one design consisting of the basic building blocks needed for the implementation of the 8×8 multi-beam OBFN. Figure 6.23 depicts the functional layout of Module-1. In this prototype, the optical carrier is generated by an external laser source which is coupled to the TriPleX chip via the fiber array. On TriPleX, the optical carrier is firstly split into 2 branches by a tunable coupler (TC). The

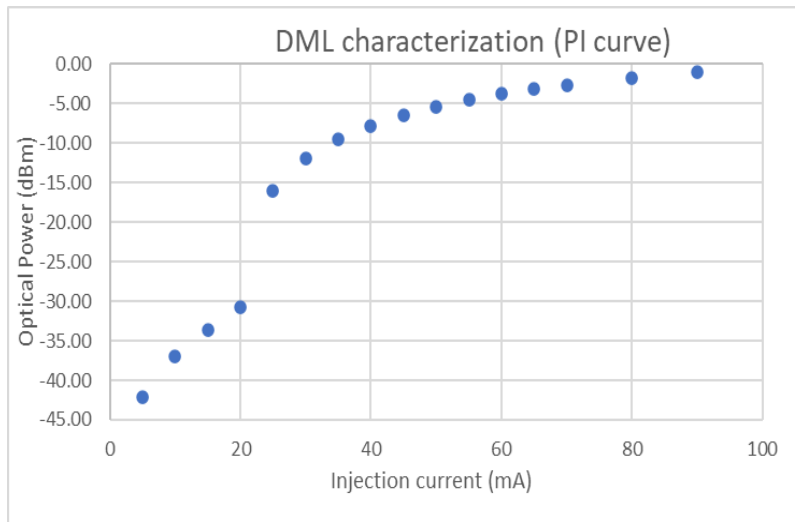


Figure 6.25: Measured P-I curve of the integrated DML laser used for the interconnection of Module-1 with an optical fronthaul network.

lower branch contains a 1×8 splitter, consisting of TCs, to supply an array of eight InP-EAMs. The upper branch is used as CLA. The modulated optical signals propagate over the interface between PolyBoard and TriPleX. At TriPleX, the signals are filtered by ring based single sideband suppressed carrier filters. Afterward the processed signals are coupled to the 8×8 Blass matrix OBFN where they acquire the proper relative amplitude and phase relationships according to the desired steering angle of each beam. At the output of the OBFN, the signals are coherently combined with the unmodulated carrier from the CLA on TriPleX. This mixing is performed by the CRI section consisting of TCs. The mixed signals are detected by sixteen balanced photodiodes. The photodiodes are integrated on an InP platform and mounted on top of the PolyBoard chip which is placed on the interface opposite to the InP-PolyBoard modulator array chip. The TriPleX chip is also equipped with test ports to mainly analyse the performance of the individual components within OBFN building block. Both chips have a set of waveguides in order to perform the alignment procedures between the two platforms using 2D integration engine. Additionally, for the generation of the data signal that is transmitted into the optical fronthaul network, a directly modulated laser (DML) is used. The DML is butt-coupled to the PolyBoard/InP chip.

Finally, it should be mentioned that the phase actuators integrated inside the Blass matrix are PZT-based while the actuators of the splitting, combining, and filtering stages are thermo-optical. Figure 6.24 presents picture of the assembled Module-1 prototype.

The first step for the baseline characterization of the prototype was to assess the performance of the integrated DML and more specifically, to evaluate its capability to generate optical modulated signal with On-Off Keying (OOK) modulation format. As it is described in Chapter 3 [32], the DML can modulate the amplitude of the generated optical carrier by modulating the injection current of its gain section. Figure 6.25 shows the output optical power of the DML with respect to the amplitude of the injection current (P-I curve). As observed, for currents below 20 mA, the DML operates within the spontaneous emission regime while for higher currents, the DML works within its stimulated emission regime. The output saturated power was equal to 0 dBm for 90 mA injection current. For a direct modulation, the injection current should be limited between 20 mA and 90 mA. However, for linear amplitude modulation, the injection current should be further limited to a smaller regime in order to ensure the DML operates in the most linear part of its P-I curve.

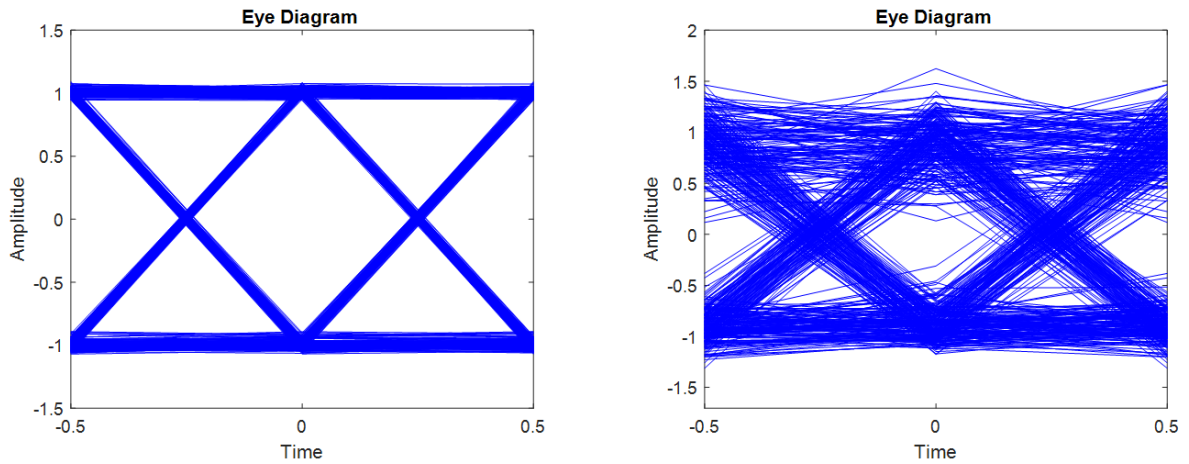


Figure 6.26: (Left) Eyediagram of the generated electrical signal at 2 Gbaud symbol rate that modulated the amplitude of the optical carrier of the integrated DML laser and (right) the eyediagram of the recovered electrical signal after the photodetection stage, using an external photodiode, and the offline processing by the DSP toolkit.

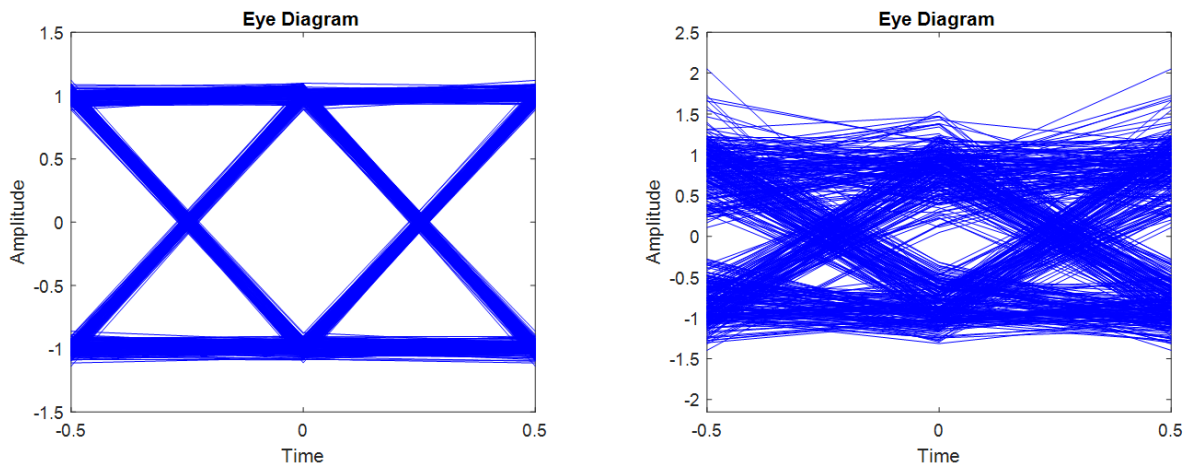


Figure 6.27: (Left) Eyediagram of the generated electrical signal at 3 Gbaud symbol rate that modulated the amplitude of the optical carrier of the integrated DML laser and (right) the eyediagram of the recovered electrical signal after the photodetection stage, using an external photodiode, and the offline processing by the DSP toolkit.

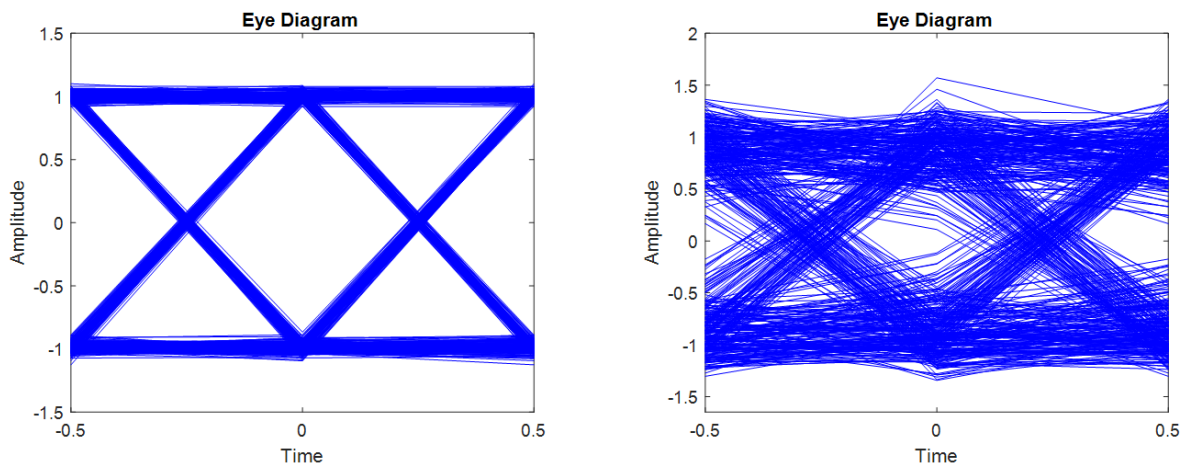


Figure 6.28: (Left) Eyediagram of the generated electrical signal at 4 Gbaud symbol rate that modulated the amplitude of the optical carrier of the integrated DML laser and (right) the eyediagram of the recovered electrical signal after the photodetection stage, using an external photodiode, and the offline processing by the DSP toolkit.

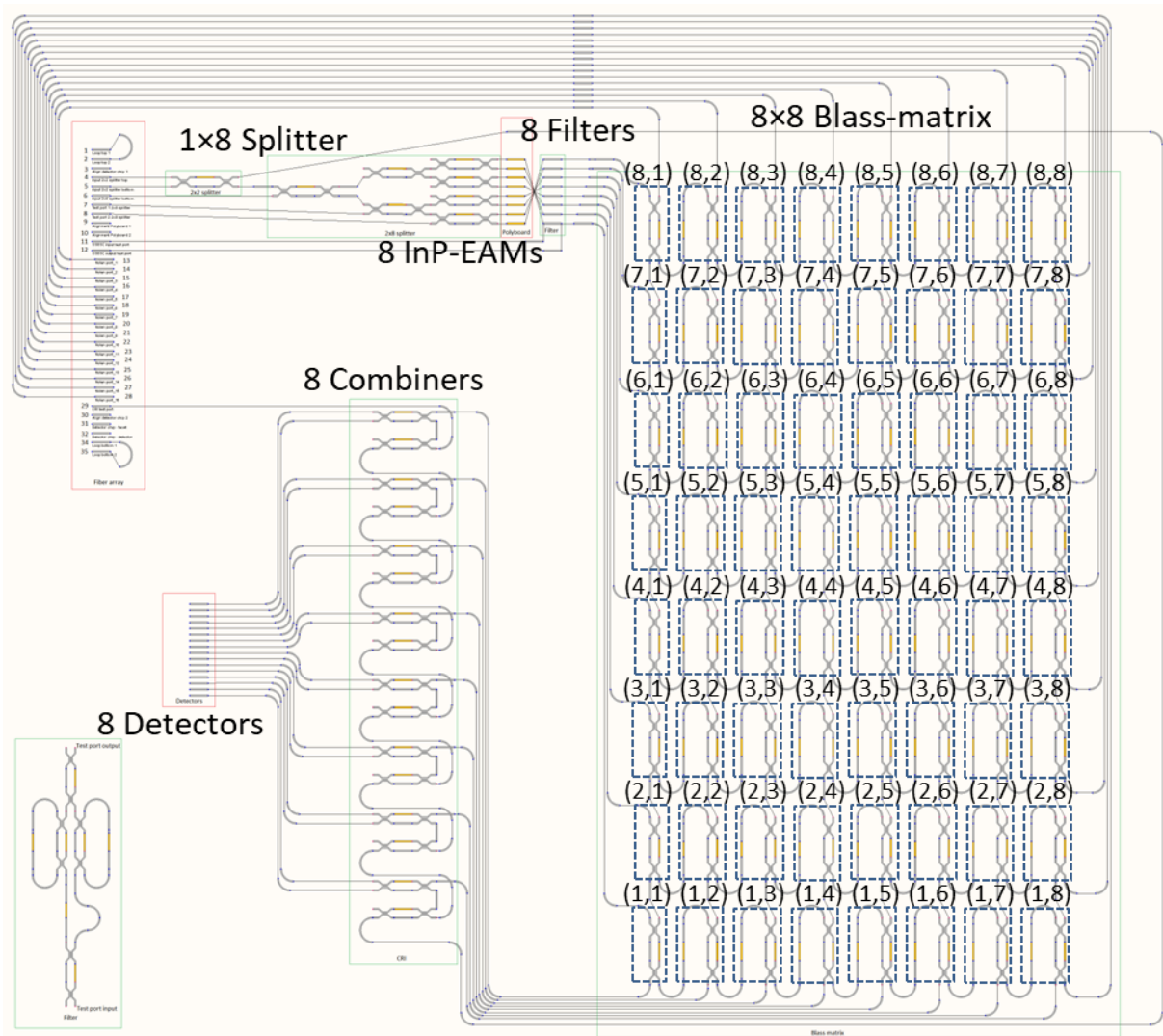


Figure 6.29: Layout of the TriPleX chip of the assembled Module-1. It includes a 1×8 splitting network, 8 SSBSC filters, 8×8 Blass-matrix OBFN, and 8 power combiners.

For the purposes of this testing campaign, a state-of-the-art Keysight arbitrary waveform generator and an external bias-Tee was used to generate the baseband electrical signal that was coupled to the DML with the proper DC bias. The output of the DML was coupled to a port of the fiber array and by using an external photodiode, the optical modulated signal was detected. The generated electrical signal was sampled and stored by a Keysight real-time oscilloscope and processed by the developed DSP toolkit. **Error! Reference source not found.** Figure 6.26 - Figure 6.28 present on the left-hand side, the eyediagram of the input electrical signals at 1 Gbaud, 2 Gbaud, 3 Gbaud, and 4 Gbaud symbol rate, respectively, and on the right-hand side, the eyediagrams of the recovered signals after the DSP toolkit. As observed from the graphs, an error-free operation could be achieved for symbol rates up to 4 Gbaud assuming that a FEC code is used at the receiving side.

The next step in the characterization of the prototype was the testing of the 8×8 Blass matrix beamforming network. The network consisted of 64 MZIs with a PZT-based phase actuator integrated in one of their two arms and 56 PZT-based phase actuators integrated in one of their two output ports. Therefore, for the proper tuning of the Blass matrix, 120 PTZ-based phase actuators should be configured, without taking into account the thermo-optical phase actuators of the splitting, combining, and filtering stages. As explained in 6.2 paragraph (Step 4), for the correct routing of the optical signals from the input ports to the

output ports, we need to know the self- and cross-coupling coefficients of all the MZIs of the network. To do so, we utilized the additional fiber array ports that are directly connected to the unused input port of the MZIs of the eighth row (see Figure 6.29) and the ports connected to the unused output ports of the MZIs of the eighth column (see Figure 6.29). More specifically, we coupled an unmodulated optical carrier, centered at 1560 nm, to the input ports of the MZIs of the eighth row and we monitored the optical power at the output ports using a sensitive optical power meter. Taking into account the network topology and how the MZIs are interconnected, we started our characterization procedure from the MZI located to the eighth row and column because its input and output ports are accessible from the fiber array. After the characterization of the (8,8) MZI, we continued with the characterization of the (8,7) MZI and for this, we coupled the optical carrier to its unused input port while we set the (8,8) MZI at the cross-biasing point, meaning that the optical signal from the (8,7) MZI is coupled to the optical power meter. Following this approach, the MZIs of the eighth row were fully characterized. For the characterization of the MZIs of the seventh row, we set the MZIs of the eighth row to the bar-biasing point and we repeated the same procedure starting from the (7,8) MZI. Using this methodology, all the MZIs were fully characterized. Figure 6.30 depicts the measured extinction ratios of the all the MZIs of the matrix. As observed, from the total 64 MZIs, after several actuations (from cross to bar and vice versa), only 23 were fully functional with extinction ratios from 23.3 dB to 1.75 dB. These results show that the yield of the PZT-based phase actuators was 36 %. Consequently, the poor performance of the phase actuators did not allow the signals to be routed from any the input to any output ports and as a result, we could not use this 8×8 matrix or any other submatrix as a beamforming network.

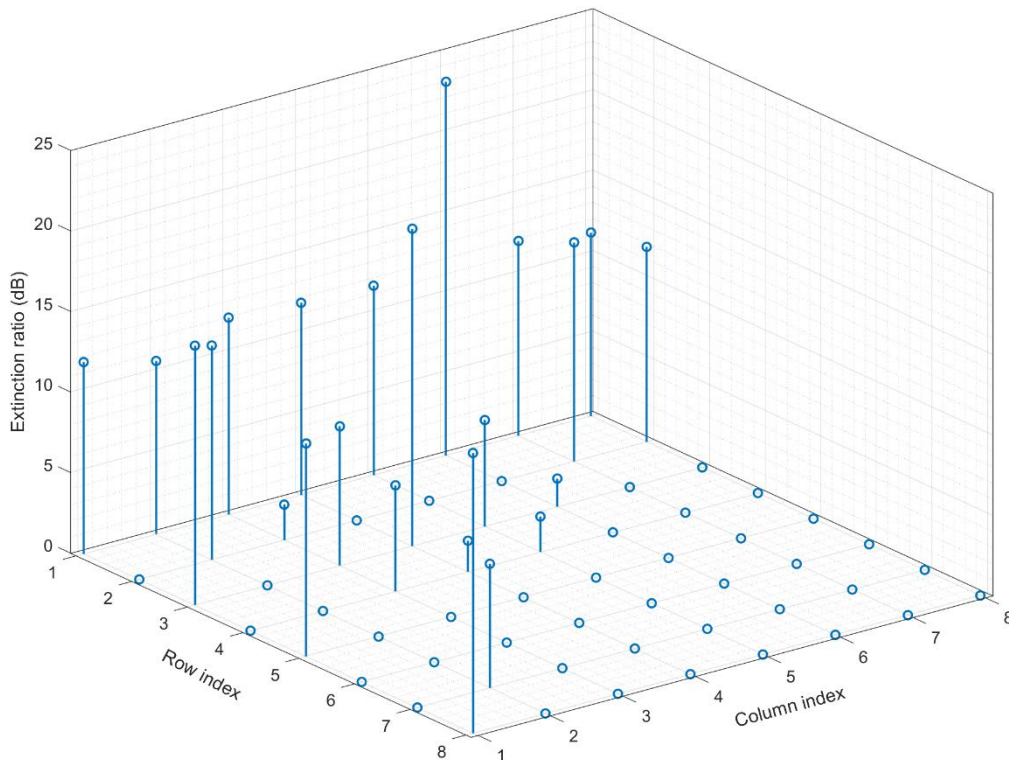


Figure 6.30: Extinction ratios of the MZIs constituting the Blass-matrix beamforming network. The performance of the PZT-based actuators was deteriorated after several actuations.

Conclusions of Chapter 6

Using a theoretical analysis and extensive simulation studies, this Chapter has set a solid background for the optical implementation of a Blass-matrix network using MZIs and optical phase shifters and has described its possible use as a multi-beam optical beamforming network in next generation of wireless systems. Working with optical signals that are amplitude modulated by microwave tones, the possibility to transparently translate the optical phase shifts inside the Blass matrix into an equivalent set of phase shifts in the microwave domain was proved. Based on this translation, an algorithm for the configuration of an $M \times N$ matrix, taking into account the inherent properties and the limitations of the MZIs as tunable optical couplers was presented. Moreover, using a simulation setup that models the operation of the Blass-matrix in the case of optical inputs with microwave QAM signals, the possibility for multi-beam operation at 28.5 GHz was validated and evaluated by calculating the BER performance of the decoded signals with respect to the order of the QAM format, the symbol rate and the pulse shaping parameters. Despite the presence of the beam squinting effect, in all cases, where the symbol rate was lower than 3 Gbaud, the BER was lower than 10^{-3} , showing that the impact of the specific effect can be tolerated. Finally, the impact of the additional frequency dependence of the optical Blass matrix operation due to the inevitable fabrication asymmetry of the MZIs and the Blass matrix itself was investigated as well as the impact of the inaccuracy in the adjustment of the phase shifters and the fabrication of the 3-dB couplers inside the MZIs. In all cases the limits that ensure high-quality operation were identified, and it was confirmed that the current fabrication techniques and optical building blocks can respect these limits.

An actual implementation of this type of optical beamforming network requires the use of a photonic integration platform for the fabrication of the circuit as a compact device with stable optical phase relations. TriPleX appears as an ideal platform for the core part of this circuit thanks to its low propagation loss and its possibility to offer dense photonic integration leading to large-scale circuitry. Apart from its fabrication, a crucial issue for the practical operation of this circuit is its power consumption requirements. Main sources of power consumption comprise the laser, the amplitude modulators, the driving circuits for the amplitude modulators, the PDs, the transimpedance amplifiers after the PDs and of course the phase shifters that are needed in the waveguides of the Blass matrix, in the MZIs of the Blass matrix, in the MZIs and the MRRs of the optical filters and in the waveguides that bring the optical carrier to the couplers for the carrier reinsertion process. While the exact power consumption of all these elements can vary significantly depending on the specific technology that is employed for their implementation, it is clear that the main problem in an actual device can originate from the large number of phase shifters. As only an example, the implementation of the 4×16 beamforming network that has been used as a reference in the simulation study of the previous section would require a total number of at least 156 phase shifters on an integrated circuit. Assuming that these phase shifters are thermal in nature with heating electrodes, and taking into account that the power consumption of a heating electrode on the TriPleX platform can be as high as 200 mW for π phase shift, the total power consumption of the phase shifters can be close to 32 W, and thus problematic. This power consumption refers to a reconfiguration rate of 1 kHz, which is sufficient for the reconfiguration of beamforming networks in modern 5G systems. Using this value, the total power consumption of the phase shifters becomes less than 625 mW leading to practical implementations.

Within the European project ICT-HAMLET, two optical beamforming networks based on Blass matrix architecture based on the hybrid integration of InP-PolyBoard-TriPleX platforms and the use of PZT-based optical phase shifters have been fabricated. More

specifically, the first prototype (Precursor-1) included an InP laser source, two InP-EAMs, a 2×2 optical beamforming network, with PZTs and thermal heaters actuators, and two optical filters both integrated in TriPleX, and four InP photodiodes. Due to the limitations imposed by the low optical power at the CLA path and the poor modulation performance of the EAMs, the assessment of the beamforming network was impossible using the on-chip laser and the EAMs. Using external opto-electronics components, the on-chip filters were characterized, demonstrating 14 dB attenuation at the stopband.

By analysing and applying the lessons learned from the fabrication and testing of the first prototype, the next prototype (Module-1) increased the integration complexity by including more building blocks that enhanced its system capabilities. In Module-1, the optical carrier was generated externally and was coupled to the prototype using the fiber array. The first building block of Module-1 was the splitting stage, consisting of MZIs connected in a binary tree topology in TriPleX, where the optical carrier was split into eight equal power copies. Afterward the optical signals were coupled to PolyBoard and from there to eight InP-EAMs. The modulated signals were then coupled back to TriPleX where were filtered (rejection of the one sideband and of the carrier) and processed by an 8×8 Blass matrix based optical beamforming network. The Blass matrix was purely based on PZT-based phase actuators. Finally, the output signals were re-combined with the initial optical carrier and detected by an array of sixteen InP photodiodes. Additionally, for the communication with an optical fronthaul network, the prototype hosted a DML. The baseline characterization of Module-1 started from the testing of the DML where it was successfully demonstrated that it could support OOK modulation format with symbol rates up to 4 Gbaud. The next step was the characterization of the 8×8 Blass matrix optical beamforming network. To do so, all the MZIs of the matrix were characterized and their extinction ratios were measured and reported. Based on these measurements, the yield of the PZT-based phase actuators was 36 %. Consequently, due to the poor performance of the phase actuators, the matrix could not operate as a multi-beam optical beamforming network since it was not possible to route any input to any output.

The ICT-HAMLET has reached the end of its contractual lifetime in May 2019. Within 42 months, two integrated optical beamformers based Blass-matrix were designed and fabricated for the very first time. On top of this huge effort, LioniX Int. and SolMateS [13] have heterogeneously integrated also for the first-time piezoelectric films on TriPleX platform, forming ultra-low power stress-optic modulators which were used as the basic building blocks of the optical beamforming network. Therefore, despite the shortcomings related to the system evaluation of its prototypes, HAMLET was clearly an ambitious project pushing beyond their current technological capabilities, both TriPleX and PolyBoard platforms, setting the bar too high for all the following endeavours in the field of Microwave Photonics. In particular, regarding the core building block of the HAMLET's prototypes, the PZT-based phase actuators, LioniX has only recently reported that the current yield of the PZT is around 90 % which is undoubtedly a significant improvement compared to the PZT technology used in HAMLET and enables its use in LiDAR systems, tuneable laser, telecommunications, and data center systems [14]. Moreover, the development OBFNs based on the hybrid integration of the TriPleX, PolyBoard and InP platforms are currently pursuing by the European project ICT-TERAWAY [15] which aims to provide a set of photonics-enabled transceivers for application in beyond 5G networks operating in W (92-114.5 GHz), D (130-174.8 GHz) or THz (252-322) bands.

References of Chapter 6

- [1] G. Agrawal, *Fiber-optic communication systems*. Hoboken, N.J.: Wiley, 2010.
- [2] S. Mosca, F. Bilotti, A. Toscano and L. Vegni, "A novel design method for Blass matrix beam-forming networks", *IEEE Transactions on Antennas and Propagation*, vol. 50, no. 2, pp. 225-232, 2002.
- [3] R. Mailloux, *Phased Array Antenna Handbook* (Artech House antennas and propagation library). Artech House, 2005.
- [4] A. Duerinckx, "Matched gaussian apodization of pulsed acoustic phased arrays", *Ultrasonic Imaging*, vol. 2, no. 4, pp. 338-369, 1980.
- [5] J. Anzalchi, et al., "Optical beamforming based on microwave photonic signal processing", *International Conference on Space Optics — ICSO 2016*, 2017.
- [6] C. Roeloffzen et al, "Low-Loss Si₃N₄ TriPleX Optical Waveguides: Technology and Applications Overview," *IEEE Journal of Selected Topics in Quantum Electronics*, vol. 24, no. 4, pp. 1-21, 2018.
- [7] R. Heideman et al, "Large-scale integrated optics using TriPleX waveguide technology: from UV to IR," *Photonics Packaging, Integration, and Interconnects IX*, 2009.
- [8] J. Epping et al., "Ultra-low-power stress-optics modulator for microwave photonics", *Integrated Optics: Devices, Materials, and Technologies XXI*, 2017.
- [9] <https://cordis.europa.eu/project/id/688750>.
- [10] P. Groumas et al., "Photonic integration technology for the interface between the optical and wireless part in 5G networks: The H2020-ICT-HAMLET approach," *2017 IEEE Photonics Society Summer Topical Meeting Series (SUM)*, 2017, pp. 57-58, doi: 10.1109/PHOSST.2017.8012649.
- [11] C. Tsokos, P. Groumas, V. Katopodis, H. Avramopoulos and C. Kouloumentas, "Enabling photonic integration technology for microwave photonics in 5G systems," *2017 19th International Conference on Transparent Optical Networks (ICTON)*, 2017, pp. 1-4, doi: 10.1109/ICTON.2017.8024906.
- [12] C. Liu, L. Zhang, M. Zhu, J. Wang, L. Cheng, and G. Chang, "A Novel Multi-Service Small-Cell Cloud RadioAccessNetwork for Mobile Backhaul and Computing Based on Radio-Over-Fiber Technologies," *J. Lightwave Technol.* 31, 2869-2875 (2013)
- [13] <https://www.solmates-pld.com/>
- [14] A. S. Everhardt, et al. "Ultra-low power stress-based phase actuation in TriPleX photonic circuits." *Integrated Optics: Devices, Materials, and Technologies XXVI*. Vol. 12004. SPIE, 2022.
- [15] <https://ict-teraway.eu/>

Chapter 7 – Conclusions and future work

7.1 Conclusions

Microwave photonics, as its name suggests, is an interdisciplinary research field that combines microwave and photonics technologies. The added value that this field brings stems from the fact that it can realize key functionalities that in the microwave systems are either complex or even not directly possible. Among the various systems that microwave photonics can really revolutionize, beamforming networks for communication or ranging systems stand out on top of the list.

Within this framework, in this dissertation, the design, implementation, system integration and performance evaluation of optical beamforming networks (OBFNs) for multi-element antenna arrays were addressed. Following a holistic and systematic approach, we started by analysing the theory that dictates the operation of such complex systems and we continued with the design, implementation, system integration as well as performance evaluation of four different OBFNs.

In particular, in **Chapter 2** was described the theory of antenna arrays. Starting from the fundamental characteristics of a single antenna, we introduced the concept of multi-element antenna arrays, focusing on the arrays following a linear geometry. Subsequently, the array factor of linear antenna arrays was derived and its relation with the underlying beamforming networks was discussed. More specifically, we investigated which conditions should be met in order to achieve single-beam, multi-beam, and multicast beamforming operation. Next, we discussed the main difference between the two different OBFN approaches and in particular, OBFNs based on true time delay and OBFNs based on pure phase shifters, which is related to the beam squinting effect. In this chapter, we concluded presenting the amplitude tapering technique which is an efficient approach to suppress the power of the sidelobes.

In **Chapter 3**, we described the principle operation of the microwave photonics systems by analysing the light generation, optical modulation, and photodetection units. The outcome of this work was the development of a simulation platform that can emulate the operation of the MWP systems developed into this dissertation. Additionally, in this chapter, we reported on the key figure of merits of MWP system which are the link gain, noise figure, and SFDR₃.

Having a solid theoretical background, in **Chapter 4**, we reported on the design, implementation, system integration and performance evaluation of a 2×4 OBFN based on bulk micro-optics elements. More specifically, the 2×4 TTD-OBFN was developed using commercial off-the-shelf optical modulators, optical delay lines, optical attenuators, optical couplers and photodiodes and it can support single-beam, multi-beam and multicast beamforming with continuous tuning of the beam angles and feed an antenna array with four elements. The operation of the proposed OBFN is based on a number of ODLs for introduction of time delays to the copies of the signals that correspond to different wireless beams and different AEs. Through extensive simulation studies, we validated its principle of operation and continued to its implementation, developing a complex experimental setup that occupied almost 4 m². In order to minimize the footprint of the OBFN and significantly reduce its reconfiguration time, the OBFN was mounted into three rack units while its reconfiguration process was automatized using a microprocessor and an array of servo motors. Using QAM signals modulated around 15 GHz, the OBFN exhibited an error-free performance for all three modes of operation (single-beam, multi-beam, and multicast).

The OBFN demonstrated in the previous chapter was a successful testing vehicle to validate the theory, the simulation platform but also to demonstrate the inherent advantages

of MWP field for OBFNs. However, it was evident that the use of bulk optical components increases the size, weight and cost of the OBFNs. To tackle this shortcoming and leveraging the advancements of the photonic integrated circuit technology, in **Chapter 5**, we reported on the development and system evaluation of a 1×4 OBFN-PIC based on the hybrid integration of InP components in a TriPleX platform. More specifically, the OBFN-PIC consisted of a hybrid external cavity laser, two InP phase modulators, a TriPleX SSBFC optical filter, four TriPleX OTTDLs based on tunable eight MRRs, and four InP photodetectors. The OBFN-PIC could process microwave signals with central frequencies up to 40 GHz and impose continuously tunable time delays over wide operating bandwidths without deteriorating the system performance. To that end, we assessed the performance of the OBFN-PIC by measuring the link gain for operating frequencies from 0.04 GHz up to 40 GHz, and the NF as well as the SFDR_{2,3} at 5 and 10 GHz. The maximum link gain was -36.98 dB measured at 2.6 GHz. The NF was calculated to be equal to 38.28 dB and 41.95 dB at 5 GHz and 10 GHz, respectively, and the SFDR₂ and SFDR₃ around 5 GHz were 70.5 dB·Hz^{1/2} and 89.9 dB·Hz^{2/3}, respectively, whereas around 10 GHz were 67.7 dB·Hz^{1/2} and 88.8 dB·Hz^{2/3}, respectively. Additionally, using 500 Mbaud QAM signals at 5 and 10 GHz as input signals and an experimental setup that emulates the operation of the OBFN-PIC in the downlink direction of a wireless system, we have evaluated the EVM and BER performance of the decoded signals for beam angles ranging from 45° to 135°. In all cases, error-free performance has been successfully achieved. This was the first time that a concrete analysis of the system performance of a fully integrated OBFN-PIC was reported.

In **Chapter 6**, using a theoretical analysis and extensive simulation studies, we have set a solid background for the optical implementation of a Blass-matrix network using MZIs and optical phase shifters, and described its possible use as a multi-beam optical beamforming network. For the configuration of a such M×N matrix, we have developed an algorithm that takes into account the inherent properties and the limitations of the MZIs as tunable optical couplers. Moreover, using a simulation setup that models the operation of the Blass-matrix in the case of optical inputs with microwave QAM signals, the possibility for multi-beam operation at 28.5 GHz was validated and evaluated by calculating the BER performance of the decoded signals with respect to the order of the QAM format, the symbol rate and the pulse shaping parameters. Despite the presence of the beam squinting effect, in all cases, where the symbol rate was lower than 3 Gbaud, the BER was lower than 10⁻³, showing that the impact of the specific effect can be tolerated. Finally, the impact of the additional frequency dependence of the optical Blass matrix operation due to the inevitable fabrication asymmetry of the MZIs and the Blass matrix itself was investigated as well as the impact of the inaccuracy in the adjustment of the phase shifters and the fabrication of the 3-dB couplers inside the MZIs. In all cases the limits that ensure high-quality operation were identified, and it was confirmed that the current fabrication techniques and optical building blocks can respect these limits.

Within the European project ICT-HAMLET, two optical beamforming networks based on Blass-matrix architecture have been fabricated. Both prototypes were based on the hybrid integration of InP-PolyBoard-TriPleX platforms while their core building block, the optical beamforming network, consisted of PZT-based optical phase shifters. The first prototype (Precursor-1) included a 2×2 optical beamforming network and was the testing vehicle to optimize the efficient integration of the different photonic platform. Due to the high propagation and coupling loss as well as the poor modulation performance of the EAMs, the assessment of the beamforming network was impossible. Using external opto-electronics components, the on-chip filters were characterized, demonstrating 14 dB stopband attenuation.

By analysing and applying the lessons learned from the fabrication and testing of the first prototype, the next prototype (Module-1) increased the integration complexity by including more building blocks that enhanced its system capabilities. The baseline characterization of Module-1 started from the testing of the integrated DML, which would ensure the communication between the prototype and an optical fronthaul network. The DML was successfully characterized, achieving the generation of optical signals with OOK modulation format and symbol rates up to 4 Gbaud. Subsequently, the Blass-matrix was characterized by measuring the extinction ratios of all the MZIs of the matrix. Based on these measurements, the yield of the PZT-based phase actuators was 36 %. Consequently, due to the low yield of the phase actuators, the matrix could not operate as a multi-beam optical beamforming network since it was not possible to route signals from any input to any output port.

Table 13 outlines the research objectives, formulated at the beginning of this dissertation, as well as the key scientific results that were achieved and fulfilled these objectives.

Table 13: Summary of research objectives and key achievements of the present dissertation.

Objective number and short description	Key achievements
1 Development of a sophisticated simulation engine and a DSP toolkit tailored to MWP systems	<ul style="list-style-type: none"> • Development of a simulation engine that models the key building blocks of a MWP systems and emulates the operation of TTD- or PS-based OBFNs and linear antenna arrays. Related Chapters: 2, 3, 4, 5, and 6 • Development of a DSP toolkit including time recovery, amplitude level control, IQ imbalance compensation, adaptive equalization, and carrier recovery algorithms Related Chapters: 4, 5, 6, and Appendix I
2 Design and implement an OBFN based on bulk micro-optics components	<ul style="list-style-type: none"> • Development of a 2×4 OBFN based on arrays of tuneable OTTDL and VOAs. Automatization of its reconfiguration procedure using a programmable micro-processor and servo motors Related Chapters: 4
3 Experimentally validate the ability of the OBFNs to support single-beam, multi-beam and multicast operation	<ul style="list-style-type: none"> • Demonstration of single-beam, multi-beam, and multicast beamforming using the 2×4 OBFN Related Chapters: 4
4 Characterize a fully integrated TTD-OBFNs	<ul style="list-style-type: none"> • Experimental performance evaluation of a 1×4 TTD-OBFN by measuring the link gain, NF, SFDR₃ and assessing its system performance using RF signals carrying with QAM modulation formats Related Chapters: 5
5 Analyse the operating principle of OBFNs based on Blass-matrix architecture and develop a novel configuration algorithm for controlling the optical components	<ul style="list-style-type: none"> • Development of a configuration algorithm for M×N OBFNs taking into account the inherent characteristics of the optical components Related Chapters: 6
6 Characterize the performance of integrated OBFNs based on Blass-matrix architecture	<ul style="list-style-type: none"> • Experimental baseline testing of a 2×2 and 8×8 integrated OBFNs based on Blass matrix architecture Related Chapters: 6

7.2 Future work

During the course of this work, several new ideas have been shaped and formulated thanks to the fruitful discussions with many colleagues, but it was not feasible to be thoroughly assessed due to time constraints. However, most of these ideas are currently investigated within the context of Master or PhD theses. Future work concerns deeper analysis of microwave photonics technology in order to improve the system performance of integrated MWP system in terms of link gain, noise figure, and linearity and also to investigate possible new MWP techniques and OBFN architectures that will enable its truly commercial uptake not only in the 5G but also in the future 6G networks.

▪ Improvement of a MWP link/system

High-power laser sources: Tunable semiconductor lasers with a narrow linewidth have found a wide range of important applications, reaching from coherent communications to optical sensing. In particular, in a MWP link, the link gain depends quadratically on the emitted power of the laser source. Therefore, it is of utmost importance the development of high-power laser source in order to increase the link gain. Towards this target, LioniX Int. has recently developed a dual gain laser cavity consisting of a tunable dual-ring cavity, two InP gain sections equipped with phase tuners and two tuneable Mach-Zehnder integrated in the TriPleX platform [1]. This novel laser can exhibit on-chip optical powers up to 20.7 dBm. As an example, by utilizing this laser source, the link gain of the 1×4 TTD-OBFN reported in Chapter 5 can be potentially improved by 20 dB.

Modulator technology: Another crucial parameter that determine the link gain of a MWP link is the $V\pi$ of the modulators. As explained through this dissertation, lower values of $V\pi$ lead to higher link gains and higher SFDRs. An approach to achieve this reduction is to use push-pull MZMs that exhibit half $V\pi$ compared to the phase modulators. For example, the minimum $V\pi$ of the InP-MZM provided by FhG-HHI is 2V [2]. Apart from the significant reduction that can be achieved by using push-pull MZM instead of phase modulators is the fact that can be monolithically combined with semiconductor optical amplifiers. In such a way, the optical amplifier can boost the power of the modulated signal right after the MZM and increase the link gain of the system. To avoid the saturation of the amplifiers, the MZMs should be biased at the zero-transmission point in order to suppress the power of the unmodulated carrier, as it is explained in Chapter 3. However, this approach increases the system complexity since an “new” optical carrier should be re-inserted before the photodetection stage to enable the proper detection of the processed microwave signal. Another excited alternative to the mature technology of InP modulators is the lithium niobate on insulator (LNOI) technology. LNOI is one of the most attractive material for photonics, not only due to its exceptional electro-, nonlinear-, and acousto-optic properties, but also thanks to its potential to reduce the cost and enable scalable PIC manufacturing. Combining the LNOI and TriPleX platforms allows to combine their strengths, offering a unique solution beyond the capabilities of any platform that exist today. LNOI-MZM can potentially exhibit $V\pi < 0.9$ V and insertion loss < 1 dB.

Power consumption: As described in Chapter 6, in order to solve the issue of the high-power consumption of the thermo-optic phase actuators and eliminate the thermal crosstalk, LioniX Int. has developed an alternative type of phase actuators based on the stress-optic effect. In these stress-optic actuators, the stress is induced into the waveguide by a piezoelectric PZT (lead zirconate titanate) layer, which is actuated by applying a voltage at an electrode. When the PZT on top of the waveguide is exposed to an electric field, a uniform electrical field is created in the vertical direction. Since the PZT layer is fixed, this

expansion generates mechanical stress that is transferred to the underlying waveguide and results in changes in the refractive indices of the SiO_2 and Si_3N_4 layers, and thus changing

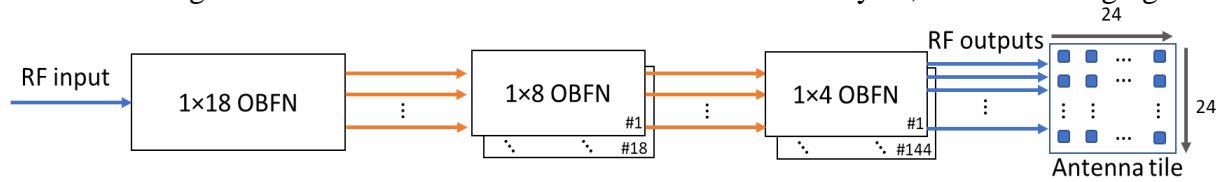


Figure 7.1: Layout of a multi-stage OBFN architecture that can support the operation of antenna tiles with hundreds of antenna elements.

the effective refractive index of the optical mode. The measured crosstalk of the PZT-based shifters is almost 10 times lower compared to the thermo-optic phase shifter when the distance between the waveguides is greater than $20 \mu\text{m}$. The measured static power consumption of is well below $1 \mu\text{W}$ and less than 4mW for π shift at 1kHz excitation, and therefore, more than 5 orders of magnitude lower than that of conventional thermo-optic phase actuators. For example, the replacement of all thermal-phase shifters by their PZT-based counterpart in the OBFN-PIC, presented in Chapter 5, can lead to a total power consumption of less than 0.5W and achieve reconfiguration times in the MHz regime. Additionally, the total footprint of the stress-optic actuator is similar to that of thermo-optic actuators due to the lower crosstalk to adjacent waveguides. These advantages make the stress-optic actuator an excellent choice for the implementation of larger OBFNs and for the next generation integrated photonic circuits. However, in order to fully replace the thermo-optic phase shifters and develop fully functional prototype, PZT technology should be improved in terms of yield.

- **Novel OBFN architectures for serving large antenna arrays**

Optical beamforming networks based on modular architectures: For large antenna arrays with hundreds or even thousands of antenna elements, larger OBFNs are required. However, larger OBFNs impose strict requirements in terms of fabrication yield and increase the complexity of the packaging procedure. In order to extend efficiently the capability of the OBFN these antenna structures, a modular design of multi-stage beamformers. Following this design approach, multiple, small-sized OBFNs are combined in a tree architecture to feed a large antenna tile. For example, assuming an antenna tile with 576 antenna elements (24×24), as the one shown in Figure 7.1, a three-stage optical beamformer network can be practically implemented based on the use of TTD-OBFNs sizes 1×18 , 1×8 , and 1×4 . More specifically, at the first stage, the modulated microwave signal is transferred to the optical domain and processed by a single 1×18 OBFN with 18 parallel OTTDLs. The output of each OTTDL is further connected to a 1×8 OBFN at the second stage which includes in total 18 1×8 OBFNs. Subsequently, at the third stage the outputs of the OTTDLs of the 1×8 OBFNs are connected to 144 1×4 OBFNs. Finally, at the end of the third stage, the signals are converted back to the microwave domain and feed the 576 antenna elements. In order to compensate the high losses of this architecture, high-power SOAs should be placed between the stages.

- **Microwave Photonics for THz communication systems:**

As part of the European project ICT-TERAWAY [3], OBFNs based on the hybrid integration of the TriPleX and InP platform using PZT-based phase shifters are pursuing for application in beyond 5G networks operating in W (92-114.5 GHz), D (130-174.8 GHz) or THz (252-322) bands. Leveraging MWP concepts and photonic integration techniques, TERAWAY will develop a common technology base for the generation, emission, and detection of wireless signals within an ultra-wide range of carrier frequencies that will cover the W (92-114.5 GHz), D (130-174.8 GHz) and THz band (252-322 GHz). In this way, the project will provide for the first time the possibility to organize the spectral resources of a

network within these bands into a common pool of radio resources that can be flexibly coordinated and used. Figure 7.2 depicts an artistic layout of the TERAWAY transmitter.

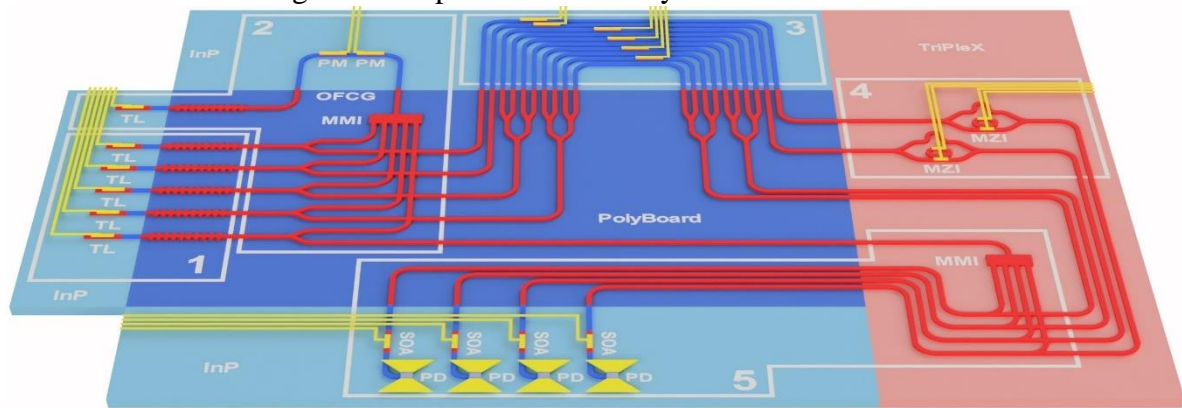


Figure 7.2: Artistic layout of the hybrid, photonics-enabled platform for the generation of W/D and THz signals. The following units are comprised and shown in the diagram: (1) Optical carrier generation unit, (2) Optical phase locking unit, (3) Optical modulation unit, (4) Optical filtering unit, and (5) Optical amplification, up-conversion and wireless emission unit. The structures are not shown in scale.

The units that will be brought together for the realization of this technology include:

Optical carrier generation unit (1): This unit will consist of a set of tunable lasers (TLs). Each one of them will have a cavity that will span across an InP gain chip and the polymer motherboard, and will generate an optical carrier with free selection of the emission wavelength over a range of more than 10 nm (i.e. 1.25 THz) [4]. In order to keep this unit compact, a single InP chip with parallel gain sections will be used. All TLs in this array apart from the last one will generate the optical carriers that will be modulated by the baseband or IF signals of the wireless channels. The last TL will be used for the generation of the reference optical carrier that will be mixed with the other ones, enabling the up-conversion process at the pin-photodiodes of the platform.

Optical phase locking unit (2): This unit will comprise an optical frequency comb generator (OFCG) [5] and the necessary optical circuit in order to direct the optical comb inside the TLs and lock their phases. As a result of this mechanism, the phase noise of the generated signals at the PDs can be drastically reduced [6], [7]. The OFCG will be based on a cascade of two PMs on a second InP chip.

Optical modulation unit (3): This unit will consist of a set of PMs on the same InP chip as above, and will be responsible for the generation of the optical waveforms that will carry the information content of the wireless channels. The PMs will be used in two modes. In the first one, each PM will serve as a standalone modulator for the modulation of the optical carrier by the waveform of a channel with 2.16 GHz bandwidth at an IF of 5 GHz. In the second mode, the PMs will be part of an IQ modulator (IQM) and will be driven by the I/Q components of a channel with 25.92 GHz bandwidth. The passive circuit of the IQMs will be formed on the polymer motherboard.

Optical filtering and beamforming unit (4): This unit will be present in the TriPleX part of the hybrid platform and will comprise a set of optical filters based on the combination of a MZI with MRRs inside its arms. The design has a well-proven potential for high selectivity and sharp transitions between its stop- and pass-bands. In TERAWAY, these filters will be used for the suppression of the optical carrier and the lower sideband of the optical waveforms carrying the IF signals, enabling their detection by the PDs. Moreover, within this unit an OBFN based on Blass matrix architecture will be integrated. The OBFN will accommodate the formation of up to four independent beams by a multi-element bow-tie antenna with up to 16 elements (4×16 matrix).

Optical amplification, up-conversion and wireless emission unit (5): This unit will be responsible for the actual generation and emission of the wireless channels to the air. Within this unit the optical waveforms will be combined with the reference optical carrier, will be

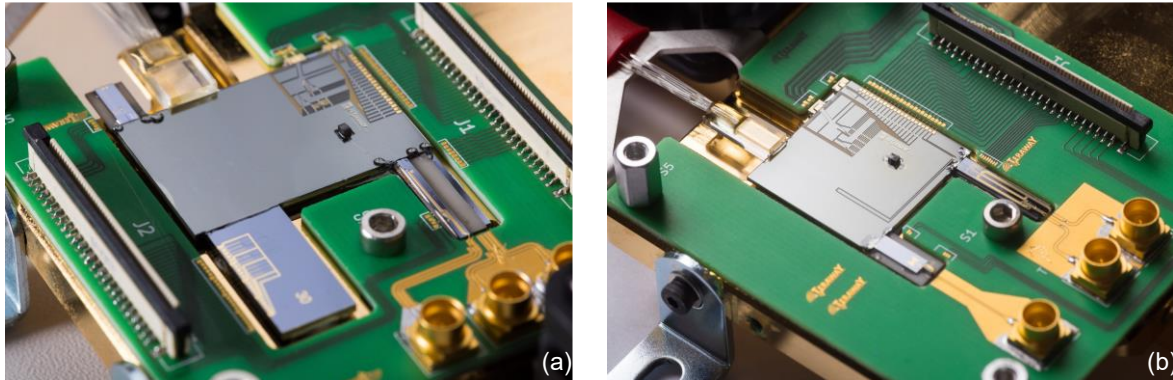


Figure 7.3: Pictures of the first assembled TERAWAY Tx (a) and Rx (b), supporting the generation, processing, amplification, emission, and detection of a wireless signal with central frequency from 92 GHz up to 322 GHz.

amplified by SOAs to 20 mW per channel, and will be detected by PDs that will be co-integrated with the SOAs on the same InP chip. The incidence of each optical waveform together with the reference carrier on a PD will force this PD acting as a photonic mixer and will result in the up-conversion of the IF or baseband signal carried by the specific waveform. The carrier frequency after the up-conversion process will be equal to the wavelength separation between the reference optical carrier and the optical waveform, and will be controlled by the corresponding TL. After its generation at a PD, each signal will drive a self-complementary bow-tie antenna [8] that will be part of the same layer stack in the InP chip.

Figure 7.3 shows picture of the first assembled Tx and Rx TERAWAY prototypes. Combined together, these prototypes can support the generation, processing, amplification, emission, and detection of a wireless signal with central frequency from 92 GHz up to 322 GHz by a single antenna element at each side. Next steps include the design and fabrication of a 1×4 Tx and 4-channel Rx, 2×16 Tx and 2-channel Rx, and 4×16 and 4-channel Rx. At the core of the transmitters, an OBFN based on Blass matrix architecture with size 1×4 , 2×16 , and 4×16 will process and steer the emitted beams towards the receiver.

To conclude, microwave photonics is an exciting research field with a bright future. Especially with the advent of the new generations of communication networks that push the operating frequencies deeper in the mmWave range or even in the THz band, microwave photonics can provide the techniques to generate, process, steer, and detect these high-frequency signals. Of course, microwave photonics is still in its infancy compared to classic microwave technology and a lot of improvements need to be done before its commercial exploitation. However, thanks to the inherent advantages over the pure microwave architectures and its capability to operate almost transparently to any microwave or THz frequency have make Microwave Photonics the prominent candidate technology for future communication systems. So, buckle up and enjoy the ride!

References of Chapter 7

- [1] J. P. Epping, R. M. Oldenbeuving, D. Geskus, I. Visscher, R. Grootjans, C. G. H. Roeloffzen, and R. G. Heideman, "High power, tunable, narrow linewidth dual gain hybrid laser," in Laser Congress 2019 (ASSL, LAC, LS&C), OSA Technical Digest (Optica Publishing Group, 2019), paper ATu1A.4.
- [2] https://www.hhi.fraunhofer.de/fileadmin/PDF/PC/MOD/datasheet_module_MZM_1550_56Gbaud_TE_Cincl.pdf
- [3] <https://ict-teraway.eu/>
- [4] Z. Zhang et al., "Hybrid Photonic Integration on a Polymer Platform", Photonics, vol. 2, no. 3, pp. 1005-1026, 2015.
- [5] G. Carpintero, S. Hisatake, D. de Felipe, R. Guzman, T. Nagatsuma and N. Keil, "Wireless Data Transmission at Terahertz Carrier Waves Generated from a Hybrid InP-Polymer Dual Tunable DBR Laser Photonic Integrated Circuit," Scientific Reports, vol. 8, no. 1, 2018.
- [6] T. Nagatsuma and G. Carpintero, "Recent Progress and Future Prospect of Photonics-Enabled Terahertz Communications Research", IEICE Transactions on Electronics, vol. 98, no. 12, pp. 1060-1070, 2015. Available: 10.1587/transele.e98.c.1060.
- [7] T. Nagatsuma, G. Ducournau and C. Renaud, "Advances in terahertz communications accelerated by photonics", Nature Photonics, vol. 10, p. 371, 2016.
- [8] B. Globisch, R. Kohlhaas, L. Liebermeister, M. Schell and S. Nellen, "Recent progress of continuous-wave terahertz systems for spectroscopy, non-destructive testing, and telecommunication", Terahertz, RF, Millimeter, and Submillimeter-Wave Technology and Applications XI, 2018.

Appendix I: Digital signal processing toolbox

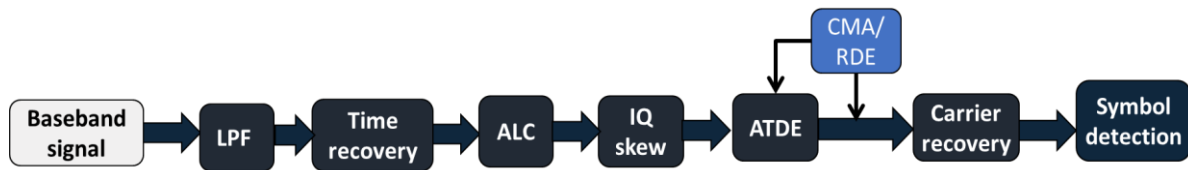


Figure AI.1: Reference DSP suite for the demodulation of the high-speed QAM signals of the high-bandwidth channels

In this section, the key algorithms that have been developed for the demodulation of the QAM signal throughout this work are described. Figure AI.1 depicts the block diagram of the DSP suite that is implemented in the Matlab environment and will be served as a reference for the implementation of the algorithms in the receiving baseband unit.

Timing recovery algorithm

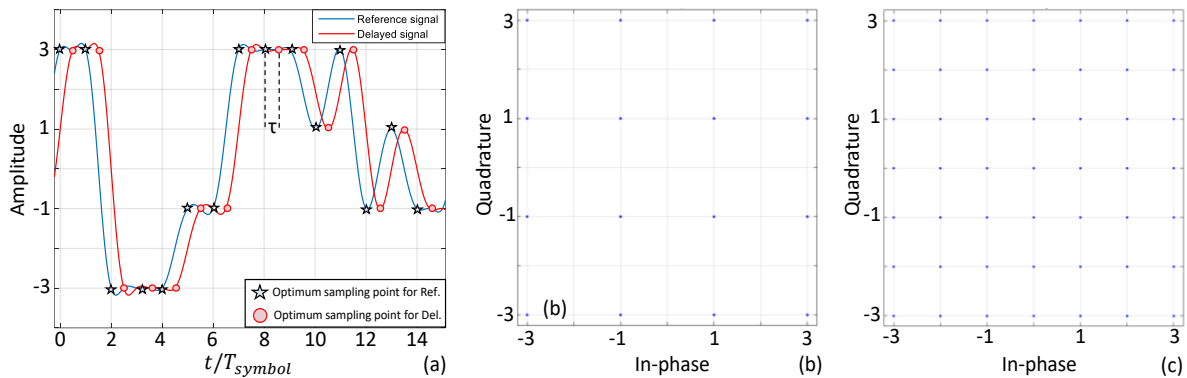


Figure AI.2: (a) Real part of low-pass 16-QAM signal and its delayed version by half the symbol period, (b) scatterplot of the reference signal assuming sampling frequency equal to the symbol rate and (c) scatterplot of its delayed version.

In a wireless communication system, the output signal of the detector must be sampled periodically, twice per symbol interval, to recover the transmitted information. However, the sampling clock frequency is not synchronized with the symbol rate of the received signal which results in a timing error. The effect of this timing error can be easily understood by analysing Figure AI.2. More specifically, Figure AI.2 (a) presents the equivalent real part of a low-pass 16-QAM signal as well as its delayed version by half the symbol period. The timing error in this example is set at half the symbol period. Figure AI.2 (b) presents the scatterplot of the reference signal assuming sampling frequency equal at the symbol frequency while Figure AI.2 (c) presents the scatterplot of the delayed version using the same sampling frequency. As it can be observed, when the timing error is not negligible, after the sampling process pseudo-amplitude levels are created which can potentially deteriorate the system performance. The square timing recovery (STR) algorithm is an efficient, stable and non-data-aided (NDA) timing recovery algorithm [1]. This algorithm does not require feedback of the signal and directly extracts the timing information from the received signal, so that the timing error can be quickly captured. The timing recovery is not influenced by the frequency offset and phase offset of the carrier, so it is prior to carrier synchronization, right after the match filter and the analog-to-digital converter, as it is shown in Figure AI.3. Based on the estimated timing error, the STR algorithm controls an interpolator by determining the specific interpolation time. As a result, the output bit-sequence of the interpolator is synchronized with the transmitted signal.

Figure AI.3 (b) presents the block diagram of the algorithm. At the input of this chain, it is assumed that the received signal, $r(t)$, is a low-pass QAM signal that can be written as:

$$r(t) = \sum_{n=-\infty}^{\infty} a_n g_T(t - nT - \varepsilon(t)T) + n(t) \quad (\text{I.1})$$

, where a_n is the complex transmitted symbol sequence, g_T is the transmission signal pulse, T is the duration of the symbol, $n(t)$ is the channel noise which is assumed to be white with a Gaussian distribution, and $\varepsilon(t)$ is an unknown, slowly varying timing error.

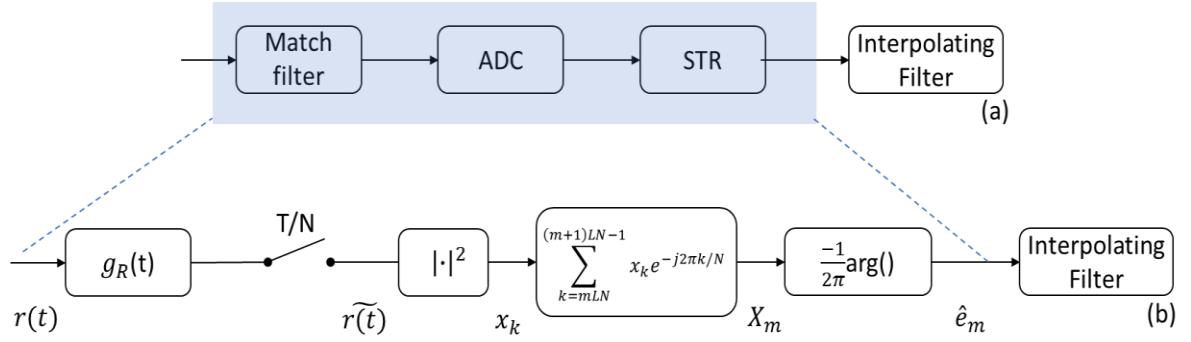


Figure AI.3: (a) High-level and (b) block-diagram representation of square timing recovery algorithm.

The signal is passed through a match filter with $g_R(t)$ impulse response and is sampled at N/T rate. The signal at the input of the STR algorithm can be written as:

$$\widetilde{r}(t) = r\left(\frac{kT}{N}\right) = \sum_{n=-\infty}^{\infty} a_n g\left(\frac{kT}{N} - nT - \varepsilon T\right) + n\left(\frac{kT}{N}\right) \quad (\text{I.2})$$

, where $g(t) = g_T(t) \cdot g_R(t)$. Afterwards, the signal is squared as it is shown in Figure AI.3 and its spectrum includes a spectral component at the symbol rate $1/T$. The timing error of the sampling point is expressed in the frequency domain as phase rotation of this spectral component. The signal then can be expressed as following:

$$x_k = \left| \sum_{n=-\infty}^{\infty} a_n g\left(\frac{kT}{N} - nT - \varepsilon T\right) + n\left(\frac{kT}{N}\right) \right|^2 \quad (\text{I.3})$$

Since $\varepsilon(t)$ varies very slowly compared to the symbol rate, we can assume that it remains constant for a period of time, so we can group the data and then process the received signals section by section. In order to extract the spectral component at the symbol rate, the DFT of x_k should be computed to get the complex Fourier coefficient at the symbol rate. Assuming that each section comprises of L symbols, the length is LN . The LN -DFT of the x_k is given by the following equation:

$$X_w = \sum_{k=mLN}^{(m+1)LN-1} x_k e^{-\frac{2\pi w k}{NL}} \quad (\text{I.4})$$

For $w=L$ the Fourier coefficients of the spectral component at the symbol rate are obtained and given by the following equation:

$$X_{w=L} = \sum_{k=mLN}^{(m+1)LN-1} x_k e^{-\frac{2\pi k}{N}} \quad (\text{I.5})$$

The calculation of the unbiased estimate of the normalized timing offset is actually the calculation of the normalized phase of the $X_{w=L}$ and be expressed as:

$$\hat{\varepsilon}_w = -\frac{1}{2\pi} \arg(X_{w=L}) \quad (\text{I.6})$$

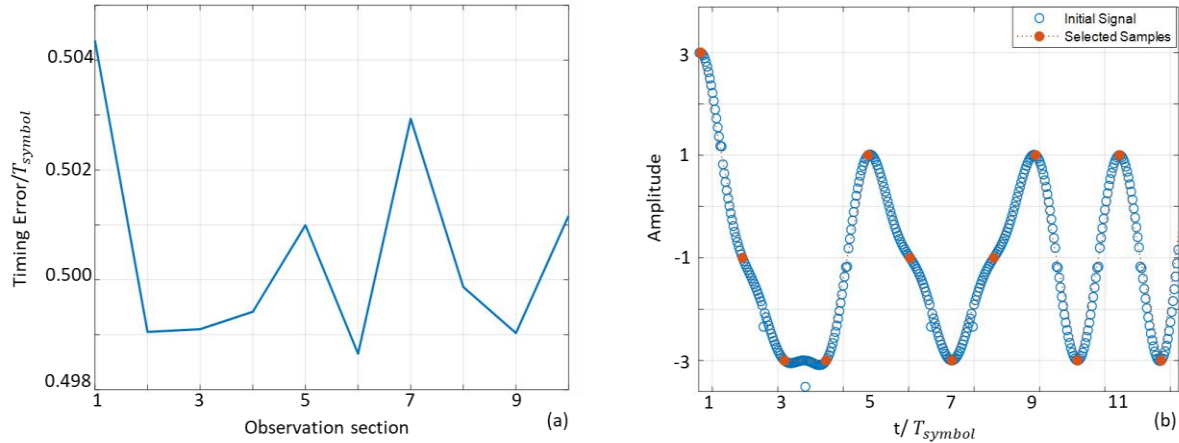


Figure AI.4: (a) Estimated timing error and (b) the time delayed input signal and the selected samples after the STR

By using this timing estimation, the received signal is interpolated at the correct time instants. Following this analysis and assuming that the time delayed signal of Figure AI.2, the estimated normalized timing error is 0.5 as it is depicted in Figure AI.4 (a). After the interpolation, the STR algorithm selects the optimum samples as it is shown in Figure AI.4 (b).

Amplitude level control

Signal level is an important parameter in discrete-time processing because many of the DSP functions that need to be performed require precise knowledge of the signal amplitude. The signal amplitude is dictated by the selected modulation format. To our specific interest, for the modulation formats that have been used during this thesis, i.e., QPSK, 16-QAM, 64-QAM, the power normalization factor (PNF) is 2, 10, and 42, respectively. Therefore, the signal could be normalized using the following equation:

$$SS_{norm} = SS_{in} \sqrt{PNF/P_{signal}} \quad (I.7)$$

IQ imbalance compensation

Ideally, the in-phase (I) and the quadrature (Q) components of a QAM modulation format are orthogonal to each other. Within the system experiments, the QAM signals were formed purely in the electrical domain using state-of-the-art high-speed signal generators by mixing the two components with an intermediate frequency (IF). From the system perspective, in practice the orthogonality depends on the physical dimensions, the impulse responses, and the bias point settings of several electrical components and therefore any slight deviation from the optimum operation point of any of these components can destroy it. Therefore, the main component that could introduce this deviation in our experimental setups was signal generators. The compensation of the nonorthogonality is based on the Gram-Schmidt orthogonalization procedure (GSOP) [2]. The GSOP enables a set of nonorthogonal samples to be transformed into a set of orthogonal samples. Considering the two nonorthogonal components of the received signal, rx_I and rx_Q , the algorithm returns a new pair of orthonormal signals, I_o and Q_o . Assuming a baseband QAM modulated signal, the I/Q amplitude and phase imbalance can be described as following:

$$y_{rx} = \text{Re}(s_{rx}) \cdot e^{j\left(-0.5\pi\frac{I_p}{180}\right)} \cdot 10^{\left(\frac{0.5I_a}{20}\right)} + \text{Im}(s_{rx}) \cdot e^{j\left(\frac{\pi}{2}+0.5\pi\frac{I_p}{180}\right)} 10^{\left(-\frac{0.5I_a}{20}\right)} \quad (\text{I.8})$$

$$y_{rx} = rx_I + jrx_Q \quad (\text{I.9})$$

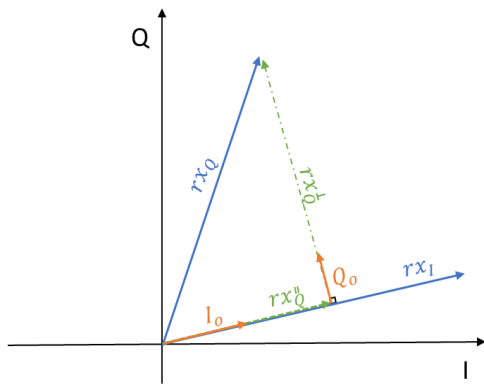
,where I_a and I_p correspond to the amplitude and phase imbalance. The new pair of orthonormal is given by the following equations:

$$I_o = \frac{rx_I}{\sqrt{P_I}} \quad (\text{I.10})$$

$$Q'_o = rx_Q - \frac{\rho rx_I}{P_I} \quad (\text{I.11})$$

$$Q_o = \frac{Q'_o}{\sqrt{P_Q}} \quad (\text{I.12})$$

,where $\rho = \langle rx_I \cdot rx_Q \rangle$ is the inner product, $P_I = E\{rx_I^2\}$ and $P_Q = E\{Q'_o\}$ are the average power of the rx_I and Q'_o signals, respectively. In essence, GSOP subtracts the projection of the vector rx_Q to the rx_I from the rx_Q , as it is presented in Figure AI.5.



- Step 1:** Calculate the unitary vector, I_o

$$I_o = \frac{rx_I}{\|rx_I\|}$$

Step 2: Calculate the projection of rx_Q to I_o

$$rx_Q^* = \frac{\langle rx_I \cdot rx_Q \rangle}{\|rx_I\|^2} rx_I$$

Step 3: Calculate the orthogonal vector, rx_Q^{\perp}

$$rx_Q^{\perp} = rx_Q - rx_Q^* = rx_Q - \frac{\langle rx_I \cdot rx_Q \rangle}{\|rx_I\|^2} rx_I$$

Step 4: Calculate the orthonormal vector, Q_o

$$Q_o = \frac{rx_Q^{\perp}}{\|rx_Q^{\perp}\|}$$

Figure AI.5: Vector representation and the key steps of the GSOP algorithm.

Figure AI.6 depicts the effect of phase imbalance set at 15° and 30° degrees and Figure AI.7 depicts the effect of amplitude imbalance set at 3 dB and 6 dB on the constellation diagram of a QPSK signal with 20 dB SNR.

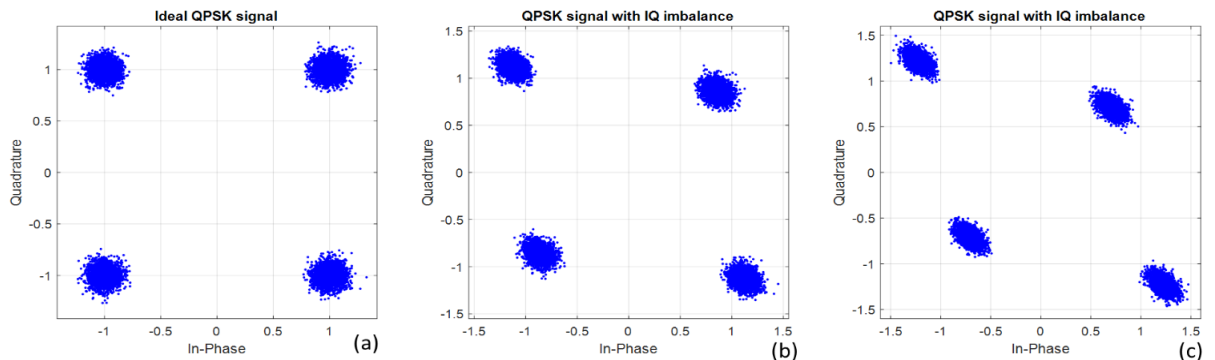


Figure AI.6: (a) Scatterplot of an ideal QPSK signal with 20 dB SNR, and the effect of the phase imbalance on the constellation diagrams considering (b) 15° and (c) 30° , respectively.

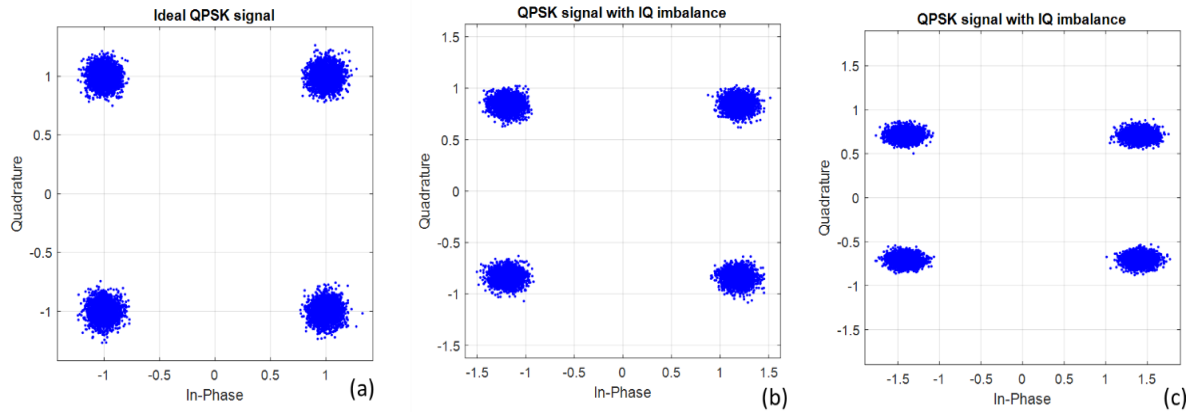


Figure AI.7: (a) Scatterplot of an ideal QPSK signal with 20 dB SNR, and the effect of amplitude imbalance on the constellation diagrams considering (b) $I_a = 3$ dB and (c) $I_a = 6$ dB of amplitude imbalance, respectively.

Figure AI.8 presents the case where both phase and amplitude imbalance deteriorate the performance of the QPSK signal while Figure AI.8 (c) presents the output of the GSOP algorithm.

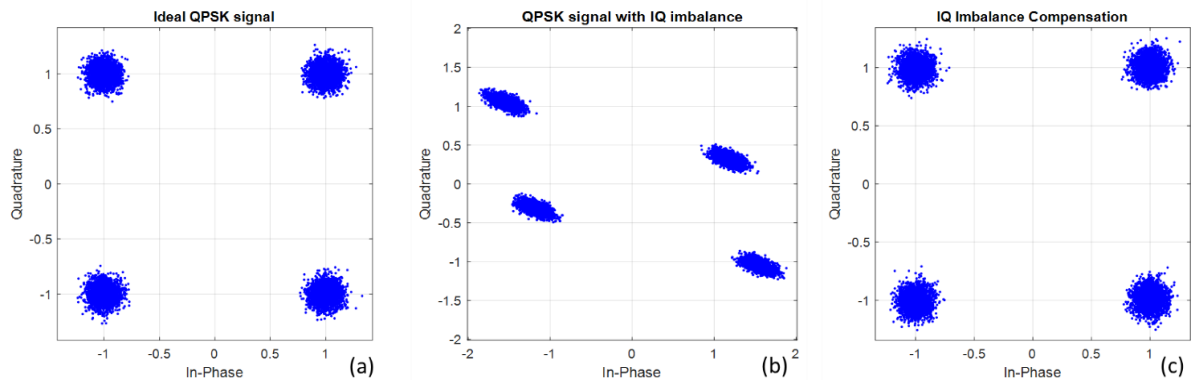


Figure AI.8: Scatterplots of (a) an ideal QPSK signal with 20 dB SNR, (b) the same signal with 30° phase imbalance and 6 dB amplitude imbalance, and (c) the signal after the GSOP algorithm.

Adaptive equalization

In a time-variant multipath and frequency selective wireless environment, the receiver detects several constantly changing, delayed version of the transmitted signal. Therefore, the propagation through this kind of wireless environments causes ISI. ISI deteriorate the system performance since at each time instant multiple delayed symbols are overlapped and detected simultaneously. As a result, the transmitted symbol at a specific time instant is interfered by the symbols detected due to the multipath effect and are becoming indistinguishable, increasing in this way the symbol to error rate. The ISI can become even more severe in the case of bandwidth limitations either at the transmitter or at the receiver side.

The equalizers are filters that attempt to mitigate ISI and improve the receiver performance by emulating the inverse propagation channel response. Especially, in the case of time-varying propagation channels, the filter tap weights should be adaptive in order to adapt to the channel response over time. The estimation of the channel response can be facilitated by the transmission of a training symbol sequence that is a priori known at the receiver. However, in many communication systems, the transmission of a training sequence is either impractical or very costly in terms of data throughput. For this reason,

blind adaptive equalizers that do not rely on training sequence have been developed. In the blind method of equalization, a property of the signal is used for the determination of the instantaneous error $e(n)$, which is used for updating the taps of the adaptive filter. The most common used adaptive algorithm for blind equalization is the constant modulus algorithm (CMA) which uses the constant modularity of the signal as the desired property [2]. CMA assumes that the input signal has a constant amplitude at every instant in time. Any deviation of the received signal amplitude from the constant value is considered as a distortion induced by the channel. CMA attempts to remove the effect of the channel from the received signal by forcing the output of the equalizer to be of constant amplitude. The error is calculated constantly by the following equation:

$$e_{\text{cma}} = y(R - |y|^2) \quad (\text{I.13})$$

,where y is the signal at the output of the equalizer and R is dictated by the modulation format and in the case of QPSK is equal to 2. The taps of the filter are updated using the following equation:

$$w_{\text{new}} = w_{\text{curr}} + \mu * \text{conj}(rx) * e \quad (\text{I.14})$$

Figure AI.9 presents an example of the channel equalization of a QPSK signal transmitted through an ideal transmitter in a wireless channel with impulse response $h = [1+3i \ -5i \ 0.5 \ 2-3i \ 1]$. Additive white noise is also added so the received signal has 20 dB SNR. After the CMA, the signal has been equalized and the error has converged.

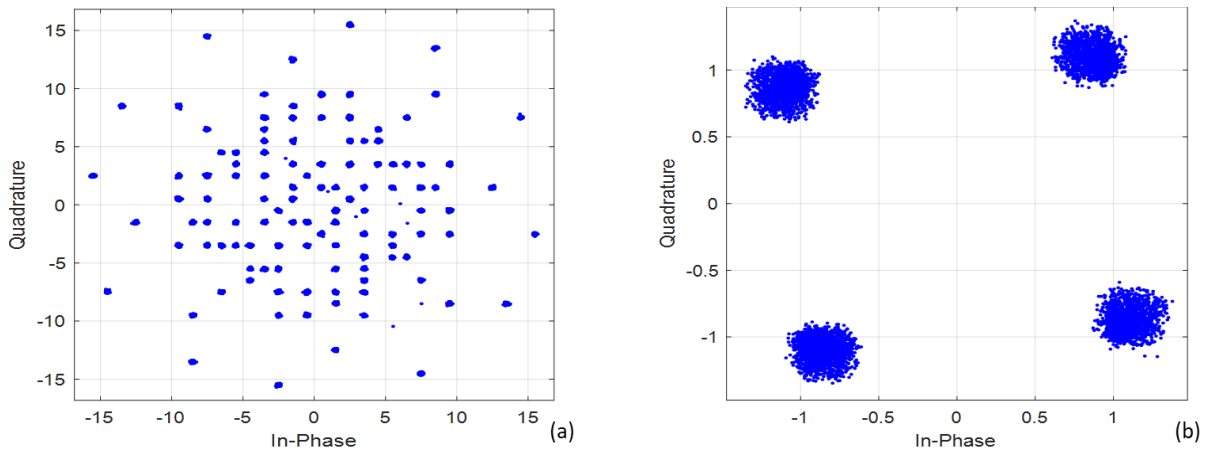


Figure AI.9: Channel equalization of QPSK signal. (a) scatterplot of the received signal after propagating through a channel with $h=[1+3i \ -5i \ 0.5 \ 2-3i \ 1]$ and SNR 20 dB (b) scatterplot of the equalized signal after a CMA with 17 taps.

The residual phase shift is fully compensated by the next algorithm. When high-order QAM modulation formats with multiple radius are used, the CMA is replaced by the radius directed equalizer (RDE) [3]. Compared to CMA equalizer, the error criterion in RDE is based on the error between the equalizer output and the nearest constellation radius and is defines as:

$$e_{\text{RDE}} = y(R_k - |y|^2) \quad (\text{I.15})$$

, where R_k is the radius of the nearest constellation symbol for each equalizer output.

Carrier recovery

The received complex symbols contain not only the desired phase modulation but also the phase noise induced by the laser sources, the optical amplifiers and the photodiodes and a

frequency offset in case of a frequency mismatch between the transmitter and receiver. The variation of this noise is typically slower than the modulation rate and therefore, by averaging the carrier phase over many symbol periods, we can obtain an accurate phase estimation. The phase noise can be extracted by raising the received complex signal at the M th-power, where M is the number of the different symbols in a specific modulation format [4]. The block diagram of the carrier phase recovery algorithm is presented in Figure AI.10. For an example, for a QPSK signal, the received complex symbols are raised to the 4th power to remove the phase modulation and ensure that only the phase noise is present. After averaging this phase component with the phases of the adjacent symbols, the estimated phase is unwrapped and applied to the symbol sequence, removing in this way the unwanted phase shift.

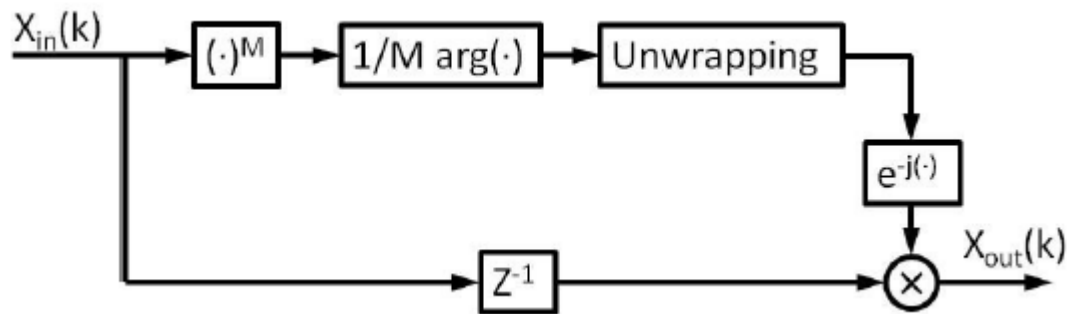


Figure AI.10: Block diagram of the carrier recovery algorithm [4].

Figure AI.11 (a) depicts a typical constellation diagram of a received QPSK signal with significant phase noise while Figure AI.11(b) depicts the same signal after the carrier phase recovery.

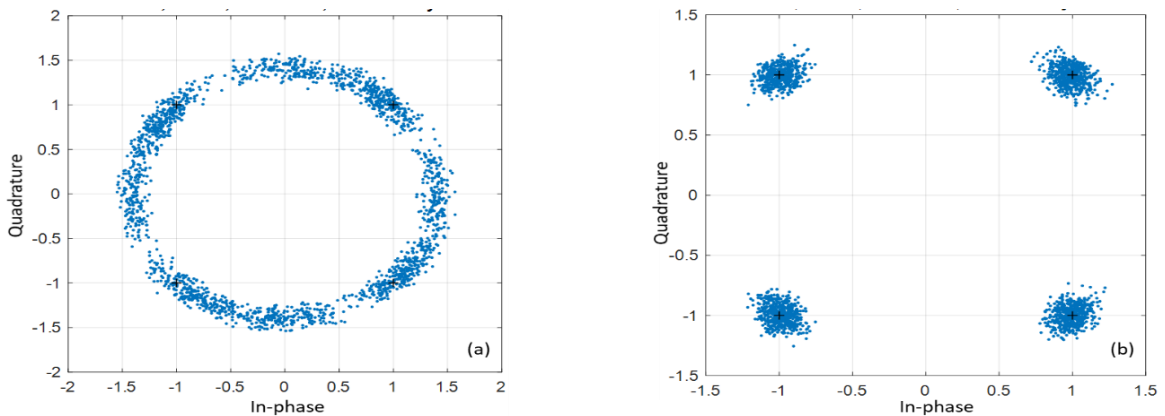


Figure AI.11: (a) QPSK signal with significant phase noise before, (a), and after, (b), the carrier phase recovery.

References of Appendix I

- [1] Oerder, Martin, and Heinrich Meyr. "Digital filter and square timing recovery." *IEEE Transactions on communications* 36.5 (1988): 605-612.
- [2] Savory, S. J. (2010). Digital coherent optical receivers: Algorithms and subsystems. *IEEE Journal of selected topics in quantum electronics*, 16(5), 1164-1179.
- [3] Fatadin, I., Ives, D., & Savory, S. J. (2009). Blind equalization and carrier phase recovery in a 16-QAM optical coherent system. *Journal of lightwave technology*, 27(15), 3042-3049.
- [4] Ip, E., & Kahn, J. M. (2007). Feedforward carrier recovery for coherent optical communications. *Journal of Lightwave Technology*, 25(9), 2675-2692.

List of figures

Figure 1.1: (a) Global mobile network data traffic forecast for 5G and 4G networks. (b) Total number of mobile subscriptions forecast for four generations of wireless communications technologies. (c) Mobile traffic by application category forecast. (d) Graphical comparison between the total number of mobile subscriptions of 5G and 4G networks during the first nine years since their first deployment. (source: Ericsson [14])	22
Figure 1.2: The 5G use cases are categorized into three families; the extreme Mobile Broadband (blue color), the Massive Scale Communication (orange color), and the Ultra-Reliable Low Latency Service (green color). Each of these families poses a different set of requirements in the 5G networks. In some use cases, these sets may overlap, such as in the industrial automation sector (source: [15]).	23
Figure 1.3: Frequency spectrum bands and bandwidth availability (source: [21]).	25
Figure 1.4: (a) Use of 5G spectrum between 24.5 GHz and 29.5 GHz, countries plotted by status of most advanced operator activities and (b) announced devices by the Global Mobile Suppliers Association with known spectrum support (source: Hellenic Telecommunications and Post Commission [20]).	25
Figure 1.5: (a) Artistic representation of an urban environment with indicative definition of 5G cells and allocation of RAUs (from [26]). (b) Reference architecture of 5G networks with centralization of base-band processing units (BBUs) in large pools and connection of each BBU pool to a large number of remote antenna units (RAU) via a ring-based optical fronthaul [27].	26
Figure 1.6: (Left) Analog radio over fiber (ARoF) scenario for the interconnection of each BBU with the corresponding RAU, based on the execution of all digital processing (including the DAC/ADC functions for the wireless transmission) taking place at the BBU site. (Right) Digital radio over fiber (DRoF) scenario for the same interconnection, based on digital optical transmission over the fronthaul link and execution of a large part of the digital processing at the site of the RAU [28].	26
Figure 1.7: A beamforming network process the signals transmitted or received by a multi-element antenna in such a way that wireless signals at particular angles experience constructive interference (right) while others experience destructive interference (left).	27
Figure 1.8: (a) Reference architecture of a receive analog beamforming network (BFN). (b) Schematic representation of an $M \times N$ BFN based on Blass matrix architecture capable of forming M beams and feeding N AEs. (c) Schematic representation of a 4×4 BFN based on Butler architecture for forming up to 4 orthogonal beams and feeding a 4-element antenna array and (d) schematic representation of an $M \times N$ BFN based on Nolen architecture capable of forming M orthogonal beams, feeding an antenna array with N AEs.	28
Figure 1.9: Pictures of assembled analog BFNs. (a) A 4×16 Blass matrix for operation in Ku-band (12-18 GHz) [48], (b) a 4×4 Butler matrix [49] (c) a 3×3 symmetrical Nolen matrix [50], and (d) 7×9 Rotman lens for operation in Ka-band (27-40 GHz) [51].	29
Figure 1.10: Reference architecture of a fully digital (a) and hybrid (b) BFNs, both operating at the receiver side of a communication system.	30
Figure 1.11: Artistic layout of an indicative microwave photonics system. A representative functionality of such a system is the true-time delay of RF signals. As an example of such a system, the inset graphs show how a time delay is introduced to an RF signal. More specifically, insets (a)-(d) depict the time-domain representation of the input (a) and output (d) microwave signal as well as the modulated signal optical signal before (b) and (c) the insertion of the time delay.	31
Figure 1.12: Pictures of optical beamforming networks reported in this dissertation. (a) 2×4 OBFN based on bulk optical delay lines and optical attenuators, serving as a testing vehicle for validating the principle of operation of single-beam, multi-beam, and multicast operations (see Chapter 4). (b) The first-ever 1×4 fully integrated Si ₃ N ₄ -InP OBFN based on a binary architecture with tunable optical true time delay elements, tested with high-order modulated RF signals (see Chapter 5). (c) 2×2 OBFN based on Blass matrix architecture (see Chapter 6), and (d) 8×8 OBFN based on Blass matrix architecture (see Chapter 6).	35
Figure 2.1: Inverse square law of the power decay	42
Figure 2.2: Typical 2D radiation patterns at the azimuthal plane and elevation plane as well as 3D radiation patterns of a short dipole antenna (a-c), half-wave dipole antenna (d-f), and a horn antenna (g-i).	43
Figure 2.3: Indicative radiation pattern in polar coordinates presenting the three types of lobes, the main, side, and back lobes [4].	44
Figure 2.4: Schematic representation of (a) an arbitrary array antenna geometry and (b) a linear array antenna with antenna elements placed along the x-axis.	45
Figure 2.5: Normalized AFs of a 4-element linear array antenna with $d = \lambda/2$ spacing configured for single-beam operation and maximum radiation at (a) 60° and (b) 130°	48

Figure 2.6: Normalized AFs of a 4-element linear array antenna with $d=\lambda/2$ spacing configured for multi-beam operation and maximum radiation at (a) 60° and (b) 130°	48
Figure 2.7: Normalized AFs of an 8-element linear array antenna with $d=\lambda/2$ spacing configured for multi-beam operation and maximum radiation at (a) 60° and (b) 130°	49
Figure 2.8: (a) Normalized Afs of a 16-element linear array antenna with $d=\lambda/2$ spacing configured for multi-cast operation with a single information signal and maximum radiations at 50° and 120° . The amplitude and phase of the excitation signals are plotted in (b) and (c), respectively.	50
Figure 2.9: (a) Normalized Afs of a 16-element linear array antenna with $d=\lambda/2$ spacing configured for multi-cast operation with a two information signals. The first beam is steered to 50° and 120° while the second to 90° . The amplitude and phase of the excitation signals are plotted in (b) and (c), respectively.	50
Figure 2.10: Schematic representation of beamforming networks based on (a) phase shifters and (b) true time delay elements.	51
Figure 2.11: Ideal phase response of a (a) TTD element and (b) a phase shifter.	52
Figure 2.12: Frequency squint effect in a 16-elements linear array. The nominal pointing direction is $\psi = 60^\circ$. A percentage variation of $\pm 0.1\%$ creates already visible change in the pointing direction	53
Figure 2.13: (a) The normalized amplitudes of the excitation signals of a 16-element linear array antenna with $d=\lambda/2$ spacing in case of uniform distribution and (b) the resulted normalized AF.	54
Figure 2.14: The normalized amplitudes of the excitation signals of a 16-element linear array antenna with $d=\lambda/2$ spacing in case of Gaussian distribution with $\gamma=2$ and (b) the resulted normalized AF.	54
Figure 3.1: Artistic layout of a microwave photonics system for transmitting microwave signals over an optical fiber. The time-domain representation of the optical (a and c) and microwave signals (b and d) are presented as insets.	57
Figure 3.2: Artistic layout of an indicative microwave photonics system for delaying a microwave signal by 0.3 of its period. Insets (a)-(d) depict the time-domain representation of the input (a) and output (d) microwave signal as well as the modulated signal optical signal before (b) and (c) the insertion of the time delay.	57
Figure 3.3: High-level representation of (a) direct and (b) external modulation schemes.	60
Figure 3.4: Schematic representation of a (a) optical phase modulator and (b) Mach-Zehnder modulator (MZM).	61
Figure 3.5: Operating the MZM at the (a) zero-transmission point and (b) quadrature point.	62
Figure 3.6: Optical spectra of an MZM operating in the (a) zero and (b) quadrature transmission point.	62
Figure 3.7: Normalized transfer curves for a commercial EAM for different operating wavelengths.	63
Figure 3.8: Schematic for intensity modulated optical carrier and direct detection (IM-DD), consisting of a lasers source, a modulator driven by cosine wave, and a photodiode. At each stage, the spectrum of the signal is presented.	63
Figure 3.9: MWP link modelled as a 2-port microwave system, connected to source and a load.	64
Figure 3.10: Circuit representation of noise source as current sources.	65
Figure 3.11: Representation of the third-order spurious-free dynamic range in a log-log scale.	67
Figure 4.1: Layout of the proposed $M \times N$ OBFN operating (a) in the downlink direction, feeding an N -element antenna, and supporting the formation of M beams.	72
Figure 4.2: Layout of the proposed $M \times N$ OBFN operating in the uplink direction, fed by an N -element antenna array, and forming M independent output microwave signals.	73
Figure 4.3: Block diagram of the mathematical analysis for proving that the excitation signal after the PD is a linear superposition of the individual signals that correspond to the different beams and are destined to the specific AE.	74
Figure 4.4: Simulation results for single-beam operation of a 2×4 TTD OBFN assuming transmission of a 16-QAM signal at 1 Gbaud symbol rate at 60° . (a) Normalized amplitudes and phases of the excitation signals applying a Gaussian distribution with standard deviation equal to 1.5, (b) calculated array factor, (c) and (d) resulting constellation diagrams at 60° and 110° , respectively.	76
Figure 4.5: Simulation results for single-beam operation of a 2×4 TTD OBFN assuming transmission of a 64-QAM signal at 1 Gbaud symbol rate at 135° . (a) Normalized amplitudes and phases of the excitation signals applying a uniform amplitude distribution, (b) calculated array factor, (c) and (d) resulting constellation diagrams at 135° and 70° , respectively.	76
Figure 4.6: Simulation results for single-beam operation of a 2×8 TTD OBFN assuming transmission of a 64-QAM signal at 1 Gbaud symbol rate at 135° . (a) Normalized amplitudes and phases of the excitation signals applying a uniform amplitude distribution, (b) calculated array factor, (c) and (d) resulting constellation diagrams at 135° and 70° , respectively.	77

Figure 4.7: Simulation results for multi-beam operation of a 2×4 TTD OBFN assuming transmission of a QPSK signal at 1 Gbaud symbol rate at 110° and a 16-QAM signal at 1 Gbaud symbol rate at 50°. (a) Normalized amplitudes and phases of the excitation signals applying a uniform amplitude distribution, (b) calculated array factor, (c) and (d) resulting constellation diagrams at 50° and 110°, respectively.	78
Figure 4.8: Simulation results for multi-beam operation of a 2×4 TTD OBFN assuming transmission of a QPSK signal at 1 Gbaud symbol rate at 120° and a 16-QAM signal at 1 Gbaud symbol rate at 67°. (a) Normalized amplitudes and phases of the excitation signals applying a uniform amplitude distribution, (b) calculated array factor, (c) and (d) resulting constellation diagrams at 120° and 67°, respectively.	79
Figure 4.9: Simulation results for multicast operation of a 2×4 TTD OBFN assuming transmission of a 16-QAM signal with 1 Gbaud symbol rate at 75° and 140°. (a) Normalized amplitudes and phases of the excitation signals, (b) calculated array factor, (c) and (d) constellation diagrams at 75° and 140°, respectively.	80
Figure 4.10: Simulation results for multicast operation of a 2×4 TTD OBFN assuming transmission of a 16-QAM signal with 1 Gbaud symbol rate at 65° and 140° for different combination of amplitude apodization schemes. (a) – (c) calculated array factors and constellation diagrams applying a uniform distribution for both steering angles, (d)-(f) and (g)-(j) corresponding results applying a uniform-Gaussian (std=1.5) and a Gaussian-Gaussian (std=1.5) distribution, respectively.	81
Figure 4.11: Simulation results for multicast operation of a 2×4 TTD OBFN assuming transmission of a 16-QAM signal with 1 Gbaud symbol rate at 75° and 140° for different combination of amplitude apodization schemes. (a) – (c) calculated array factors and constellation diagrams applying a uniform distribution for both steering angles, (d)-(f) and (g)-(j) corresponding results applying a uniform-Gaussian (std=1.5) and a Gaussian-Gaussian (std=1.5) distribution, respectively.	82
Figure 4.12: Simulation results for multicast operation of a 2×8 TTD OBFN assuming transmission of a 16-QAM signal with 1 Gbaud symbol rate at 45°, 90°, and 140°. (a) Normalized amplitudes and phases of the excitation signals, (b) calculated array factor, (c), (d), and (e) constellation diagrams at 45°, 90°, and 140°, respectively.	83
Figure 4.13: Experimental setup for the evaluation of a 2×4 TTD OBFN based on an array of ODLs and an array of VOAs, operating at the downlink direction.	84
Figure 4.14: Block diagram of the deployed offline DSP chain for the calculation of the array factor of the two beams and the decoding of the mQAM signals.	85
Figure 4.15: key optical components used in the experimental testbed. (a) Electro-absorption modulator, (b) Mach-Zehnder modulator, (c) Arrayed waveguide grating, and variable optical attenuators.	85
Figure 4.16: Key optical components of the experimental testbed. (a) and (b) Optical delay line arrays, (c) a dual photodetector, and (d) a general aspect of the experimental testbed.	86
Figure 4.17: Wiring diagram for connecting the Raspberry Pi 3 Model B+ microcontroller to the stepper motor, utilizing an A4988 stepper motor driver carrier.	86
Figure 4.18: (a) Aspect of the experimental setup after automating its reconfiguration procedure, (b) picture of the Raspberry Pi microcontroller and the corresponding electrical driver circuits and (c) a zoom in picture of a stepper motor.	87
Figure 4.19: Pictures of the graphical user interface developed to facilitate the user to insert the information about the direction and the operating microwave frequency of each beam.	87
Figure 4.20: Images of the rack-based testbed which will host the whole OBFN. In total three shelves will be used and will host successively the optical splitters, the programmable ODLs, the VOAs and the optical couplers.	88
Figure 4.21: (a) Screenshot captured at the real-time oscilloscope presenting the four 16-QAM electrical signals with 1 Gbaud symbol rate after the photodetection stage for case 2. (b) Polar diagrams for all the cases operating with microwave signals with central frequencies at 15 GHz, (c) and (d) indicative constellation diagrams of the demodulated signals of case 6 and with modulation format 16-QAM and QPSK, respectively.	89
Figure 4.22: BER curves for all the experimental cases operating (a) with QPSK and (b) 16-QAM modulation formats.	90
Figure 4.23: (Bottom) Polar diagram of the second experimental case assuming a linear antenna array with 4 omnidirectional AEs. (Top) The corresponding constellation diagrams of the two beams for -3 dBm received optical power.	91
Figure 4.24: (a) – (d) BER curves as a function of the optical received power at the photodiode array in case of operating the 2×4 OBFN in multi-beam operation for the experimental cases 1, 2, 3, and 4 of Table 6, respectively.	91

Figure 4.25: (a) and (b) BER curves as a function of the optical received power at the photodiode array in case of operating the 2×4 OBFN in multicast operation for the experimental cases 1a, 1b and 2a, 2b of Table 2, respectively. 92

Figure 5.1 (a) Picture of the 1×4 InP-TriPleX OBFN-PIC and (b) picture of the assembled OBFN-PIC with the driving electronics. 95

Figure 5.2 : Layout of the fully hybrid integrated 1×4 OBFN-PIC. It comprises a hybrid InP-TriPleX external cavity laser, two InP phase modulators, a TriPleX SSBFC filter followed by a 1×4 splitter, and four OTTDLs based on 8 MRRs each, and four InP photodetectors 95

Figure 5.3: Generic process flow for the fabrication of the ADS waveguide geometry [1]. 96

Figure 5.4: (a) Layout of the MZI, serving as coupler inside the Blass matrix, and definition of its coupling coefficients and (b) dependence of the phase and amplitude of the self- and cross-coupling coefficients of the MZI as a function of the phase shift ϕ_1 in the lower arm. 97

Figure 5.5: Layout of an asymmetric Mach-Zehnder interferometer, designed with ΔL path length difference between the upper and the lower branches. 99

Figure 5.6: (a) Power transfer functions and (b) phase response of the two output ports of an aMZI with respect to the normalized frequency. 100

Figure 5.7: Power transfer functions and (b) phase response of the two output ports of an aMZI with respect to the normalized frequency and $\theta = 0$, $\theta = \pi/4$, and $\theta = \pi/2$ 100

Figure 5.8: Layout of a micro-ring resonator, implemented as a balanced MZI. 101

Figure 5.9 (a) Power and phase transmission spectra of a MRR under different configurations. 102

Figure 5.10: Layout of the single-sideband full carrier optical filter consisting of an asymmetrical MZI having each arm side-coupled to a micro-ring resonator. 103

Figure 5.11: (a) Power transfer function and phase response of the SBBFC optical filter and (b) the phase responses of the shorter and longer path without taking into account the phase induced by the two tunable couplers at the input and output. 103

Figure 5.12: (a) Experimental setup for characterizing the performance of the optical filter (SSBFC). A broadband source is coupled to FA 1, passes through PM2 by setting the tunable coupler at the cross-state and is coupled to the lower input of SSBFC filter (see Figure 5.2) . (b) Measured transfer function at the output of the PIC (FA 2) when the integrated laser source is OFF and (c)-(d) experimental optical spectra when the integrated laser is ON and the generated optical carrier is not modulated by PM1 and when PM1 is driven by a 5 GHz, 10 GHz, and 15 GHz sine waves, respectively. 104

Figure 5.13: Imposed delay by an MRR for different coupling coefficient (k) of the companion MZI. 105

Figure 5.14: Cross section and equivalent electrical circuit of the InP phase modulator, (b) its measured half-wave voltage, V_π as function of the modulation microwave frequency, and (c) a picture of fabricated InP PIC. 106

Figure 5.15: (a) Layout of the quad InP photodiode array and (b) the measured dark current of the photodiodes as a function of the bias voltage. 107

Figure 5.16 (a) Schematic view of the WECL and (b) its characteristic I-V curve. 108

Figure 5.17: (a) Experimental set-up for measuring the link gain of the four independent MWP links (PM1-PD1, PM1-PD2, PM1-PD3, and PM1-PD4) of the PIC-OBFN and (b) – (d) the link gains spectra of the MWP links for biasing voltages of the photodiodes from 0 V up to -3 V. 109

Figure 5.18: Experimental set-up for measuring the noise figure of the OBFN-PIC at 5 GHz and 10 GHz carrier frequencies. 110

Figure 5.19: (a) Two-tone experimental set-up for measuring the SFDR₃ of the OBFN-PIC and (b) – (c) the measured electrical spectra of the PM1-PD4 MWP link, showing the power of the fundamental tones as well as of the 3rd intermodulation tones. 110

Figure 5.20: (a) Imposed delay by one MRR for different coupling coefficients of the MZI and phase shifts on the feedback loop waveguide and (b) imposed delay by the OTTDL that corresponds to PD1, setting all the MRRs at adjacent resonance frequencies. 111

Figure 5.21: Optical spectra of the (I) modulated optical signal, (II) the transfer function of the optical filter, and (III) the power transmission of a single MRR, for driving frequencies (a) 8 GHz, (b), 1 GHz, (c) 3 GHz, and 23 GHz. 112

Figure 5.22: Experimental setup for the system evaluation of the OBFN-PIC using QAM modulated signals at 5 GHz and 10 GHz. It consists of a measuring part (blue solid lines) and a virtual part (blue dashed lines). . 113

Figure 5.23: Indicative microwave waveforms with central frequencies at 5 GHz (a) and 10 GHz (b) as they were captured at the oscilloscope while the OBFN was configured to steer the 5 GHz signal at 90° and the 10 GHz signal at 45°. 114

Figure 5.24: Theoretical and experimental average array factors after configuring the OBFN PIC to operate with sine waves with central frequencies at (a) 5 GHz and (b) 10 GHz. Target beam angles were 45°, 60°, 70°, 90°, 110°, 120° and 135°.	116
Figure 5.25: (a) Array factor of the 500 Mbaud QPSK signal modulated with a 10 GHz microwave carrier and steered at 60°. (b)-(d) Constellation diagrams of the received signal at the observation angle 60°, 20° and 110°, respectively.	116
Figure 5.26: Reconstructed constellation diagrams for each experimental case. As insets are shown the calculated EVM values.	118
Figure 5.27: Constellation diagrams and the calculated EVMs for the case of steering a 500 Mbaud microwave signal modulated around a 5 GHz carrier at 45°, sampled and stored by the oscilloscope at different time instants.	119
Figure 6.1: (a) Block diagram for the introduction of a phase shift on a microwave or mm-wave signal via the introduction of the same phase shift in the optical domain. The processing steps are based on microwave photonics techniques with optical carrier suppression, SSB propagation and carrier re-insertion. (b) Block diagram for the extension of the same concept to the case of multiple microwave signals carried by optical waves with the same optical carrier. At the end of the processing chain, the output signal is the sum of the input microwave signals, each with an independently selected phase shift.	124
Figure 6.2: Layout of optical beamforming network based on Blass matrix feeding N antenna elements and supporting operation with up to M wireless beams.	126
Figure 6.3: Example simulation of an optical Blass matrix beamforming network: Resulting array factor after configuration of a 3×8 Blass matrix for a wireless carrier at 28.5 GHz. Target beam directions were 40°, 85° and 135°, and the type of excitation was uniform for beam 1 and Gaussian for beams 2 and 3.	131
Figure 6.4: Layout of optical beamformer based on Blass matrix supporting operation with up to M beams in the uplink direction in a wireless network.	132
Figure 6.5: Beam squinting effect in optical Blass matrix beamforming network: Error of steering angle compared to the nominal value θ_m as a function of θ_m for different degrees of frequency offset from the nominal frequency f_c .	132
Figure 6.6 (a) Phase offset between the frequency under investigation and the nominal frequency f_c at 60° observation angle, as a function of the number of AEs for different degrees of frequency offset from f_c and (b) amplitude of frequency under investigation at 60° observation angle, as a function of the number of AEs for different degrees of frequency offset from the nominal value f_c . The amplitude is normalized to the corresponding amplitude of f_c at the same observation angle.	133
Figure 6.7: Set up for the simulation of a communication system involving the generation of microwave QAM signals, the beamforming process using an M×N Blass-matrix network, the interaction with an AWGN RF channel model, the signal reception at an observation angle, and the final decoding of the information.	134
Figure 6.8: Decoded constellation diagrams at 40°, 60°, 85° and 135° observation angles for the multi-beam operation example summarized in Table 12.	135
Figure 6.9: (a) Simulated BER as a function of the symbol rate for a 16-QAM signal with roll-off factor equal to 0.25, in the case of an antenna with 8 and 16 AEs, (b) RF spectrum after the AWGN channel for a 2 Gbaud signal and 16 AEs, and (c) the corresponding constellation diagram after the DSP. The SNR is 22 dB in the case of 8 AEs and 25 dB in the case of 16 AEs. (d) Simulated BER as a function of the symbol rate for a 16-QAM signal with roll-off factor equal to 1, in the case of an antenna with 8 and 16 AEs, (e) RF spectrum after the AWGN channel for a 2 Gbaud signal and 16 AEs, and (f) the corresponding constellation diagram after the DSP. The SNR is 22 dB in the case of 8 AEs and 25 dB in the case of 16 AEs.	136
Figure 6.10: (a) Simulated BER as a function of the symbol rate for a 64-QAM signal with roll-off factor equal to 0.25, in the case of an antenna with 8 and 16 AEs, (b) RF spectrum after the AWGN channel for a 2 Gbaud signal and 16 AEs, and (c) the corresponding constellation diagram after the DSP. The SNR is 28 dB in the case of 8 AEs and 31 dB in the case of 16 AEs. (d) Simulated BER as a function of the symbol rate for a 64-QAM signal with roll-off factor equal to 1, in the case of an antenna with 8 and 16 AEs, (e) RF spectrum after the AWGN channel for a 2 Gbaud signal and 16 AEs, and (f) the corresponding constellation diagram after the DSP. The SNR is 28 dB in the case of 8 AEs and 31 dB in the case of 16 AEs.	137
Figure 6.11: (a) BER of decoded 16-QAM signal (roll-off factor 0.25) at 60° observation angle as a function of the symbol rate and the asymmetry of the MZIs (ΔLHW) inside a 4×16 optical Blass matrix. (b) BER of decoded 16-QAM signal (roll-off factor 1) at 60° observation angle as a function of the symbol rate and the asymmetry of the MZIs (ΔLHW) inside a 4×16 optical Blass matrix. (c) BER of decoded 64-QAM signal (roll-off factor 0.25) at 60° observation angle as a function of the symbol rate and the asymmetry of the MZIs (ΔLHW) inside a 4×16 optical Blass matrix. (d) BER of decoded 64-QAM signal (roll-off factor 1) at 60°	

observation angle as a function of the symbol rate and the asymmetry of the MZIs (ΔLHW) inside a 4×16 optical Blass matrix.	139
Figure 6.12: BER of decoded 16-QAM signal (roll-off factor 1) at 60° observation angle as a function of the symbol rate and the length variation of the waveguides between successive MZIs (ΔLHW) inside a 4×16 optical Blass matrix.	140
Figure 6.13: (a) BER of decoded 16-QAM signal (roll-off factor 1) at 60° observation angle as a function of the symbol rate and the variation in the power coupling ratio of the couplers inside the MZIs of a 4×16 optical Blass matrix. The variation is described by the half-width of a uniform distribution ($\Delta CRHW$). (b) BER of decoded 16-QAM signal (roll-off factor 1) at 60° observation angle as a function of the symbol rate and the variation in the phase shifts of the phase shifters inside a 4×16 optical Blass matrix. The variation is described by the half-width of a uniform distribution ($\Delta \phi HW$).	141
Figure 6.14: Modified layout of the optical Blass matrix ensuring equal path lengths for all input signals propagating towards all possible output ports. In this way the differences in the optical loss that would be otherwise present are eliminated. The example shown in the figure refers to a 3×4 Blass matrix case.	143
Figure 6.15: Schematic of HAMLET transceiver module (example with 4×4 Blass matrix). Top right: close up of a Blass matrix node showing the 2×2 tuneable coupler and tuneable phase shifter.	145
Figure 6.16 (a) Functional layout and (b) picture of the 2×2 fully integrated Blass matrix based optical beamformer.	146
Figure 6.17: (a) Block diagram of the experimental testbed for the static characterization of the carrier re-insertion process by measuring the optical power at the FA port and (b) Block diagram of the experimental testbed for the configuration of the optical tunable SSBSC filter using an ASE broadband light source as input to the top filter.	147
Figure 6.18: Optical spectra of the on-chip tuneable filter for different configurations of the heater elements: (a) 22 GHz passband with 14 dB attenuation at the stopband and (b) 7.5 GHz passband with 13 dB attenuation at the stopband.	147
Figure 6.19: Block diagram of the experimental testbed for the characterization of the on-chip optical tuneable filter.	148
Figure 6.20: Optical spectrum (a) of the amplitude modulated optical carrier by 10 GHz microwave carrier at the input of the module, (b) of the amplified optical signal at the input port (c) of the transfer function of the on-chip optical tuneable filter, (d) of the filtered optical signal with suppressed the one sideband and the optical carrier at the output of the module.	148
Figure 6.21: Block diagram of the experimental testbed for the validation of the carrier re-insertion concept using external DFB laser, EAM, EDFAs and OBPFs. The insets indicate the optical spectra at each stage of the experiment.	149
Figure 6.22: Received electrical eye-diagram of the 15 GHz sinusoidal wave, after the combination of the optical carrier and single sideband optical signal within the prototype.	150
Figure 6.23: Functional layout of the Module-1 consisting of the 2 PolyBoard chips (in blue) with eight InP-EAMs integrated on the PolyBoard chip; and TriPleX chip (in red) with 8×8 multi beam OBFN.	151
Figure 6.24: a) Picture of the assembled Module-1 prototype that accommodates an array of 8 InP-EAMs and an 8×8 optical beamforming network and (b) & (c) zoom-in pictures of the PolyBoard-InP section and TriPleX chip, respectively.	151
Figure 6.25: Measured P-I curve of the integrated DML laser used for the interconnection of Module-1 with an optical fronthaul network.	152
Figure 6.26: (Left) Eyediagram of the generated electrical signal at 2 Gbaud symbol rate that modulated the amplitude of the optical carrier of the integrated DML laser and (right) the eyediagram of the recovered electrical signal after the photodetection stage, using an external photodiode, and the offline processing by the DSP toolkit.	153
Figure 6.27: (Left) Eyediagram of the generated electrical signal at 3 Gbaud symbol rate that modulated the amplitude of the optical carrier of the integrated DML laser and (right) the eyediagram of the recovered electrical signal after the photodetection stage, using an external photodiode, and the offline processing by the DSP toolkit.	153
Figure 6.28: (Left) Eyediagram of the generated electrical signal at 4 Gbaud symbol rate that modulated the amplitude of the optical carrier of the integrated DML laser and (right) the eyediagram of the recovered electrical signal after the photodetection stage, using an external photodiode, and the offline processing by the DSP toolkit.	153
Figure 6.29: Layout of the TriPleX chip of the assembled Module-1. It includes a 1×8 splitting network, 8 SSBSC filters, 8×8 Blass-matrix OBFN, and 8 power combiners.	154
Figure 6.30: Extinction ratios of the MZIs constituting the Blass-matrix beamforming network. The performance of the PZT-based actuators was deteriorated after several actuations.	155

Figure AI.1:Reference DSP suite for the demodulation of the high-speed QAM signals of the high-bandwidth channels	167
Figure AI.2: (a) Real part of low-pass 16-QAM signal and its delayed version by half the symbol period, (b) scatterplot of the reference signal assuming sampling frequency equal to the symbol rate and (c) scatterplot of its delayed version.	167
Figure AI.3: (a) High-level and (b) block-diagram representation of square timing recovery algorithm.	168
Figure AI.4: (a) Estimated timing error and (b) the time delayed input signal and the selected samples after the STR.....	169
Figure AI.5: Vector representation and the key steps of the GSOP algorithm.	170
Figure AI.6: (a) Scatterplot of an ideal QPSK signal with 20 dB SNR, and the effect of the phase imbalance on the constellation diagrams considering (b) 15° and (c) 30°, respectively.	170
Figure AI.7: (a) Scatterplot of an ideal QPSK signal with 20 dB SNR, and the effect of amplitude imbalance on the constellation diagrams considering (b) $I_a = 3$ dB and (c) $I_a = 6$ dB of amplitude imbalance, respectively.....	171
Figure AI.8: Scatterplots of (a) an ideal QPSK signal with 20 dB SNR, (b) the same signal with 30° phase imbalance and 6 dB amplitude imbalance, and (c) the signal after the GSOP algorithm.	171
Figure AI.9: Channel equalization of QPSK signal. (a) scatterplot of the received signal after propagating through a channel with $h=[1+3i \ -5i \ 0.5 \ 2-3i \ 1]$ and SNR 20 dB (b) scatterplot of the equalized signal after a CMA with 17 taps.....	172
Figure AI.10: Block diagram of the carrier recovery algorithm [4].....	173
Figure AI.11: (a) QPSK signal with significant phase noise before, (a), and after, (b), the carrier phase recovery.	173

List of tables

Table 1 Boundaries for near field, Fresnel region, and far-field [1]	41
Table 2 Amplitude and phase coefficients of the excitation signals that correspond to the AFs of Figure 2.5 .	48
Table 3: Amplitude and phase coefficients of the excitation signals that correspond to the AF of Figure 2.6..	48
Table 4: Amplitude and phase coefficient of the excitation signals that correspond to the AF of Figure 2.7 ...	49
Table 5: Experimental use cases in single-beam beamforming	89
Table 6: Experimental use cases in multi-beam beamforming	90
Table 7: Experimental Use Cases in Multicast beamforming	92
Table 8: Simulation parameters for the transmission and phase spectra of an MRR presented in Figure 5.9 .	101
Table 9: Simulation parameters for the transmission and phase spectra of an MRR presented in Figure 5.11	103
Table 10: Modulation and beamforming parameters of the evaluation cases.	113
Table 11: Configuration of MZIs and phase shifters of the 3×8 optical Blass matrix for example of Figure 6.3: Amplitude of self-coupling coefficients and phase shifts.	131
Table 12: Modulation and beamforming parameters in a specific operation example of a 3×16 optical Blass- matrix beamforming network.	135
Table 13: Summary of research objectives and key achievements of the present dissertation.	161

Abbreviations

ADC	Analog-to-digital converter
ADS	asymmetric double-strip
AE	Antenna element
AF	Array factor
aMZI	Asymmetric Mach-Zehnder interferometer
ARoF	Analog radio-over-fiber
ASE	Amplified spontaneous emission
AWG	Arrayed waveguide grating
AWG	Arbitrary waveform generator
AWGN	Additive white Gaussian noise
BBU	Baseband unit
BER	Bit-error rate
BFN	Beamforming network
CLA	Carrier lead around
CRI	Carrier re-inserted
CW	Continuous wave
DAC	Digital-to-analog converter
DBR	Distributed Bragg reflector
DFB	Distributed-feedback
DFT	Discrete Fourier transformation
DML	Direct modulated laser
DRoF	Digital radio-over-fiber
DSP	Digital signal processing
EAM	Electro-absorption modulator
ECL	External cavity lasers
EDFA	Erbium-doped fiber amplifier
eMBB	Enhanced Mobile Broadband
EOM	Electro-optic modulation
ER	Extinction ratio
EVM	Error-Vector Magnitude
F	Noise factor
FSR	Free spectral range
GaAs	Gallium Arsenide
GP	Group Delay
GS	Gain section
GSOP	Gram-Schmidt orthogonalization
GUI	Graphical user interface
IF	Intermediate frequency
IIP	Input intermodulation product
IMD	Intermodulation distortion
IM-DD	Intensity-modulation, direct detection
InGaAs	Indium Gallium Arsenide
InP	Indium Phosphide
iOBFN	Integrated optical beamforming network

IoE	Internet of Things
LNA	Low noise amplifier
LNOI	Lithium niobate on insulator
LPF	Low-pass filter
MC	Microwave chain
MIMO	Multiple-input-multiple-output
mMTC	Massive Machine Type Communications
MRR	Micro-ring resonator
MWP	Microwave Photonics
MZI	Mach-Zehnder Interferometers
MZM	Mach-Zehnder modulator
NF	Noise figure
OBFN	Optical beamforming network
OIP	Output intermodulation product
OOK	On-off keying modulation
OTTDL	Optical true time delay lines
PIC	Photonic integrated circuits
PM	Phase modulator
QAM	Quadrature amplitude modulation
QCSE	Quantum confined Stark effect
QP	Quadrature point
RAU	Remote antenna unit
RIN	Relative intensity noise
RTT	Round-trip time
SFDR	Spurious free dynamic range
SNIR	Signal-to interference plus noise ratio
SNR	Signal-to-noise ratio
SOA	Semiconductor optical amplifier
SSB	Single-sideband
SSBFC	Single sideband full carrier filter
SWDL	Switchable waveguide delay line
TR	Time recovery
TTD	True-time delay
TW	Travelling-wave
URLLC	Ultra-Reliable and Low-Latency Communications
VCSEL	Vertical-cavity surface-emitting lasers
VNA	Vector Network analyzer
VOAs	Variable optical attenuators
WECL	Waveguide-based external cavity laser
ZP	Zero transmission point

Glossary

Analog-to-digital converter	Μετατροπέας αναλογικού σήματος σε ψηφιακό
asymmetric double-strip	Ασύμμετρη διπλή λωρίδα
Antenna element	Ακτινοβολητής
Array factor	Παράγοντας διάταξης
Asymmetric Mach-Zehnder interferometer	Ασύμμετρο συμβολόμετρο Mach-Zehnder
Amplified spontaneous emission	Ενισχυμένη αυθόρμητη εκπομπή
Arrayed waveguide grating	Συστοιχία κυματοδηγών Grating
Arbitrary waveform generator	Γεννήτρια τυχαίων κυματομορφών
Additive white Gaussian noise	Προσθετικός λευκός θόρυβος Γκάους
Baseband unit	Επεξεργαστική μονάδα βασικής ζώνης
Bit-error rate	Ρυθμός εσφαλμένων ψηφίων
Beamforming network	Δίκτυο σχηματοποίησης δεσμών
Digital-to-analog converter	Μετατροπέας ψηφιακού σε αναλογικό
Distributed Bragg reflector	Κατανεμημένος ανακλαστήρας Bragg
Discrete Fourier transformation	Διακριτός μετασχηματισμός Fourier
Direct modulated laser	Οπτική πηγή άμεσης διαμόρφωσης
Digital signal processing	Ψηφιακή επεξεργασία σήματος
Electro-absorption modulator	Ηλεκτρο-απορροφητικός διαμορφωτής
External cavity lasers	Οπτική πηγή εξωτερικής κοιλότητας
Erbium-doped fiber amplifier	Οπτικός ενισχυτής-Ίνας πρόσμιξης ερβίου
Electro-optic modulation	Ηλεκτρο-οπτικός διαμορφωτής
Extinction ratio	Λόγος αποσβέσεως
Error-Vector Magnitude	Μέτρο διανύσματος σφάλματος
Noise factor	Εικόνα θορύβου
Free spectral range	Ελεύθερο φασματικό εύρος
Group Delay	Καθυστέρησης ομάδας
Gain section	Στοιχείο κέρδους οπτικής πηγής
Input intermodulation product	Προϊόν ενδοδιαμόρφωσης εισόδου
Intermodulation distortion	Παραμόρφωση ενδοδιαμόρφωσης
Intensity-modulation, direct detection	Διαμόρφωση πλάτους, άμεση ανίχνευση
Integrated optical beamforming network	Ολοκληρωμένο οπτικό δίκτυο σχηματοποίησης μικροκυματικών δεσμών
Low noise amplifier	Ενισχυτής χαμηλού θορύβου
Low-pass filter	Βαθυπερατό φίλτρο
Microwave chain	Μικροκυματική αλυσίδα
Multiple-input-multiple-output	Πολλαπλοί είσοδοι - πολλαπλοί έξοδοι
Micro-ring resonator	Συντονιστής μικρό-δακτυλίου
Microwave Photonics	Μικροκυματική φωτονική
Mach-Zehnder Interferometers	Συμβολόμετρο Mach-Zehnder
Mach-Zehnder modulator	Διαμορφωτής Mach-Zehnder
Noise figure	Εικόνα θορύβου
Optical beamforming network	Οπτικό δίκτυο σχηματοποίησης μικροκυματικών δεσμών
Output intermodulation product	Προϊόν ενδοδιαμόρφωσης εξόδου
Optical true time delay lines	Οπτική γραμμή πραγματικής καθυστέρησης

Photonic integrated circuits	Φωτονικά ολοκληρωμένα κυκλώματα
Phase modulator	Διαμορφωτής φάσης
Relative intensity noise	Σχετική ένταση θορύβου
Round-trip time	Χρόνος πλήρους διαδρομής
Spurious free dynamic range	Δυναμική περιοχή απαλλαγμένη παρασιτικών
Signal-to interference plus noise ratio	Αναλογία σήματος προς παρεμβολές συν θόρυβο
Signal-to-noise ratio	Λόγος σήματος προς θόρυβο
Semiconductor optical amplifier	Οπτικός ενισχυτής ημιαγωγού
Single sideband full carrier filter	Οπτικό φίλτρο απόρριψης μιας πλευρικής ζώνης
Switchable waveguide delay line	Διατάξεις καθυστέρησης διακοπών κυματοδηγών
True-time delay	Πραγματική καθυστέρηση
Vertical-cavity surface-emitting lasers	Οπτικές πηγές κάθετης εκπομπής
Variable optical attenuators	Μεταβλητοί οπτικοί εξασθενητές

List of own publications

Journal Articles

- [1] Vasilis Katopodis, David de Felipe, **Christos Tsokos**, Panos Groumas, Maria Spyropoulou, Antonio Beretta, Alberto Dede, Marco Quagliotti, Annachiara Pagano, Antonello Vannucci, Norbert Keil, Hercules Avramopoulos, Christos Kouloumentas "Multi-Flow Transmitter Based on Polarization and Optical Carrier Management on Optical Polymers," in *IEEE Photonics Technology Letters*, vol. 28, no. 11, pp. 1169-1172, 1 June1, 2016, doi: 10.1109/LPT.2016.2533663.
- [2] **Christos Tsokos**, Elias Mylonas, Panos Groumas, Vasilis Katopodis, Lefteris Gounaridis, Roelof Bernardus Timens, Ruud M. Oldenbeuving, Chris G. H. Roeloffzen, Hercules Avramopoulos, and Christos Kouloumentas, "Analysis of a Multibeam Optical Beamforming Network Based on Blass Matrix Architecture," *J. Lightwave Technol.* 36, 3354-3372 (2018)
- [3] Vasilis Katopodis, Haik Mardoyan, **Christos Tsokos**, David Felipe, Agnieszka Konczykowska, Panos Groumas, Maria Spyropoulou, Lefteris Gounaridis, Philippe Jennevé, Fabien Boitier, Filipe Jorge, Tom Keinicke Johansen, Marcello Tienforti, Jean-Yves Dupuy, Antonello Vannucci, Norbert Keil, Hercules Avramopoulos, and Christos Kouloumentas, "Multiflow Transmitter With Full Format and Rate Flexibility for Next Generation Networks," *J. Lightwave Technol.* 36, 3785-3793 (2018)
- [4] **Christos Tsokos**, Elias Mylonas, Panos Groumas, Lefteris Gounaridis, Hercules Avramopoulos, Christos Kouloumentas, "Optical Beamforming Network for Multi-Beam Operation With Continuous Angle Selection," in *IEEE Photonics Technology Letters*, vol. 31, no. 2, pp. 177-180, 15 Jan.15, 2019, doi: 10.1109/LPT.2018.2889411.
- [5] Christos Kouloumentas, **Christos Tsokos**, Panos Groumas, Lefteris Gounaridis, Adam Raptakis, Elias Mylonas, Efstathios Andrianopoulos, Kerstin Wörhoff, Katarzyna Ławniczuk, Arne Leinse, Hercules Avramopoulos, "Multi-Rate and Multi-Channel Optical Equalizer Based on Photonic Integration," *IEEE Photonics Technology Letters*, 32(23), pp.1465-1468.(2020)
- [6] **Christos Tsokos**, Efstathios Andrianopoulos, Adam Raptakis, Nikolaos K. Lyras, Lefteris Gounaridis, Panos Groumas, Roelof Bernardus Timens, Ilka Visscher, Robert Grootjans, Lennart S. Wefers, Dimitri Gekus, Edwin Klein, Hercules Avramopoulos, René Heideman, Christos Kouloumentas, and Chris G. H. Roeloffzen, "True Time Delay Optical Beamforming Network Based on Hybrid InP-Silicon Nitride Integration," *J. Lightwave Technol.* 39, 5845-5854 (2021)
- [7] Adam Raptakis, Lefteris Gounaridis, Madeleine Weigel, Moritz Kleinert, Michalis Georgiopoulos, Elias Mylonas, Panos Groumas, **Christos Tsokos**, Norbert Keil, Hercules Avramopoulos, and Christos Kouloumentas, "2D Optical Phased Arrays for Laser Beam Steering Based On 3D Polymer Photonic Integrated Circuits," *J. Lightwave Technol.* 39, 6509-6523 (2021)
- [8] Efstathios Andrianopoulos, Nikolaos K. Lyras, **Christos Tsokos**, Tianwen Qian, Simon Nelle, David De Felipe, Panos Groumas, Adam Raptakis, Lefteris Gounaridis, Norbert Keil, Christos Kouloumentas, Hercules Avramopoulos "Optical Generation and Transmission of mmWave Signals in 5G ERA: Experimental Evaluation Paradigm," in *IEEE Photonics Technology Letters*, vol. 34, no. 19, pp. 1011-1014, 1 Oct.1, 2022, doi: 10.1109/LPT.2022.3196632.

Conference papers

- [1] Vasilis Katopodis, Maria Spyropoulou, **Christos Tsokos**, Panos Groumas, David de Felipe, Norbert Keil, Antonio Beretta, Antonello Vannucci, Tom K Johansen, Marco Quagliotti, Annachiara Pagano, Jean-Yves Dupuy, Agnieszka Konczykowska, Camille Delezoide, Haik Mardoyan, Christos Kouloumentas, Hercules Avramopoulos "Polarization-, carrier-, and format-selectable optical flow generation based on a multi-flow transmitter using passive polymers," *2016 18th International Conference on Transparent Optical Networks (ICTON)*, 2016, pp. 1-4, doi: 10.1109/ICTON.2016.7550583.
- [2] **Christos Tsokos**, Panos Groumas, Vasilis Katopodis, Hercules Avramopoulos and Christos Kouloumentas, "Enabling photonic integration technology for microwave photonics in 5G systems," *2017 19th International Conference on Transparent Optical Networks (ICTON)*, 2017, pp. 1-4, doi: 10.1109/ICTON.2017.8024906.
- [3] Panos Groumas, **Christos Tsokos**, Moritz Kleinert, Denys Marchenko, Vasilis Katopodis, Matthijn Dekkers, M. Falcucci, Roelof B. Timens, Lefteris Gounaridis, Chris G. Roeloffzen, Antonello Vannucci, Rene G. Heideman, Norbert Keil, Christos Kouloumentas, Hercules Avramopoulos "Photonic integration technology for the interface between the optical and wireless part in 5G networks: The H2020-ICT-HAMLET approach," *2017 IEEE Photonics Society Summer Topical Meeting Series (SUM)*, 2017, pp. 57-58, doi: 10.1109/PHOSST.2017.8012649.
- [4] Vasilis Katopodis, **Christos Tsokos**, David de Felipe Mesquida, Maria Spyropoulou, Agnieszka Konczykowska, Andrea Aimone, Panos Groumas, Jean-Yves Dupuy, Florbela Jorge, Haik Mardoyan, Rafael Rios-Müller, Jeremie Renaudier, Philippe Jennevé, Fabien Boitier, Annachiara Pagano, Marco Quagliotti, Diego Roccatto, Tom K. Johansen, Marcello Tienforti, Antonello Vannucci, Heinz-G. Bach, Norbert Keil, Hercules Avramopoulos, and Christos Kouloumentas "Optical terabit transmitter and receiver based on passive polymer and InP technology for high-speed optical connectivity between datacenters", *Proc. SPIE 10561, Next-Generation Optical Communication: Components, Sub-Systems, and Systems VII*, 1056107 (29 January 2018); <https://doi.org/10.1117/12.2290258>
- [5] Annachiara Pagano, Vasilis Katopodis, **Christos Tsokos**, Haik Mardoyan, Roberto Morro, Alessandro Percelsi, Diego Roccatto, David De Felipe, Florbela Jorge, Maria Spyropoulou, Panos Groumas, Philippe Jennevé, Fabien Boitier, Marco Tienforti, Andrea Annoni, Hercules Avramopoulos, "Field trial evaluation and SDN configurability of an optical terabit transmitter based on passive polymer and InP technology," 20th Italian National Conference on Photonic Technologies (Fotonica 2018), 2018, pp. 1-4, doi: 10.1049/cp.2018.1619.
- [6] Lefteris Gounaridis, Panos Groumas, Erik Schreuder, **Christos Tsokos**, Elias Mylonas, Adam Raptakis, Rene Heideman, Hercules Avramopoulos, and Christos Kouloumentas "Design of ultra-compact multimode interference (MMI) couplers and high efficiency grating couplers in TriPleX platform as part of a photonic-based sensor", *Proc. SPIE 10921, Integrated Optics: Devices, Materials, and Technologies XXIII*, 1092127 (4 March 2019); <https://doi.org/10.1117/12.2510053>
- [7] Panos Groumas, **Christos Tsokos**, David de Felipe Mesquida, Ute Troppenz, Romain Hersent, Paraskevas Bakopoulos, Boaz Atias, Jean-Yves Dupuy, Annachiara Pagano, Anna Chiado Piat, Simon Kibben, Lefteris Gounaridis, Adam Raptakis, Moritz Seyfried, Martin Moehrle, Christos Kouloumentas, Norbert Keil, and Hercules Avramopoulos "Enabling low-cost high-volume production compatible terabit transceivers with up to 1.6 Tbps capacity and 100Gbps per lane PAM-4 modulation for

intra-data center optical interconnects up to 2km: The TERIPHIC project approach", *Proc. SPIE 11308, Metro and Data Center Optical Networks and Short-Reach Links III*, 113080C (2020); <https://doi.org/10.1117/12.2545352>

- [8] **Christos Tsokos**, Efstathios Andrianopoulos, Adam Raptakis, Nikolaos Lyras, Lefteris Gounaridis, Panos Groumas, Hercules Avramopoulos, and Christos Kouloumentas, "Optical Beamforming Networks Supporting Multibeam and Multicast Operation," *2020 22nd International Conference on Transparent Optical Networks (ICTON)*, pp. 1-5, (2020), doi: 10.1109/ICTON51198.2020.9203380

Acknowledgements

Η εκπόνηση μιας διδακτορικής διατριβής, σε ένα τόσο επιτυχημένο και διεθνώς αναγνωρισμένο ερευνητικό εργαστήριο, όπως αυτό του Εργαστηρίου Φωτονικών Επικοινωνιών (ΕΦΕ) του Εθνικού Μετσόβιου Πολυτεχνείου, αποτελεί ξεκάθαρα μια μεγάλη πρόκληση αλλά ταυτόχρονα και μια τεράστια ευκαιρία για κάθε ερευνητή για να διαπρέψει στο πεδίο της Φωτονικής. Για να το πετύχει κάποιος αυτό, εκτός από τις προσωπικές αρετές και την εσωτερική κινητήρια δύναμη που θα τον ωθεί ώστε να εξερευνήσει νέα πράγματα και να εξελιχθεί, χρειάζεται να περιτριγυρίζεται από σπουδαίους ανθρώπους. Έτσι λοιπόν, φτάνοντας αισίως προς το τέλος αυτού του “ταξιδιού”, έπειτα από επτά χρόνια, γεμάτα χαρές και όμορφες στιγμές, θα ήθελα να ευχαριστήσω τους ανθρώπους που συνέβαλαν, ο καθένας με τον δικό του, μοναδικό τρόπο, στην εκπόνηση της παρούσας διατριβής.

Καταρχάς, θα ήθελα να ευχαριστήσω θερμά τον κ. Ηρακλή Αβραμόπουλο, διευθυντή του ΕΦΕ και επιβλέποντα καθηγητή μου, για την καθοδήγηση και την εμπιστοσύνη που μου έδειξε. Δίπλα μου, τόσο στις ευχάριστες αλλά και όσο στις δύσκολες στιγμές, πάντα με ένα ειλικρινές χαμόγελο να μου δίνει δύναμη και κουράγιο να συνεχίσω. Η πλήρη στήριξη που μου προσέφερε και οι συμβουλές του αποτέλεσαν τον οδηγό στην ερευνητική και στην προσωπική μου εξέλιξη.

Επίσης, οφείλω ένα μεγάλο ευχαριστώ στον Χρήστο Κουλουμένα, ο οποίος με καθοδηγούσε από την πρώτη στιγμή και συνέβαλε τα μέγιστα στην ολοκλήρωση της παρούσας διατριβής. Η μεθοδικότητα, η επιμονή και υπομονή του, αποτέλεσαν πηγή έμπνευσης και τη πυξίδα μου στο πως να αντιμετωπίζω ερευνητικές προκλήσεις και πως να γίνω όσο το δυνατόν καλύτερος ερευνητής.

Εν συνεχεία, θα ήθελα να ευχαριστήσω και τα υπόλοιπα μέλη της ομάδας, με τα οποία είχα την τύχη και χαρά να συνεργαστώ όλα αυτά τα χρόνια. Συγκεκριμένα, ένα μεγάλο ευχαριστώ στον Πάνο Γκρούμα, ο οποίος αποτέλεσε αδελφική φιγούρα για μένα σε αυτό το “ταξίδι” καθώς ήταν πάντα δίπλα μου για να με βοηθήσει και να με συμβουλευτεί. Επίσης, θα ήθελα να ευχαριστήσω τον Βασίλη Κατωπόδη, τον πρώτο μου πειραματικό συνεργάτη, για όλη τη βοήθεια του. Παρομοίως, ευχαριστώ τον Λευτέρη Γουναρίδη για τις αμέτρητες εποικοδομητικές συζητήσεις αλλά κυρίως επειδή το χαμόγελο και ο θετικός χαρακτήρας του αποτέλεσαν φάροι αισιοδοξίας στις δύσκολες στιγμές. Ακόμα, θα ήθελα να ευχαριστήσω τον Ηλία Μυλωνά και Αδάμ Ραπτάκη για την πολύτιμη βοήθεια τους. Νιώθω τυχερός που μέσα στα πλαίσια του εργαστηρίου, γνώρισα αυτά τα δυο παιδιά, για τα οποία όσα επίθετα και να χρησιμοποιήσεις, δύσκολα μπορείς να περιγράψεις τον αδαμάντινο χαρακτήρα τους. Επίσης, θα ήθελα να ευχαριστήσω τον Στάθη Ανδριανόπουλο, ένα πολλά υποσχόμενο ερευνητή, με τον οποίο είχα την χαρά να συνεργαστώ στενά τα τελευταία χρόνια και του οποίου η βοήθεια ήταν πάρα πολύ σημαντική. Το γεγονός ότι σε κάθε ερευνητικό πρόβλημα, καταλήγαμε στο ίδιο συμπέρασμα, ακολουθώντας διαφορετικά μονοπάτια συνεχίζει ακόμα και τώρα να με εκπλήσσει. Ακόμα, θα ήθελα να ευχαριστήσω τον Νικόλαο Λύρα και την Μαρία Μασσαούτη για τις ενδιαφέρουσες συζητήσεις και πολύτιμες συμβουλές τους. Τέλος, θα ήθελα να ευχαριστήσω από καρδιάς τον Κωστή Χριστογιάννη για την πολύτιμη βοήθεια, την υποστήριξή του και για τις ευχάριστες στιγμές μας στην “θέα”.

Παράλληλα, θα ήθελα να ευχαριστήσω θερμά τον Chris Roeloffzen, τον επιστημονικό υπεύθυνο της Lionix International για την πολύτιμη βοήθειά του καθώς μεγάλο μέρος της διατριβής είναι το αποτέλεσμα της εξαιρετικής μας συνεργασίας.

Ευχαριστίες για την αρμονική συνύπαρξή μας στο ΕΦΕ, οφείλω τόσο στα νεότερα όσο και παλαιότερα μέλη, Μαριλύ Σπυροπούλου, Δημήτρη Αποστολόπουλο, Παρασκευά Μπακόπουλο, Σάννου Παρασκευοπούλου, Γιάννη Γιαννούλη, Γιάννη Κανάκη, Κώστα Τόκα,

Χάρη Ζέρβο, Γιάννη Πουλόπουλο, Νίκο Ηλιάδη, Νίκο Αργύρη, Δημήτρη Καλαβρουζιώτη, Χρήστο Σπαθαράκη, Κωνσταντίνα Καντά, Δημήτρη Ζαβιτσάνο, Παναγιώτη Τουμάση, Δημήτρη Γουναρίδη, Βάσια Λαμπροπούλου και Πόλυ Βλάση.

Φυσικά, δεν θα μπορούσα να παραλείψω την σύντροφό μου, Νικολέττα Παυλίτινα, η οποία αποτελεί το δικό μου απάνεμο λιμάνι. Την ευχαριστώ για την αγάπη της και για την αμέριστη υποστήριξη της που μου δίνουν δύναμη να συνεχίσω να εξελίσσομαι και να προοδεύω.

Κλείνοντας, θα ήθελα να πω τα μεγαλύτερα ευχαριστώ στον πατέρα μου, Βασίλη και στη μητέρα μου, Γεωργία, για την αγάπη τους και για όλες τις θυσίες που έκαναν τόσα χρόνια για να μπορέσω να σπουδάσω και να κυνηγήσω τα όνειρα μου. Στα αδέρφια μου, Μαρίνο, Λευτέρη και Ταξιάρχη, στα ανίψια μου, Γεωργία, Ιωάννα, Βασίλη και στον διάδοχο, Χρήστο αλλά και στην αγαπημένη μου Χαρά για την ανιδιοτελή αγάπη και στοργή τους. Σας ευχαριστώ που είστε πάντα δίπλα μου και μου δίνετε απλόχερα όλη την αγάπη σας.